



Durham E-Theses

Breakup of the Gondwana supercontinent: East African perspectives from the Early Jurassic to Cretaceous

PHETHEAN, JORDAN, JERAD, JOHN

How to cite:

PHETHEAN, JORDAN, JERAD, JOHN (2018) *Breakup of the Gondwana supercontinent: East African perspectives from the Early Jurassic to Cretaceous*, Durham theses, Durham University. Available at Durham E-Theses Online: <http://etheses.dur.ac.uk/12667/>

Use policy

The full-text may be used and/or reproduced, and given to third parties in any format or medium, without prior permission or charge, for personal research or study, educational, or not-for-profit purposes provided that:

- a full bibliographic reference is made to the original source
- a [link](#) is made to the metadata record in Durham E-Theses
- the full-text is not changed in any way

The full-text must not be sold in any format or medium without the formal permission of the copyright holders.

Please consult the [full Durham E-Theses policy](#) for further details.

Academic Support Office, Durham University, University Office, Old Elvet, Durham DH1 3HP
e-mail: e-theses.admin@dur.ac.uk Tel: +44 0191 334 6107
<http://etheses.dur.ac.uk>

Breakup of the Gondwana supercontinent: East African perspectives from the Early Jurassic to Cretaceous



Jordan Jerad John Phethean

A thesis submitted in partial fulfilment of the requirements for the degree of Doctor of

Philosophy at Durham University

Department of Earth Sciences

October, 2017

1 **Abstract**

2

3 Accurate mapping of first-order tectonic features such as oceanic fracture zones and continental
4 margins is vital for the production of reliable plate reconstructions. These reconstructions allow
5 for a better understanding of the palaeo-configuration of continental fragments within
6 Gondwana and ultimately provide insight into how and why supercontinents break apart.
7 Detection of spreading lineaments within the heavily sedimented Western Somali Basin (WSB)
8 has been achieved using a novel technique based on directional derivatives of free-air gravity.
9 This new lineament dataset allows for the construction of a high-resolution plate tectonic
10 reconstruction of the WSB, which is in good agreement with ocean magnetic data and the
11 position of the abandoned WSB spreading centre. The model also reveals a change in spreading
12 direction, from NNW-SSE to N-S, during the Late Jurassic. This controversial spreading
13 direction change places the origin of Madagascar within the Tanzania Coastal Basin (TCB),
14 inboard of the Davie Fracture Zone (DFZ), which was previously believed to be the continent-
15 ocean transform margin of the WSB. This tight-fit of Gondwana fragments prior to continental
16 breakup necessitates a reassessment of both the crustal nature of the TCB, which is shown to be
17 partly oceanic in nature, and of the nature of the margins surrounding the WSB. The northern
18 margins of the WSB are likely orthogonally rifted margins. However, the western margins are
19 likely highly segmented and/or obliquely rifted margins. The model also predicts a large
20 transform offset along the Rovuma Basin.

21 Systematic gravity modelling and combined seismic investigations along the Rovuma basin
22 reveals the ‘Rovuma Transform Margin’, which offsets the obliquely rifted margins of northeast
23 Mozambique and Tanzania. The discovery of this transform margin confirms the initial SSE
24 plate motion predicted from gravity lineament analysis and plate reconstructions, and shows that
25 the breakup of the Gondwana supercontinent occurred not just along pre-existing lithospheric
26 weaknesses associated with the Karoo rift system, but also along newly developed highly
27 oblique deformation zones as well. The final breakup of the Gondwana supercontinent, which
28 followed extensive and episodic Karoo aged rifting, was coincident with extensive magmatism
29 in Mozambique and may therefore have been triggered by the interaction of several facilitators
30 of continental breakup (i.e. oblique rifting, pre-existing weaknesses, and magmatism).

31 The oblique breakup of Gondwana along the TCB led to the development of a segmented mid-
32 ocean ridge system within this basin, offset by SSE trending fracture zones. These fracture
33 zones were incompatible with the N-S spreading that followed the Late Jurassic change in plate
34 motion, resulting in the abandonment of mid-ocean ridge segments and compression within this

35 basin. This compression led to the formation of the 250 km long Tanzania Coastal Basin thrust
36 belt, the largest intraplate oceanic thrust belt yet discovered. The cessation of compression
37 within the TCB followed the development of the DFZ, which propagated from south to north.
38 This structure was subsequently dominated by transpression throughout its history, suggesting it
39 was not perfectly compatible with plate driving forces. Formation of the DFZ along aligned
40 weak rifted margins and young oceanic crust may have resulted in the mismatch of plate
41 motions and driving forces, and also suggests a first order 'top-down' control on plate motions
42 during the breakup of Gondwana.

43

44	Contents	
45		
46	Abstract	i
47	Contents	iii
48	List of figures	viii
49	Declaration	xi
50	Acknowledgements	xii
51	1. Introduction	1
52	1.1. Motivation and methods summary	1
53	1.2. Plate tectonics, the Wilson cycle, and what drives them	2
54	1.3. Passive continental margins	6
55	1.3.1. Divergent Margins	7
56	1.3.2. Transform and oblique Margins	8
57	1.3.2.1. Transform development at the onset of rifting or shortly after	8
58	1.3.2.2. Transform development at the onset of spreading or later	10
59	1.3.3. Characterisation of passive margins	11
60	1.3.3.1. Volcanic rifted margins	12
61	1.3.3.2. Magma-poor rifted margins	12
62	1.3.4. Characterisation of Transform Margins	14
63	1.4. Gondwana assembly and breakup	15
64	1.5. Thesis outline	18
65	1.6. References	19
66	2. Madagascar's escape from Africa: A high-resolution plate reconstruction for the Western	
67	Somali Basin and implications for supercontinent dispersal	24
68	Abstract	24
69	2.1. Introduction	25
70	2.2. Data and processing	28
71	2.2.1. Gravity data	28

72	2.2.1.1. Bandpass filtering and gravity gradients.....	28
73	2.2.1.2. Testing the detection method.....	29
74	2.2.2. Magnetics.....	30
75	2.2.3. Seismic reflection data.....	31
76	2.3. Feature identification.....	31
77	2.3.1. Mid-oceanic ridge segments.....	31
78	2.3.2. Fracture zones.....	32
79	2.4. Plate tectonic reconstruction.....	33
80	2.5. Results.....	33
81	2.5.1. MOR segment locations.....	34
82	2.5.2. Fracture zone trends.....	36
83	2.5.3. Plate tectonic model.....	41
84	2.6. Discussion.....	43
85	2.6.1. The nature of the WSB's margins and of gravity lineaments in the coastal basins...	43
86	2.6.2. Rifting mechanisms and Gondwana breakup.....	46
87	2.6.3. Plate tectonic reconstruction.....	48
88	2.7. Conclusions.....	50
89	2.8. References.....	51
90	2.9. Supplementary material.....	54
91	3. The Rovuma Transform Margin: Pinning down the East African continent-ocean transform	
92	margin using seismic and gravity methods.....	64
93	Abstract.....	64
94	3.1. Introduction.....	64
95	3.2. Characterisation of passive continental margins.....	67
96	3.3. Data and Methods.....	68
97	3.3.1. Seismic reflection data and interpretation.....	69
98	3.3.2. Gravity data.....	69
99	3.3.3. Gravity modelling.....	70
100	3.3.3.1. Modelling type 1: Systematic investigation of Moho geometry.....	71

101	3.3.3.1.1. Bathymetry surface	73
102	3.3.3.1.2. Sediment density	74
103	3.3.3.1.3. Sediment thickness.....	75
104	3.3.3.1.4. Crustal density and thickness in the ocean and continent.....	75
105	3.3.3.2. Model type 2: Determining the margin trend	76
106	3.3.3.3. Model type 3: Detailed 2D gravity models.....	77
107	3.4. Results.....	78
108	3.4.1. Seismic reflection observations	78
109	3.4.1.1. Mz1_8100	78
110	3.4.1.2. Mz1_8000	78
111	3.4.1.3. Mz1_7500	79
112	3.4.1.4. Mz1_1030	81
113	3.4.2. Gravity	82
114	3.4.2.1. Model type 1: Best fit ramp-style Moho geometries across the margin	82
115	3.4.2.1.1. Comparison of crustal thickness profiles to a global compilation of margins	
116	84
117	3.4.2.2. Model type 2: Best-fit locations for average margin geometries and margin trend	
118	85
119	3.4.2.3. Model type 3: Detailed 2D gravity modelling	89
120	3.5. Discussion	92
121	3.5.1 The continental margin of northern Mozambique and southern Tanzania	92
122	3.5.2 Changes in margin style across the Lurio Belt	93
123	3.5.3 Possible plate tectonic models	95
124	3.5.4 Transform margin development and impacts	96
125	3.6. Conclusions.....	97
126	3.7. References.....	98
127	3.8. Supplementary material	101
128	3.8.1. Misfit between gravity datasets	101
129	3.8.2. Examples of seabed surfaces generated using alternative filter cut-off wavelengths	
130	103

131	3.8.3. Deriving an average sediment density for the WSB for use in 2D gravity models .	105
132	3.8.4. Determination of the thickness of continental crust	108
133	3.8.5. Resolving gravity misfits of type 2 models	108
134	4. Compressional consequences of complex spreading: Formation of the Tanzania Coastal Basin	
135	and Davie Fracture Zone during the Mesozoic East Africa breakup.....	110
136	Abstract.....	110
137	4.1. Introduction.....	111
138	4.2. Database.....	112
139	4.3. Pre-breakup position of Madagascar	114
140	4.4. Major tectonic signatures of the TCB, DFZ, and Western Somali Basin.....	116
141	4.4.1. Cessation of spreading in the TCB	117
142	4.4.2. Compression post SSE spreading	118
143	4.4.2.1. Line tz1_4000 (west)	119
144	4.4.2.2. Line tz3_3600 (west)	121
145	4.4.2.3. Line tz4_3300	123
146	4.4.2.4. Line tz4_2950	125
147	4.4.2.5. Summary of compressional deformation within the TCB.....	128
148	4.4.3. The DFZ.....	130
149	4.4.3.1. Line tz1_4000 (east)	130
150	4.4.3.2. Line tz3_3600 (east)	132
151	4.4.3.3. Line tz4_3350	135
152	4.4.3.4. Line tz4_2850	137
153	4.4.3.5. Line tz3_2101	139
154	4.4.3.6. South of the Quirimbas Graben	142
155	4.4.3.7. Summary of the DFZ formation	144
156	4.5. Regional tectonic interpretation.....	148
157	4.6. Implications for plate motion controls.....	151
158	4.7. Conclusions.....	152
159	4.8. References.....	152

160	4.9. Supplementary material	155
161	4.9.1. Alternative interpretation of seismic line tz4_3300.....	155
162	5. Discussion, conclusions, and future work.....	156
163	5.1. References.....	160
164		
165		

166 **List of figures**

167

168	1.1	Known distribution of the continents in 1912.....	3
169	1.2	Known configuration of the tectonic plates in 1968	4
170	1.3	Movement of plates on a sphere	5
171	1.4	Periodic events linked to the Wilson Cycle throughout Earth's history.....	6
172	1.5	Development of transform and oblique margins	9
173	1.6	Interbasinal transfer zone geometries	10
174	1.7	Key characteristics for each of the continental margin types	11
175	1.8	Supercontinent reconstructions for Rodinia and Gondwana	16
176	1.9	Schematic development of the Karoo rift system.....	18
177	2.1	Previous plate reconstructions of Madagascar.....	27
178	2.2	Testing the gravity processing technique.....	30
179	2.3	Identification of the mid-ocean ridge system in the Western Somali Basin.....	35
180	2.4	Free-air gravity anomaly.....	38
181	2.5	E-W derivative of a Gaussian band-pass filtered free-air anomaly.....	39
182	2.6	The EMAG2 non-directionally gridded magnetic anomaly dataset	40
183	2.7	Plate tectonic reconstruction of Madagascar's escape from Africa from the Early	
184		Jurassic to the cessation of spreading in the Cretaceous.....	42
185	2.8	Oceanic crust within the Tanzania Coastal Basin.....	45
186	2.9	Concluding figure for Chapter 2	50
187	S2.1	Maximum free-air gravity directional derivative from azimuths of	
188		240°/250°/260°/270°/280°/290°/300°	56
189	S2.2	Maximum free-air gravity directional derivative from azimuths of	
190		250°/260°/270°/280°/290°	57
191	S2.3	Maximum free-air gravity directional derivative from azimuths of	
192		260°/270°/280°	58

193	S2.4	Free-air gravity directional derivative at an azimuth of 270°	59
194	S2.5	Maximum free-air gravity directional derivative from azimuths of	
195		330°/340°/350°/0°/10°/20°/30°	60
196	S2.6	Maximum free-air gravity directional derivative from azimuths of	
197		340°/350°/0°/10°/20°	61
198	S2.7	Maximum free-air gravity directional derivative from azimuths of 350°/0°/10°	62
199	S2.8	Free-air gravity directional derivative at an azimuth of 0°	63
200	3.1	Location map for Chapter 3	66
201	3.2	Normalised frequency distribution of average Moho slope angles across the	
202		necking zones of magma-poor rifted margins and transform margins	68
203	3.3	Locations of seismic and gravity profiles, and summary of gravity modelling	
204		methods	72
205	3.4	Bathymetry data	74
206	3.5	ION seismic reflection profiles crossing the continental margin	80
207	3.6	Depth-converted ION seismic reflection LINE mz1_1030	82
208	3.7	RMSD fits of Moho location and angle configurations for gravity profiles 1-3 as	
209		determined from type 1 modelling	84
210	3.8	Normalised crustal thickness profiles across transform and rifted margins	85
211	3.9	Comparison of Type 1 and Type 2 model results for profile 1	86
212	3.10	Results for Type 2 modelling	88
213	3.11	Detailed crustal structure as determined from type 3 modelling	91
214	S3.1	Comparison of different gravity datasets	102
215	S3.2	Seabed surface without short wavelength replacement	103
216	S3.3	Seabed surface with replacement of wavelengths <10 km	103
217	S3.4	Seabed surface with replacement of wavelengths <20 km	104
218	S3.5	Seabed surface with replacement of wavelengths <30 km	104
219	S3.6	Measured and seismic-derived sediment velocities from DSDP 241	105
220	S3.7	Measured and seismic-derived sediment densities at DSDP 241	106

221	S3.8	Seismic-derived sediment densities along seismic line V3618	107
222	S3.9	Type 1 modelling results using different thicknesses for the continental crust.	108
223	S3.10	Best-fit result of Type 2 modelling of profile 6.....	109
224	S3.11	Adjustments required to remove misfits following Type 2 modelling of profile	
225		6.....	109
226	4.1	Location map for Chapter 4	113
227	4.2	Satellite image of faults in the Bajocian-Bathonian deposits of the northern	
228		Morondava Basin	116
229	4.3	Extinct ocean spreading segment identified within the TCB.....	117
230	4.4	Thrusting and folding of the basement along seismic line tz1_4000 (west).....	120
231	4.5	Thrusting and folding of the basement along seismic line tz3_3600 (west).....	122
232	4.6	Thrusting of the basement along seismic line tz4_3300	124
233	4.7	Folding and thrusting of the basement along seismic line tz4_2950	127
234	4.8	Folding, thrusting, and strike slip deformation along seismic line tz1_4000 (east)	
235		131
236	4.9	Folding, thrusting, and strike slip deformation along seismic line tz3_3600	133
237	4.10	Folding, thrusting, and strike slip deformation along seismic line tz4_3350	136
238	4.11....	Folding, thrusting, and strike slip deformation along seismic line tz4_2850 ..	138
239	4.12	Folding, thrusting, and strike-slip deformation along seismic line tz3_2101	140
240	4.13	Reinterpreted seismic lines from the literature	144
241	4.14	Alignment of weak lithosphere during the Late Jurassic change in plate motion	
242		147
243	4.15	Major tectonic events of the Western Somali basin in the regional context.....	150
244	S4.1	Alternative interpretation of seismic line tz4_3300.....	155
245	5.1	Possible microcontinent cleaving during Late Jurassic plate motion changes	159
246			
247			

248 **Declaration**

249 I declare that this thesis, which I submit for the degree of Doctor of Philosophy at Durham
250 University, is my own work and not substantially the same as any which has previously been
251 submitted at this or any other university.

252

253 Jordan J. J. Phethean

254 Durham University

255 October 2017

256

257 Signed: _____

258 Jordan Phethean

259 Date: _____

260

261

262

263

264

265

266

267

268

269

270 © The copyright of this thesis rests with the author. No quotation from it should be
271 published without prior written consent and information derived from it should be
272 acknowledged.

273 **Acknowledgements**

274 I am very thankful to my supervisory team, whose endless support, encouragement,
275 and expert training has enabled me to make it this far. Firstly, I would like to give
276 special thanks to Jeroen van Hunen for his truly invaluable guidance and advice in
277 all matters, both academic and beyond. In all circumstances, Jeroen makes time for
278 his students and without his constant positive outlook some obstacles would have
279 seemed unsurmountable. I would also like to thank Lara Kalnins for taking me under
280 her wing and providing me with outstanding technical guidance when it was needed
281 most. She is an exceptional and rigorous scientist, whose input has improved the
282 quality of my work to no end. Thanks also go to Ken McCaffrey for his academic
283 insights, which are always delivered with a chuckle, and to Paolo G. Biffi for his
284 great observations and ability to keep my best interests at heart. Finally, I would like
285 to thank Richard Davies for believing in me and for his endless ‘can-do’ attitude that
286 led to this project.

287 I would also like to thank my friends and colleagues at ENI who made me feel so
288 welcome in a place so far from home, particularly Dorina Testi.

289 Colin Reeves and David Boote provided insightful discussions, which proved
290 extremely useful to me, and I hope they continue in the coming years.

291 Special thanks go to my parents, John and Kath, whose encouragement, guidance,
292 and help throughout my life has helped me reach where I am today. I would also like
293 to thank my Nana, Grandad, Aunti Guina, and Uncle Donald for their support both
294 before and during this project. My brother James, niece Beth, and Jade are thanked
295 for the good times gone and those yet to come.

296 I would like to thank my friends in Durham and elsewhere for their kindness and for
297 making life so much fun. The list is large, and you know who you are, so I’m going
298 to spare us all. However, in particular I would like to thank Alex Peace, Bob
299 Jamieson, Chris Harbord, Matt Keeves, Kate Horan and Sarah Clancy, with whom I
300 have a particularly large number of fond memories.

301

1. Introduction

302

1.1. Motivation and methods summary

303

Rifted margins are of significant interest as they provide insight into the causes and

304

mechanisms of supercontinent breakup (e.g. Bercovici and Long, 2014). But besides this

305

academic interest, they have also provided a reliable worldwide source of hydrocarbon

306

resources for over 30 years (Levell et al., 2010) and economic and political forces have

307

recently driven a strong shift towards the exploration of deep-water (500-2500 m below sea

308

level) regions of these margins (White et al., 2003). A wealth of research, focused on the

309

evolution of volcanic and magma-poor rifted margins (e.g. Afilhado et al., 2008; Brune et

310

al., 2013; Geoffroy et al., 2015; Manatschal, 2004; Reston and Mcdermott, 2014), shows

311

that the extent of continental crust and the nature of the continent-ocean transition in these

312

deep-water settings are highly variable (e.g. Stab et al., 2016; Unternehr et al., 2010), and

313

have strong impacts on the presence and maturation of source rocks (e.g. Waples, 2002).

314

Transform margins, on the other hand, have been relatively poorly studied (Mercier de

315

Lépinay et al., 2016) and, in the past, have not presented a major target for the hydrocarbon

316

industry. The 2007 discovery of the Jubilee field along the West Africa transform margin

317

(Dailly et al., 2013), however, opened up a new play type and dramatically increased interest

318

in transform margins. East Africa is, at a basic level, understood to represent such a

319

transform margin, and as such new interest in the region is rapidly growing. However, the

320

details of kinematic and dynamic margin development, as well as the extent of continental

321

crust is poorly understood along the East African margins and at transform margins in

322

general.

323

Reducing these uncertainties invites further interest in the exploration of the East African

324

rifted margins for hydrocarbon resources, and is crucial for the successful discovery and

325

development of said resources. In order for East Africa to benefit economically from its

326

potential natural resources, and to allow associated benefits of development opportunities,

327

stability, and prosperity to East Africa, it is therefore necessary to constrain these unknowns.

328

Plate motions during Gondwana disassembly, and the initial configuration of continental

329

fragments and deformation zones in Gondwana, are a matter of particular controversy (e.g.

330

Bunce and Molnar, 1977; Coffin and Rabinowitz, 1987; Davis et al., 2016; Gaina et al.,

331

2013; Klimke et al., 2017; Lawver and Scotese, 1987; Norton and Sclater, 1979; Pinna,

332

1995; Project, 2015; Reeves, 2014; Scrutton et al., 1981; Ségoufin and Patriat, 1980;

333 Shackleton, 1996; Smith and Hallam, 1970; Windley et al., 1994), and so the development
334 of accurate and reliable plate tectonic models for the region is fundamental before more
335 detailed understanding of the margin can be attempted. In order to constrain the plate
336 motions during the disruption of Gondwana we apply novel processing techniques to
337 recently available and highly accurate marine satellite gravity data. This successfully allows
338 us to develop a highly accurate plate reconstruction for the region that, due to the nature of
339 continental margins being dependant on plate motions relative to zones of lithospheric
340 deformation (e.g. Basile and Braun, 2016), indicates which styles of continental margin
341 should develop along different regions of the East Africa coast; a crucial step in the
342 development of our understanding of this enigmatic region.

343 The extent of continental crust along rifted margins is another key parameter in resource
344 prospectivity, however, is not well constrained by such kinematic plate tectonic
345 reconstructions. We therefore also perform rigorous 2D gravity modelling of the margin
346 structure to locate the boundary between oceanic and continental crust. This confirms the
347 proposed natures of the East African margins gained from Plate tectonic modelling.

348 Finally, in order to better understand transform margin development in general, which can
349 not only reduce risk and interest in the study region but can also contribute to our
350 understanding of transform margins worldwide, we perform a detailed study of the structural
351 development of this margin through the interpretation of high quality deep imaging seismic
352 reflection data. This interpretation allows for a model of the development of the East African
353 margins to be constructed, which bears strong similarities to other transform systems
354 worldwide (e.g. Whittaker et al., 2016; Schiffer et al., 2017) and may therefore contribute to
355 a unified understanding of transform margin processes.

356 **1.2. Plate tectonics, the Wilson cycle, and what drives them**

357 The theory of plate tectonics was formulated in 1968 (Morgan, 1968) and is one of the
358 fundamental principles on which the work presented herein relies. The roots of this theory,
359 however, lie much earlier.

360 As early as 1596, the ‘lock and key’ geometry of Africa-Europe and America (Figure 1.1)
361 was noted by the Flemish-Dutch cartographer Abraham Ortelius in ‘Thesaurus
362 Geographicus’ (Ortelius, 1596). He went on to propose that the continents were “torn
363 away...by earthquakes and floods”. This remarkable insight was, however, ahead of its time
364 and it was not until 1912 that the German meteorologist Alfred Wegener developed the
365 hypothesis for ‘continental drift’. Importantly, Wegener used observations from the

366 geologic, climatic, fossil, and palaeo-topographic records to support the argument for an
367 original connection of the continents in his seminal work ‘Die Entstehung der Kontinente’
368 (‘The Origin of the Continents’) (Wegener, 1912).

369



370

371 **Figure 1.1.** Known distribution of landmasses (thin black lines) and continental shelf edges
372 (thick black lines), in 1912, showing the similarity in the outlines of the east and west
373 Atlantic margins. Image extract from Wegener (1912).

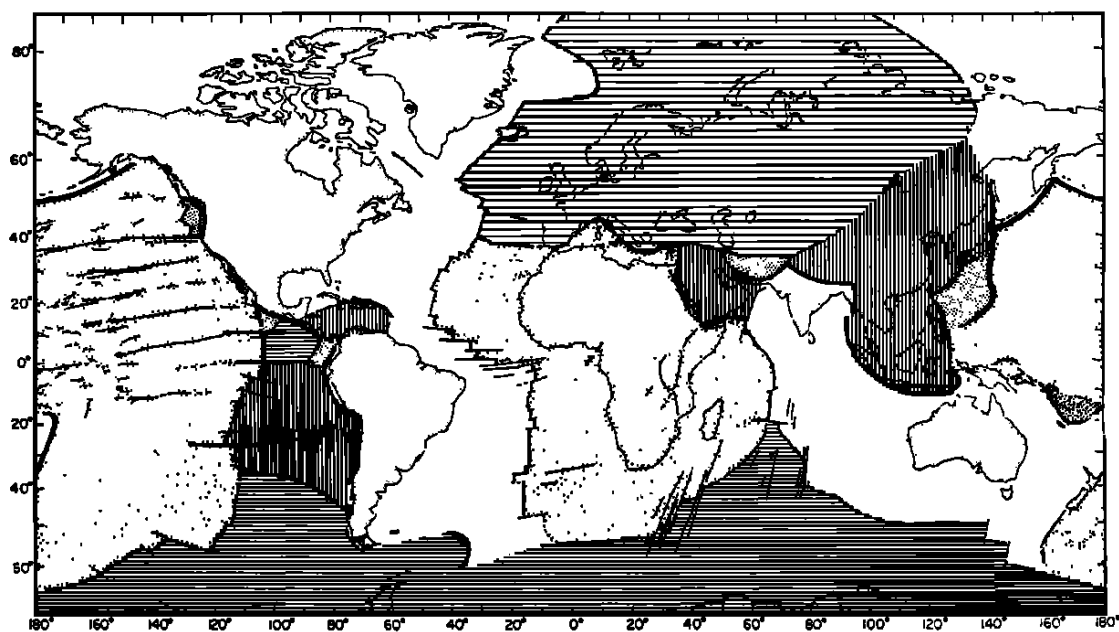
374 At first, this paradigm shifting hypothesis was strongly opposed by many due to the lack of a
375 viable mechanism by which the continents could ‘plough through’ solid oceanic crust (e.g.
376 Frankel, 1990). And at the time ‘Geosynclinal Theory’, developed in the 1800’s by James
377 Hall and James Dwight Dana (e.g. Knopf, 1948), was able to explain the major observations
378 from orogenic belts and sedimentary basins, as well as ocean development.

379 Support for continental drift, nonetheless, built throughout the 20th century, attested by the
380 publication of ‘Our Wandering Continents: An Hypothesis of Continental Drift’ by Alex du
381 Toit in 1937 (Du Toit, 1937). This shift was assisted by several key events that paved the
382 way for plate tectonics:

- 383 ○ 1931: Arthur Holmes hypothesises the occurrence of thermal convection within the
384 Earth due to the heat generated by radioactive decay, providing a driving mechanism
385 for plate motions (Holmes, 1931).
- 386 ○ 1935: Haskell determines the fluid behaviour of the mantle from the study of glacial
387 rebound, allowing for the drift of continents (Haskell, 1935).

- 388 ○ 1949: Benioff discovers Wadati-Benioff zones, suggesting a solution to space
- 389 problems associated with drifting continents and shrinking oceans (Benioff, 1949).
- 390 ○ 1962: Harry Hess proposes ‘seafloor spreading’ to occur along mid-ocean rises
- 391 (Hess, 1962).
- 392 ○ 1963: Vine and Matthews prove the occurrence of seafloor spreading using linear
- 393 magnetic reversals recorded in the oceanic crust ‘tape recorder’ (Vine and
- 394 Matthews, 1963).
- 395 ○ 1965: Runcorn uses polar wander to support the motion of the continents through
- 396 geologic time (Runcorn, 1965), and Wilson proposes the ‘transform fault’, the
- 397 “missing” type of plate boundary (Wilson, 1965).
- 398 ○ 1968: Jason Morgan coins the term ‘plate tectonics’, or the theory that ‘the surface
- 399 of the Earth is composed of several rigid plates all in relative motion about each
- 400 other as a natural consequence of thermal convection in the mantle’ (Figure 1.2),
- 401 and describes the motion of plates on the globe about poles of rotation (Morgan,
- 402 1968; Figure 1.3).

403



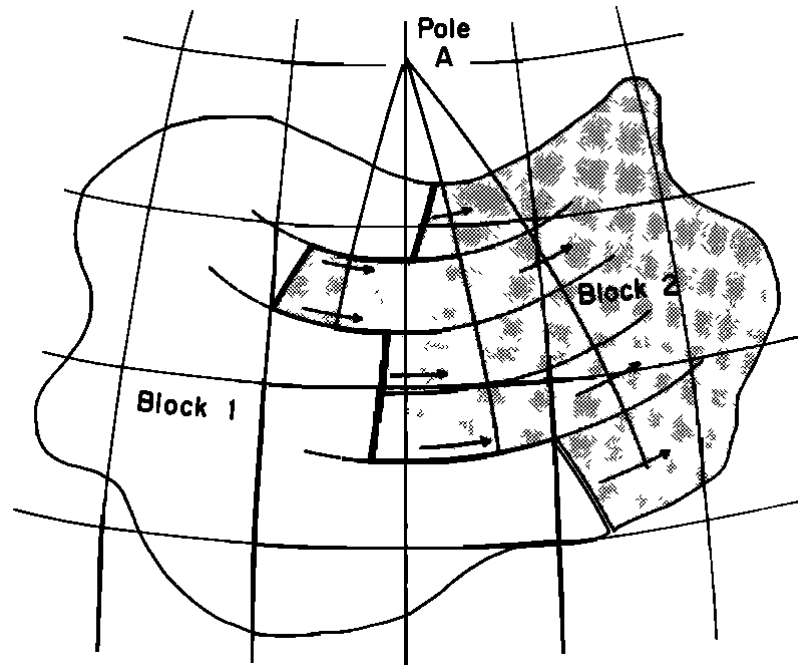
404

405 **Figure 1.2.** Configuration of the tectonic plates as initially described by Morgan (1968). The

406 boundaries between tectonic plates are seafloor spreading centres, ocean trenches

407 (subduction zones), and transform faults. Image from Morgan (1968).

408

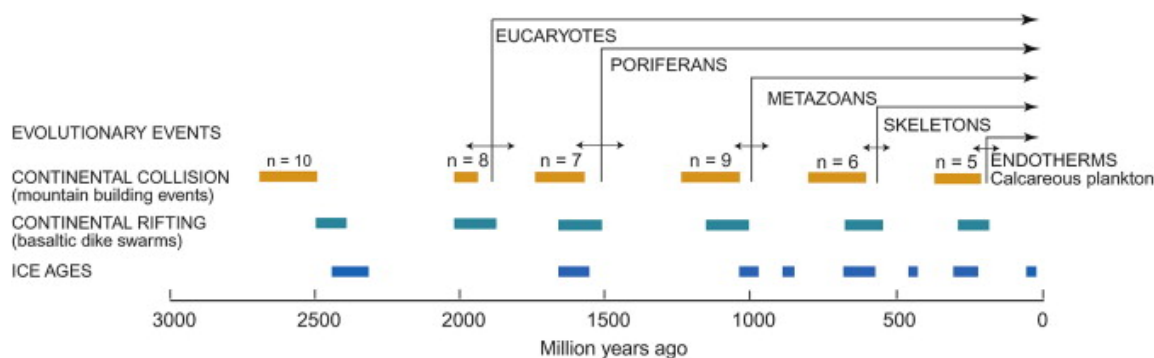


410

411 **Figure 1.3.** The motions of tectonic plates (Block 1 and Block 2) on the surface of a sphere
 412 must follow small circles about a pole of rotation (Pole A). Image from Morgan (1968).

413 Around this time it was also discovered that not only do tectonic plates collide and rift apart
 414 from each other, but that this process was cyclic. Careful analysis of the distribution of
 415 faunal realms on either side of the Atlantic Ocean by Wilson (1966) showed that a ‘proto-
 416 Atlantic’ must have opened and closed prior to the opening of the present day Atlantic
 417 Ocean. This cycle of rifting, continental breakup, ocean spreading, subduction initiation,
 418 ocean closing, and continental collision thus became known as the Wilson Cycle.

419 An inherent periodicity to such events of mountain building, sea level change, magmatism,
 420 climate, and even evolution was documented as early as the 1940’s by Umbgrove in “The
 421 Pulse of the Earth” (Umbgrove, 1947), however, it was not until 1984 that Worsley
 422 recognised these cycles as the manifestation of supercontinent assembly and breakup
 423 (Worsley et al., 1984). Regular episodes of continental collision and breakup related mafic
 424 magmatism throughout Earth’s history had been recognised through Rb/Sr and K/Ar dating
 425 (Condie, 1976; Windley, 1977) and were shown to occur at roughly 500 m.y. intervals
 426 (Figure 1.4). Subsequently, 4 or 5 supercontinent amalgamations have been proposed prior
 427 to the most recent assembly of Pangea.



429

430 **Figure 1.4.** Periodic events linked to the Wilson Cycle throughout Earth's history (Worsley
 431 et al., 1984). Image from Nance and Murphy (2013).

432 The driving force behind the Wilson (supercontinent) Cycle is, however, still a matter of
 433 debate today, and, whilst mantle convection is still generally recognised as an important
 434 factor in controlling plate motions (e.g. Ziegler, 1993), other drivers have been proposed to
 435 also play important roles. Common suggestions include ridge-push and slab-pull (e.g.
 436 Lithgow-Bertelloni, 2014), gravitational collapse along orogenic belts (e.g. Rey et al., 2001),
 437 and mantle plumes (a special case of mantle convection; e.g. Larson, 1991). The coincidence
 438 of many continental breakups with large igneous provinces has been used to support the role
 439 of hot mantle plumes in this phase of the Wilson Cycle (e.g. White and McKenzie, 1989).
 440 Examples of continental breakup lacking evidence for abnormal mantle temperatures during
 441 breakup, however, preclude the ubiquitous involvement of mantle plumes in this process
 442 (e.g. Storey, 1995). A distinction has therefore arisen between 'active' and 'passive' rifting
 443 to explain the generic observations from rifted margins: uplift, magmatism, and extension.
 444 During active rifting, uplift and melting are attributed to the impingement of a mantle plume
 445 or convection cell on the base of the lithosphere resulting in extension. During passive
 446 rifting, extension is attributed to an alternative driving force and results in the uplift and
 447 melting observed during rifting (e.g. Turcotte and Emerman, 1983).

448 **1.3. Passive continental margins**

449 Both active and passive rifting may result in a complete thinning of the continental
 450 lithosphere and the onset of seafloor spreading. This transition is termed continental
 451 breakup, and the zone of recently rifted continental crust becomes a passive margin. These
 452 features form 105,000 km of the world's continental margins, almost twice the length of
 453 convergent boundaries (53,000 km; Bradley, 2008), where one tectonic plate subducts
 454 beneath another. The term 'passive margin' may, however, be misleading as these types of
 455 margins are more and more commonly being found to undergo significant tectonic inversion,

456 resulting from compression, and uplift, possibly due to mantle dynamics, during their
457 'passive' stage (e.g. Japsen et al., 2012; Yamato et al., 2013). The causes of continental
458 rifting and the subsequent reactivation of passive margins are still a matter of debate and
459 form a key area of research today (e.g. Geoffroy et al., 2015; Rabineau et al., 2015)

460 Depending on the stress conditions under which they form, two endmember groups of
461 passive margins can develop. Where the trend of a deforming lithospheric zone is closely
462 orthogonal to the extension direction across it, divergent (rifted) margins are formed. When
463 the extension direction is closely parallel to the overall trend of a lithospheric deformation
464 zone, transform margins develop. Between these two endmembers, oblique margins may
465 develop and strain may be accommodated along transtensional normal faults, or may
466 become partitioned onto alternating divergent and transform segments (Basile and Braun,
467 2016).

468 1.3.1. Divergent Margins

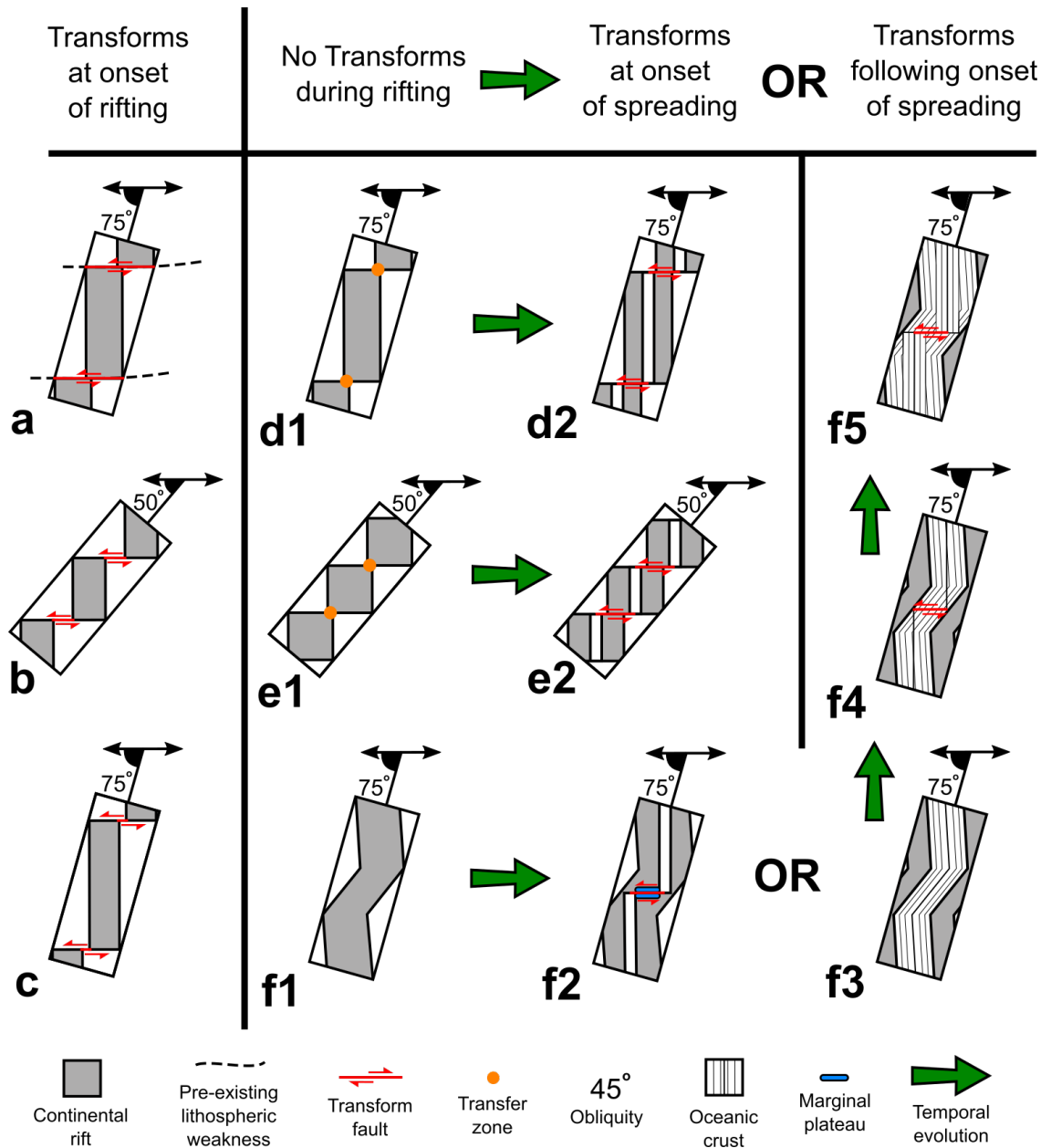
469 Divergent margins are commonly categorised by two end-member extremes. These are
470 volcanic rifted margins and magma-poor rifted margins, and are commonly distinguished by
471 the volume of syn-rift igneous rocks emplaced. Following breakup, passively upwelling
472 mantle replaces material that moves laterally away from an ocean spreading centre, and
473 consistently results in decompression melting, which produces an ~7 km thick crust (e.g.
474 Katz et al., 2003; White et al., 1992). Generally, an elevated mantle temperature, due to
475 continental insulation (e.g. Brandl et al., 2013) or mantle plumes (e.g. White and McKenzie,
476 1989), is invoked to explain the greater melt volumes observed at some volcanic rifted
477 margins. Several alternative hypotheses have, however, also been proposed including; rifting
478 speed (van Wijk et al., 2001), small-scale convection (SSC; Boutilier and Keen, 1999;
479 Mutter et al., 1988; Simon et al., 2009), chemical enrichment of the mantle (Lizarralde et al.,
480 2007), and rifting history (Armitage et al., 2010). The development of magma-poor rifted
481 margins may therefore be explained as the result of rifting away from mantle thermal
482 anomalies (e.g. Reston, 2009), although depth-dependent stretching of the lithosphere (e.g.
483 Huisman and Beaumont, 2011) and presence of a partially depleted sub-lithospheric mantle
484 (e.g. Pérez-Gussinyé et al., 2006) have also been proposed to control their development.
485 Significant variations in magmatism and rifting style over different length scales (e.g. Behn
486 and Lin, 2000; Franke et al., 2007; Lizarralde et al., 2007) precludes one single causal
487 mechanism, and demonstrates our incomplete understanding of the development of rifted
488 margins. In reality, a spectrum between the two endmember rifted margin types likely exist
489 (Franke, 2013) as the natural result of interplay between different mechanisms.

490 1.3.2. Transform and oblique Margins

491 In cases of continental rifting where the extension direction is not perpendicular to a
492 lithospheric deformation zone, oblique and/or transform margins develop. Following
493 breakup, mature ocean spreading centres predominantly accommodate extension in a fully
494 partitioned manner, i.e. along extension-perpendicular rifts connected by extension-parallel
495 transform faults. Exceptions are limited to slow and very slow spreading centres, e.g. the
496 Mohns (Dauteuil and Brun, 1996) and Reykjanes (Peyve, 2009) ridges, where oblique
497 oceanic accretion occurs. Strain partitioning thus occurs at the majority of plate boundaries
498 that developed in an oblique setting. The timing of this partitioning (i.e. transform fault
499 development) is, however, variable and several possible scenarios have been described by
500 Basile (2015) and are summarised below.

501 **1.3.2.1. Transform development at the onset of rifting or shortly after**

502 Where extension is closely parallel to pre-existing lithospheric weaknesses, such weaknesses
503 may be reactivated as transform faults at the onset of rifting (Figure 1.5a). This has been
504 proposed for several instances where oceanic transform faults are aligned with an onshore
505 tectonic structure such as in the South Atlantic (e.g. Wright, 1976) and Gulf of Aden
506 (Bellahsen et al., 2013). Alternatively, where a deformation zone is at low angles to the
507 extension direction (Figure 1.5b), or where narrow rifts predominate (Figure 1.5c),
508 individual rift segments do not overlap and may be connected by transform faults at the
509 onset of rifting or shortly thereafter.



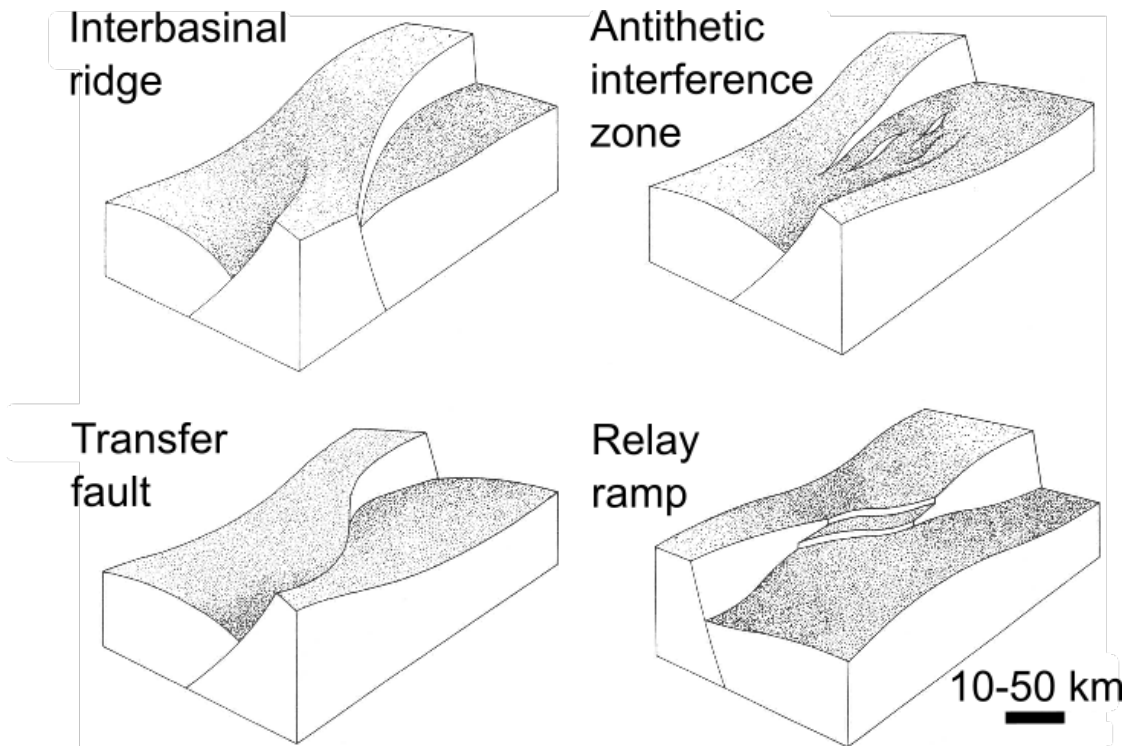
511

512 **Figure 1.5.** Development of transform and oblique margins. Left column: transform faults
 513 may be present at the onset of rifting along pre-existing lithospheric weaknesses (a) or
 514 between non-overlapping rift segments, which may result from a high obliquity (b) or
 515 narrow rift segments (c). Other columns: transform faults may not develop during rifting if
 516 rift segments overlap, which may occur in low obliquity settings (d1) or where wide rifts
 517 predominate (e1), or if transtensional rifting occurs (f1). In these cases, strain partitioning
 518 generally occurs at the onset of oceanic spreading (d2, e2, and f2) and new transform faults
 519 cut older rift structures in the continental crust. In the case of transtensional rifting,
 520 partitioning may also occur after a phase of oblique spreading (f3-5), in which case
 521 transforms may not develop in the continental crust and no transform margin will result.
 522 Figure after Basile (2015).

523 **1.3.2.2. Transform development at the onset of spreading or later**

524 Where a deformation zone lies at high angles to the extension direction (Figure 1.5d1), or
525 where wide rifts develop in more oblique settings (Figure 1.5e1), individual rift segments
526 may overlap. In this setting, transfer fault zones (e.g. Basile, 2015; Milani and Davison,
527 1988) separate rift segments and may accommodate the offset without the need for transform
528 faults. Common structures forming interbasin transfer zones include interbasinal ridges,
529 antithetic interference zones, transfer faults, and relay ramps (e.g. Gawthorpe and Hurst,
530 1993; Figure 1.6). Transtensional rifting is also able to accommodate oblique extension
531 without the need for transform faults (Figure 1.5f1). In these cases, strain partitioning onto
532 transforms may occur at the onset of oceanic spreading (Figure 1.5d2-f2; e.g Taylor et al.,
533 2009), in which case transform faults cut older rift structures and may result in the
534 development of marginal plateaus (Mercier de Lépinay et al., 2016). Alternatively, for the
535 case of transtensional rifting, partitioning may also occur after a phase of oblique spreading.
536 In this instance transform faults may not be present in the continental domain of an oblique
537 rifted margin (Figure 1.5f3-5).

538
539



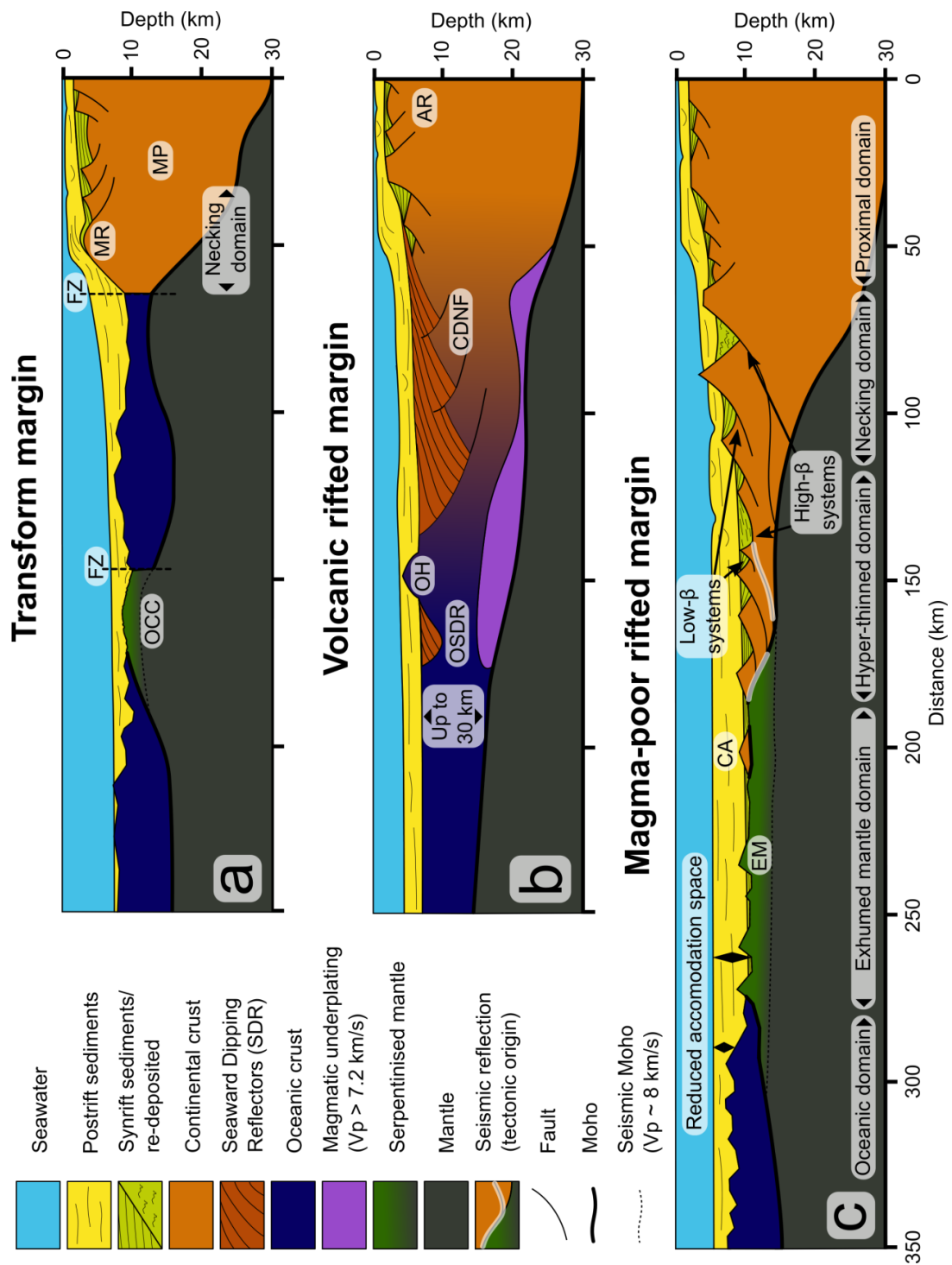
540

541 **Figure 1.6.** Interbasinal transfer zone geometries that may link offset, but overlapping, rift
542 systems without the need for transform faults. The vertical scale is greatly exaggerated.
543 Image from Gawthorpe and Hurst (1993).

544 1.3.3. Characterisation of passive margins

545 Each margin type is characterised by features that develop under the different rifting
 546 regimes. Identification of these features, through the use of geophysical methods, can allow
 547 for a robust differentiation between divergent and transform type margins. The main
 548 distinguishing features of the different categories of passive margin are summarised below
 549 and are shown in Figure 1.7.

550



551
 552
 553

554 **Figure 1.7.** Key characteristics of each margin type as described in Section 1.2. (a)
555 Transform margins commonly exhibit: narrow necking domains of the Moho and basement,
556 marginal plateaus, marginal ridges, adjacent thin oceanic crust and exhumed mantle at
557 oceanic core complex. (b) Volcanic rifted margins often show: continentward dipping
558 normal faults, adjacent abandoned rifts, SDRs, underplated high velocity lower crust,
559 initially thick ocean crust. (c) Magma-poor rifted margins generally display: up to 200 km of
560 thinned crust, both low- β and high- β fault systems, high amplitude seismic reflections along
561 low angle faults, exhumed and serpentinised mantle, initially thin oceanic crust. AR:
562 abandoned rift; CA: continental allochthon; CDFN: continentward dipping normal faults;
563 EM: exhumed mantle; FZ: fracture zone; MP: marginal plateau; MR: marginal ridge; OCC:
564 ocean core complex; OH: outer high; OSDR: outer seaward dipping reflectors.

565 **1.3.3.1. Volcanic rifted margins**

566 Where large volumes of melt are emplaced during rifting, volcanic rifted margins develop
567 (Figure 1.7b), and may indicate the breakup of the lithospheric mantle before or at the same
568 time as that of the crust (Franke, 2013). This magmatism manifests itself as thick wedges of
569 volcanic flows, identified in seismic reflection data as seaward dipping reflectors (SDRs),
570 and magmatic underplating, identified in seismic refraction studies as high velocity (>7.2
571 km/s) lower crustal bodies (Franke, 2013). As these margins develop and become
572 submerged, the introduction of water may result in explosive volcanism resulting in the
573 formation of an outer high, beyond which outer SDRs may develop as deep sea volcanic
574 sheet flows before the onset of normal oceanic crust production (Planke et al., 2000). The
575 enhanced melt production during breakup often also results in an initially over-thickened
576 oceanic crust up to 30 km thick (Geoffroy, 2005).

577 Crustal thinning at volcanic rifted margins often occurs adjacent to previous sedimentary
578 basins and is quite abrupt, occurring over 50-100 km (Figure 1.7b). Continentward dipping
579 normal faults may also accommodate the extension, although the large volumes of extrusive
580 volcanic rocks at these margins often masks rift structures making accurate identifications of
581 the last continental crust and the COT difficult (Stab et al., 2016). The considerable amounts
582 of intrusive magmatism and magmatic underplating also alter Moho geometries, which
583 therefore provide little insight into the structure of the continental crust as a result of rifting.

584 **1.3.3.2. Magma-poor rifted margins**

585 Where exhumation of the mantle occurs and limited melt is produced during rifting, magma-
586 poor passive margins develop (Figure 1.7c), indicating a complete thinning of the crust
587 before the breakup of the lithospheric mantle (Franke, 2013). These margins typically
588 display five domains. Starting from the continent and moving oceanwards, these are: 1)

589 proximal domain, where crustal thinning and accommodation space are minimal; 2) necking
590 domain, where the crust is thinned most intensively resulting in the steepest Moho slopes; 3)
591 hyper-thinned domain, where thinned continental crust (sometimes less than 10 km thick)
592 forms an extensive continental rise; 4) exhumed mantle domain, where complete thinning of
593 the crust occurs and lithospheric mantle is exhumed along detachment faults and becomes
594 partially serpentinised ; and 5) oceanic domain, where following sufficient thinning of the
595 lithosphere, mantle melting occurs to produce oceanic crust (Reston, 2009; Tugend et al.,
596 2015).

597 Crustal thinning at magma-poor rifted margins occurs through both low- β and high- β
598 extensional systems, where β is the crustal extension factor. Low- β systems accommodate
599 small amounts of extension through high-angle normal faults, forming classic half-graben
600 structures with wedge-shaped sedimentary fills (Figure 1.7c). This type of extensional
601 system can occur all along the margin (Tugend et al., 2015), and most magma-poor rifted
602 margins display well defined fault blocks of this type (Reston, 2009). High- β systems allow
603 large amounts of extension to be accommodated through long-offset normal faults. These
604 detachment faults exhume the underlying footwall over large areas forming smooth fault-
605 related topography and hyperextended sag basins. These basins often contain syn-rift
606 sediments that gently onlap the low-angle basement, or that have been redeposited due to
607 significant fault block rotation (Wilson et al., 2001), losing their initial syn-rift sedimentary
608 wedge configuration. Where the low angle faults of high- β systems are intracrustal, or form
609 the boundary between crust and mantle, they are commonly imaged as high amplitude
610 seismic reflections (e.g. Davy et al., 2016; Dean et al., 2008). High- β systems tend to
611 develop in the necking, hyperthinned, and exhumed mantle domains alongside low- β
612 systems (Tugend et al., 2015). These extensional systems lead to complete crustal thinning,
613 from a thickness of ~ 30 km, over a long distance of 100-200 km (Figure 1.7c), with most of
614 the crustal thinning (from ~ 20 -10 km) occurring in the necking zone (Reston, 2009). This
615 region of sharp crustal thinning generally has average Moho slopes of between 5° - 25° ,
616 although average Moho slopes across the necking zone have reached 33 and 36 degrees
617 across the Porcupine Basin (O'Reilly et al., 2006) and Newfoundland margin, respectively.
618 In the latter example, however, the steepness is thought to have been influenced by lower
619 crustal gabbroic lenses localising deformation (Van Avendonk et al., 2009).

620 Following complete crustal thinning, partially serpentinised peridotites of the exhumed
621 mantle domain form the OCT (Tugend et al., 2015). In these domains no clear Moho
622 reflection is present due to the gradual downward decrease in the amount of serpentinisation
623 (Gillard et al., 2015). The onset of magmatism and production of oceanic crust marks the
624 beginning of the oceanic domain. Oceanic crust is often initially thin (e.g. (Davy et al.,

625 2016)) but its presence is often marked by (sometimes weak) Moho reflections. The
626 boundary between the oceanic and exhumed mantle domains may correspond to a step in the
627 basement topography and smaller accommodation space within the oceanic domain (Figure
628 1.7c) due to the relative buoyancy of the oceanic crust over mantle (Tugend et al., 2015).

629 1.3.4. Characterisation of Transform Margins

630 When oblique extension is partitioned onto transform and divergent margins early enough,
631 transform faults cut the continental crust and lithosphere, facilitating plate separation and
632 forming transform margins (Figure 1.7a; Basile, 2015). As the transform faults of the
633 lithospheric deformation zone at transform margins are sub-vertical, extremely narrow
634 'necking zones', typically 50 km wide, develop (Mercier de Lépinay et al., 2016). This sharp
635 zone of crustal thinning is accompanied by the development of steep average Moho slopes,
636 commonly between 8° - 40°, although sub-vertical Moho slopes have been observed at the
637 Côte d'Ivoire-Ghana transform margin (Sage et al., 2000). At the oceanward edge of the
638 necking zone, a steep basement slope may also be present, the base of which often coincides
639 with the COT. The Falkland escarpment basement slope lies at 13 degrees (Lorenzo and
640 Wessel, 1997), Ghana at 12 degrees (Sage et al., 2000), the Northern Demerara and French
641 Guiana margins show slopes of 24 and 13 degrees respectively (Greenroyd et al., 2008), and
642 the Newfoundland Fracture Zone basement slope forms a slope of ~40 degrees (Keen et al.,
643 1990). Rift basins are generally not seen within this slope region, although any present may
644 not have been clearly imaged using seismic reflection techniques due to the slope steepness.

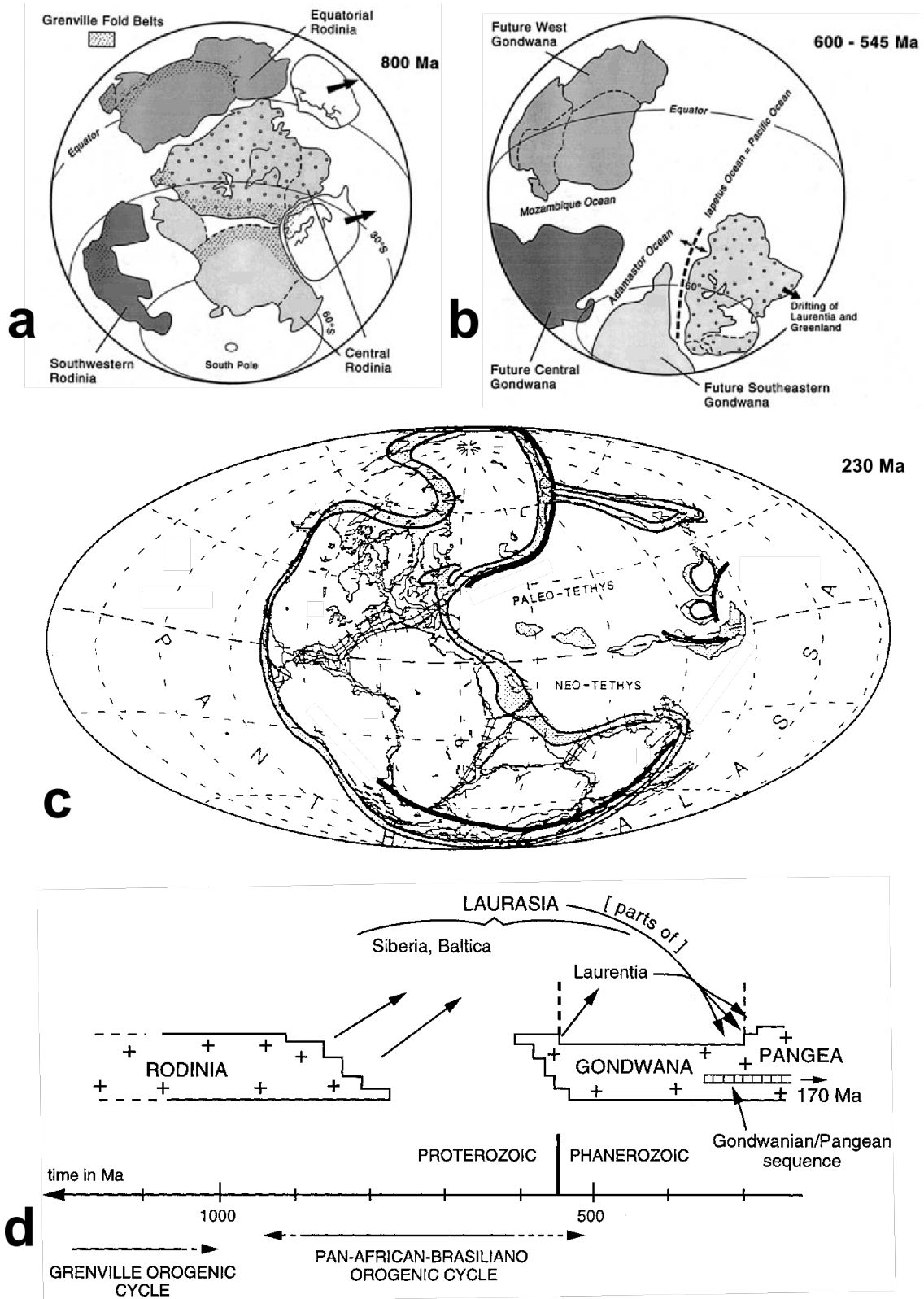
645 The presence of thick continental lithosphere adjacent to MORs at transform margins results
646 in a high thermal contrast between the continental and oceanic lithospheres. Thin oceanic
647 crust may therefore be formed adjacent to transform margins due to heat conduction away
648 from the spreading centre, resulting in reduced melting (e.g., Ghana: 4 km (White et al.,
649 1992); Agulas-Falkland FZ: 4 km (Becker et al., 2012)). This process is analogous to those
650 occurring at long offset transform faults in the oceanic domain. In these settings, the reduced
651 melt supply results in tectonic accommodation of extension and lower crust or mantle rocks
652 may be exhumed to the surface at oceanic core complexes up to 50 km wide (e.g. Karson,
653 1999). The high thermal contrast across transform margins also results in differential
654 subsidence, and where the oceanic and continental plates are coupled flexural downwarping
655 of the continental side may occur (Lorenzo and Wessel, 1997; Mercier de Lépinay et al.,
656 2016).

657 Marginal plateaus, possibly inherited from continental thinning prior to the partitioning of
658 oblique strain onto transform faults (Basile, 2015)(Figures 1.5f1-2), are also commonly
659 observed adjacent to transform margins (Mercier de Lépinay et al., 2016). A marginal ridge

660 (e.g. Bird, 2001), where crust or pre/syn-rift sediments are elevated linearly along the margin
661 near the top of the continental slope, may also be present (Figure 1.7a). However, the
662 mechanisms for forming marginal ridges are still under debate and possibly diverse in
663 origin; for a full review the reader is referred to (Basile, 2015).

664 **1.4. Gondwana assembly and breakup**

665 The paleomagnetic, stratigraphic, and tectonic records of the continental crust span Earth's
666 almost entire history, as they are not systematically destroyed like those of the oceanic crust,
667 which is subducted comparatively soon after its formation (e.g. Roberts et al., 2015). They
668 therefore make a useful tool for reconstructing Wilson Cycles that occurred before the
669 formation of the Earth's present day oceanic crust. The formation of the supercontinent
670 Gondwana, a long lived accumulation of much of the earth's continental lithosphere into one
671 landmass, represents such a cycle. Gondwana was reconstructed from the lithospheric mega-
672 plates formed during the disintegration of the previous supercontinent Rodinia between 1000
673 and 700 Ma (Veevers, 2004). These plates were reunited during the Pan-African orogeny
674 between 650 and 500 Ma, which brought together the present day landmasses of Africa,
675 Antarctica, Australia, India, the Middle East, North America, South America, and also
676 briefly North America (Laurentia). The return of Laurentia with Baltica and Siberia, together
677 forming Laurasia, to Gondwana at ~320 Ma resulted in the Variscan orogeny along the
678 north-eastern margin of Gondwana, and formation of the supercontinent Pangea. Gondwana
679 remained intact within Pangea and was surrounded by the near global Panthalassic Ocean,
680 which by ~300 Ma had renewed subduction beneath the southern margin of Gondwana
681 (Veevers, 2004).



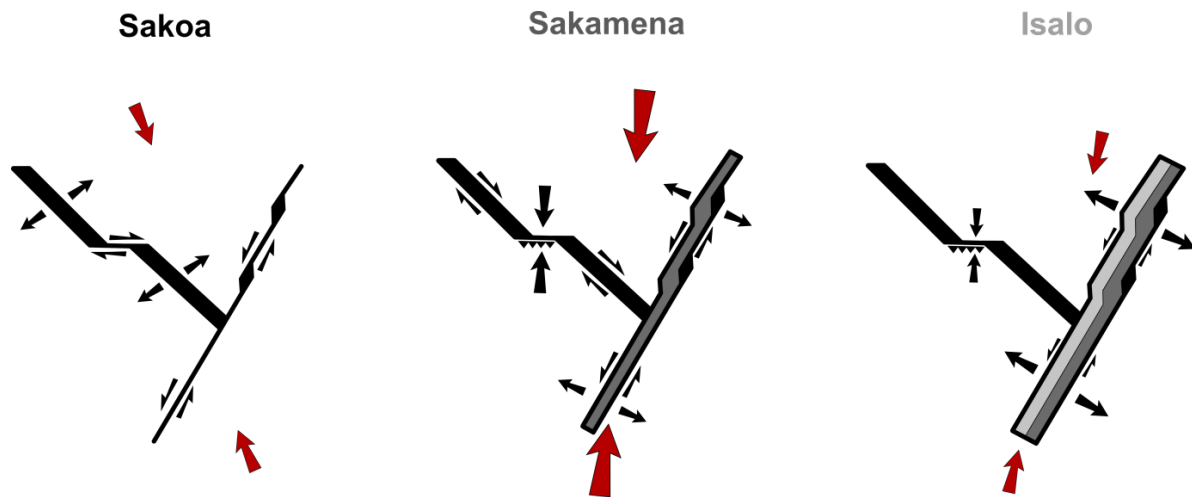
683

684 **Figure 1.8.** Disassembly of Rhodinia (a) and reassembly into Gondwana (b). Later merging
 685 of Gondwana with Laurasia forms Pangea, surrounded by the Panthalassas Ocean (c and d).
 686 Images a, b, and d are modified from Trompette (2000), image c is modified from Veevers
 687 (2004).

688 This subduction and accretion led to the development of foreland basins and the Cape Fold
689 Belt in South Africa between 220 and 290 Ma (Frimmel et al., 2001) with fluctuating
690 deformation intensity. This compression became more widespread, also affecting South
691 America to the west, at ~258 Ma (Veevers, 2004). The episodic and changeable
692 development of the Karoo rift system (Hankel, 1994; Schandelmeier et al., 2004) across
693 Gondwana at this time (Reeves et al., 2016) may therefore be the result of this compression
694 (Delvaux, 2001a), which varied temporally in orientation and intensity, reactivating pre-
695 existing basement weaknesses along the northern parts of the Karoo rift system (Reeves,
696 2014). Studies of Karoo rifts, which predominantly follow a NW-SE trend (Delvaux, 2001b)
697 or a NE-SW trend (Schandelmeier et al., 2004) in the present day East Africa region, show
698 the general progression:

- 699 1) Sinistral strike-slip along NE-SW trending basins with local deposition in left lateral
700 step-over basins. Extension along NW-SE trending basins with strike-slip deformation
701 along E-W trending offsets in the rift system. This phase of rifting led to the deposition
702 of Sakoa aged deposits between ~265 Ma and ~300 Ma (Figure 1.9), which are capped
703 by the Vohitolia marine limestones (Hankel, 1994) suggesting a connection to the
704 NeoTethys Ocean in the north at this time.
- 705 2) After a brief pause in rifting, a reconfiguration occurred between ~259 and ~264 Ma
706 (Hankel, 1994), coincident with the broadening and intensification of compression
707 along southern Gondwana (Veevers, 2004). The onset of rapid subsidence in NE-SW
708 trending basins (Schandelmeier et al., 2004), along with strike slip deformation along
709 formerly extensional NW-SE trending basins and compression along their E-W trending
710 offsets, resulted in deposition of Sakamena aged deposits (Figure 1.9).
- 711 3) A second larger pause in rifting occurred around ~249 Ma, and was followed by a
712 rejuvenation of rifting along NE-SW trending rifts at ~242 Ma with little activity along
713 NW-SE trending rifts, which led to the development of Isalo aged deposits until ~210
714 Ma (Figure 1.9; Hankel, 1994).

715 Following the cessation of compression along the cape fold belt, a substantial period of
716 quiescence along the Karoo rifts ensued (Geiger et al., 2004). Rejuvenation of rifting did not
717 occur until the Early Jurassic (Toarcian), coincident with eruption of the Karoo large
718 igneous province in Mozambique. This Early Jurassic rifting at ~182 Ma culminated in the
719 breakup of East and West Gondwana, which had thus remained intact for over 520 Myr. The
720 kinematics and dynamics during this drifting apart of East and West Gondwana form the
721 main focus of this thesis.



723

220-290 Ma Cape Fold Belt metamorphism

724 **Figure 1.9.** Schematic of Karoo rift development in East Africa, possibly in response to
 725 varying intensities and orientations of compression along the Cape Fold Belt. The
 726 distributions Sakoa aged deposits are shown in black, Sakamena deposits in dark grey, and
 727 Isalo deposits in light grey.

728 1.5. Thesis outline

729 Chapters 2 to 4 of this thesis are the results chapters of this thesis. They are presented as
 730 three ‘journal-style’ academic papers or manuscripts, and as such are designed to be stand-
 731 alone. Nonetheless, they contain a through-going theme and are further tied together in the
 732 conclusions chapter at the end of this thesis.

733 Each results chapter has either been published in, or is intended for submission to, a relevant
 734 academic journal within the field of Earth Sciences. These papers are multi-authored and as
 735 such my contributions to each chapter are outlined below:

736 Chapter 2 - ‘Madagascar’s escape from Africa: A high-resolution plate reconstruction for the
 737 Western Somali Basin and implications for supercontinent dispersal: this chapter has been
 738 published in *Geochemistry, Geophysics, Geosystems* in 2016. As first author of this paper
 739 my contributions included: concept design, gravity modelling, plate tectonic modelling, and
 740 manuscript preparation. Co-authors have contributed training, useful discussion, and
 741 editorial assistance.

742 Chapter 3 - ‘The Rovuma Transform Margin: Pinning down the East African continent-
 743 ocean transform margin using seismic and gravity methods’: this chapter is intended for
 744 submission to *Tectonics*. As first author of this paper my contributions included: Moho and

745 bathymetry data digitisation, seismic interpretation, Matlab code development, gravity
746 modelling, manuscript preparation. Concept design was joint between myself and co-
747 authors. Co-authors have contributed training, useful discussion, and editorial assistance.

748 Chapter 4 – ‘Compressional consequences of complex spreading: Formation of the Tanzania
749 Coastal Basin and Davie Fracture Zone during the Mesozoic East Africa breakup’: this
750 chapter is also intended for submission to *Tectonics*. As first author of this paper my
751 contributions included: analysis of satellite image data, seismic interpretation, regional
752 tectonic model development, and manuscript preparation. Co-authors have contributed
753 training, useful discussion, and editorial assistance.

754 1.6. References

- 755 Afilhado, A., Matias, L., Shiobara, H., Hirn, A., Mendes-Victor, L., Shimamura, H., 2008. From
756 unthinned continent to ocean: The deep structure of the West Iberia passive continental margin at
757 38°N. *Tectonophysics* 458, 9–50. doi:10.1016/j.tecto.2008.03.002
- 758 Armitage, J.J., Collier, J.S., Minshull, T.A., 2010. The importance of rift history for volcanic margin
759 formation. *Nature* 465, 913–917. doi:10.1038/nature09063
- 760 Basile, C., 2015. Transform continental margins - part 1: Concepts and models. *Tectonophysics* 661,
761 1–10. doi:10.1016/j.tecto.2015.08.034
- 762 Basile, C., Braun, J., 2016. The initiation of pull-apart basins and transform continental margins:
763 Results from numerical experiments of kinematic partitioning in divergent settings. *Terra Nov.* 28,
764 120–127. doi:10.1111/ter.12198
- 765 Becker, K., Franke, D., Schnabel, M., Schreckenberger, B., Heyde, I., Krawczyk, C.M., 2012. The
766 crustal structure of the southern Argentine margin. *Geophys. J. Int.* 189, 1483–1504.
767 doi:10.1111/j.1365-246X.2012.05445.x
- 768 Behn, M.D., Lin, J., 2000. Segmentation in gravity and magnetic anomalies along the U.S. East Coast
769 passive margin: Implications for incipient structure of the oceanic lithosphere. *J. Geophys. Res.*
770 105, 25769. doi:10.1029/2000JB900292
- 771 Bellahsen, N., Leroy, S., Autin, J., Razin, P., d’Acremont, E., Sloan, H., Pik, R., Ahmed, A.,
772 Khanbari, K., 2013. Pre-existing oblique transfer zones and transfer/transform relationships in
773 continental margins: New insights from the southeastern Gulf of Aden, Socotra Island, Yemen.
774 *Tectonophysics* 607, 32–50. doi:10.1016/j.tecto.2013.07.036
- 775 Benioff, H., 1949. Seismic evidence for the fault origin of oceanic deeps. *Bull. Geol. Soc. Am.* 60,
776 1837–1866.
- 777 Bercovici, D., Long, M.D., 2014. Slab rollback instability and supercontinent dispersal. *Geophys.*
778 *Res. Lett.* 41, 6659–6666. doi:10.1002/2014GL061251
- 779 Bird, D., 2001. Shear margins: Continent-ocean transform and fracture zone boundaries. *Lead. Edge*
780 20, 150. doi:10.1190/1.1438894
- 781 Boutilier, R.R., Keen, C.E., 1999. Small-scale convection and divergent plate boundaries. *J. Geophys.*
782 *Res.* 104, 7389. doi:10.1029/1998JB900076
- 783 Bradley, D.C., 2008. Passive margins through earth history. *Earth-Science Rev.* 91, 1–26.
784 doi:10.1016/j.earscirev.2008.08.001
- 785 Brandl, P.A., Regelous, M., Beier, C., Haase, K.M., 2013. High mantle temperatures following rifting
786 caused by continental insulation. *Nat. Geosci.* 6, 391–394. doi:10.1038/ngeo1758
- 787 Brune, S., Heine, C., Pérez-gussinyé, M., Sobolev, S., 2013. High resolution 2D numerical models
788 from rift to break-up : Crustal hyper-extension , Margin asymmetry , Sequential faulting 15, 6015.
- 789 Bunce, E.T., Molnar, P., 1977. Seismic reflection profiling and basement topography in the somali
790 basiin: possible fracture sones between Madagascar and Africa. *J. Geophys. Res.* 82, 5305–5311.
- 791 Coffin, M.F., Rabinowitz, P.D., 1987. Reconstruction of Madagascar and Africa: Evidence From the
792 Davie Fracture Zone and Western Somali Basin 92, 9385–9406.
- 793 Condie, K.C., 1976. *Plate Tectonics and Crustal Evolution*. Chem. ... 294.

794 Dailly, P., Henderson, T., Hudgens, E., Kanschat, K., Lowry, P., 2013. Exploration for Cretaceous
795 stratigraphic traps in the Gulf of Guinea, West Africa and the discovery of the Jubilee Field: a play
796 opening discovery in the Tano Basin, Offshore Ghana. *Geol. Soc. London, Spec. Publ.* 369, 235–
797 248. doi:10.1144/SP369.12

798 Damian Nance, R., Brendan Murphy, J., 2013. Origins of the supercontinent cycle. *Geosci. Front.* 4,
799 439–448. doi:10.1016/j.gsf.2012.12.007

800 Dauteuil, O., Brun, J.-P., 1996. Deformation partitioning in a slow spreading ridge undergoing
801 oblique extension: Mohns Ridge, Norwegian Sea. *Tectonics* 15, 870–884.
802 doi:10.1029/95TC03682

803 Davis, J.K., Lawver, L.A., Norton, I.O., Gahagan, L.M., 2016. New Somali Basin magnetic
804 anomalies and a plate model for the early Indian Ocean. *Gondwana Res.* 34, 16–28.
805 doi:10.1016/j.gr.2016.02.010

806 Davy, R.G., Minshull, T.A., Bayrakci, G., Bull, J.M., Klaeschen, D., Papenberg, C., Reston, T.J.,
807 Sawyer, D.S., Zelt, C.A., 2016. Continental hyperextension, mantle exhumation, and thin oceanic
808 crust at the continent-ocean transition, West Iberia: New insights from wide-angle seismic 121,
809 3177–3199. doi:10.1002/2016JB012825.

810 Dean, S.M., Minshull, T.A., Whitmarsh, R.B., 2008. Seismic constraints on the three-dimensional
811 geometry of low-angle intracrustal reflectors in the Southern Iberia Abyssal Plain. *Geophys. J. Int.*
812 175, 571–586. doi:10.1111/j.1365-246X.2008.03869.x

813 Delvaux, D., 2001a. Tectonic and palaeostress evolution of the Tanganyika-Rukwa-Malawi rift
814 segment, East African Rift System. *Peri-Tethys Mem.* 6 Peri-Tethyan Rift. *Basins Passiv. Margins*
815 545–567.

816 Delvaux, D., 2001b. Karoo rifting in western Tanzania: precursor of Gondwana break-up? *Contrib. to*
817 *Geol. Palaeontol. Gondwana honour Helmut Wopfner* 111–125.

818 Du Toit, A.L., 1937. *Our Wandering Continents: An Hypothesis of Continental Drifting.* Edinburgh
819 Oliver Boyd.

820 Franke, D., 2013. Rifting, lithosphere breakup and volcanism: Comparison of magma-poor and
821 volcanic rifted margins. *Mar. Pet. Geol.* 43, 63–87. doi:10.1016/j.marpetgeo.2012.11.003

822 Franke, D., Neben, S., Ladage, S., Schreckenberger, B., Hinz, K., 2007. Margin segmentation and
823 volcano-tectonic architecture along the volcanic margin off Argentina/Uruguay, South Atlantic. *Mar.*
824 *Geol.* 244, 46–67. doi:10.1016/j.margeo.2007.06.009

825 Frankel, H., 1990. The development of plate tectonics by J. Morgan and D. McKenzie. *Terra Nov.* 2,
826 202–214. doi:10.1111/j.1365-3121.1990.tb00067.x

827 Frimmel, H.E., Fölling, P.G., Diamond, R., 2001. Metamorphism of the permo-triassic cape fold belt
828 and its basement, South Africa. *Mineral. Petrol.* 73, 325–346. doi:10.1007/s007100170005

829 Gaina, C., Torsvik, T.H., van Hinsbergen, D.J.J., Medvedev, S., Werner, S.C., Labails, C., 2013. The
830 African plate: A history of oceanic crust accretion and subduction since the Jurassic.
831 *Tectonophysics* 604, 4–25. doi:10.1016/j.tecto.2013.05.037

832 Gawthorpe, R.L., Hurst, J.M., 1993. Transfer zones in extensional basins: their structural style and
833 influence on drainage development and stratigraphy. *J. Geol. Soc. London.* 150, 1137–1152.
834 doi:10.1144/gsjgs.150.6.1137

835 Geiger, M., Clark, D.N., Mette, W., 2004. Reappraisal of the timing of the breakup of Gondwana
836 based on sedimentological and seismic evidence from the Morondava Basin, Madagascar. *J.*
837 *African Earth Sci.* 38, 363–381. doi:10.1016/j.jafrearsci.2004.02.003

838 Geoffroy, L., 2005. Volcanic passive margins. *Comptes Rendus - Geosci.* 337, 1395–1408.
839 doi:10.1016/j.crte.2005.10.006

840 Geoffroy, L., Burov, E.B., Werner, P., 2015. Volcanic passive margins: another way to break up
841 continents. *Sci. Rep.* 5, 14828. doi:10.1038/srep14828

842 Gillard, M., Autin, J., Manatschal, G., Sauter, D., Munsch, M., Schaming, M., 2015.
843 Tectonomagmatic evolution of the final stages of rifting along the deep conjugate Australian-
844 Antarctic magma-poor rifted margins: Constraints from seismic observations 753–783.
845 doi:10.1002/2015TC003850.

846 Greenroyd, C.J., Peirce, C., Rodger, M., Watts, A.B., Hobbs, R.W., 2008. Demerara Plateau - The
847 structure and evolution of a transform passive margin. *Geophys. J. Int.* 172, 549–564.
848 doi:10.1111/j.1365-246X.2007.03662.x

849 Hankel, O., 1994. Early Permian to Middle Jurassic rifting and sedimentation in East Africa and
850 Madagascar. *Geol. Rundschau* 83, 703–710. doi:10.1007/BF00251069

851 Haskell, N.A., 1935. The motion of a fluid under a surface load. *Physics (College Park, Md).* 6, 265–
852 269.

853 Hess, H.H., 1962. History of Ocean Basins. *Petrol. Stud. A Vol. to Honor A. F. Buddingt.* 599–620.

854 Holmes, A., 1931. Radioactivity and earth movements. *Trans. Geol. Soc. Glas.* 18, 559–606.

855 Huismans, R., Beaumont, C., 2011. Depth-dependent extension, two-stage breakup and cratonic
856 underplating at rifted margins. *Nature* 473, 74–78. doi:10.1038/nature09988

857 Japsen, P., Chalmers, J.A., Green, P.F., Bonow, J.M., 2012. Elevated, passive continental margins:
858 Not rift shoulders, but expressions of episodic, post-rift burial and exhumation. *Glob. Planet.*
859 *Change* 90–91, 73–86. doi:10.1016/j.gloplacha.2011.05.004

860 Karson, J.A., 1999. Geological investigation of a lineated massif at the Kane Transform Fault:
861 implications for oceanic core complexes. *Philos. Trans. R. Soc. a-Mathematical Phys. Eng. Sci.*
862 357, 713–736. doi:10.1098/rsta.1999.0350

863 Katz, R.F., Spiegelman, M., Langmuir, C.H., 2003. A new parameterization of hydrous mantle
864 melting. *Geochemistry, Geophys. Geosystems* 4, 1–19. doi:10.1029/2002GC000433

865 Keen, C.E., Kay, W.A., Roest, W.R., 1990. Crustal anatomy of a transform continental margin.
866 *Tectonophysics* 173. doi:10.1016/0040-1951(90)90244-3

867 Klimke, J., Franke, D., Mahanjane, E.S., Leitchenkov, G., 2017. Tie-points for Gondwana
868 reconstructions from a structural interpretation of the Mozambique Basin, East Africa, and the
869 Riiser-Larsen Sea, Antarctica. *Solid Earth Discuss.* 1–28.

870 Knopf, A., 1948. The Geosynclinal Theory. *Bull. Geol. Soc. Am.* 59, 649–670.

871 Larson, R.L., 1991. Geological consequences of superplumes. *Geology* 19, 963–966.
872 doi:10.1130/0091-7613(1991)019<0963:GCOS>2.3.CO

873 Lawver, L.A., Scotese, C.R., 1987. A revised reconstruction of Gondwanaland. *Geophys. Monogr.*
874 *Ser.*
875 40, 17–23.

876 Levell, B., Argent, J., Fraser, S., 2010. Session : Passive Margins. *Pet. Geol. Conf. Ser.* 823–830.
877 doi:10.1144/0070823

878 Lithgow-Bertelloni, C., 2014. Driving Forces: Slab Pull, Ridge Push BT - Encyclopedia of Marine
879 Geosciences, in: Harff, J., Meschede, M., Petersen, S., Thiede, J. (Eds.), . Springer Netherlands,
880 Dordrecht, pp. 1–6. doi:10.1007/978-94-007-6644-0_105-1

881 Lizarralde, D., Axen, G.J., Brown, H.E., Fletcher, J.M., González-Fernández, A., Harding, A.J.,
882 Holbrook, W.S., Kent, G.M., Paramo, P., Sutherland, F., Umhoefer, P.J., 2007. Variation in styles
883 of rifting in the Gulf of California. *Nature* 448, 466–469. doi:10.1038/nature06035

884 Lorenzo, J.M., Wessel, P., 1997. Flexure across a continent-ocean fracture zone: the northern
885 Falkland/Malvinas Plateau, South Atlantic. *Geo-Marine Lett.* 17, 110–118.
886 doi:10.1007/s003670050015

887 Lottes, A.L., Rowley, D.B., 1990. Reconstruction of the Laurasian and Gondwanan segments of
888 Permian Pangaea. *Geol. Soc. Mem.* 12, 383–395.

889 Manatschal, G., 2004. New models for evolution of magma-poor rifted margins based on a review of
890 data and concepts from West Iberia and the Alps. *Int. J. Earth Sci.* 93, 432–466.
891 doi:10.1007/s00531-004-0394-7

892 Mercier de Lépinay, M., Loncke, L., Basile, C., Roest, W.R., Patriat, M., Maillard, A., De Clarens, P.,
893 2016. Transform continental margins – Part 2: A worldwide review. *Tectonophysics* 693, 96–115.
894 doi:10.1016/j.tecto.2016.05.038

895 Milani, E.J., Davison, I., 1988. Basement control and transfer tectonics in the Reconcavo-Tucano-
896 Jatoba rift, Northeast Brazil. *Tectonophysics* 154. doi:10.1016/0040-1951(88)90227-2

897 Morgan, W.J., 1968. Rises, Trenches, Great Faults and Crustal Blocks. *J. Geophys. Res.* 73, 1959–
898 1982.

899 Mutter, J.C., Buck, W.R., Zehnder, C.M., 1988. Convective partial melting: 1. A model for the
900 formation of thick basaltic sequences during the initiation of spreading. *J. Geophys. Res.* 93,
901 1031–1048. doi:10.1029/JB093iB02p01031

902 Norton, I.O.I., Sclater, J.G., 1979. A model for the evolution of the Indian Ocean and the breakup of
903 Gondwanaland. *J. Geophys. Res.* 84, 6803–6830.

904 O'Reilly, B.M., Hauser, F., Ravaut, C., Shannon, P.M., Readman, P.W., 2006. Crustal thinning,
905 mantle exhumation and serpentinitization in the Porcupine Basin, offshore Ireland: evidence from
906 wide-angle seismic data. *J. Geol. Soc. London.* 163, 775–787. doi:10.1144/0016-76492005-079

907 Ortelius, A., 1596. *Thesaurus geographicus.*

908 Pérez-Gussinyé, M., Morgan, J.P., Reston, T.J., Ranero, C.R., 2006. The rift to drift transition at non-
909 volcanic margins: Insights from numerical modelling. *Earth Planet. Sci. Lett.* 244, 458–473.
910 doi:10.1016/j.epsl.2006.01.059

911 Peyve, A.A., 2009. Accretion of oceanic crust under conditions of oblique spreading. *Geotectonics*
912 43, 87–99. doi:10.1134/S0016852109020022

- 913 Pinna, P., 1995. On the dual nature of the Mozambique Belt, Mozambique to Kenya. *J. African Earth*
914 *Sci.* 21, 477–480. doi:10.1016/0899-5362(95)00077-7
- 915 Planke, S., Symonds, P.A., Alvestad, E., Skogseid, J., 2000. Seismic volcanostratigraphy of large-
916 volume basaltic extrusive complexes on rifted margins. *J. Geophys. Res. Solid Earth* 105, 19335–
917 19351. doi:10.1029/1999JB900005
- 918 Rabineau, M., Cloetingh, S., Kuroda, J., Aslanian, D., Droxler, A., Gorini, C., Garcia-Castellanos, D.,
919 Moscariello, A., Burov, E., Sierro, F., Lirer, F., Roure, F., Pezard, P.A., Matenco, L., Hello, Y.,
920 Mart, Y., Camerlenghi, A., Tripathi, A., 2015. Probing connections between deep earth and surface
921 processes in a land-locked ocean basin transformed into a giant saline basin: The Mediterranean
922 GOLD project#. *Mar. Pet. Geol.* 66, 6–17. doi:10.1016/j.marpetgeo.2015.03.018
- 923 Reeves, C., 2014. The position of Madagascar within Gondwana and its movements during
924 Gondwana dispersal. *J. African Earth Sci.* 94, 45–57. doi:10.1016/j.jafrearsci.2013.07.011
- 925 Reeves, C. V., Teasdale, J.P., Mahanjane, E.S., 2016. Insight into the Eastern Margin of Africa from a
926 new tectonic model of the Indian Ocean. *Geol. Soc. London, Spec. Publ.* 431, 1–24.
927 doi:10.1144/SP431.12
- 928 Reston, T., Mcdermott, K., 2014. An assessment of the cause of the “extension discrepancy” with
929 reference to the west Galicia margin. *Basin Res.* 26, 135–153. doi:10.1111/bre.12042
- 930 Reston, T.J., 2009. The structure, evolution and symmetry of the magma-poor rifted margins of the
931 North and Central Atlantic: A synthesis. *Tectonophysics* 468, 6–27.
932 doi:10.1016/j.tecto.2008.09.002
- 933 Rey, P., Vanderhaeghe, O., Teyssier, C., 2001. Gravitational collapse of continental crust: definitions,
934 regimes, mechanisms and modes. *Tectonophysics* 342, 435–449.
- 935 Roberts, N.M.W., Van Kranendonk, M.J., Parman, S., Clift, P.D., 2015. Continent formation through
936 time. *Geol. Soc. London, Spec. Publ.* 389, 1–16. doi:10.1144/SP389.13
- 937 Runcorn, S.K., 1965. Palaeomagnetic Comparisons between Europe and North America. *Philos.*
938 *Trans. R. Soc. London. Ser. A, Math. Phys. Sci.* 258, 1–11.
- 939 Sage, F., Basile, C., Mascle, J., Pontoise, B., Whitmarsh, R.B., 2000. Crustal structure of the
940 continent-ocean transition off the Cote d’Ivoire-Ghana transform margin: Implications for thermal
941 exchanges across the palaeotransform boundary. *Geophys. J. Int.* 143, 662–678.
942 doi:10.1046/j.1365-246X.2000.00276.x
- 943 Schandelmeier, H., Bremer, F., Holl, H.G., 2004. Kinematic evolution of the Morondava rift basin of
944 SW Madagascar - From wrench tectonics to normal extension. *J. African Earth Sci.* 38, 321–330.
945 doi:10.1016/j.jafrearsci.2003.11.002
- 946 Schiffer, C., Peace, A., Phethean, J., Gernigon, L., McCaffrey, K.J.W., Petersen, Kenni, D., Foulger,
947 G., n.d. The Jan Mayen Microplate Complex and the Wilson Cycle. *Geol. Soc. London, Spec.*
948 *Publ.*
- 949 Scrutton, R.A., Heptonstall, W.B., Peacock, J.H., 1981. Constraints on the motion of Madagascar
950 with respect to Africa. *Mar. Geol.* 43, 1–20. doi:10.1016/0025-3227(81)90126-2
- 951 Ségoufin, J., Patriat, P., 1980. Existence d’anomalies mésozoïques dans le bassin de Somalie.
952 Implications pour les relations Afrique-Antarctique-Madagascar. *Comptes Rendus l’Académie des*
953 *Sci.* 291, 85–88.
- 954 Shackleton, R.M., 1996. The final collision zone between East and West Gondwana: where is it? *J.*
955 *African Earth Sci.* 23, 271–287.
- 956 Simon, K., Huismans, R.S., Beaumont, C., 2009. Dynamical modelling of lithospheric extension and
957 small-scale convection: Implications for magmatism during the formation of volcanic rifted
958 margins. *Geophys. J. Int.* 176, 327–350. doi:10.1111/j.1365-246X.2008.03891.x
- 959 Smith, A.G., Hallam, A., 1970. The Fit of the Southern Continents. *Nature* 225, 139–144.
- 960 Stab, M., Bellahsen, N., Pik, R., Quidelleur, X., Ayalew, D., Leroy, S., 2016. Modes of rifting in
961 magma-rich settings: Tectono-magmatic evolution of Central Afar. *Tectonics* 35, 2–38.
962 doi:10.1002/2015TC003893
- 963 Storey, B.C., 1995. The role of mantle plumes in continental breakup: case histories from
964 Gondwanaland. *Nature.* doi:10.1038/377301a0
- 965 Taylor, B., Goodliffe, A., Martinez, F., 2009. Initiation of transform faults at rifted continental
966 margins. *Comptes Rendus - Geosci.* 341, 428–438. doi:10.1016/j.crte.2008.08.010
- 967 Tugend, J., Manatschal, G., Kusznir, N.J., Masini, E., 2015. Characterizing and identifying structural
968 domains at rifted continental margins: application to the Bay of Biscay margins and its Western
969 Pyrenean fossil remnants. *Geol. Soc. London, Spec. Publ.* 413, 171–203. doi:10.1144/SP413.3
- 970 Turcotte, D.L., Emerman, S.H., 1983. Mechanisms of active and passive rifting. *Dev. Geotecton.* 19,
971 39–50. doi:10.1016/B978-0-444-42198-2.50010-9
- 972 Umbgrove, J.M.F., 1947. *The Pulse of the Earth.* Martinus Nijhoff, The Hague, Netherlands.

973 Unternehr, P., Peron-Pinvidic, G., Manatschal, G., Sutra, E., 2010. Hyper-extended crust in the South
 974 Atlantic: in search of a model. *Pet. Geosci.* 16, 207–215. doi:10.1144/1354-079309-904
 975 Van Avendonk, H.J.A., Lavier, L.L., Shillington, D.J., Manatschal, G., 2009. Extension of continental
 976 crust at the margin of the eastern Grand Banks, Newfoundland. *Tectonophysics* 468, 131–148.
 977 doi:10.1016/j.tecto.2008.05.030
 978 van Wijk, J.W., Huisman, R.S., ter Voorde, M., Cloetingh, S.A.P.L., 2001. Melt generation at
 979 volcanic continental margins: No need for a mantle plume? *Geophys. Res. Lett.* 28, 3995–3998.
 980 doi:10.1029/2000GL012848
 981 Veevers, J.J., 2004. Gondwanaland from 650-500 Ma assembly through 320 Ma merger in Pangea to
 982 185-100 Ma breakup: Supercontinental tectonics via stratigraphy and radiometric dating. *Earth-*
 983 *Science Rev.* 68, 1–132. doi:10.1016/j.earscirev.2004.05.002
 984 Vine, F.J., Matthews, D.H., 1963. Magnetic Anomalies Over Oceanic Ridges. *Nature* 199, 947–949.
 985 Waples, D.W., 2002. A new model for heat flow in extensional basins: estimating radiogenic heat
 986 production. *Nat. Resour. Res.* 11, 125–133. doi:10.1023/A:1015568119996
 987 Wegener, A., 1912. Die Entstehung der Kontinente. Dr. A. Petermanns Mitteilungen aus Justus
 988 Perthes' Geogr. Anstalt 63, 185–195, 253–256, 305–309.
 989 White, N., Thompson, M., Barwise, T., 2003. deep-water continental margins 426.
 990 White, R., McKenzie, D., 1989. Magmatism at rift zones: The generation of volcanic continental
 991 margins and flood basalts. *J. Geophys. Res.* 94, 7685. doi:10.1029/JB094iB06p07685
 992 White, R.S., McKenzie, D., O'Nions, R.K., 1992. Oceanic crustal thickness from seismic
 993 measurements and rare earth element inversions. *J. Geophys. Res.* 97, 19683–19715.
 994 doi:10.1029/92JB01749
 995 Whittaker, J.M., Williams, S.E., Halpin, J.A., Wild, T.J., Stilwell, J.D., Jourdan, F., Daczko, N.R.,
 996 2016. Eastern Indian Ocean microcontinent formation driven by plate motion changes. *Earth*
 997 *Planet. Sci. Lett.* 454, 203–212. doi:10.1016/j.epsl.2016.09.019
 998 Wilson, J.T., 1965. A New Class of Faults and their Bearing on Continental Drift. *Nature* 207, 343–
 999 347. doi:10.1038/207343a0
 1000 Wilson, R.C.L., Manatschal, G., Wise, S., 2001. Rifting along non-volcanic passive margins:
 1001 stratigraphic and seismic evidence from the Mesozoic successions of the Alps and western Iberia.
 1002 *Geol. Soc. London, Spec. Publ.* 187, 429–452. doi:10.1144/GSL.SP.2001.187.01.21
 1003 Wilson, T.J., 1966. Did the Atlantic close and then re-open? *Nature* 211, 676–681.
 1004 Windley, B.F., 1977. The evolving continents. *Geol. J.*
 1005 Windley, B.F., Razafiniparany, A., Razakamanana, T., Ackermann, D., 1994. Tectonic framework of
 1006 the Precambrian of Madagascar and its Gondwana connections: a review and reappraisal. *Geol.*
 1007 *Rundschau* 83, 642–659. doi:10.1007/BF00194168
 1008 Worsley, T.R., Nance, D., Moody, J.B., 1984. Global tectonics and eustasy for the past 2 billion
 1009 years. *Mar. Geol.* 58, 373–400. doi:10.1016/0025-3227(84)90209-3
 1010 Wright, J.B., 1976. fracture systems in Nigeria and initiation of fracture zones in the South Atlantic
 1011 Figure 1 represents the convergence of two quite different lines of evidence which together make a
 1012 compelling case for proposing that initiation of the Romanche and Chain fr. Atlantic 34, 43–47.
 1013 Yamato, P., Husson, L., Becker, T.W., Pedoja, K., 2013. Passive margins getting squeezed in the
 1014 mantle convection vice. *Tectonics* 32, 1559–1570. doi:10.1002/2013TC003375
 1015 Ziegler, P.A., 1993. Plate-moving mechanisms: their relative importance. *J. Geol. Soc. London.* 150,
 1016 927–940. doi:10.1144/gsjgs.150.5.0927
 1017

1018 **2. Madagascar's escape from**
1019 **Africa: A high-resolution plate**
1020 **reconstruction for the Western**
1021 **Somali Basin and implications for**
1022 **supercontinent dispersal**

1023 **Abstract**

1024 Accurate reconstructions of the dispersal of supercontinent blocks are essential for testing
1025 continental breakup models. Here, we provide a new plate tectonic reconstruction of the
1026 opening of the Western Somali Basin during the breakup of East and West Gondwana. The
1027 model is constrained by a new comprehensive set of spreading lineaments, detected in this
1028 heavily sedimented basin using a novel technique based on directional derivatives of free-air
1029 gravity anomalies. Vertical gravity gradient and free-air gravity anomaly maps also enable
1030 the detection of extinct mid-ocean ridge segments which can be directly compared to several
1031 previous ocean magnetic anomaly interpretations of the Western Somali Basin. The best-
1032 matching interpretations have basin symmetry around the M0 anomaly; these are then used
1033 to temporally constrain our plate tectonic reconstruction. The reconstruction supports a tight
1034 fit for Gondwana fragments prior to breakup, and predicts that the continent-ocean transform
1035 margin lies along the Rovuma Basin, not along the Davie Fracture Zone (DFZ) as commonly
1036 thought. According to our reconstruction, the DFZ represents a major ocean-ocean fracture
1037 zone formed by the coalescence of several smaller fracture zones during evolving plate
1038 motions as Madagascar drifted southwards, and offshore Tanzania is an obliquely rifted,
1039 rather than transform, margin. New seismic reflection evidence for oceanic crust inboard of
1040 the DFZ strongly supports these conclusions. Our results provide important new constraints
1041 on the still enigmatic driving mechanism of continental rifting, the nature of the lithosphere
1042 in the Western Somali Basin, and its resource potential.

1043

1044 **2.1. Introduction**

1045 Continental breakup is a fundamental, but poorly understood, part of the plate tectonic cycle.
1046 Our understanding of the conditions needed for successful rift formation is particularly
1047 limited. Besides pre-existing weak zones (Ziegler and Cloetingh, 2004) and thermal
1048 weakening due to rifting-related magmatism (Buck, 2007), it has also recently been shown
1049 that oblique rifting is an important mechanism to facilitate the breakup (Brune et al., 2012).
1050 To further investigate these concepts, accurate reconstructions of rifting events with high
1051 spatial resolution are essential to enable detailed comparisons between models and
1052 observations (Nance and Murphy, 2013). Detailed history of rifted margin evolution is also
1053 key in hydrocarbon exploration by enabling the prediction of the petroleum potential for
1054 conjugate basins with similar tectonostratigraphic histories (Beglinger et al., 2012). Some of
1055 the most significant rifting episodes in Earth's history occurred during supercontinent
1056 breakup, e.g. rifting between East and West Gondwana, which spanned many of our present
1057 day continents.

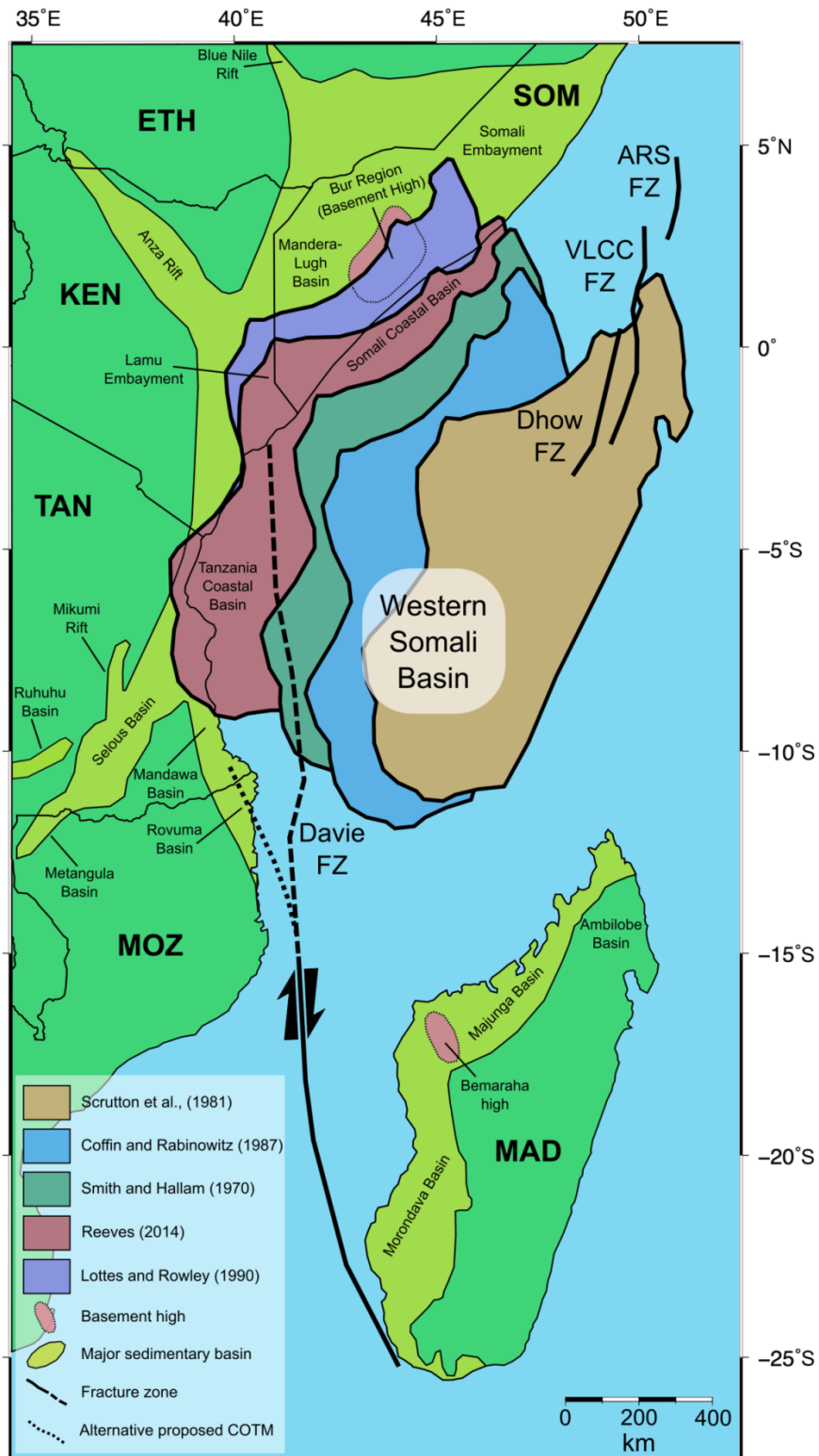
1058 Gondwana was assembled between 600 and 500 Ma in the Pan-African orogeny (e.g.
1059 Trompette, 2000; Van Hinsbergen et al., 2011). Beginning in the Jurassic the subsequent
1060 breakup of East and West Gondwana carried Madagascar approximately southwards, as
1061 shown by ocean magnetic anomalies (Ségoufin and Patriat, 1980; Rabinowitz et al., 1983;
1062 Cochran, 1988; Eagles and König, 2008; Davis et al., 2016), forming the Western Somali
1063 Basin (WSB) (Coffin and Rabinowitz 1987; Geiger et al., 2004). Knowledge of
1064 Madagascar's former position within Gondwana, and the path it followed during its
1065 southward drift, is crucial for creating accurate plate tectonic reconstructions of Gondwana's
1066 dispersal.

1067 Paleogeographic reconstructions of Madagascar's position in Africa (Figure 2.1) have a large
1068 range of fits, suggesting significantly different locations for the continent-ocean transition.
1069 This is primarily due to the lack of fracture zone expressions in bathymetry data, where the
1070 characteristic fracture zone topography is commonly obscured by over 5 km of sediment
1071 (Coffin et al., 1986). The Davie Fracture Zone (DFZ), commonly assumed to form the
1072 western transform fault (Coffin et al., 1986) or continental ocean transform margin (e.g.
1073 Gaina et al., 2013) of the WSB, is one of the few fracture zones confidently identified.
1074 However, the DFZ is overlapped by several independently generated reconstructions (e.g.
1075 Smith and Hallam, 1970; Lottes and Rowley, 1990; Reeves, 2014). This puts our
1076 understanding of this feature into doubt, and highlights the need for the comprehensive
1077 detection of fracture zones to support plate tectonic reconstructions of the basin.

1078 In this paper we present a detailed and self-consistent plate tectonic reconstruction of the
1079 WSB that can be used to further our understanding of the dynamics of continental breakup.
1080 We use a novel combination of free-air gravity, vertical gravity gradient and filtered free-air
1081 gravity directional derivatives to determine the location of the extinct mid-ocean ridge
1082 (MOR) segments and a comprehensive set of gravity lineaments related to fracture zones in
1083 the WSB. Using global gravity datasets with 1 arc-minute resolution captures the complexity
1084 of the breakup geometry and motion, beyond what can be seen in widely spaced shipboard
1085 magnetic profiles, and also constrains the history of the basin to the west of 43°E where no
1086 magnetic anomaly identifications are available (e.g. Davis et al., 2016). These spreading-
1087 related features are tested against existing magnetic and seismic reflection data before being
1088 used to produce a high-resolution plate tectonic reconstruction.

1089 The model provides new insight into Madagascar' s position in Africa prior to Gondwana
1090 breakup, the nature of the DFZ, and the geometry and structure of the East African
1091 continental margin. This provides a significant advance towards a more comprehensive
1092 understanding of the nature of the margins and underlying lithosphere of the WSB, as well
1093 as a broader understanding of rifting events and continental breakup mechanisms.

1094



1096

1097 **Figure 2.1.** Published reconstructions for Madagascar's paleo-position in Africa are shown
 1098 alongside major continental basins, basement highs, and previously identified oceanic
 1099 fracture zones. ARS - Auxiliary Rescue and Salvage; VLCC - Very Large Crude Carrier;
 1100 ETH - Ethiopia; KEN - Kenya; MAD - Madagascar; MOZ - Mozambique; SOM - Somalia;
 1101 TAN - Tanzania; COTM – Continent-ocean transform margin.

1102 **2.2. Data and processing**

1103 In this study, we used the distribution and orientation of fracture zones (FZs) and extinct
1104 MORs to construct a plate tectonic model for the WSB. These tectonic features were
1105 detected using a combination of gravity, magnetic and seismic data.

1106 2.2.1. Gravity data

1107 We used version 23 of the Sandwell and Smith gravity model (Sandwell et al., 2014), which
1108 now has an accuracy of ~2 mGal (compared to 3-5 mGal in previous versions) following the
1109 addition of retracked CryoSat-2 and Jason-1 satellite altimetry data. This improvement
1110 allows detection of many buried structures, particularly short wavelength features such as
1111 extinct MORs and FZs (e.g. Sandwell et al., 2014). In addition to the widely-used free-air
1112 gravity anomaly, gradients such as the vertical gravity gradient (VGG) amplify short
1113 wavelength gravity signals, aiding the detection of relatively small features such as
1114 seamounts and ocean spreading structures (e.g. Kim and Wessel, 2011).

1115 FZs are the inactive extensions of transform faults along the MOR, which run parallel to the
1116 spreading direction during their formation and therefore record plate motions. Oceanic plate
1117 ages, and thus seafloor depths, are offset across transform faults, causing a distinct
1118 bathymetric feature, which is permanently locked in by welding at ridge-transform
1119 intersections (Sandwell, 1984). Variations in crustal thickness due to melt supply (Blackman
1120 and Forsyth, 1991; Gente et al., 1995), transpression or transtension (Menard and Atwater,
1121 1969), and thermal contraction (Collette, 1974) can also result in bathymetric expressions
1122 along fracture zones. The resulting linear ridges and troughs can be traced in bathymetric
1123 data in order to track the spreading history, which in turn may be used in constructing a plate
1124 tectonic model.

1125 In heavily sedimented regions, however, spreading features may be completely buried.
1126 Fortunately, expressions of the spreading features are also preserved in gravity data, even
1127 when buried by sediments, due to lateral density contrasts between sediment, crust, and
1128 mantle across the structures. Gravity data therefore allows the derivation of paleo-spreading
1129 directions in heavily sedimented regions of the ocean (Sandwell et al., 2014).

1130 **2.2.1.1. Bandpass filtering and gravity gradients**

1131 We used a combination of directional derivatives and bandpass filtering to further enhance
1132 the portion of the gravity field associated with FZs. First, a Gaussian bandpass filter was
1133 used to remove short wavelength noise and shallow features within the sediment layer,
1134 together with long wavelength signals from deep mantle heterogeneities. Mulder and
1135 Collette (1984) found that most FZs produce anomalies with intermediate wavelengths

1136 between 50 and 200 km. We further refined these bounds empirically, looking for sharp,
1137 continuous linear anomalies parallel to the overall spreading direction derived from ocean
1138 magnetic anomalies, and found that wavelengths of 55-85 km best highlighted fracture zone
1139 structure.

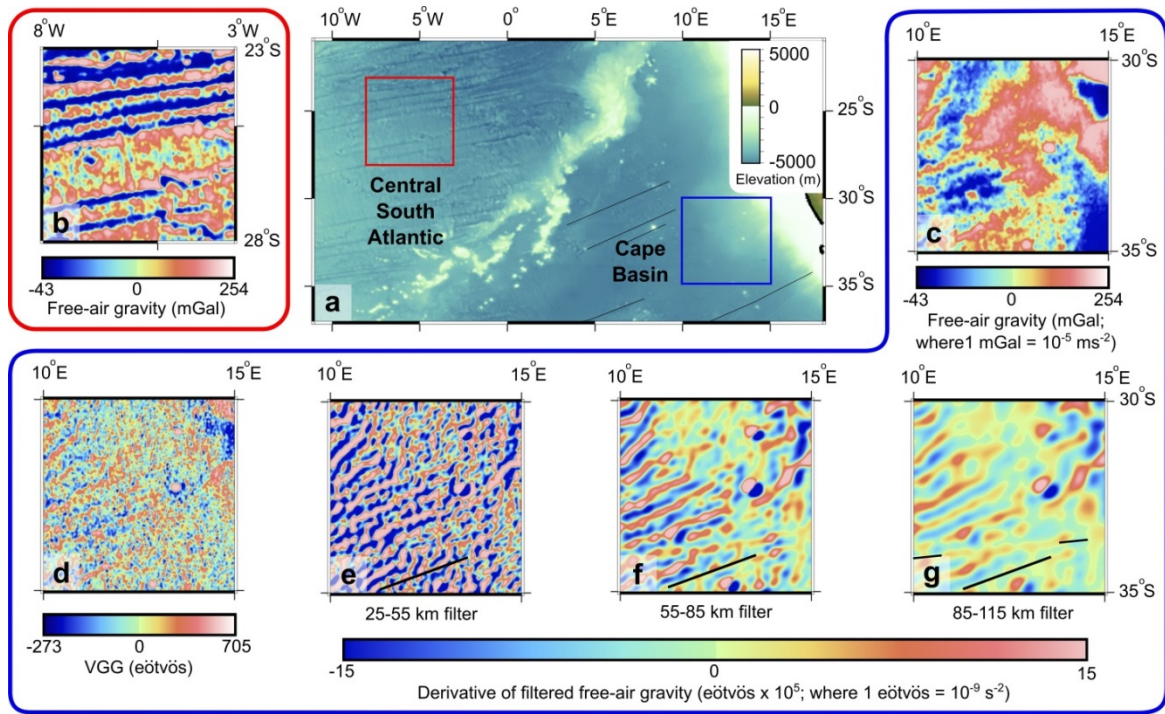
1140 After filtering, we exploited the linear nature of spreading features by taking directional
1141 gradients of the free-air gravity to emphasise lineations of a given orientation (e.g. Mitchell
1142 and Park, 2014). This procedure has similar advantages to illuminating a topographic map to
1143 highlight fault scarps (e.g. Arrowsmith and Zielke, 2009). In the case of the WSB, the ocean
1144 magnetic anomalies indicate an approximately N-S spreading direction. Therefore gradients
1145 taken along this strike would highlight spreading-perpendicular features, such as MOR
1146 segments, and those taken with an E-W strike would highlight spreading-parallel features,
1147 such as FZs. To account for local variability and changes in spreading direction, we took the
1148 directional gradient at 10° intervals between 30° clockwise and anti-clockwise of the chosen
1149 azimuth. This allowed near-perpendicular gradients to be sampled at all points along curved
1150 lineations, ensuring an unbiased sampling of the greatest gradient magnitudes. Examples
1151 showing the effect of changing the orientation and range of gradient sampling are provided
1152 in the supplementary material.

1153 **2.2.1.2. Testing the detection method**

1154 To check our methodology's usefulness in detecting spreading-related structures in buried
1155 oceanic crust, we tested it on a region of the Cape Basin, offshore South Africa (Figure
1156 2.2a). Like the WSB this basin has a thick sedimentary cover (2-5+ km), resulting in
1157 enigmatic spreading features that are difficult to interpret from free-air gravity and VGG
1158 alone. The overall spreading rate is also similar to the WSB (e.g. Eagles, 2007) likely
1159 resulting in similar FZ morphology; making this a very good natural laboratory. The free-air
1160 gravity anomaly of the test region within the Cape Basin was compared to that of an
1161 unsedimented example location from the Central Atlantic (Figures 2.2b-c), demonstrating
1162 the masking effect of sedimentation on the spreading features: clear lineations are visible in
1163 the Central Atlantic (Figure 2.2b), but lineations are only poorly distinguishable in the Cape
1164 Basin (Figure 2.2c). In this case, the VGG does little to enhance the spreading lineations
1165 (Figure 2.2d). Derivatives of the gravity anomaly, perpendicular to the spreading direction
1166 for the Cape Basin, were taken after filtering to retain different wavelengths (Figures 2.2e-g)
1167 to check which wavelengths best enhance spreading features. Shorter wavelengths (25-55
1168 km, Figure 2.2e) are noisy and reduce the continuity of spreading parallel anomalies, whilst
1169 longer wavelengths (85-115 km, Figure 2.2g) reduce the sharpness of individual lineations
1170 and can also merge anomalies into false lineations (example indicated by black arrows).

1171 Intermediate wavelengths of 55-85 km give the best balance between noise reduction and
 1172 imaging of sharp FZ-related anomalies.

1173



1175
 1176

1177 **Figure 2.2.** (a) Test location for the processing technique within the heavily sedimented
 1178 Cape Basin, and an unsedimented example location in the Central South Atlantic. Major
 1179 fracture zones of the Cape basin are marked as thin black lines. (b) Free-air gravity example
 1180 of non-sedimented Central Atlantic spreading features. (c) Free-air gravity from the heavily
 1181 sedimented test location. (d) VGG from the test location. (e-g) Spreading parallel derivatives
 1182 of gravity after filtering to retain specified wavelength bands. Black lines indicate spreading
 1183 direction as constrained by major FZs from elsewhere in the Cape Basin; arrows in g
 1184 indicate merged anomaly lineations.

1185 2.2.2. Magnetics

1186 We used two primary magnetic data types to inform our final model: the Earth Magnetic
 1187 Anomaly Grid (EMAG2 – Maus et al., 2009), and published ocean magnetic anomaly
 1188 interpretations from ship-track data. EMAG2 (non-directionally gridded version) shows the
 1189 large scale trend of magnetic anomalies in the WSB, where many individual linear ocean
 1190 magnetic anomalies are identifiable. The requirement for orthogonality between these linear
 1191 ocean magnetic anomalies and identified FZs allowed us to check our interpretation.

1192 Of the published ocean magnetic anomaly interpretations, those by Sègoufin and Patriat
 1193 (1980), Cochran (1988), and Davis et al. (2016) show strong similarities to each other, with

1194 the basin's centre of symmetry lying around the M0 ocean magnetic anomaly (125 Ma) and
1195 the oldest anomalies detected in the basin reaching between M21 and M24. Rabinowitz et al.
1196 (1983) and Eagles and König (2008) choose an alternative interpretation with the basin's
1197 centre of symmetry around M10, and located significantly farther south. We compare these
1198 lines of symmetry with MOR segments identified in the gravity data and used the best
1199 matching interpretations to temporally constrain our reconstruction. All interpretations
1200 suggest slow-intermediate spreading rates for the WSB

1201 2.2.3. Seismic reflection data

1202 The East AfricaSPAN seismic reflection lines were used to identify the nature of the top
1203 basement reflector and measure the crustal thickness, thus helping determine whether the
1204 underlying basement is continental, oceanic, or transitional in nature. In addition, faults
1205 associated with the tectonic fabric at mature slow/intermediate spreading centres dip towards
1206 the MOR (e.g. Carbotte and Macdonald, 1990; Behn and Ito, 2008). Therefore fault polarity
1207 switches were used to help constrain the location of the MOR to the east of the DFZ, when
1208 spreading ceased ~50 Ma after breakup.

1209 **2.3. Feature identification**

1210 Spreading features of the WSB, including the extinct MOR and FZs, must be detected in
1211 order to constrain plate tectonic reconstructions. To do this we identify the characteristics
1212 that define each group of features. We must, however, also be careful to avoid interpretation
1213 of areas modified by young rifts, such as the Quirimbas Graben, and post spreading
1214 magmatic additions, such as the Comoros Islands, Cosmoledo Group, and Wilkes Rise (e.g.
1215 Figure 2.3), which have strong expressions in the gravity data and mask the true nature of
1216 spreading features.

1217 2.3.1. Mid-oceanic ridge segments

1218 Extinct MOR segments have orientations perpendicular to the final spreading direction, and
1219 appear as a free-air gravity low due to a persistent low density gabbroic root (Jonas et al.,
1220 1991). These linear anomalies usually lie close to the basin's centre of symmetry, with the
1221 exception of basins undergoing subduction, such as the Pacific Ocean (Müller et al., 2008),
1222 or those having undergone spreading centre reorganisation and ridge jumps. To identify the
1223 extinct MOR from gravity anomalies, we therefore looked for three characteristics: 1) a
1224 linear free-air gravity low, 2) an orientation perpendicular to the approximately N-S paleo-
1225 spreading direction (e.g. Ségoufin and Patriat, 1980), and 3) a location close to the axis of
1226 symmetry for the WSB. Free-air gravity and VGG maps were used for this task.

1227 Regions where only one gravity lineament with these characteristics was identified provided
1228 reliable MOR segment interpretations. These segments were therefore compared with the
1229 ocean magnetic anomaly interpretations of Ségoufin and Patriat (1980), Rabinowitz et al.
1230 (1983), Cochran (1988), Eagles and König (2008), and Davis et al. (2016) to assess
1231 confidence in these interpretations. Where multiple possible MOR anomalies existed,
1232 seismic reflection data were used to locate the MOR using basement fault polarity (e.g. Behn
1233 and Ito, 2008). If no seismic data were available, we chose the lineament that was most
1234 consistent with the ocean magnetic anomaly interpretations verified by our reliable MOR
1235 segments

1236 2.3.2. Fracture zones

1237 In the WSB, 2-5+ km of sediment have accumulated since the Jurassic (Coffin et al., 1986),
1238 removing most bathymetric expressions of FZs. A limited set of major lineations related to
1239 fracture zones can, however, be seen in the free-air gravity anomaly, reflecting crustal
1240 thickness variations, basement offsets, and infilling sediments along the FZs. We further
1241 highlighted FZ-related anomalies using a 55-85 km bandpass filter and an E-W directional
1242 derivative, orthogonal to the overall N-S spreading direction, as illustrated for the Cape
1243 Basin in Figure 2.2.

1244 The resulting linear anomalies relating to the FZ trends are generally of low amplitude
1245 compared with those arising from volcanic edifices or active rifts. This is primarily the result
1246 of the FZs' comparatively small scale, greater depth, and lower density contrast across the
1247 structural boundary. However, to map FZs, we were primarily interested in fairly continuous
1248 linear anomalies that form a consistent pattern, even if low in amplitude due to the thick
1249 sedimentary cover. These lineations (e.g. Figure 2.2f) can be mapped along minima,
1250 maxima, or polarity changes in the gravity gradient; all have the same orientation and thus
1251 lead to the same plate tectonic model. However, for consistency, we have manually picked
1252 along the polarity change in the gravity gradient, except in cases where this is poorly defined
1253 and the maximum or minimum shows the orientation more clearly.

1254 The Tanzania Coastal Basin, inboard of the DFZ, has previously been assumed to be
1255 underlain by continental crust. To determine whether to interpret any gravity lineations
1256 within this basin as continental shear zones or oceanic fracture zones, the East AfricaSPAN
1257 seismic reflection dataset was used to determine the nature of the crust. Oceanic crust was
1258 identified through the recognition of a rough high amplitude top reflector with a tectonic
1259 spreading fabric, lacking significant syn-rift deposits (Davies et al., 2005; Rodger et al.,
1260 2006) or by a hummocky reflector with continuous overlying sedimentary deposits (Soto et

1261 al., 2011), and, for normal oceanic crust, a two-way travel time (TWTT) between top
1262 basement and any Moho reflections of ~2 seconds (e.g. White et al., 1992).

1263 **2.4. Plate tectonic reconstruction**

1264 After establishing the FZ lineations for the WSB, we used the plate tectonic reconstruction
1265 software Gplates (e.g. Williams et al., 2012), populated with the plate polygons of Seton et
1266 al. (2012), to retrace Madagascar's path back to Africa. The previously identified Dhow and
1267 VLCC fracture zones (Bunce and Molnar, 1977) were not used as input to the model
1268 because Coffin and Rabinowitz (1987) suggested they may be the result of tectonic
1269 processes other than oceanic spreading. Once the general origin for Madagascar was
1270 established, its position was refined by aligning conjugate continental shear zones and
1271 sedimentary basins, following Windley et al. (1994) and Reeves (2014). Artificial flowlines
1272 were then seeded at the deepest points of the basins between Madagascar and Africa
1273 according to the CRUST1.0 model (Laske et al., 2013), assumed to be the original centre of
1274 symmetry for spreading. In an iterative process, the motion of Madagascar away from Africa
1275 was then refined by aligning model-generated flowlines with the interpreted fracture zone
1276 trends. The plate model was temporally constrained by the ocean magnetic anomaly
1277 interpretations of Cochran (1988) and Davis et al. (2016), whose centres of symmetry
1278 around M0 most reliably matched the observed MOR segments. However, no plate velocity
1279 constraints exist between the initiation of rifting in the Toarcian (182 Ma) and the oldest
1280 ocean magnetic anomaly detected in the basin (M22, 150.5 Ma – Cochran, 1988; Gradstein,
1281 2012). Between the onset of rifting and breakup at 170 Ma in the Bajocian (Geiger et al.,
1282 2004) we imposed an extensional velocity of 3.3 mm/y. This was based on well constrained
1283 present day extension rates along the East African Rift System between Malawi and Afar
1284 (Saria et al., 2014) and may therefore represent a realistic estimate for Jurassic extensional
1285 rates during the rifting phase. Following this rifting episode ~390 km remained between the
1286 spreading centre and the M22 magnetic anomaly, which was bridged with a constant
1287 velocity of 40 mm/y.

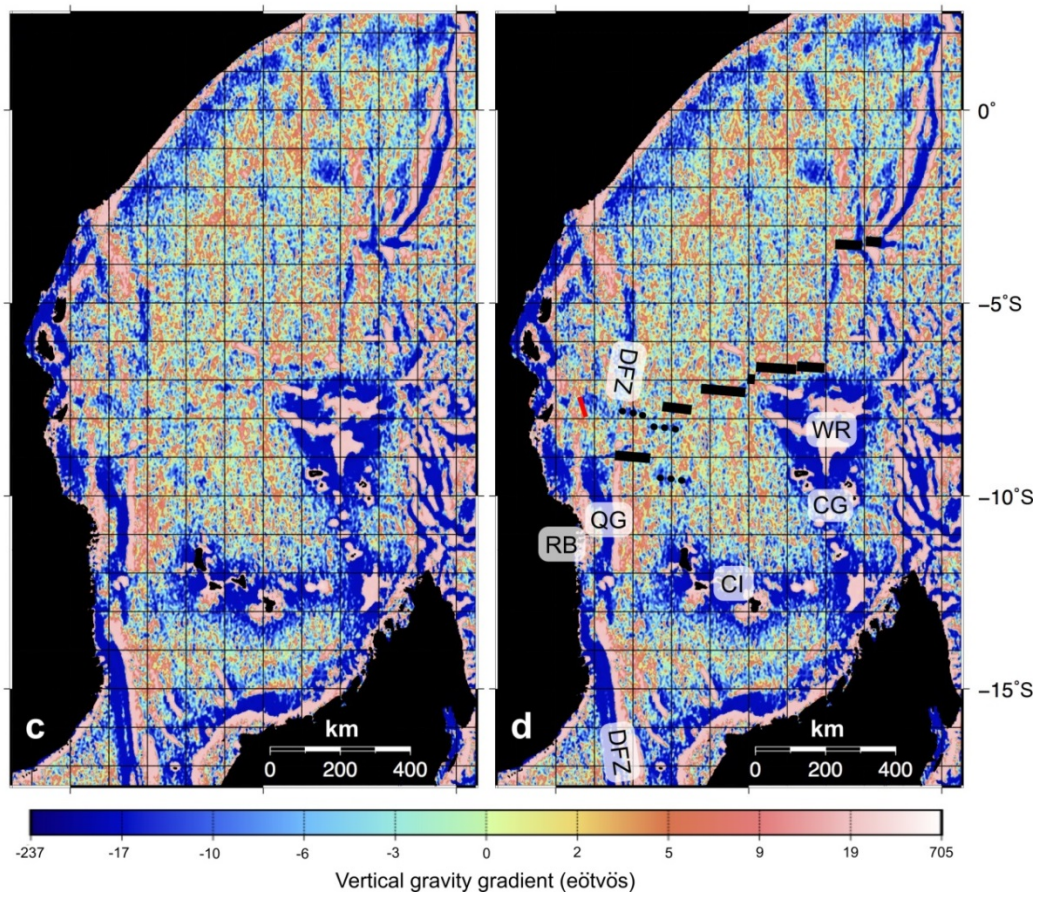
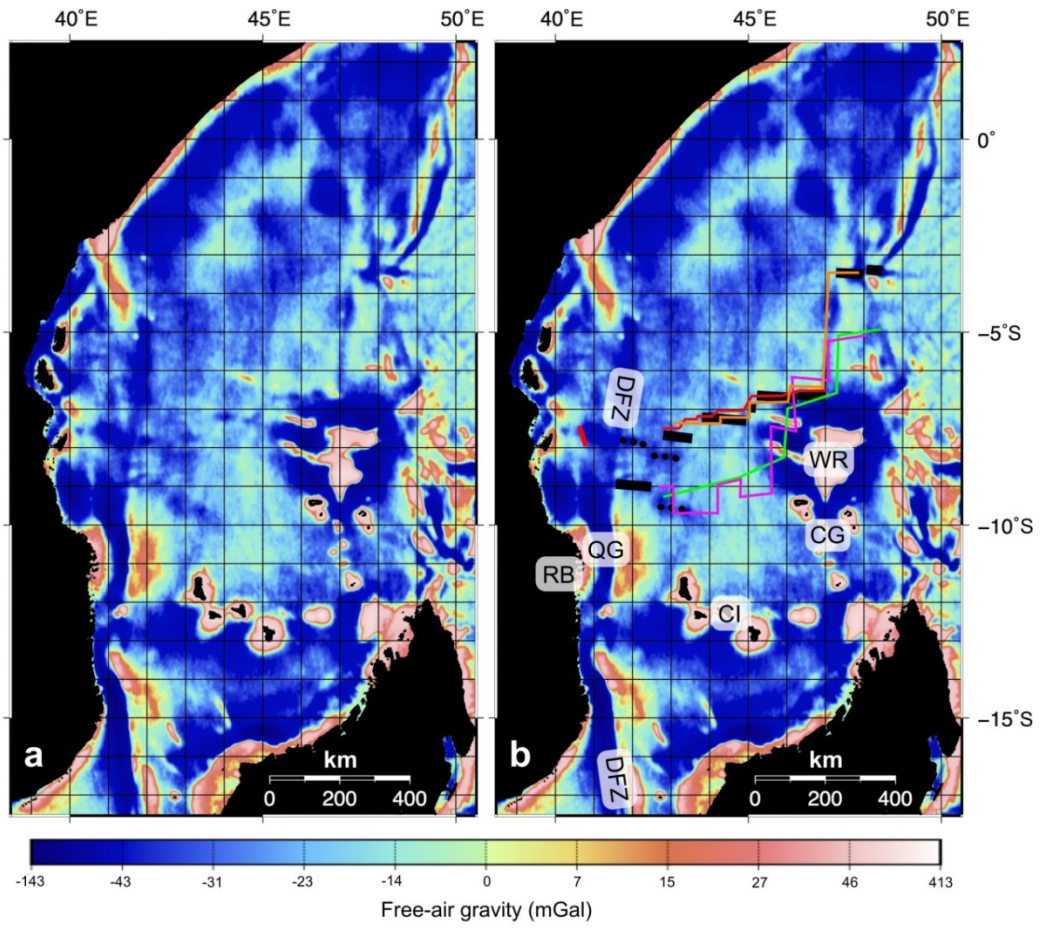
1288 **2.5. Results**

1289 Using free-air gravity, VGG, and directional derivatives of filtered gravity from version 23
1290 of the Sandwell and Smith gravity model, we have detected the extinct MOR segments and a
1291 comprehensive set of lineaments relating to spreading features in the Western Somali Basin.
1292 These features are tested against magnetic and seismic reflection data before being used to
1293 produce a high-resolution plate tectonic reconstruction of the basin.

1294 2.5.1. MOR segment locations

1295 Oceanic magnetic anomalies in the WSB show that spreading occurred in a generally N-S
1296 direction (Ségoufin and Patriat, 1980). Following this, and the NE-SW trends of the Kenya-
1297 Somalia and Northern Madagascar coastlines, we expect the extinct MOR to be composed of
1298 E-W trending segments with an overall NE-SW trend following the basins centre of
1299 symmetry. We identify short linear gravity lows following this pattern in both the free-air
1300 gravity anomaly (Figure 2.3a and b) and the VGG (Figure 2.3c and d). The MOR segments
1301 generally range from 30-100 km in length, with offsets between segments ranging from as
1302 little as 20 km up to 350 km between the two easternmost segments.

1303 On the eastern side of the basin, single gravity lineaments point unambiguously to the MOR.
1304 This region is therefore used as an independent check of the previous ocean magnetic
1305 anomaly interpretations. This shows that interpretations with the basin's centre of symmetry
1306 based on M0 are most reliable, and therefore the ocean magnetic anomaly interpretations of
1307 Cochran (1988) and Davis et al. (2016) are used to temporally constrain our plate tectonic
1308 model. In the western region of the basin, close to the DFZ, two segments have several
1309 possible MOR anomalies identifiable in the gravity data (Figure 2.3 – dashed lines). For the
1310 westernmost segment, seismic reflection data covers the southern gravity lineament and
1311 shows a flip in half graben polarity centred at its location. The next segment to the east is
1312 covered by magnetic data along ship tracks and the verified ocean magnetic anomaly
1313 interpretations show the northern gravity lineament to be most consistent (Figure 2.3 – solid
1314 lines).



1317 **Figure 2.3.** (a) Free-air gravity anomaly. (b) Figure 2.3a overlain with the picked MOR
1318 (solid black lines) and alternative segment possibilities (dashed black lines). Location of the
1319 East AfricaSpan seismic reflection line shown in this study is indicated by the thick red line
1320 in the Tanzania Coastal Basin. Previously determined basin symmetries are shown as
1321 coloured lines where constrained by ocean magnetic anomalies. The interpretations of
1322 Cochran (1988 – orange) and Davis et al. (2016 – red) are centred on M0 and lie in good
1323 agreement with the MOR defined by gravity. The interpretations of Coffin and Rabinowitz
1324 (1987 - green) and Eagles and König (2008 - pink) are centred on M10 and deviate
1325 significantly from the gravity MOR. RB – Rovuma Basin; QG – Quirimbas graben (active
1326 rift). DFZ – Davie Fracture Zone; Post spreading volcanism: CI – Comoros islands; CG –
1327 Cosmoledo Group; WR – Wilkes Rise. (c) Vertical gravity gradient. (d) Figure 2.3c overlain
1328 with MOR picks and abbreviations as for Figure 2.3b.

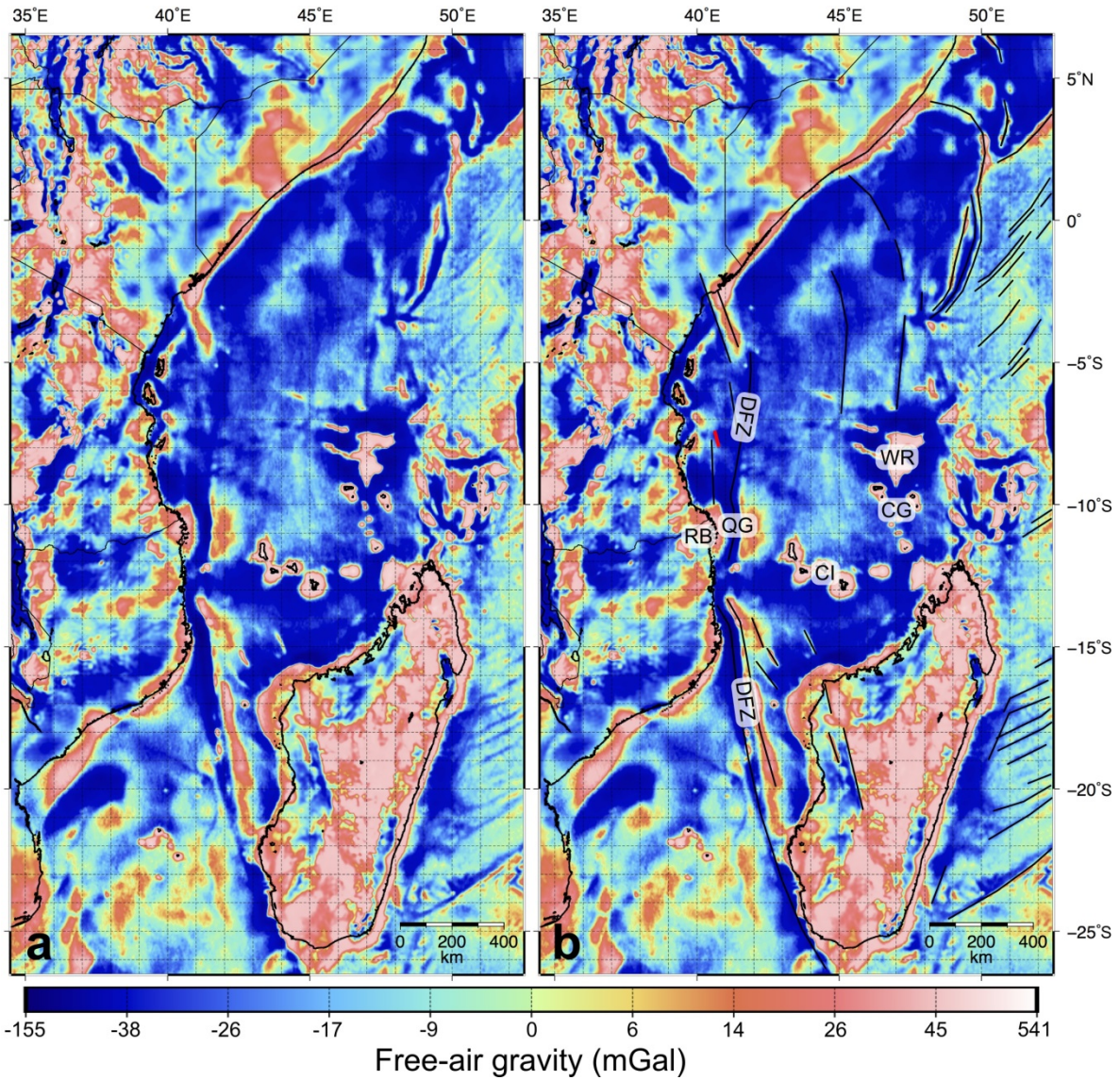
1329 2.5.2. Fracture zone trends

1330 The free-air gravity anomaly shows a number of major lineaments in the Western Somali
1331 Basin, including the Davie, ARS, Dhow, and VLCC fracture zones, as well as number of
1332 more subtle lineaments with a similar trend (Figure 2.4). Fracture zones in the Indian Ocean,
1333 which has much thinner sediment cover (<1 km; Whittaker et al., 2013), are also clearly
1334 seen. These lineaments often display a significant anomaly in the gravity field, from ~20
1335 mGal to over 100 mGal compared to their surroundings, and can be traced for several
1336 hundreds of kilometres, including over 1000 km in the case of the DFZ. They show an
1337 arcuate spreading pattern for the Western Somali Basin. This trend can not only be seen in
1338 the north of the basin, but is also defined by a striking bend in the DFZ located at 41° E, 14
1339 ° S, which appears to deflect the trend of the continent-ocean transform margin onshore
1340 along the Rovuma Basin.

1341 Lineaments detected only in the filtered and directionally differentiated gravity data are
1342 generally shorter and less continuous, ranging in length from less than 100 km up to
1343 approximately 600 km (Figure 2.5). In several instances, extensions to fracture zones
1344 detected in the free-air anomaly can be made, such as at 45° E 7° S, where a conjugate
1345 fracture zone to one detected in the north becomes apparent in the southern half of the basin.
1346 On the whole, these lineaments align with the framework laid out by anomalies detected in
1347 the free-air gravity and provide a comprehensive record of plate spreading directions. A few
1348 short lineaments, however, lie at significant angles to the general fabric. It is likely that these
1349 lineaments are the result of structures unrelated to spreading (which should produce a
1350 consistent and predictable network of FZs), such as small volcanic chains or large infilled

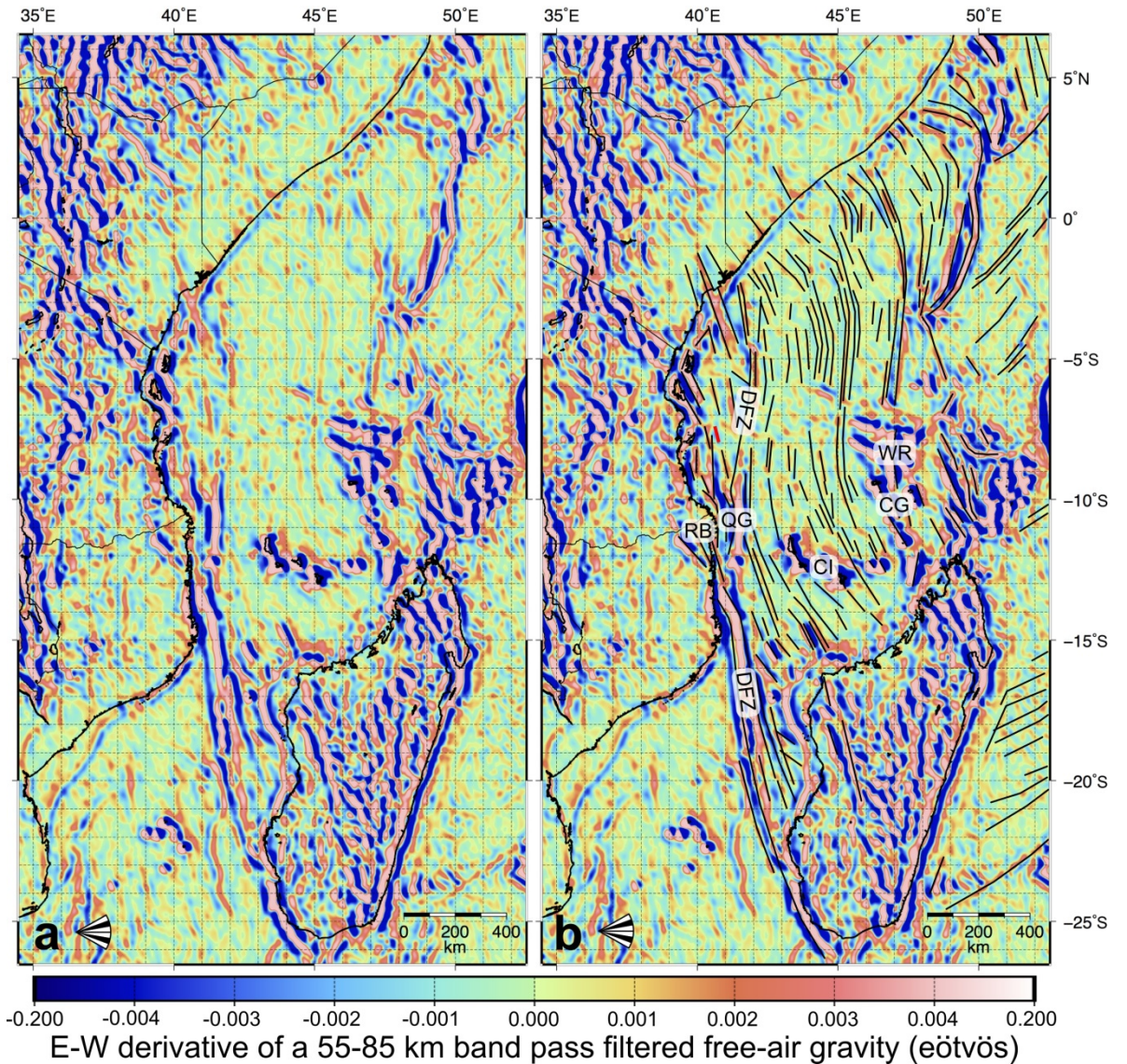
1351 submarine channels, producing gravity anomalies with a similar wavelength to those of
1352 spreading features.

1353 The EMAG2 gridded magnetic dataset (Figure 2.6a) contains several linear magnetic trends
1354 within the central region of the WSB where the basement is oceanic in nature (Coffin et al.,
1355 1986). Away from magmatic structures such as the Wilkes Rise and Comoros Islands these
1356 anomalies should be due to magnetization of oceanic crust during seafloor spreading,
1357 producing ocean magnetic anomalies. Their orientation appears variable and they do not
1358 seem to define a consistent spreading direction. When, however, the magnetics are overlain
1359 by the FZ trends identified in the gravity data, the linear magnetic anomalies can be seen to
1360 lie consistently perpendicular to the arcuate fracture zone lineaments (Figure 2.6b),
1361 providing independent confirmation of our proposed fracture zone structure.



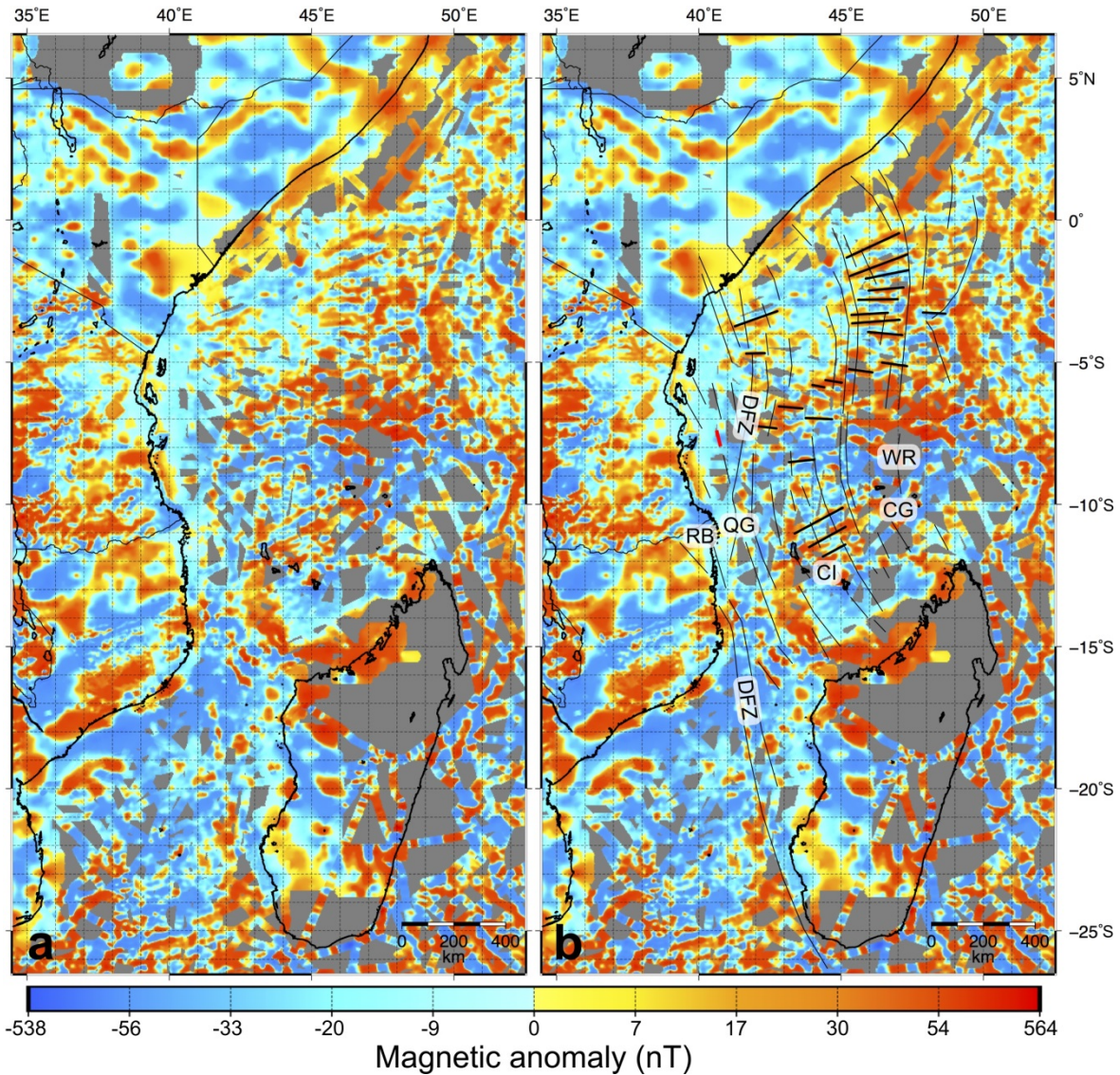
1363

1364 **Figure 2.4.** (a) Free-air gravity anomaly. (b) Figure 2.4a overlain with the linear anomalies
1365 related to potential fracture zones. Abbreviations as for Figure 2.3. Location of the East
1366 AfricaSPAN seismic reflection line shown in this study is indicated by the red line in the
1367 Tanzania Coastal Basin.



1369

1370 **Figure 2.5.** (a) E-W derivative of a Gaussian band-pass filtered free-air anomaly, 50% long
 1371 and short wavelength cutoffs at 85 and 55 km, respectively, to best retain anomalies related
 1372 to fracture zones. (b) Figure 2.5a overlain with the linear anomalies identified here and in
 1373 Figure 2.4. Abbreviations as for Figure 2.3. Location of the East AfricaSpan seismic
 1374 reflection line shown in this study is indicated by the red line in the Tanzania Coastal Basin



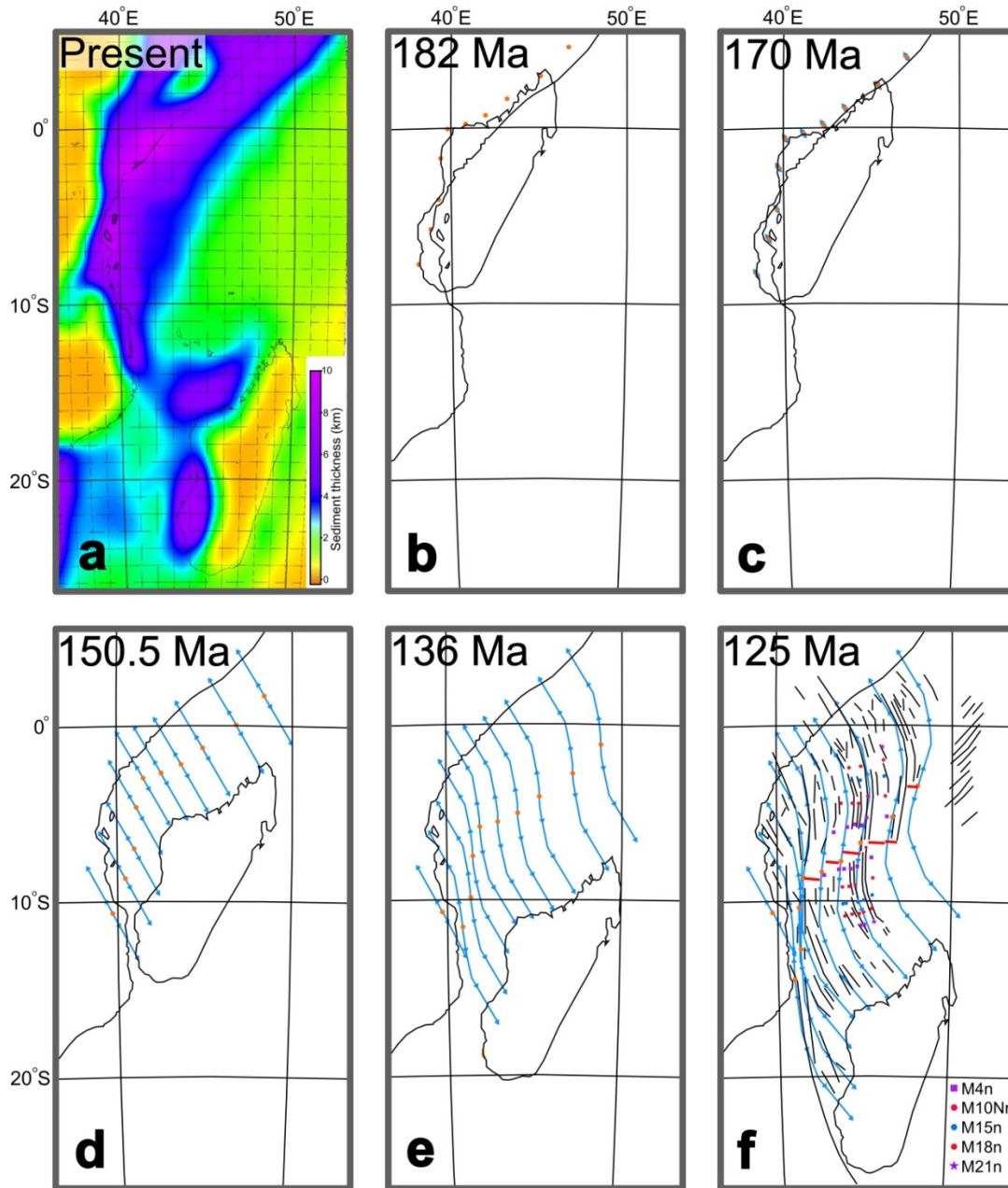
1376

1377 **Figure 2.6.** (a) The EMAG2 non-directionally gridded magnetic anomaly dataset. (b) Figure
 1378 2.6a with broadly E-W linear magnetic anomalies detected from unmodified oceanic crust
 1379 (thick black lines) and fracture zones (thin black lines) marked, showing a consistently
 1380 orthogonal relationship. Abbreviations as for Figure 2.3. Location of the East AfricaSpan
 1381 seismic reflection line shown in this study is indicated by the red line in the Tanzania
 1382 Coastal Basin.

1383 2.5.3. Plate tectonic model

1384 Using our new fracture zone lineaments, shear zone data from Reeves and De Wit (2000),
1385 and basin depth data from CRUST1.0, we developed a new plate tectonic reconstruction for
1386 Madagascar's separation from Africa (Figure 2.7).

1387 An initial phase of continental rifting from 182 Ma leads to continental break up at
1388 approximately 170 Ma (Figure 2.7b-c). Oceanic spreading commences in a NNW-SSE
1389 direction and results in strike slip tectonics between Madagascar and northern Mozambique,
1390 forming the Rovuma Basin (Figure 2.7c-d). At ~150.5 Ma the spreading direction changes to
1391 almost N-S, resulting in the near alignment of several flow lines in the west of the basin
1392 (Figure 2.7d-e). After 136 Ma the spreading direction continues to rotate causing full
1393 convergence of the flow lines in the west of the basin along the trace of the DFZ. Faster
1394 spreading in the west compared to the east also results in an anti-clockwise rotation of
1395 Madagascar to its present day position, which was reached when oceanic spreading ceased
1396 in the basin at ~125 Ma (Figure 2.7e-f).



1398

1399 **Figure 2.7.** Plate tectonic reconstruction of Madagascar's escape from Africa from the Early
 1400 Jurassic to the cessation of spreading in the Cretaceous. Madagascar is shown without the
 1401 remainder of East Gondwana (India, Antarctica and Australia) attached. (a) Present day
 1402 sediment thickness in the Western Somali Basin taken from the CRUST1.0 model. (b-e) The
 1403 key stages of Madagascar's motion out of Africa. Modelled flowlines are shown as blue
 1404 arrowed lines where the centre of symmetry is marked by orange circles. (f) Madagascar's
 1405 present-day position, which is reached at around 125 Ma. Flowlines closely match the
 1406 fracture zone pattern of the basin (additional black lines), and the basin's predicted final
 1407 symmetry (orange circles) lies in good agreement with the interpreted extinct mid-ocean

1408 ridge system (red lines). Locations of magnetic anomalies used to temporally constrain plate
1409 motions shown with symbols as interpreted by Davis et al. (2016).

1410 **2.6. Discussion**

1411 2.6.1. The nature of the WSB's margins and of gravity lineaments in the coastal 1412 basins

1413 Modern concepts of passive margin formation define two end member types. 1) At volcanic
1414 rifted margins, crustal thinning occurs over relatively short distances (50-100 km (e.g.
1415 Franke, 2013)) and is accompanied by large volumes of magmatism. These are characterised
1416 by both thick wedges of volcanic flows that appear as seaward dipping reflectors in seismic
1417 reflection data (e.g. Planke and Eldholm, 1994; Geoffroy, 2005) and by high velocity
1418 underplating and heavily intruded crust identified in seismic refraction studies (e.g.
1419 Korenaga et al., 2000; Hirsch et al., 2009). 2) At magma-poor rifted margins, largely
1420 unthinned continental crust of the proximal domain passes into a hyperextended domain
1421 containing three sub domains (necking, hyperthinned, and exhumed mantle domains), before
1422 oceanic crust marks the onset of the oceanic domain (Tugend et al., 2015). The necking
1423 domain and hyperthinned domains accommodate most of the crustal thinning, containing
1424 continental crust of <10 km thick, and typically extend 100-200 km from the proximal
1425 domain (e.g. Reston, 2009; Sutra and Manatschal, 2012). The exhumed mantle domain
1426 forms the continent-ocean transition and is thought to consist of mantle material unroofed
1427 and serpentised during extensional detachment faulting (e.g. Bayrakci et al., 2016; Gillard
1428 et al., 2016), which separates continental crust from oceanic crust. These margins
1429 characteristically experience limited magmatism during extension (Franke, 2013).

1430 To understand the style of margin formation in the WSB, we draw together a combination of
1431 seismic, gravity, magnetic and geological evidence. Coffin et al. (1986) confirmed the
1432 existence of oceanic crust just offshore of the Kenya-Somalia border as far north and west as
1433 42.05° E 2.52° S, but inboard of this within the Tanzania Coastal Basin and extending
1434 onshore within the Lamu Embayment, thin crust (<13 km thick; Reeves et al., 1987) of an
1435 ambiguous nature is covered by thick sediments (up to +12 km, Yuan et al., 2012 and
1436 references therein). Based on gravity and magnetic modelling, Reeves et al. (1987) proposed
1437 that this crust is oceanic in nature, consistent with observations of necking zones (as defined
1438 by Tugend et al., 2015) onshore along the western edge of the Lamu Embayment from
1439 seismic refraction data, which suggest a sharp crustal thinning from over 40 km to probably
1440 less than 15 km at this location (Prodehl et al., 1997). This implies that offshore seismic
1441 reflection data along the Tanzanian and Kenyan margins is located seaward of the necking

1442 zones. Ascertaining the margin nature is thus more difficult, since seaward dipping
1443 reflectors, which are characteristic of volcanic margins, form in vicinity to the necking zone
1444 and therefore may not be detected, whilst exhumed mantle domains, as seen at magma-poor
1445 margins, can be difficult to distinguish from oceanic crust formed at slow spreading centres
1446 when using seismic reflection data alone (e.g. Davy et al., 2016).

1447 Furthermore, the already thin crust onshore within the Lamu Embayment suggests that the
1448 ‘shelf edge’ high, seen in the free-air gravity along the Somali coast east of the DFZ, is not
1449 indicative of crustal thinning, and may not coincide with the continent-ocean transition as
1450 proposed elsewhere (e.g. Bauer et al., 2000). The effects of increasing water depth and thick
1451 sedimentary accumulations can also produce this pattern of gravity anomalies without an
1452 additional contribution from decreasing crustal thickness (e.g. Walcott, 1972; Watts &
1453 Stewart, 1998). Elsewhere, along the western margins of the WSB, no shelf edge gravity
1454 anomalies are present, possibly due to superimposed effects of active rifting in the area,
1455 providing little information as to the margin nature. However, as there is little evidence for
1456 Jurassic rift-related volcanic rocks exposed at the surface in Madagascar, Tanzania or Kenya
1457 (e.g. Guiraud et al., 2005), and neither have they been drilled onshore or offshore (despite
1458 the pervasive record of post-rift volcanics emplaced in the upper Cretaceous (Coffin and
1459 Rabinowitz, 1988) related to the breakup between Madagascar and India (e.g. Storey et al.,
1460 1995)), significant magmatism during rifting in the WSB seems unlikely. This apparent lack
1461 of rift related volcanism, the generally thin nature of the oceanic crust interpreted elsewhere
1462 within the WSB (5.22 ± 0.64 Km, Coffin et al., 1986), and the lack of any high velocity
1463 underplating interpreted around the necking zone from seismic refraction studies (Prodehl et
1464 al., 1997) make present observations from the margins of the WSB more consistent with the
1465 magma-poor endmember style of rifted margins.

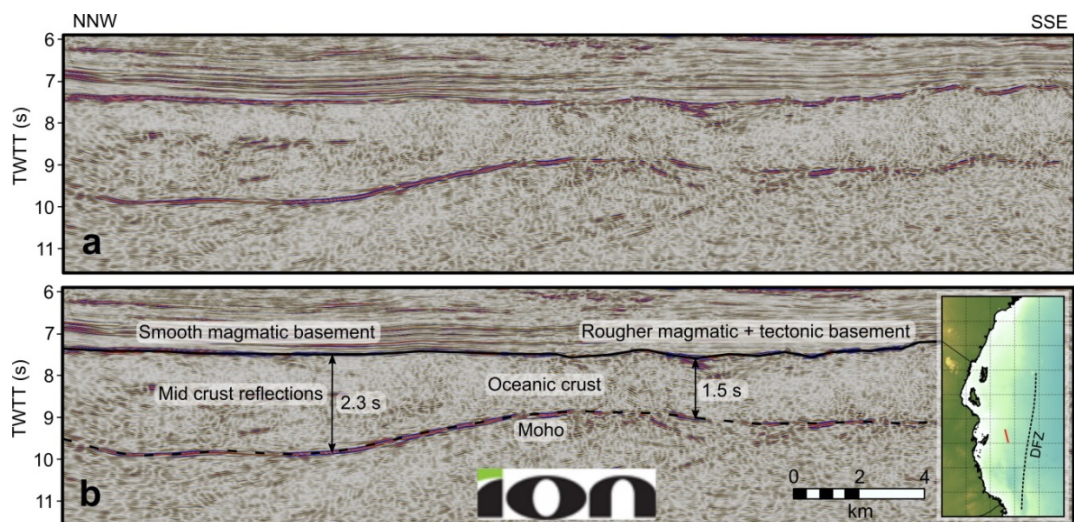
1466 The ambiguous crust within the Tanzania Coastal Basins and Lamu Embayment could
1467 therefore be either oceanic, formed after breakup, or hyperextended continental crust and
1468 mantle. Whilst the present-day high heatflow along the East African margin (attested by the
1469 significant gas discoveries in the region) possibly favours the presence of radiogenic
1470 continental crust (e.g. White et al., 2003), active lithospheric thinning along the offshore
1471 branch of the East African Rift System (e.g. Delvaux and Barth, 2010; Franke et al., 2015)
1472 would also act to increase regional heatflow. In the mid-Tanzania Coastal Basin, inboard of
1473 the DFZ, the East AfricaSPAN seismic reflection lines image a strong and continuous
1474 reflector at approximately 9.5 s TWTT, which is 1.5 to 2.3 s TWTT below the top basement
1475 (Figure 2.8). This is typical of slightly thin to normal oceanic crust (White et al., 1992), and
1476 is similar to the 1.17 to 2 s TWTT derived for oceanic crust elsewhere within the WSB

1477 (Coffin et al., 1986). Several areas within the crust also have a low reflectivity character,
 1478 often described within oceanic crust (e.g. Bécél et al., 2015).

1479 The nature of the crust changes from NNW to SSE along the line. In the NNW, a smooth top
 1480 basement reflector is imaged at 7.4 s TWTT, which is characteristic of oceanic crust formed
 1481 by relatively robust magmatic accretion with little tectonic extension (e.g. Reston et al.,
 1482 2004). Here an additional reflector can be seen at ~8.3 s TWTT (0.9 seconds below top
 1483 basement) which delineates an upper and lower crustal layer. Elsewhere within the WSB, the
 1484 oceanic layer 2 thickness has been derived as 0.93 s TWTT (Coffin et al., 1986), and so this
 1485 reflector may represent the boundary between oceanic layers 2 and 3. The smooth top
 1486 basement and Moho reflectors also extend ENE along the seismic cross line, perpendicular
 1487 to the spreading direction, with a consistent offset of between 1.8 and 2 s TWTT, before
 1488 eventually reaching the tectonically overprinted DFZ, where their character is lost. To the
 1489 SSE in Figure 2.8, following a reduction in thickness of the crust demonstrated by the
 1490 shallowing of the Moho reflector, the top basement gains a weak tectonic fabric. These
 1491 observations are consistent with a reduction in magma supply and resulting increase in the
 1492 tectonic extensional component of oceanic spreading (e.g. Reston et al., 2004).

1493 Alternatively, the Moho reflector could represent a detachment fault formed between
 1494 continental crust and mantle during hyper-extension (e.g. Tugend et al., 2015), such as the S
 1495 reflector west of Galicia (Hoffmann and Reston, 1992) and H reflector in the Iberia Abyssal
 1496 Plain (Dean et al., 2008). However, the smooth top basement reflector lacks the well-defined
 1497 fault blocks often imaged in such hyper-extended domains (Reston, 2009). This suggests
 1498 that extreme crustal extension is unlikely, especially as rift related volcanism, which could
 1499 otherwise have masked fault block topography, is extremely limited during hyper-extension
 1500 at magma-poor margins (Franke, 2013).

1501



1502

1503 **Figure 2.8.** (a) Seismic reflection line from the East AfricaSPAN (Ion Geophysical) inboard
1504 of the DFZ. (b) Figure 2.8a with interpretation overlain. Inset shows location relative to the
1505 coastline and the DFZ.

1506 All these observations thus support high levels of extension, probably including oceanic
1507 crust, in the mid-Tanzania coastal basin inboard of the DFZ. The DFZ cannot then be a
1508 simple continent-ocean transform margin. Instead, Madagascar must have originated from
1509 within the Tanzania Coastal Basins and Lamu Embayment, with the Rovuma Basin forming
1510 the continental-ocean transform margin. The onshore trend of this basin is closely aligned
1511 with the early SSE trending fracture zones detected in the gravity data (Figure 2.9b), and in
1512 fact, in our plate tectonic reconstructions, strike-slip motion of southern Madagascar along
1513 this basin is unavoidable. This is in good agreement with observations of dextral strike slip
1514 faults along the Rovuma Basin margin (Emmel et al., 2011) and an onshore sedimentary
1515 thickness of ~10 km in the northern Rovuma Basin that rapidly thins westward to <1 km
1516 (Key et al., 2008), consistent with a continent-ocean transform margin. As noted by Reeves
1517 (2014), the passage of Madagascar along the Rovuma Basin also allows for a much tighter
1518 and consistent fit of Gondwana fragments, reducing the need for gaps and non-smooth plate
1519 motions during Gondwana's disassembly.

1520 2.6.2. Rifting mechanisms and Gondwana breakup

1521 Rifting between East and West Gondwana began in the Toarcian (Geiger et al., 2004) and
1522 was probably initiated by the eruption of the Bouvet plume, resulting in a contemporaneous
1523 volcanic passive margin in Mozambique (Klausen, 2009). Here, an 8.5 km thick suite of rift-
1524 related basalts and rhyodacites defines a relatively narrow volcanic margin, where a
1525 magmatic mode of extension dominated in the lead-up to breakup (Klausen, 2009). This
1526 section of the rift system developed discordantly to the structural trend of Gondwana's
1527 sedimentary basins (Salman and Abdula, 1995), suggesting that pre-existing lithospheric
1528 structure was not a key parameter leading to breakup.

1529 In the Western Somali basin, however, there is little evidence for a magmatic breakup as
1530 discussed earlier (Section 2.6.1.). This is most likely a function of the WSB's distance from
1531 the volcanic centre in Mozambique as seen in the Gulf of Aden. Here, volcanic margins
1532 formed close to the Afar hotspot, yet farther away, east of longitude 46° E, the margins are
1533 magma-poor (Leroy et al., 2012). Breakup along the Tanzanian-Kenyan and Kenyan-
1534 Somalian rift sections is therefore less likely to have been influenced by magmatism and
1535 thermal weakening of the lithosphere (Buck, 2007). It is apparent from the spreading
1536 lineaments detected in the WSB that initial spreading occurred in a NNW-SSE direction, in
1537 agreement with principal extensional stresses around the Mozambique basin (Le Gall et al.,

1538 2005). This is consistent with the occurrence of strike-slip tectonics along the NNW-SSE
1539 trending Rovuma Basin and oblique rifting along the N-S trending Kenya-Tanzania margin
1540 (Figure 2.9b), both of which are mechanically favourable (Emmel, 2011; Brune et al., 2012).
1541 This is similar to observations from the Gulf of California where oblique rifting assisted
1542 continental breakup through the efficient focusing of crustal thinning within pull-apart
1543 basins bounded by large offset strike-slip faults (Bennett and Oskin, 2014). If this
1544 mechanism was active during the Jurassic rifting along the Tanzania-Kenya margins, it may
1545 explain the possible margin segmentation suggested by the stepped shape of Madagascar's
1546 western coastline. Margin segmentation is common to many oblique passive margins
1547 worldwide (e.g. Leroy et al., 2012; Bennett and Oskin, 2014).

1548 Conversely, the NE-SW trending Kenyan-Somalian rifted margin formed orthogonally to the
1549 breakup direction. Although the Rovuma basin shows little evidence of Karoo age rifting
1550 and sedimentation (Smelror et al., 2008), the Morondava, Majunga and Ambilobe basins of
1551 Madagascar all contain underlying Karoo sediments (e.g. Hankel, 1994). The conjugate
1552 margins on the mainland, the Tanzanian-Kenyan and Kenyan-Somalian rift systems, thus
1553 appear to have followed the pre-existing lithospheric structure of the Karoo rift system. A
1554 transition can therefore be proposed along the East African margin from dominant strike-slip
1555 tectonics and oblique rifting in the Rovuma Basin, progressing northwards to oblique rifting
1556 that also follows pre-existing lithospheric structures along the Tanzanian-Kenyan section,
1557 and finally, purely orthogonal rifting along a pre-existing lithospheric structure along the
1558 Kenyan-Somalian section. This is consistent with the obliqueness of rifting (Brune et al.,
1559 2012) and pre-existing lithospheric structure (e.g. Audet and Bürgmann, 2011) assisting
1560 supercontinent breakup.

1561 The rifting between East and West Gondwana therefore provide a good natural laboratory
1562 for the study of the spatially variable interplay between different rifting mechanisms during
1563 supercontinent breakup. Examples where each of the proposed facilitating mechanisms
1564 (magmatism, oblique rifting, and pre-existing structure) appears to dominate during breakup
1565 can be seen along the Gondwana rift system between Mozambique and Somalia, with
1566 predominantly magmatic breakup in the Mozambique Basin, apparent strike-slip and oblique
1567 tectonics along the Rovuma Basin, and coincident pre-existing lithospheric structure along
1568 the Kenyan-Somalian coast. Analogy can be made to the opening of the South Atlantic
1569 during breakup of the supercontinent Pangea, where evidence supports similar regional
1570 variation in breakup mechanism. Here, a south to north transition from magmatically
1571 dominated breakup in the southern South Atlantic (e.g. Gibson et al., 2006), inheritance
1572 driven rifting in the central South Atlantic (e.g. Lentini et al., 2010), and strongly oblique
1573 rifting in the Equatorial Atlantic (Heine and Brune, 2014) is seen. Together, these margins

1574 suggest that rifting during supercontinent dispersal may often be facilitated by multiple
1575 mechanisms, with regional variation along the margin due to different pre-existing
1576 geological structures and changing tectonic geometry on length scales as short as a few
1577 hundred kilometres.

1578 2.6.3. Plate tectonic reconstruction

1579 For the initial rifting phase we impose a plate separation rate of 3.3 mm/y, similar to that of
1580 the present day East African Rift System between Malawi and Afar (Saria et al., 2014).
1581 Breakup occurred at approximately 170 Ma, as evidenced by the Early Bajocian break up
1582 unconformity identified in the Morondava Basin (Geiger et al., 2004) and the overwhelming
1583 transition to marine deposits along the East Africa margins at this time (Coffin and
1584 Rabinowitz, 1992). Between breakup and the earliest magnetic anomaly constraint (M22) an
1585 average full spreading rate of 40 mm/y therefore occurred, similar to the average full
1586 spreading rate of ~49 mm/y determined by ocean magnetic anomalies for the younger
1587 oceanic crust between M22 and M0 (Cochran, 1988; Davis et al., 2016).

1588 Following this initial phase of spreading, which resulted in strike-slip motion between
1589 Madagascar and the Rovuma Basin, a rotation in the spreading direction occurred at ~150.5
1590 Ma. The oldest conjugate pair of magnetic anomalies detected, M22 (Cochran, 1988; Davis
1591 et al., 2016), constrains the age of this rotation, which is contemporaneous with Madagascars
1592 exit from the SSE trending Rovuma Basin, after which it began to follow a N-S spreading
1593 direction. This rotation began the cessation of any oceanic spreading in the Tanzania Coastal
1594 basin and offshore Morondava Basin as flow lines began to align along what was to become
1595 the DFZ (Figure 2.7d-e). This alignment suggests strike-slip tectonics began to dominate
1596 along this zone, and it is therefore possible that the DFZ formed at this point as several
1597 fracture zones coalesced into one major oceanic fracture zone with a significant accumulated
1598 offset.

1599 Following the first rotation in plate motions at 150.5 Ma, spreading continued relatively
1600 undisturbed in the Western Somali Basin until approximately 136 Ma, when a further
1601 change in plate motion occurred contemporaneous with Madagascar's departure from the
1602 Mozambique continental transform margin. This rotation further aligned the flowlines along
1603 the DFZ as it became the dominant strike slip fault in the basin. From here until the
1604 termination of oceanic spreading at M0 (125 Ma), Madagascar underwent a gentle anti-
1605 clockwise rotation to take its present day position relative to Africa.

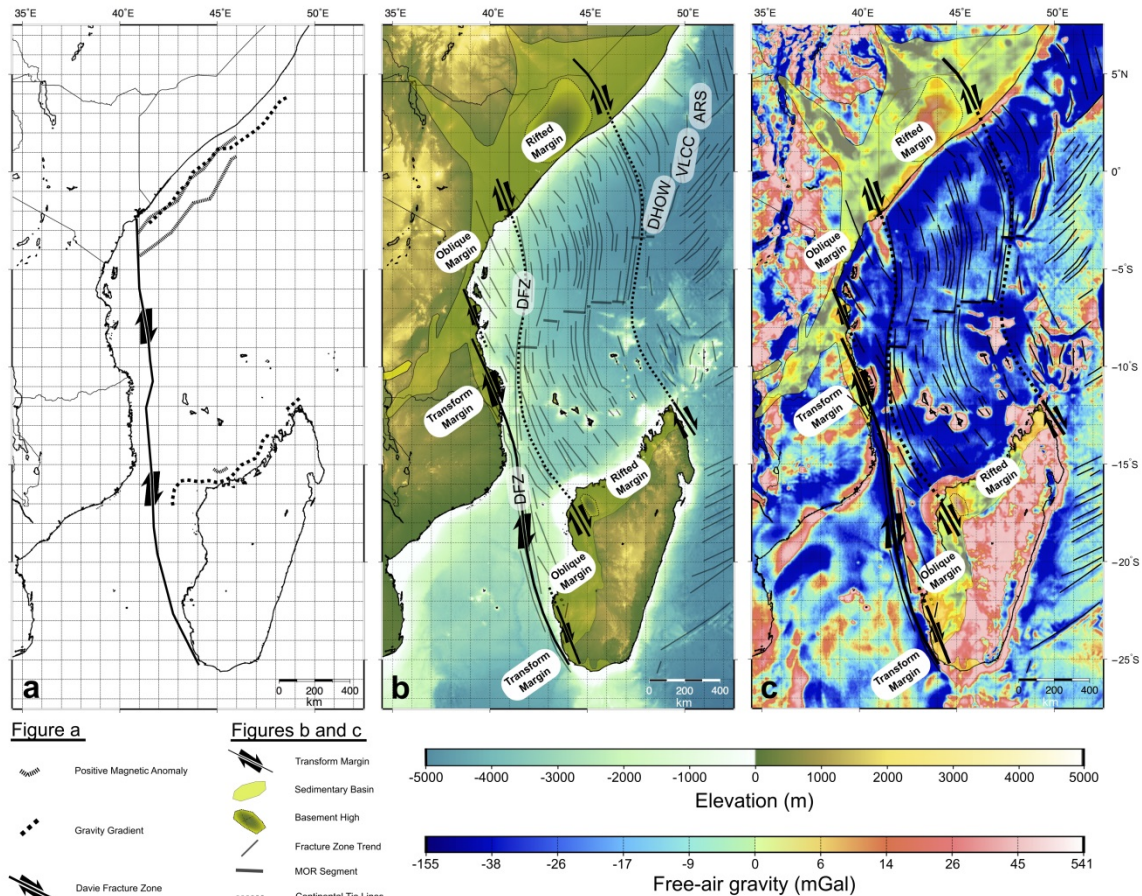
1606 The termination points for our model flowlines lie very close to the extinct MOR identified
1607 in the gravity data. We emphasise that this striking agreement is generated only from our

1608 fracture zone trends and initial seed points for the flowlines, which were chosen
1609 independently based on the CRUST1.0 dataset, and thus provides strong confirmation of the
1610 model. No ocean magnetic anomalies have been identified to help constrain the location of
1611 the westernmost segment of the MOR. However, seismic reflection data suggests a southerly
1612 location for the MOR segment in line with the symmetry predicted from the plate tectonic
1613 reconstruction.

1614 A key result of the reconstruction is that the DFZ is shown to be a major ocean-ocean FZ,
1615 where oceanic crust has formed inboard of this feature within the Tanzania Coastal Basin.
1616 This challenges many plate tectonic reconstructions which, based on the previously available
1617 literature, have defined the DFZ as the continent-ocean transform margin of the Western
1618 Somali Basin (e.g. Gaina et al., 2013), an important constraint on spreading kinematics. As
1619 the DFZ is a predominantly straight feature, treating it as the continent-ocean transition
1620 naturally results in the prediction of a less complex spreading pattern (i.e. only ~N-S without
1621 an initial NNW-SSE component) and a looser fit of Gondwana fragments due to the inability
1622 to reconstruct continents inboard of the DFZ. However, by detailed analysis of spreading
1623 lineaments on a small scale, we have been able to resolve the initial NNE-SSW spreading
1624 stage. This is in agreement with NNW-SSE principal extensional stresses during breakup
1625 around the Mozambique basin, recorded from dyke dilation in the Okavango and Limpopo
1626 dyke swarms (Le Gall et al., 2005). This spreading pattern is also strikingly similar to
1627 spreading patterns extrapolated to the WSB basin from the Mozambique basin, where they
1628 were derived from magnetic anomalies and FZs (Eagles and König, 2008). This suggests
1629 that during the earlier stages of spreading, Madagascar and Antarctica shared a similar
1630 breakup history, and moved as a cohesive unit away from Africa, as opposed to an
1631 amalgamation of continental blocks with relative motions between them. This highlights the
1632 importance of basin scale reconstructions in deciphering supercontinent dispersal
1633 mechanisms, as well as their potential for constraining the histories of neighbouring basins
1634 that lack detailed kinematic indicators and for informing larger regional reconstructions.

1635 The Dhow and VLCC fracture zones as interpreted by Bunce and Molnar (1977) were not
1636 used as input to the plate tectonic model since they may have formed by processes other than
1637 oceanic spreading (Coffin and Rabinowitz 1987). However, their trends are independently
1638 predicted by our plate model, so they are likely to have been originally formed as the result
1639 of plate spreading after all. Reactivation of these structures may have occurred during the
1640 breakup of Madagascar and India, resulting in their more prominent expression in the
1641 gravity data compared to other fracture zones in the WSB.

1642



1644

1645

1646

1647

1648

1649

1650

1651

1652

1653

1654

Figure 2.9. (a) Commonly interpreted basin configuration, where the continent-ocean transition is assumed to follow the DFZ (e.g. Bunce and Molnar, 1977; Coffin and Rabinowitz, 1987). (b) Schematic of the basin configuration suggested in this study, with strike slip tectonics dominating along the edge of the Rovuma Basin, while much of the Tanzania Coastal Basin should be considered as an obliquely rifted margin. The Davie Fracture Zone is a major ocean-ocean fracture zone, not the continent-ocean transform margin. DFZ – Davie Fracture Zone; DHOW – Dhow Fracture Zone; VLCC – Very Large Crude Carrier Fracture Zone; ARS – Auxiliary Rescue and Salvage Fracture Zone. (c) Free-air gravity overlain with interpretation as for Figure 2.9b.

1655

2.7. Conclusions

1656

1657

1658

1659

1660

1661

Using new techniques to analyse the latest Sandwell and Smith gravity datasets (V23), we have detected the location of the extinct MOR segments and, for the first time, a comprehensive set of fracture zone lineaments within the Western Somali Basin. We have used these to constrain Madagascar's position in Africa prior to breakup, validate ocean magnetic anomaly interpretations for the WSB, and construct a well constrained, high resolution plate tectonic reconstruction for the region. This plate tectonic reconstruction

1662 bears strong similarities to reconstructions from the neighbouring Mozambique Basin, and
1663 may suggest that East Gondwana broke off from West Gondwana as a cohesive unit, rather
1664 than as an amalgamation of continental blocks with relative motions between them. During
1665 this disassembly, no single parameter leads to breakup along the entire margin, with thermal
1666 weakening due to magmatism, oblique rifting, and pre-existing structure apparently
1667 dominating in turn from south to north along the Jurassic Gondwana rifts.

1668 The discovery of oceanic crust in the Tanzania Coastal Basin, fracture zone orthogonality to
1669 regional magnetic anomalies, and observations from the Rovuma Basin support this
1670 reconstruction, and show that the Davie Fracture Zone is a major ocean-ocean fracture zone,
1671 formed by the coalescence of several smaller fracture zones during changing spreading
1672 directions, and not a continent-ocean transform margin. The western edge of the basin is
1673 thus defined by a transform margin in the Rovuma Basin, whereas the Tanzanian and
1674 Kenyan margins formed in an oblique regime and are most likely segmented, magma-poor
1675 rifted margins. The change in the location and nature of the continent ocean transition has
1676 important implications for the nature of the lithosphere underlying the western portion of the
1677 basin, and thus for its thermal history and resource potential.

1678 **2.8. References**

- 1679 Arrowsmith, J.R., Zielke, O., 2009. Tectonic geomorphology of the San Andreas Fault zone from
1680 high resolution topography: An example from the Cholame segment. *Geomorphology* 113, 70-81.
- 1681 Audet, P., Burgmann, R., 2011. Dominant role of tectonic inheritance in supercontinent cycles.
1682 *Nature Geosci* 4, 184-187.
- 1683 Bayrakci, G., Minshull, T.A., Sawyer, D.S., Reston, T.J., Klaeschen, D., Papenberg, C., Ranero, C.,
1684 Bull, J.M., Davy, R.G., Shillington, D.J., Perez-Gussinye, M., Morgan, J.K., 2016. Fault-
1685 controlled hydration of the upper mantle during continental rifting. *Nature Geosci* 9, 384-388.
- 1686 Bécel, A., Shillington, D.J., Nedimović, M.R., Webb, S.C., Kuehn, H., 2015. Origin of dipping
1687 structures in fast-spreading oceanic lower crust offshore Alaska imaged by multichannel seismic
1688 data. *Earth and Planetary Science Letters* 424, 26-37.
- 1689 Beglinger, S.E., Corver, M.P., Doust, H., Cloetingh, S., Thurmond, A.K., 2012. A new approach of
1690 relating petroleum system and play development to basin evolution: An application to the
1691 conjugate margin Gabon coastal and Almada-Camamu basins. *AAPG Bulletin* 96, 953-982.
- 1692 Behn, M.D., Ito, G., 2008. Magmatic and tectonic extension at mid-ocean ridges: 1. Controls on fault
1693 characteristics. *Geochemistry, Geophysics, Geosystems* 9, n/a-n/a.
- 1694 Bennett, S.E.K., Oskin, M.E., 2014. Oblique rifting ruptures continents: Example from the Gulf of
1695 California shear zone. *Geology* 42, 215-218.
- 1696 Blackman, D.K., Forsyth, D.W., 1991. Isostatic compensation of tectonic features of the Mid-Atlantic
1697 Ridge: 25–27°30'S. *Journal of Geophysical Research: Solid Earth* 96, 11741-11758.
- 1698 Brune, S., Popov, A.A., Sobolev, S.V., 2012. Modeling suggests that oblique extension facilitates
1699 rifting and continental break-up. *Journal of Geophysical Research: Solid Earth* 117, B08402.
- 1700 Buck, W.R., 2007. *Dynamic Processes in Extensional and Compressional Settings: The Dynamics of*
1701 *Continental Breakup and Extension*, Treatise on Geophysics, Treatise on Geophysics. Elsevier,
1702 Amsterdam, pp. 335-376.
- 1703 Bunce, E.T., Molnar, P., 1977. Seismic reflection profiling and basement topography in the Somali
1704 basin: possible fracture zones between Madagascar and Africa. *Journal of Geophysical Research*
1705 82, 5305-5311.

- 1706 Cochran, J.R., 1988. Somali Basin, Chain Ridge, and origin of the Northern Somali Basin gravity and
1707 geoid low. *Journal of Geophysical Research: Solid Earth* 93, 11985-12008.
- 1708 Coffin, M.F., Rabinowitz, P.D., 1992. The Mesozoic East African and Madagascan Conjugate
1709 Continental Margins. *American Association of Petroleum Geologists Memoir* 53, 207-240.
- 1710 Coffin, M.F., Rabinowitz, P.D., Houtz, R.E., 1986. Crustal structure in the Western Somali Basin.
1711 *Geophysical Journal of the Royal Astronomical Society* 86, 331-369.
- 1712 Collette, B.J., 1974. Thermal contraction joints in a spreading seafloor as origin of fracture zones.
1713 *Nature* 251, 299-300.
- 1714 Davies, R.J., MacLeod, C.J., Morgan, R., Briggs, S.E., 2005. Termination of a fossil continent-ocean
1715 fracture zone imaged with three-dimensional seismic data: The Chain Fracture Zone, eastern
1716 equatorial Atlantic. *Geology* 33, 641-644.
- 1717 Davis, J.K., Lawver, L.A., Norton, I.O., Gahagan, L.M., 2016. New Somali Basin magnetic
1718 anomalies and a plate model for the early Indian Ocean. *Gondwana Research* 34, 16-28.
- 1719 Dean, S.M., Minshull, T.A., Whitmarsh, R.B., 2008. Seismic constraints on the three-dimensional
1720 geometry of low-angle intracrustal reflectors in the Southern Iberia Abyssal Plain. *Geophysical*
1721 *Journal International* 175, 571-586.
- 1722 Delvaux, D., Barth, A., 2010. African stress pattern from formal inversion of focal mechanism data.
1723 *Tectonophysics* 482, 105-128.
- 1724 Eagles, G., 2007. New angles on South Atlantic opening. *Geophysical Journal International* 168, 353-
1725 361.
- 1726 Eagles, G., König, M., 2008. A model of plate kinematics in Gondwana breakup. *Geophysical Journal*
1727 *International* 173, 703-717.
- 1728 Emmel, B., Kumar, R., Ueda, K., Jacobs, J., Daszinnies, M.C., Thomas, R.J., Matola, R., 2011.
1729 Thermochronological history of an orogen-passive margin system: An example from northern
1730 Mozambique. *Tectonics* 30, TC2002.
- 1731 Franke, D., 2013. Rifting, lithosphere breakup and volcanism: Comparison of magma-poor and
1732 volcanic rifted margins. *Marine and Petroleum Geology* 43, 63-87.
- 1733 Franke, D., Jokat, W., Ladage, S., Stollhofen, H., Klimke, J., Lutz, R., Mahanjane, E.S., Ehrhardt, A.,
1734 Schreckenberger, B., 2015. The offshore East African Rift System: Structural framework at the
1735 toe of a juvenile rift. *Tectonics* 34, 2086-2104.
- 1736 Gaina, C., Torsvik, T.H., van Hinsbergen, D.J.J., Medvedev, S., Werner, S.C., Labails, C., 2013. The
1737 African Plate: A history of oceanic crust accretion and subduction since the Jurassic.
1738 *Tectonophysics* 604, 4-25.
- 1739 Geiger, M., Clark, D.N., Mette, W., 2004. Reappraisal of the timing of the breakup of Gondwana
1740 based on sedimentological and seismic evidence from the Morondava Basin, Madagascar. *Journal*
1741 *of African Earth Sciences* 38, 363-381.
- 1742 Gente, P., Pockalny, R.A., Durand, C., Deplus, C., Maia, M., Ceuleneer, G., Mével, C., Cannat, M.,
1743 Laverne, C., 1995. Characteristics and evolution of the segmentation of the Mid-Atlantic Ridge
1744 between 20°N and 24°N during the last 10 million years. *Earth and Planetary Science Letters* 129,
1745 55-71.
- 1746 Gibson, S.A., Thompson, R.N., Day, J.A., 2006. Timescales and mechanisms of plume–lithosphere
1747 interactions: 40Ar/39Ar geochronology and geochemistry of alkaline igneous rocks from the
1748 Paraná–Etendeka large igneous province. *Earth and Planetary Science Letters* 251, 1-17.
- 1749 Gillard, M., Manatschal, G., Autin, J., 2016. How can asymmetric detachment faults generate
1750 symmetric Ocean Continent Transitions. *Terra Nova* 28, 27-34.
- 1751 Gradstein, F., Ogg, J., Schmitz, M., Ogg, G., 2012. *The Geologic Time Scale 2012*. Elsevier, 1144 p.
- 1752 Guiraud, R., Bosworth, W., Thierry, J., Delplanque, A., 2005. Phanerozoic geological evolution of
1753 Northern and Central Africa: An overview. *Journal of African Earth Sciences* 43, 83-143.
- 1754 Hankel, O., 1994. Early Permian to Middle Jurassic rifting and sedimentation in East Africa and
1755 Madagascar. *Geol Rundsch* 83, 703-710.
- 1756 Heine, C., Brune, S., 2014. Oblique rifting of the Equatorial Atlantic: Why there is no Saharan
1757 Atlantic Ocean. *Geology* 42, 211-214.
- 1758 Hirsch, K.K., Bauer, K., Scheck-Wenderoth, M., 2009. Deep structure of the western South African
1759 passive margin — Results of a combined approach of seismic, gravity and isostatic investigations.
1760 *Tectonophysics* 470, 57-70.
- 1761 Hoffmann, H.-J., Reston, T.J., 1992. Nature of the S reflector beneath the Galicia Banks rifted
1762 margin: Preliminary results from prestack depth migration. *Geology* 20, 1091-1094.
- 1763 Jonas, J., Hall, S., Casey, J.F., 1991. Gravity anomalies over extinct spreading centers: A test of
1764 gravity models of active centers. *Journal of Geophysical Research: Solid Earth* 96, 11759-11777.

- 1765 Key, R.M., Smith, R.A., Smelror, M., Sæther, O.M., Thorsnes, T., Powell, J.H., Njange, F.,
1766 Zandamela, E.B., 2008. Revised lithostratigraphy of the Mesozoic-Cenozoic succession of the
1767 onshore Rovuma Basin, northern coastal Mozambique. *South African Journal of Geology* 111, 89-
1768 108.
- 1769 Kim, S.-S., Wessel, P., 2011. New global seamount census from altimetry-derived gravity data.
1770 *Geophysical Journal International* 186, 615-631.
- 1771 Klausen, M.B., 2009. The Lebombo monocline and associated feeder dyke swarm: Diagnostic of a
1772 successful and highly volcanic rifted margin? *Tectonophysics* 468, 42-62.
- 1773 Korenaga, J., Holbrook, W.S., Kent, G.M., Kelemen, P.B., Detrick, R.S., Larsen, H.C., Hopper, J.R.,
1774 Dahl-Jensen, T., 2000. Crustal structure of the southeast Greenland margin from joint refraction
1775 and reflection seismic tomography. *Journal of Geophysical Research: Solid Earth* 105, 21591-
1776 21614.
- 1777 Laske, G., Masters, G., Ma, Z., Pasyanos, M.E., 2013. Update on CRUST1.0: A 1-degree Global
1778 Model of Earth's Crust. *Geophys. Res. Abstracts*, 15, Abstract EGU2013-2658.
- 1779 Le Gall, B., Tshoso, G., Dyment, J., Basira Kampunzu, A., Jourdan, F., Féraud, G., Bertrand, H.,
1780 Aubourg, C., Vétel, W., 2005. The Okavango giant mafic dyke swarm (NE Botswana): its
1781 structural significance within the Karoo Large Igneous Province. *Journal of Structural Geology*
1782 27, 2234-2255.
- 1783 Lentini, M.R., Fraser, S.I., Sumner, H.S., Davies, R.J., 2010. Geodynamics of the central South
1784 Atlantic conjugate margins: implications for hydrocarbon potential. *Petroleum Geoscience* 16,
1785 217-229.
- 1786 Leroy, S., Razin, P., Autin, J., Bache, F., d'Acremont, E., Watremez, L., Robinet, J., Baurion, C.,
1787 Denèle, Y., Bellahsen, N., Lucazeau, F., Rolandone, F., Rouzo, S., Kiel, J.S., Robin, C.,
1788 Guillocheau, F., Tiberi, C., Basuyau, C., Beslier, M.-O., Ebinger, C., Stuart, G., Ahmed, A.,
1789 Khanbari, K., Al Ganad, I., de Clarens, P., Unternehr, P., Al Toubi, K., Al Lazki, A., 2012. From
1790 rifting to oceanic spreading in the Gulf of Aden: a synthesis. *Arabian Journal of Geosciences* 5,
1791 859-901.
- 1792 Lottes, A.L., Rowley, D.B., 1990. Reconstruction of the Laurasian and Gondwanan segments of
1793 Permian Pangaea. *Geological Society, London, Memoirs* 12, 383-395.
- 1794 Maus, S., Barckhausen, U., Berkenbosch, H., Bournas, N., Brozena, J., Childers, V., Dostaler, F.,
1795 Fairhead, J.D., Finn, C., R.R.B., v.F., Gaina, C., Golynsky, S., Kucks, R., Lühr, H., Milligan, P.,
1796 Mogren, S., Müller, D.R., Olesen, O., Pilkington, M., Saltus, R., Schreckenberger, B., Thébaud,
1797 E., Caratori Tontini, F., 2009. EMAG2: A 2-arc min resolution Earth Magnetic Anomaly Grid
1798 compiled from satellite, airborne, and marine magnetic measurements. *Geochemistry, Geophysics,*
1799 *Geosystems* 10, Q08005.
- 1800 Menard, H.W., Atwater, T., 1969. Origin of Fracture Zone Topography. *Nature* 222, 1037-1040.
- 1801 Mitchell, N.C., Park, Y., 2014. Nature of crust in the central Red Sea. *Tectonophysics* 628, 123-139.
- 1802 Mulder, T.F.A., Collette, B.J., 1984. Gravity anomalies over inactive fracture zones in the central
1803 North Atlantic. *Marine Geophysical Researches* 6, 383-394.
- 1804 Müller, R.D., Sdrolias, M., Gaina, C., Roest, W.R., 2008. Age, spreading rates, and spreading
1805 asymmetry of the world's ocean crust. *Geochemistry, Geophysics, Geosystems* 9, Q04006.
- 1806 Nance, D.R., Murphy, B.J., 2013. Origins of the supercontinent cycle. *Geoscience Frontiers* 4, 439-
1807 448.
- 1808 Planke, S., Eldholm, O., 1994. Seismic response and construction of seaward dipping wedges of flood
1809 basalts: Vøring volcanic margin. *Journal of Geophysical Research: Solid Earth* 99, 9263-9278.
- 1810 Prodehl, C., Ritter, J.R.R., Mechie, J., Keller, G.R., Khan, M.A., Jacob, B., Fuchs, K., Nyambok, I.O.,
1811 Obel, J.D., Riaroh, D., 1997. The KRISP 94 lithospheric investigation of southern Kenya — the
1812 experiments and their main results. *Tectonophysics* 278, 121-147.
- 1813 Rabinowitz, P.D., Coffin, M.F., Falvey, D., 1983. The Separation of Madagascar and Africa. *Science*
1814 220, 67-69.
- 1815 Reeves, C., 2014. The position of Madagascar within Gondwana and its movements during
1816 Gondwana dispersal. *Journal of African Earth Sciences* 94, 45-57.
- 1817 Reeves, C., De Wit, M.J., 2000. Making ends meet in Gondwana: retracing the transforms
1818 of the Indian Ocean and reconnecting continental shear zones. *Terra Nova* 12, 272-280.
- 1819 Reston, T.J., 2009. The structure, evolution and symmetry of the magma-poor rifted margins of the
1820 North and Central Atlantic: A synthesis. *Tectonophysics* 468, 6-27.
- 1821 Reston, T.J., Ranero, C.R., Ruoff, O., Perez-Gussinye, M., Dañobeitia, J.J., 2004. Geometry of
1822 extensional faults developed at slow-spreading centres from pre-stack depth migration of seismic
1823 reflection data in the Central Atlantic (Canary Basin). *Geophysical Journal International* 159, 591-
1824 606.

- 1825 Rodger, M., Watts, A.B., Greenroyd, C.J., Peirce, C., Hobbs, R.W., 2006. Evidence for unusually thin
1826 oceanic crust and strong mantle beneath the Amazon Fan. *Geology* 34, 1081-1084.
- 1827 Salman, G., Abdula, I., 1995. Development of the Mozambique and Ruvuma sedimentary basins,
1828 offshore Mozambique. *Sedimentary Geology* 96, 7-41.
- 1829 Sandwell, D.T., 1984. Thermomechanical evolution of oceanic fracture zones. *Journal of Geophysical*
1830 *Research: Solid Earth* 89, 11401-11413.
- 1831 Sandwell, D.T., Müller, R.D., Smith, W.H.F., Garcia, E., Francis, R., 2014. New global marine
1832 gravity model from CryoSat-2 and Jason-1 reveals buried tectonic structure. *Science* 346, 65-67.
- 1833 Saria, E., Calais, E., Stamps, D.S., Delvaux, D., Hartnady, C.J.H., 2014. Present-day kinematics of the
1834 East African Rift. *Journal of Geophysical Research: Solid Earth* 119, 3584-3600.
- 1835 Scrutton, R.A., Heptonstall, W.B., Peacock, J.H., 1981. Constraints on the motion of Madagascar
1836 with respect to Africa. *Marine Geology* 43, 1-20.
- 1837 Ségoufin, J., Patriat, P., 1980. Existence d'anomalies mésozoïques dans le bassin de Somalie.
1838 Implications pour les relations Afrique-Antarctique-Madagascar. *Comptes Rendus de l'Académie*
1839 *des Sciences* 291, 85-88.
- 1840 Smelror, M., Key, R.M., Smith, R.A., Njange, F., 2008. Late Jurassic and Cretaceous
1841 Palynostratigraphy of the Onshore Rovuma Basin, Northern Mozambique. *Palynology* 32, 63-76.
- 1842 Smith, A.G., Hallam, A., 1970. The Fit of the Southern Continents. *Nature* 225, 139-144.
- 1843 Soto, M., Morales, E., Veroslavsky, G., de Santa Ana, H., Ucha, N., Rodríguez, P., 2011. The
1844 continental margin of Uruguay: Crustal architecture and segmentation. *Marine and Petroleum*
1845 *Geology* 28, 1676-1689.
- 1846 Storey, M., Mahoney, J.J., Saunders, A.D., Duncan, R.A., Kelley, S.P., Coffin, M.F., 1995. Timing of
1847 Hot Spot—Related Volcanism and the Breakup of Madagascar and India. *Science* 267, 852-855.
- 1848 Sutra, E., Manatschal, G., 2012. How does the continental crust thin in a hyperextended rifted
1849 margin? Insights from the Iberia margin. *Geology* 40, 139-142.
- 1850 Trompette, R., 2000. Gondwana evolution; its assembly at around 600 Ma. *Comptes Rendus de*
1851 *l'Académie des Sciences - Series IIA - Earth and Planetary Science* 330, 305-315.
- 1852 Van Hinsbergen, D.J.J., Buiter, S.J.H., Torsvik, T.H., Gaina, C., Webb, S.J., 2011. The formation and
1853 evolution of Africa from the Archaean to Present: introduction. *Geological Society, London,*
1854 *Special Publications* 357, 1-8.
- 1855 Walcott, R.I., 1972. Gravity, Flexure, and the Growth of Sedimentary Basins at a Continental Edge.
1856 *Geological Society of America Bulletin* 83, 1845-1848.
- 1857 Watts, A.B., Stewart, J., 1998. Gravity anomalies and segmentation of the continental margin offshore
1858 West Africa. *Earth and Planetary Science Letters* 156, 239-252.
- 1859 White, N., Thompson, M., Barwise, T., 2003. Understanding the thermal evolution of deep-water
1860 continental margins. *Nature* 426, 334-343.
- 1861 White, R.S., McKenzie, D., O'Nions, R.K., 1992. Oceanic crustal thickness from seismic
1862 measurements and rare earth element inversions. *Journal of Geophysical Research: Solid Earth* 97,
1863 19683-19715.
- 1864 Whittaker, J.M., Goncharov, A., Williams, S.E., Müller, R.D., Leitchenkov, G., 2013. Global
1865 sediment thickness data set updated for the Australian-Antarctic Southern Ocean. *Geochemistry,*
1866 *Geophysics, Geosystems* 14, 3297-3305.
- 1867 Williams, S.E., Müller, D.R., Landgrebe, T.C.W., Whittaker, J.M., 2012. An open-source software
1868 environment for visualizing and refining plate tectonic reconstructions using high-resolution
1869 geological and geophysical data sets. *GSA Today* 22.
- 1870 Windley, B.F., Razafiniparany, A., Razakamanana, T., Ackermann, D., 1994. Tectonic framework of
1871 the Precambrian of Madagascar and its Gondwana connections: a review and reappraisal. *Geol*
1872 *Rundsch* 83, 642-659.
- 1873 Ziegler, P.A., Cloetingh, S., 2004. Dynamic processes controlling evolution of rifted basins. *Earth-*
1874 *Science Reviews* 64, 1-50.

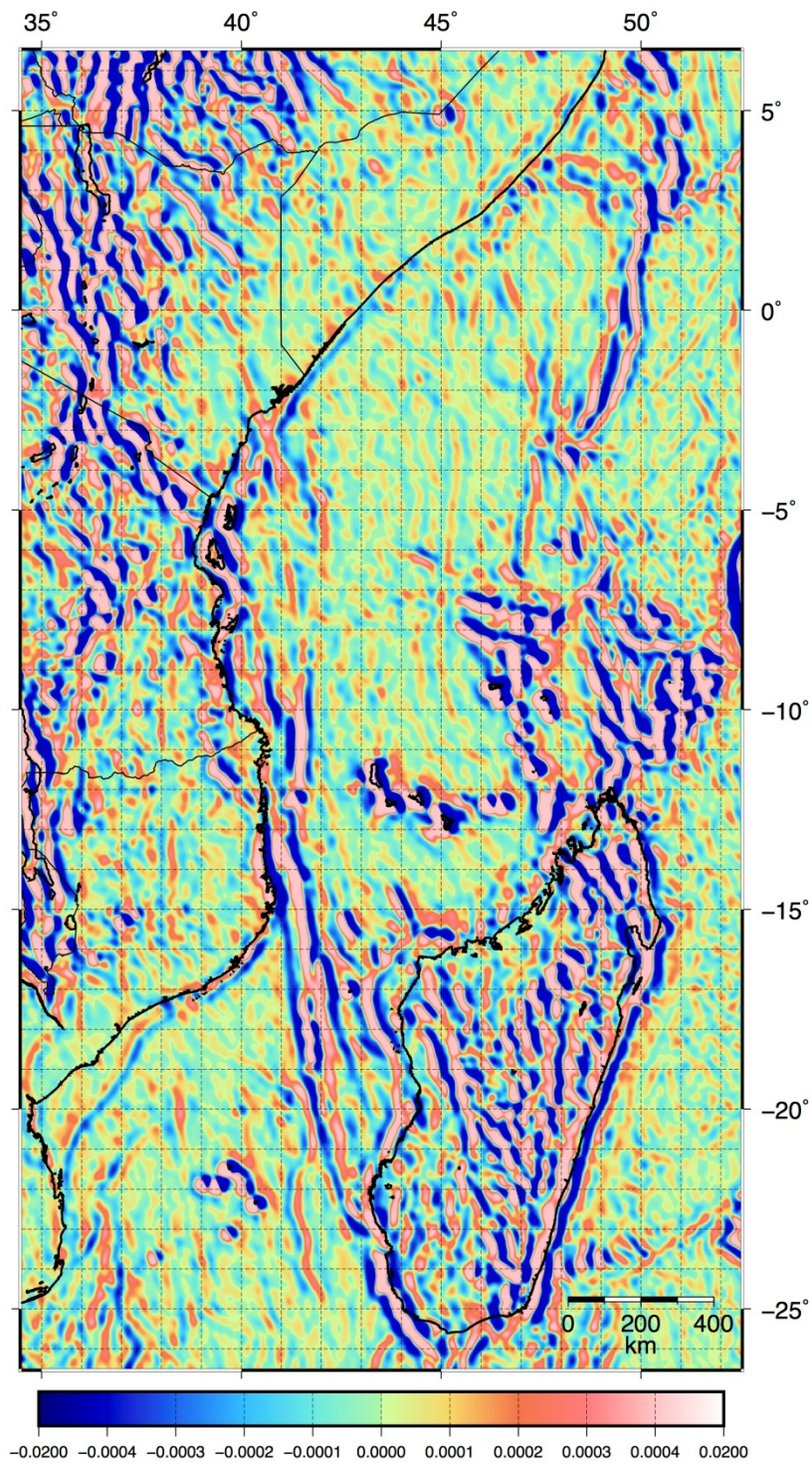
1875 **2.9. Supplementary material**

- 1876 These supplementary images show the effect of changing key parameters during the gravity
1877 processing described in the main text. Free-air gravity data from the Western Somali Basin
1878 (WSB) has been processed to enhance the expression of fracture zones. First filtering was

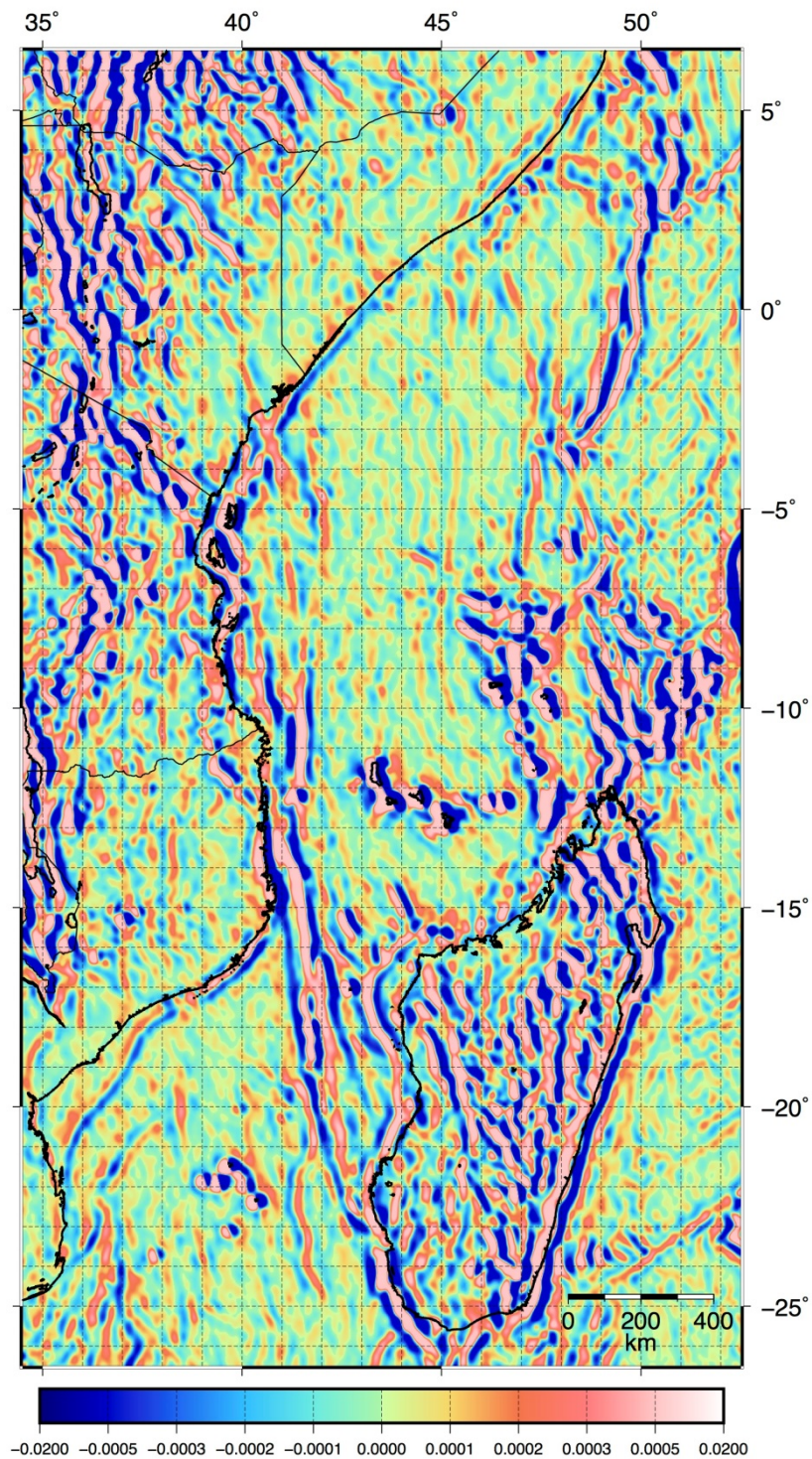
1879 performed using a Gaussian bandpass filter with 50% cutoffs at 55 and 85 km wavelengths.
1880 Following this, directional derivatives of the gravity were taken perpendicular to the
1881 approximate N-S spreading direction, as determined from ocean magnetic anomalies from
1882 the WSB. Derivatives were taken at 10° intervals between 30° clockwise and anticlockwise
1883 of E-W. The greatest gradient magnitude recorded from this set of derivatives was stored for
1884 each grid element to form the final gradient anomaly map (Figure S2.1).

1885 Supplementary Figures S2.2-4 show the effects of reducing the range of azimuths over
1886 which gradients are taken; the aim being to show that the process of taking several gradients
1887 assists in highlighting the trends of curved fracture zones. In the case of the WSB, the
1888 greatest improvements can therefore be seen closer to the continents where the spreading
1889 direction early in the basin history was ~NW-SE and not N-S.

1890 Supplementary figures S2.5-8 show result of taking gradients over these same ranges of
1891 azimuths as in supplementary figures S2.1-4, but parallel to the spreading direction as
1892 opposed to perpendicular to it. This shows that lineations do not arise purely as a result of
1893 this processing without a geological driver.

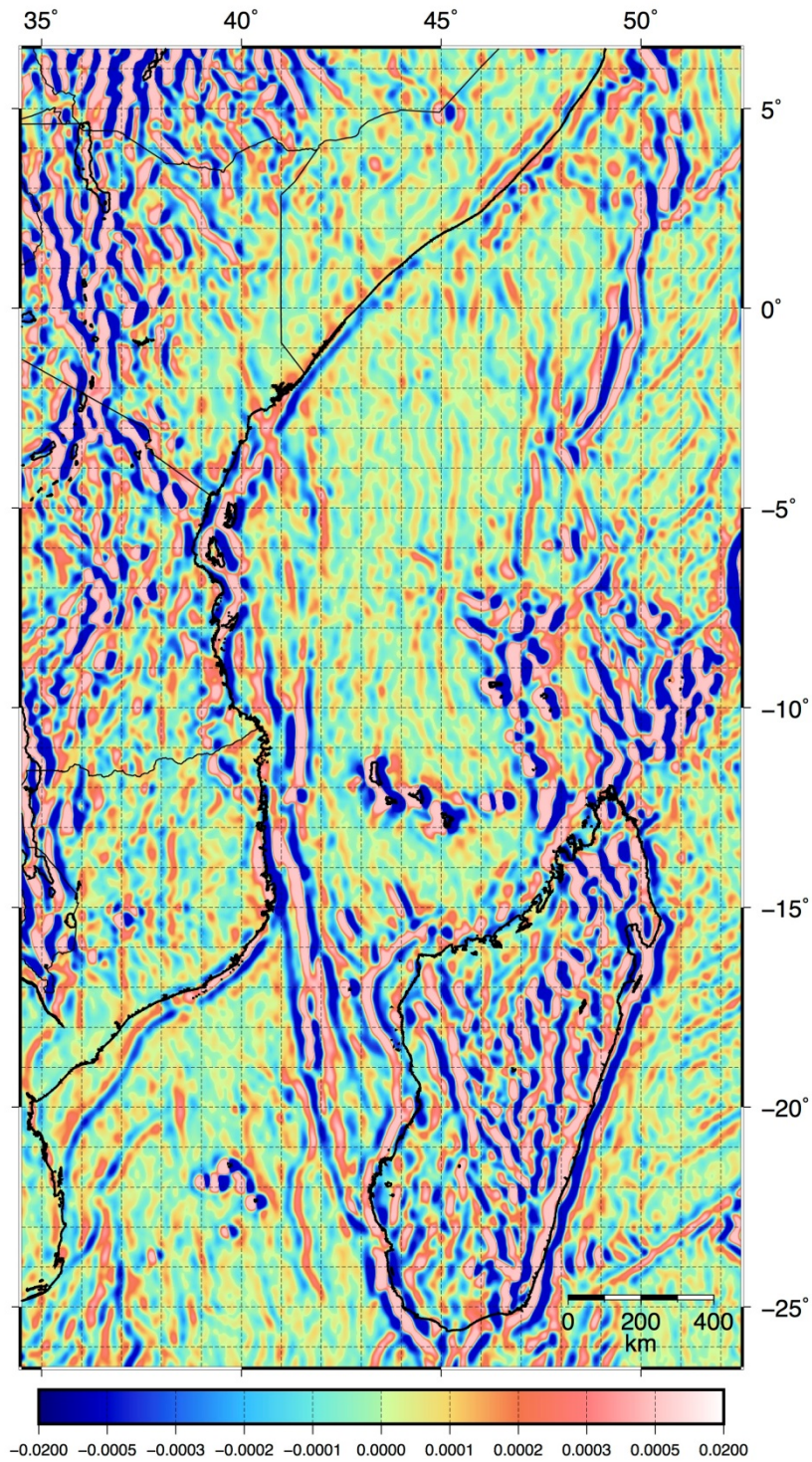


1896 **Figure S2.1.** Maximum free-air gravity directional derivative from azimuths of
 1897 240°/250°/260°/270°/280°/290°/300°. Units of scale are eötvös.



1900 **Figure S2.2.** Maximum free-air gravity directional derivative from azimuths of
 1901 250°/260°/270°/280°/290°. Units of scale are eötvös.

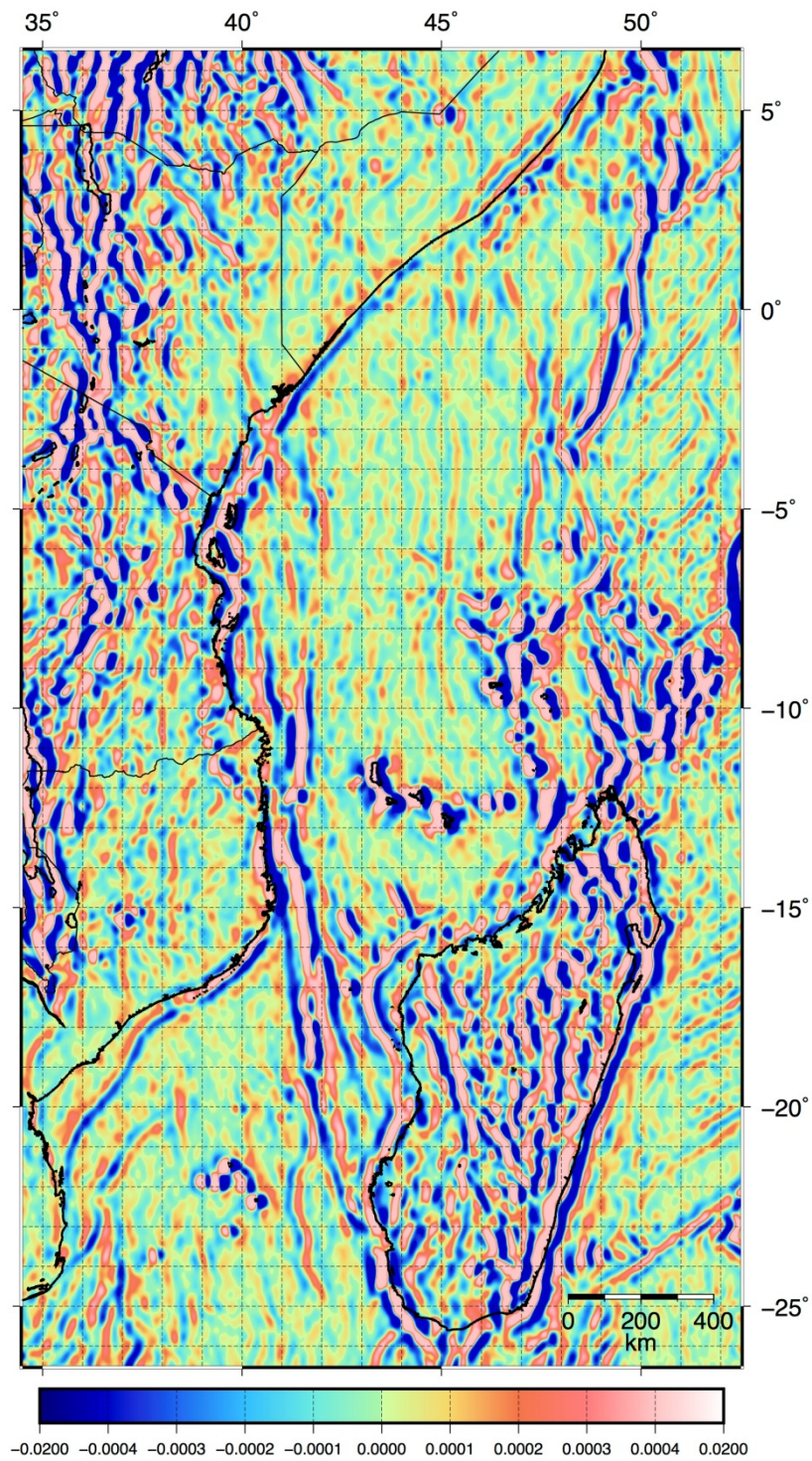
1902



1903

1904 **Figure S2.3.** Maximum free-air gravity directional derivative from azimuths of
1905 260°/270°/280°. Units of scale are eötvös.

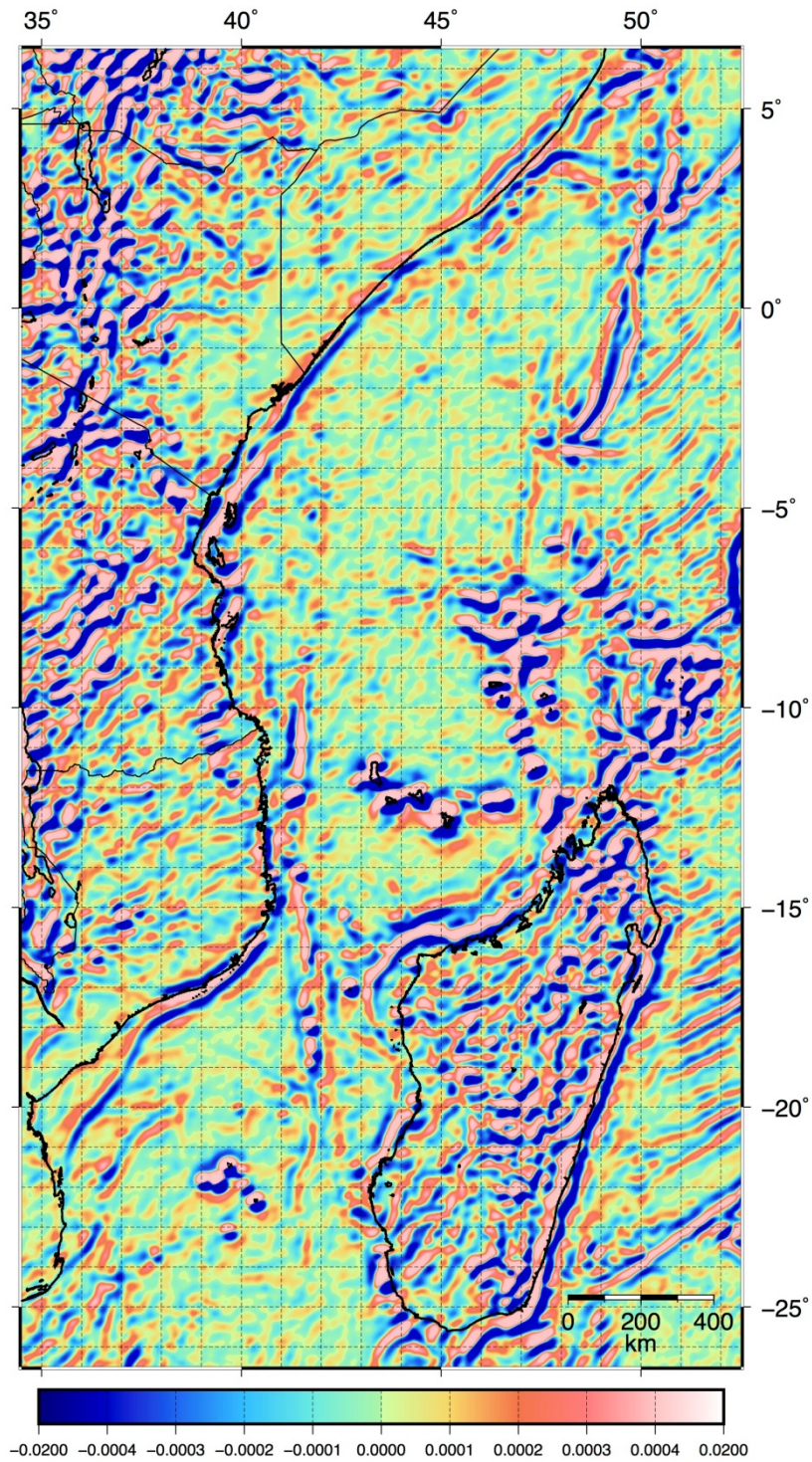
1906



1907

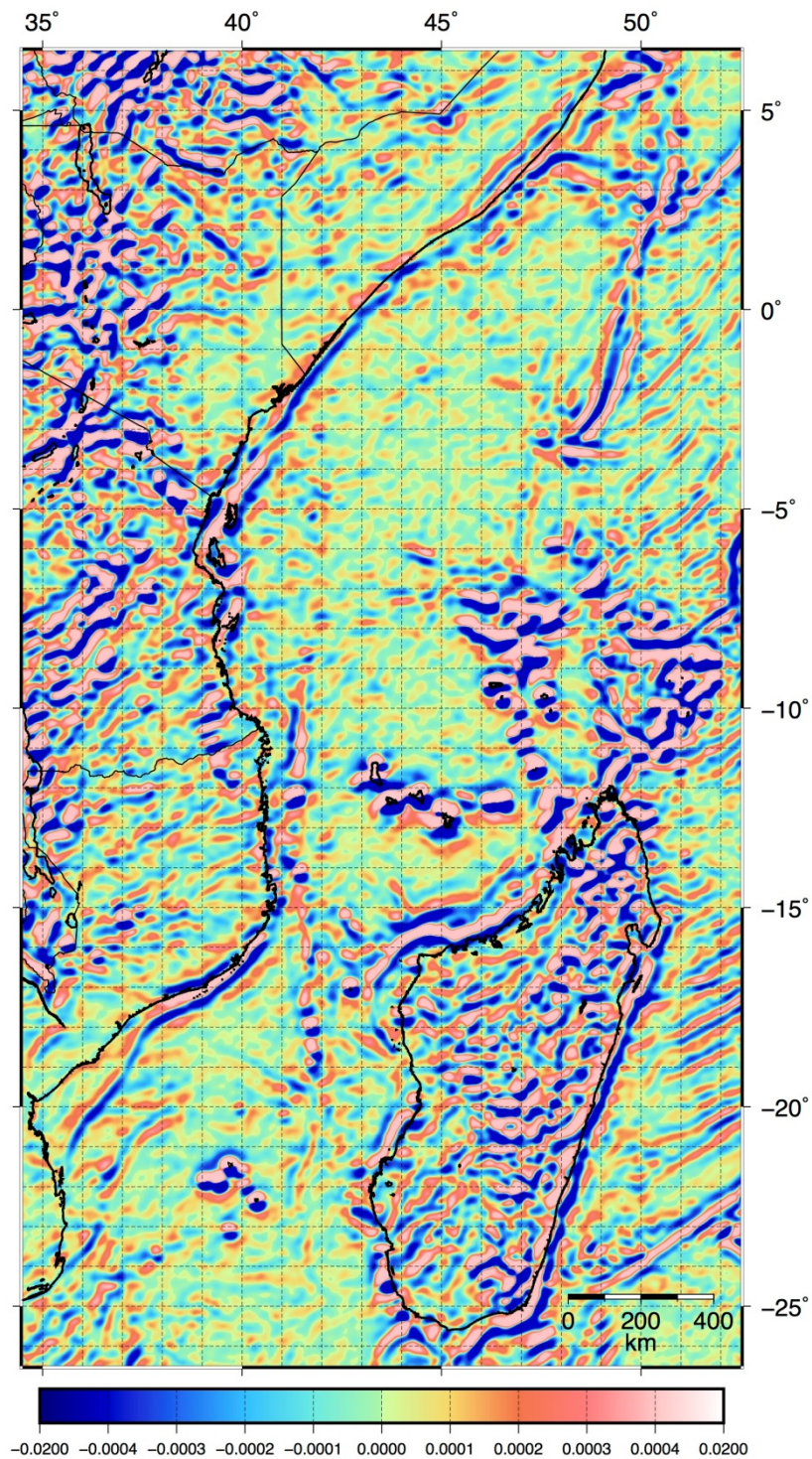
1908 **Figure S2.4.** Free-air gravity directional derivative at an azimuth of 270°. Units of scale are
1909 eötvös.

1910

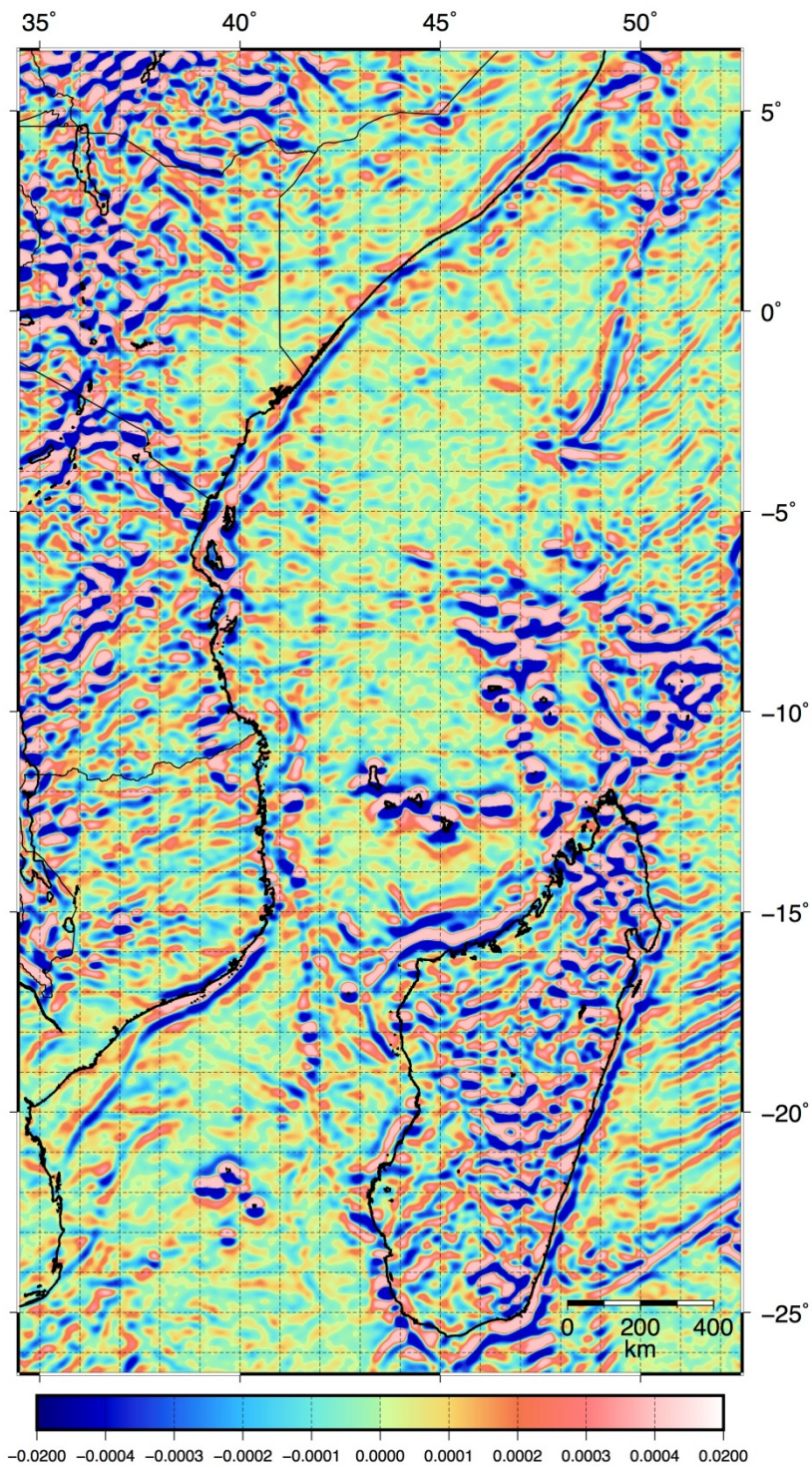


1911

1912 **Figure S2.5.** Maximum free-air gravity directional derivative from azimuths of
1913 330°/340°/350°/0°/10°/20°/30°. Units of scale are eötvös.



1918

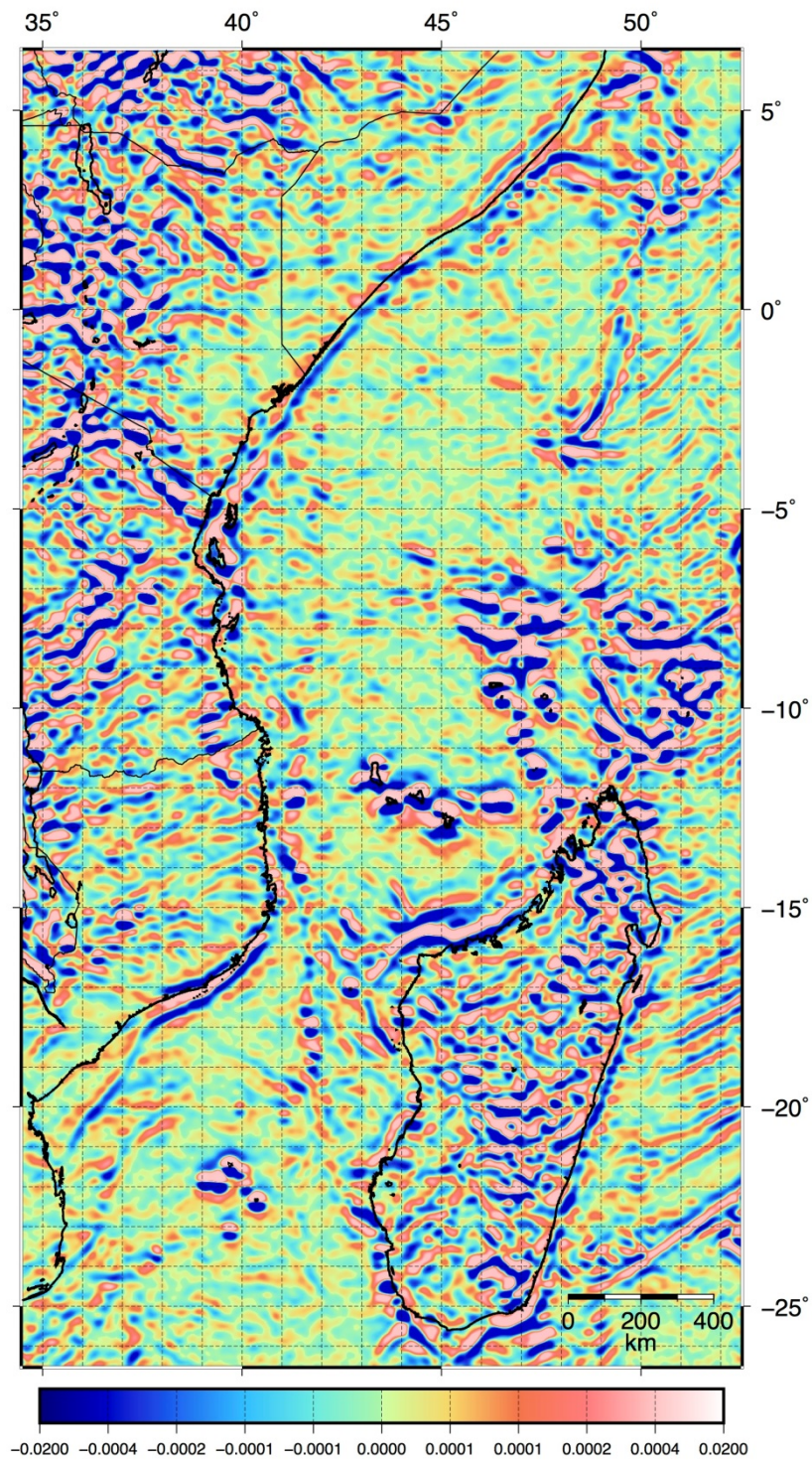


1919

1920 **Figure S2.7.** Maximum free-air gravity directional derivative from azimuths of 350°/0°/10°.

1921 Units of scale are eötvös.

1922



1923

1924 **Figure S2.8.** Free-air gravity directional derivative at an azimuth of 0° . Units of scale are
1925 eötvös.

1926 **3. The Rovuma Transform Margin:**
1927 **Pinning down the East African**
1928 **continent-ocean transform margin**
1929 **using seismic and gravity methods**

1930 **Abstract**

1931 A firm knowledge of the nature and location of the continental margins of East Africa is
1932 crucial for producing accurate plate tectonic reconstructions of Gondwana, hydrocarbon
1933 resource exploration, and for developing our understanding of how supercontinents break
1934 apart. Here, we present evidence for a newly identified continent-ocean transform margin
1935 along the Rovuma Basin, identified using seismic and gravity data. The ‘Rovuma Transform
1936 Margin’ lies landward of the Davie Fracture Zone, which has previously been interpreted as
1937 the continent-ocean transform margin of the Western Somali basin, and trends in a NNW
1938 direction, following the onshore basement outcrop of the Rovuma Basin. The >400 km long
1939 transform margin connects the obliquely rifted Tanzania Coastal Basin in the north, with the
1940 Nacala and Mozambique basins in the south. This configuration supports an origin for
1941 Madagascar within the Tanzania Coastal Basin, and tight-fit reconstructions of Gondwana
1942 fragments prior to the Jurassic.

1943 **3.1. Introduction**

1944 Continental breakup occurs when a zone of continental lithosphere is thinned to the point of
1945 rupture due to the separation of tectonic plates (Ebinger, 2005). This results in partial
1946 melting of the asthenospheric mantle, leading to oceanic crust production and the
1947 localisation of strain at the mid-ocean ridge (MOR). At this time, the region where
1948 continental lithosphere is thinned (from ~30 to 0 km) may be referred to as a passive
1949 continental margin. Due to the relation between extension and accommodation space
1950 (Tugend et al., 2015), continental margins may be readily identified between the continents
1951 and ocean by using seismic reflection data to identify the great increase in sedimentary
1952 accommodation space that occurs across them. This increase is primarily due to the

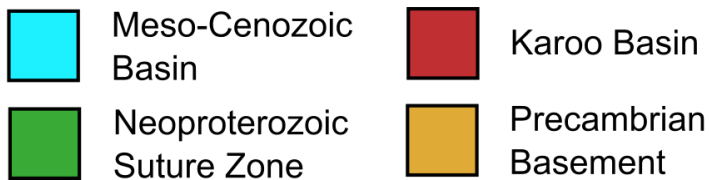
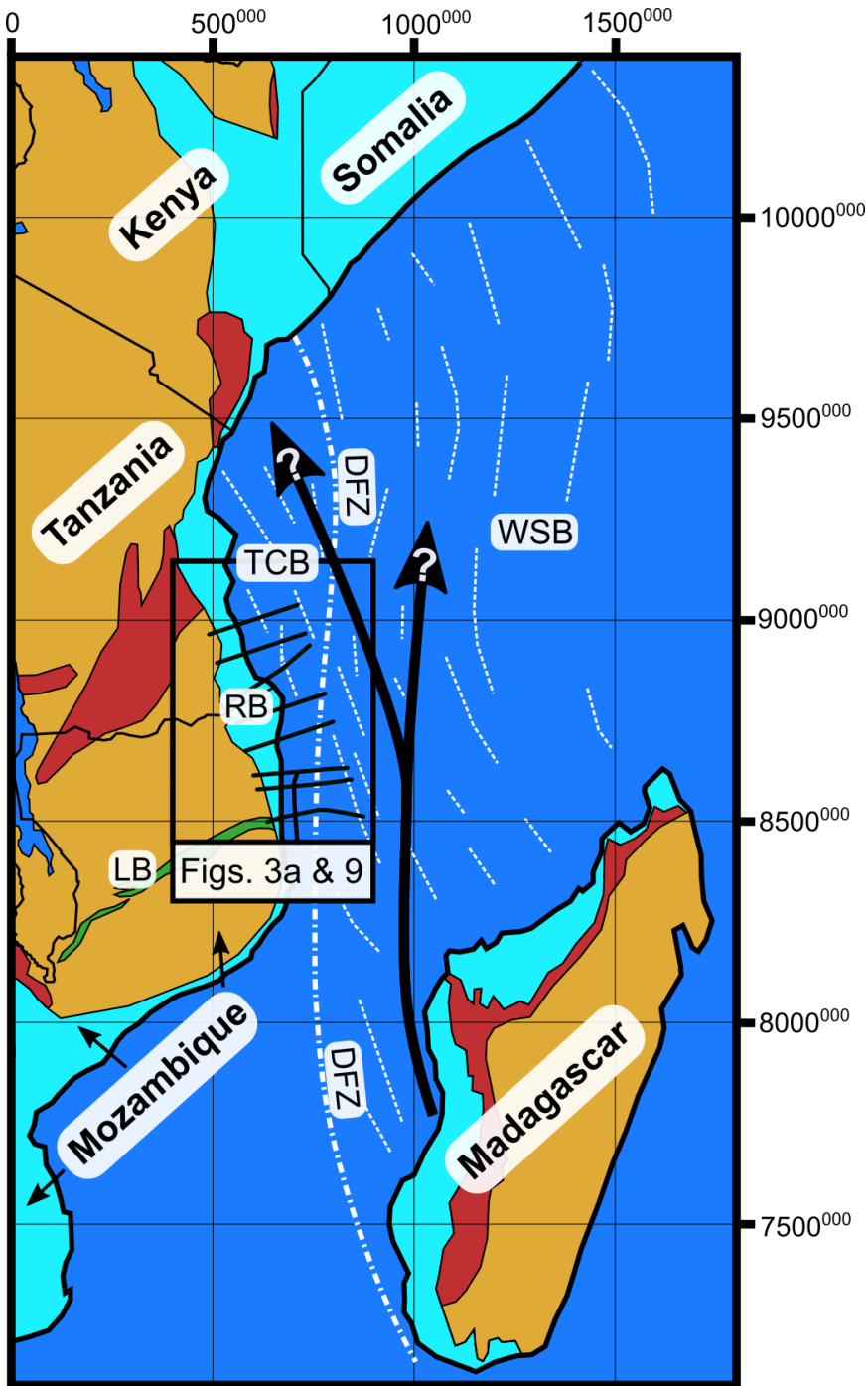
1953 subsidence that occurs across passive margins as the result of isostatic compensation
1954 following thinning of the relatively buoyant crust.

1955 The East Africa margins developed during the Early Jurassic, following the cessation of
1956 older Karoo rifting episodes (Geiger et al., 2004), by the breakup of East and West
1957 Gondwana (e.g. Reeves et al., 2016). The subsequent drift of East Gondwana (Madagascar,
1958 India, Antarctica, and Australia) away from West Gondwana (Africa, South America)
1959 generated the Western Somali Basin (WSB; e.g. Rabinowitz et al., 1983). Figure 3.1
1960 summarises the two main groups of plate tectonic models have been proposed to describe
1961 plate motions during the formation of the WSB. 1) Direct N-S motion of East Gondwana
1962 away from West Gondwana, often assumed to follow the Davie Fracture Zone (DFZ) and
1963 requiring an initial ‘loose’ fit of Gondwana fragments (e.g. Coffin and Rabinowitz, 1987). 2)
1964 A similar pattern, but where an initial NW-SE (Klimke et al., 2017; Reeves et al., 2016) or
1965 NNW-SSE (Phethean et al., 2016) motion precedes N-S spreading allowing for a ‘tight’
1966 initial configuration of Gondwana fragments.

1967 Depending on the orientation of a margin relative to the extensional direction under which it
1968 forms, margins develop under different modes (i.e. divergent, transform, or oblique). The
1969 resulting geometries and structures are characteristic of each margin type, allowing us to
1970 differentiate between them. Due to the different initial extension directions used by the two
1971 groups of plate models, each group predicts that the margins of the curved WSB will
1972 develop differently. For example, models using N-S spreading predict transform margins
1973 with a N-S trend, whereas those using NNE-SSW spreading predict a NNE-SSW trend.

1974 Understanding the mode of rifting and margin structures of the WSB is not only crucial for
1975 our understanding of how supercontinent dispersal occurs, but also has significant
1976 implications for the nature of the basement rocks surrounding the margins of East Africa and
1977 the location of the continent-ocean transition (COT), both important factors for hydrocarbon
1978 exploration. In this study we use seismic reflection data and gravity modelling to investigate
1979 the geometry, structure, and trend of the Rovuma continental margin (Northern
1980 Mozambique) in order to decipher: 1) the margin type and its mode of formation (divergent
1981 vs strike-slip), and 2) which group of plate tectonic models are best able to predict the
1982 observed structures and margin trend. For the first time, we unambiguously identify a
1983 transform continental margin in seismic reflection data from the southern Rovuma Basin and
1984 support our observations with rigorous gravity modelling. The identified margin is not
1985 coincident with the DFZ, which is often assumed to form the continent-ocean transform
1986 margin (COTM) of the WSB.

1987



1988

1989 **Figure 3.1.** Map of the Western Somali Basin (WSB) showing the location of gravity
 1990 profiles (black lines) studied in the Rovuma Basin (RB). Karoo and Jurassic aged
 1991 sedimentary basins used to reconstruct the conjugate margins are shown. White dashed lines
 1992 depict gravity lineaments related to the ocean spreading fabric of the basin (Phethean et al.,

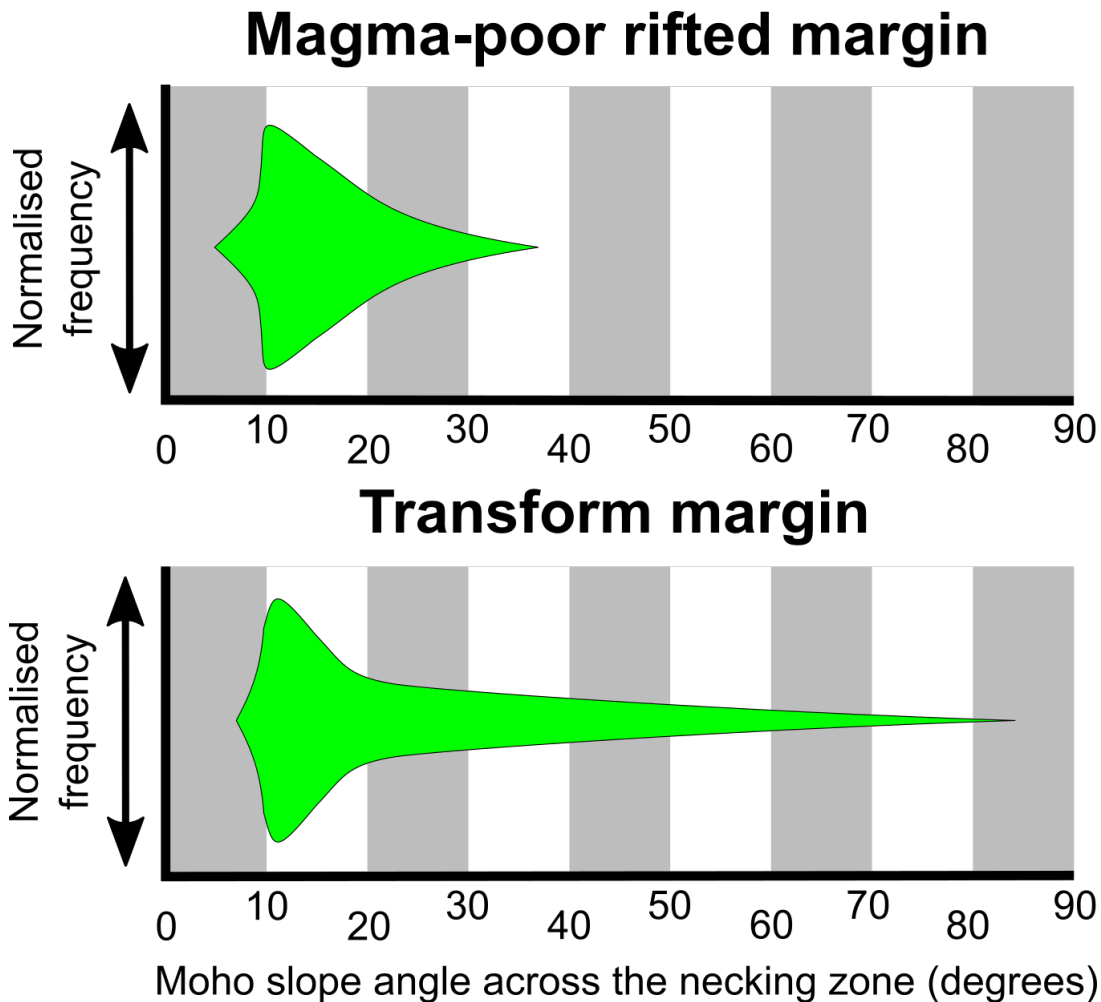
1993 2016). Large black arrows indicate the two main groups of reconstruction paths proposed for
1994 Madagascar. DFZ, Davie Fracture Zone; LB, Lurio Belt; TCB, Tanzania Coastal Basin.

1995 **3.2. Characterisation of passive continental margins**

1996 The angle between the lithospheric deformation zone and the regional extension direction
1997 (previously discussed in Chapter 1.2) controls which of the two endmember types of passive
1998 margins, divergent and transform margins, develops. Where the deformation zone lies
1999 almost perpendicular ($\sim > 80^\circ$) to the extension direction, divergent margins develop.
2000 Decreasing the obliquity between the extension direction and the deformation zone to
2001 between $\sim 60^\circ$ and $\sim 80^\circ$ results in the development of divergent margin segments linked by
2002 transfer zones. A further reduction to between $\sim 20^\circ$ and $\sim 50^\circ$ leads to the development of
2003 alternating divergent and transform margin segments, possibly connected through horsetail
2004 splay faults. Below $\sim 20^\circ$, transform margins develop (Basile and Braun, 2016).

2005 Harry et al., (2003) devised a method of differentiating between margin endmembers by
2006 comparison of crustal thickness variations across a margin to a compilation of well-studied
2007 examples. This compilation has since been updated by Mercier de Lépinay et al., (2016) and
2008 allows for a rapid identification of margin type and, therefore, mode of development.

2009 This method of margin interpretation can also be supplemented through the identification of
2010 features characteristic of each margin type to provide a more robust differentiation between
2011 divergent and transform type margins. We use the main characteristics of passive margin
2012 endmembers summarised in Chapter 1.2 for this purpose. Furthermore, average Moho slopes
2013 across the necking zones of magma-poor divergent margins and transform margins show
2014 differing distributions (Figure 3.2) and may therefore be used to differentiate between the
2015 two margin types. Whilst the bulk of Moho slopes for both transform and magma-poor
2016 divergent margins overlap, transform margins with slopes less than 7° are yet to be
2017 identified, as are magma-poor divergent margins with slopes greater than 36° . Average
2018 Moho slopes across necking zones that are lower or higher than these values therefore imply
2019 a divergent or transform margin, respectively. As the crustal necking zones of volcanic
2020 divergent margins are modified by magmatic additions, the slope of the Moho across them
2021 may not be used to identify the margin as divergent or transform in nature. These margins
2022 are, however, readily identifiable by other characteristic features in seismic reflection data
2023 (e.g. Chapter 1.2) and do not require such Moho slope analysis for identification.



2025

2026 **Figure 3.2.** Normalised frequency distribution of average Moho slope angles across the
 2027 necking zones of magma-poor rifted margins and transform margins respectively. Data is
 2028 derived from: Reston (2009) and Van Avendonk (2009) for magma-poor rifted margins; and,
 2029 Todd et al., (1988), Todd and Reid (1989), Barton et al., (1990), Keen et al., (1990),
 2030 Edwards et al., (1997), Sage et al., (2000), Greenroyd et al., (2008), and Parsiegla et al.,
 2031 (2009) for transform margins.

2032 3.3. Data and Methods

2033 Seismic reflection data and 2D gravity modelling are used to investigate the Rovuma Basin
 2034 margin geometry, structure, and trend in order to discern the margin type and therefore strain
 2035 regime under which it formed. This allows for the comparison of predictions from different
 2036 plate tectonic models with observations in order to determine which best accounts for the
 2037 evolution of the WSB.

2038 3.3.1. Seismic reflection data and interpretation

2039 Multichannel seismic reflection data from the ION East AfricaSPAN and VEMA (leg 3618)
2040 cruises are used for the geological interpretation of basement structures around the
2041 continental margin of the Rovuma Basin (Figure 3.1), and to constrain 2D gravity models.

2042 Three lines from the ION East AfricaSPAN PSDM (pre-stack depth migrated) dataset cross
2043 the continental margin of the Rovuma Basin at near perpendicular angles (Figure 3.3a).
2044 These lines are used to identify features of the Rovuma margin that are characteristic of the
2045 different endmember margin types (as described in Chapter 1.2). This assists in the
2046 interpretation of the margin type, helps to delineate the COT, and identifies the lateral
2047 position of the bottom of the basement slope, which is compared with those predicted by
2048 gravity modelling.

2049 A fourth line from the ION East AfricaSPAN PSDM dataset crosses the continental margin
2050 at a highly oblique angle and captures continental Moho reflections. Moho slope angles
2051 measured across the necking zone on this line are therefore corrected to their true dip. For
2052 this purpose, the strike of the margin is assumed to follow the onshore basement outcrop of
2053 the Rovuma Basin.

2054 3.3.2. Gravity data

2055 Three different gravity datasets are used to constrain the gravity anomaly for gravity
2056 modelling. These include the Trident Bouguer onshore, free-air offshore anomaly dataset
2057 (Trident BAFA) provided by Getech (Fairhead et al., 2009), the Sandwell and Smith V24
2058 free-air anomaly (SS24; Sandwell et al., 2014; Figure 3.3a), and the DTU15 free-air
2059 anomaly (Stenseng et al., 2015). Each dataset has its own strengths. For instance, the Trident
2060 BAFA dataset contains additional proprietary data onshore; SS24 has a ‘rich’ frequency
2061 content due to its use of residual slopes of sea surface height during gravity estimation
2062 (Pavlis et al., 2012); and DTU15 has been argued to have an increased accuracy in coastal
2063 regions due to its use of simply the residual sea surface heights in its estimation of gravity
2064 anomalies (Pavlis et al., 2012). Using the datasets together also allows a qualitative measure
2065 of uncertainty by comparing their variability and reduces the error produced by local
2066 deviations of any one dataset during modelling.

2067 To reduce the errors associated with modelling a 3D interface in 2D, and to make all three
2068 gravity datasets BAFA and thus comparable, we perform Bouguer and terrain corrections on
2069 the SS24 and DTU15 datasets before 2D modelling. Those corrections were performed in
2070 GMT using the Okabe method, which is able to handle arbitrarily complex geometries. A

2071 resolution of 1 km was used for SRTM elevation data, and we assume a density for the
2072 upper crust of 2.67 g cm^{-3} to be consistent with the Trident BAFA dataset.

2073 Following BAFA conversion, the three datasets can be directly compared. Onshore, both the
2074 DTU15 and SS24 datasets use the Earth Gravitational Model (EGM2008; Pavlis et al., 2012)
2075 solution, but where the additional proprietary data included in Trident result in significant
2076 local differences between this dataset and the others, we consider Trident more reliable.
2077 Offshore, the Trident dataset is produced primarily as a stacked solution of older versions of
2078 the SS and DTU anomalies, and so this dataset generally follows the trend of the DTU15 and
2079 SS24 anomalies. Where it does differ, it is deemed less reliable as it was produced before the
2080 addition of new CryoSat-2 and Jason-1 altimetry data. As, however, the DTU15 and SS24
2081 datasets are produced using different methodologies, differences between these datasets
2082 represent real uncertainty in the gravity anomaly. To mitigate this problem, gravity profiles
2083 for 2D modelling are located away from any significant disagreements so that differences
2084 are generally $< 10 \text{ mGal}$. Where onshore sections of gravity profiles must cross regions of
2085 significant disagreement between the Trident and SS24/DTU15 datasets, we replace the SS
2086 and DTU onshore data with that of the more reliable Trident dataset. A spline covering 10
2087 km either side of the coastline is used to produce a smooth join between the datasets. A map
2088 showing the variations between datasets is provided in the supplementary material (Figure
2089 S3.1).

2090 3.3.3. Gravity modelling

2091 Three types of gravity modelling have been performed during this study in order to
2092 determine the margin type, the margin's trend, and the detailed crustal structure of the
2093 margin, respectively.

2094 Firstly, a rigorous parameter space search investigating the preferred slope angle and
2095 location of a simple ramp-style Moho geometry is performed for the three profiles where
2096 coincident seismic data crossing the margin is available to constraint the seabed and
2097 basement interfaces (Figure 3.3b). This provides an understanding of the Moho geometry
2098 unbiased by human interpretation and is used to generate profiles of crustal thickness
2099 variation across the margin. These profiles are then compared to the global margin crustal
2100 thickness variation compilations of Harry et al., (2003), and Mercier de Lépinay et al.,
2101 (2016), providing an independent interpretation of the Rovuma Basin margin type.

2102 Secondly, the preferred Moho slope angles and locations derived for profiles 2 and 3 are
2103 used to produce a simplified average geometry of the margin. We then use this simplified
2104 geometry to find the best fitting margin location along gravity profiles 4-8, which have no

2105 seismic constraints. Profile 1, south of the Lurio belt, is used as an independent test profile
2106 for this method. These best fit locations constrain the margin trend and, in combination with
2107 the interpretation of the margin type, allow us to determine which group of plate tectonic
2108 models best predicts observations from the Rovuma Margin.

2109 Following the first-order determination of the margin type, a final procedure involves
2110 detailed 2D forward gravity modelling of the three gravity profiles with coincident seismic
2111 data, using the commercial Interpex IX2D-GM software. This modelling allows for the
2112 addition of geologically plausible refinements to reduce misfit between the modelled gravity
2113 profile and data, where required. The resulting detailed crustal structure of the margin is then
2114 used to identify features characteristic of the different margin types, providing additional
2115 constraints for the interpretation of the margin.

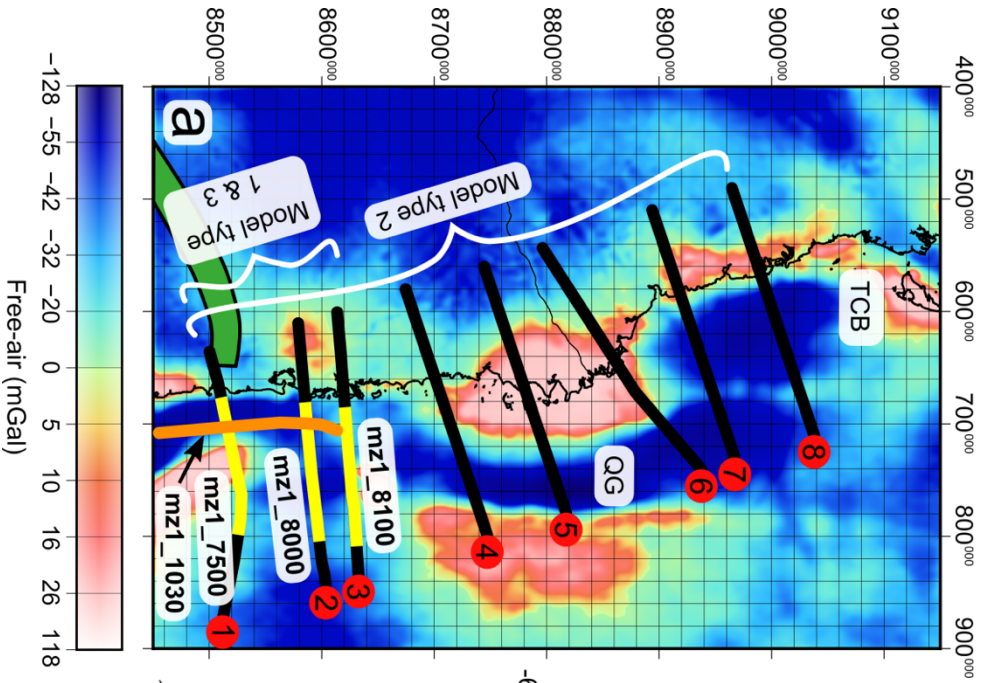
2116 **3.3.3.1. Modelling type 1: Systematic investigation of Moho geometry**

2117 Gravity profiles with coincident seismic data crossing the margin's basement slope (Profiles
2118 1,2, and 3; Figure 3.3a) were used to investigate the underlying Moho geometry using the
2119 accurate seismic constraints on the remaining density interfaces. Simple ramp-style Moho
2120 geometries were tested for slopes between 5 and 85 degrees over a 65 km distance around
2121 the bottom of the basement slope as identified from seismic data. An initial search at 5
2122 degree and 5 km intervals covers the plausible parameter space with over 250 Moho
2123 geometry combinations (Figure 3.3b). This is then followed by a refined search around the
2124 initial parameter minimum at 1 degree and 1 km intervals. The root-mean-square fit between
2125 the calculated gravity anomalies and the three gravity datasets used in this study is then
2126 determined.

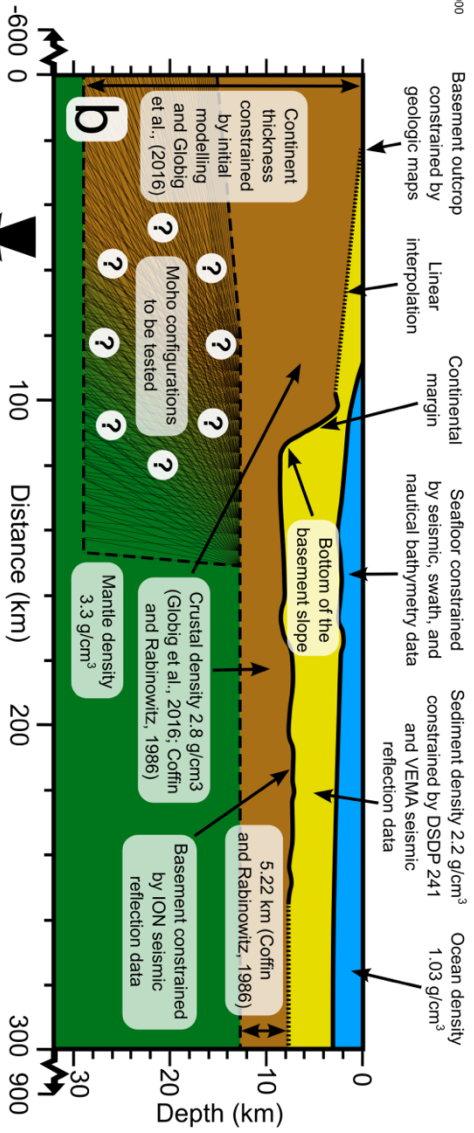
2127 The 2D forward modelling was performed in Matlab using the analytical expression for the
2128 gravity effect of line elements with horizontal and vertical dimensions of 100 m and 20 m
2129 respectively. The model domain was extended 600 km beyond the extent of the gravity
2130 profile to mitigate boundary effects, whilst linear smoothing of density contrasts was
2131 performed laterally for 500 m on either side of a density interface to reduce artefacts
2132 resulting from gravity calculations of the rectangular grid elements across extremely shallow
2133 interfaces, such as outcropping basement.

2134 The densities and geometries of the sediment and crustal layers used for all types of gravity
2135 modelling are constrained using a variety of Industry and academic data, as well as
2136 information from the literature. These are described below.

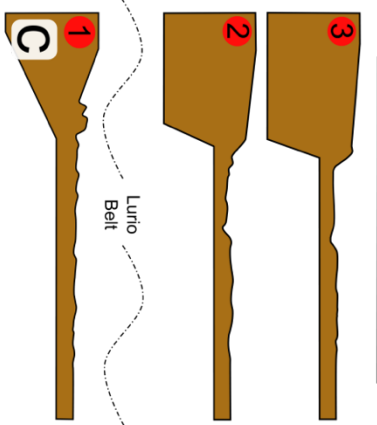
Locations of modelled gravity profiles



Model type 1: Find best-fit Moho slope angle and location for profiles with coincident seismic data (profiles 1, 2, and 3)



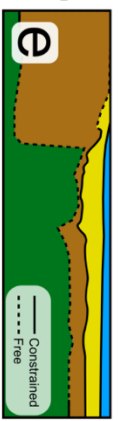
Results (model type 1): Best fit ramp-style Mohos



Model type 2: Find best-fit locations for the margin



Model type 3: Detailed models of crustal structure



Take simple average geometry

Take profiles of crustal structure across the margin for comparison to global compilation for preliminary margin interpretation

2139 **Figure 3.3.** Locations of seismic and gravity profiles, and summary of gravity modelling
2140 methods (a) Sandwell and Smith free-air gravity anomaly map showing modelled gravity
2141 profiles, which are indicated by black lines with corresponding identification number in red
2142 circles. Coincident seismic profiles that cross the continental margin are marked in yellow.
2143 Seismic profile mz1_1030 (orange) runs highly obliquely to the margin trend. The Lurio
2144 Belt is marked by the green band. QG, Quirimbas Graben; TCB, Tanzania Coastal Basin. (b)
2145 Summary of type 1 modelling – Moho geometry investigations along seismically
2146 constrained profiles. Constrained density interfaces are shown as solid lines, assumed
2147 interfaces are shown as short dashed lines, and the region of Moho configurations to be
2148 tested around the margin is marked as long dashed lines. (c) The results from type 1
2149 modelling on profiles 2 and 3 (situated to the north of the Lurio Belt) are used to generate an
2150 average margin geometry for use in type 2 models, with profile 1 used to test the method.
2151 Results from profiles 1, 2, and 3 are used as starting models for type 3 modelling. (d)
2152 Summary of type 2 modelling. The average margin geometry is modelled across the margin
2153 for all profiles (1-8) to find the best fit locations and determine the margin trend. (e)
2154 Summary of type 3 modelling. Seismically constrained lines are modelled in detail using
2155 Interpex IX2D-GM software. The Moho and unconstrained regions of the basement are
2156 allowed to move freely. Crustal thicknesses of 29 km and 5.22 km are used as continental
2157 and ocean boundary conditions, respectively.

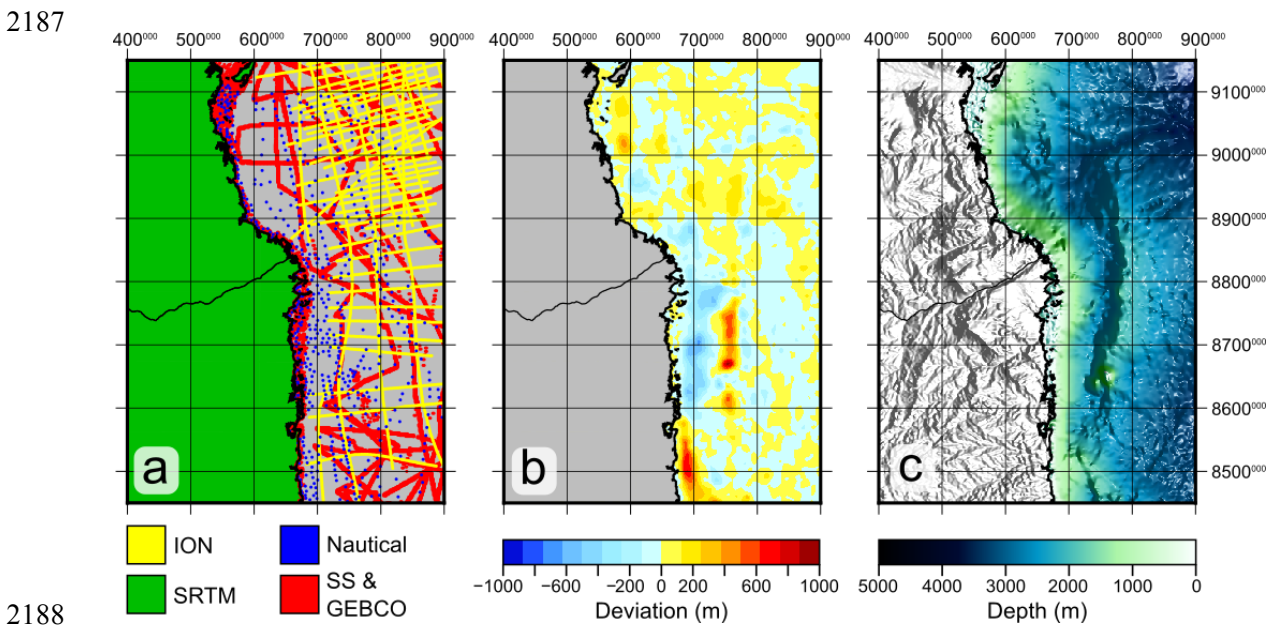
2158 **3.3.3.1.1. Bathymetry surface**

2159 The seabed is a shallow interface with a high density contrast across it. Because of this, it is
2160 one of the major contributors to the gravity anomaly, and it must be well constrained to
2161 perform accurate gravity modelling. The ION seismic reflection lines provide an extensive
2162 and high quality seabed constraint for the region. However, as they sometimes do not cross
2163 the shelf edge, they are unable to fully constrain the geometry of this major shallow
2164 structure. We therefore supplement the ION seabed constraints with available ship-based
2165 singlebeam and multibeam bathymetry data extracted from the GEBCO and Sandwell and
2166 Smith global elevation datasets, as well as additional depth soundings taken from nautical
2167 charts for the region, which significantly increase the seabed constraints around the shelf
2168 break (Figure 3.4a). In places these additional constraints deviate from global elevation
2169 datasets by more than 500 m and represent a significantly more accurate constraint on the
2170 seabed for gravity modelling (Figure 3.4b).

2171 As ship-based measurements are generally quite widely spaced, they can provide good
2172 constraints on the long wavelength information of the seabed, but provide little information
2173 on short wavelengths between data points. Following surfacing of the combined dataset
2174 (performed using Generic Mapping Tools (GMT; Wessel et al., 2013) with a tension factor

2175 of 0.25), we therefore apply a 15 km low-pass Gaussian filter and replace the short
 2176 wavelengths with those of the Sandwell and Smith gravity-derived seabed dataset, which has
 2177 full spatial coverage.

2178 The seabed interface will thus inherently account for the vast majority of the very short
 2179 wavelength (< 15 km) content of the gravity anomaly, allowing us to produce realistic
 2180 models with a full range of wavelengths without affecting the modelling of the basement and
 2181 Moho structures of interest, which inherently have longer wavelength gravity signatures due
 2182 to upward continuation. A 15-km filter is used as it provides the best trade-off between
 2183 increased continuity of structural seabed trends derived from the SS data and maximised
 2184 accuracy in regions of data constraint. The resulting seabed surface is shown in Figure 3.4c.
 2185 Examples using alternative filter cut-off wavelengths are presented in the supplementary
 2186 material (Figures S3.2-5).



2189 **Figure 3.4.** (a) Input data for the new bathymetry surface. (b) Difference between the new
 2190 bathymetry surface and global elevation models. Offsets of almost 1 km can be seen and
 2191 represent a significant improvement in the predicting capabilities of the dataset. (c) The new
 2192 bathymetry surface, illuminated from the east.

2193 **3.3.3.1.2. Sediment density**

2194 We constrain the density of the sediment layer using seismic velocities derived during post
 2195 stack migration processing of the multichannel seismic reflection line 84v, shot during the
 2196 R/V *Vema* leg 3618. This line is situated in the north of the WSB, but is chosen due to the
 2197 availability of coincident density measurements from the DSDP 241 borehole. The Nafe-
 2198 Drake relation provides a good fit of densities derived from velocity conversion to densities

2199 measured at DSDP 241, where converted densities range from 1.62 to 2.38 g cm⁻³, with a
2200 mean value of ~2.2 g cm⁻³. Further information and figures on the derivation of the sediment
2201 density are provided in the supplementary material (Figures S3.6-8).

2202 **3.3.3.1.3. Sediment thickness**

2203 Offshore, where ION PSDM seismic reflection lines are coincident with gravity profiles, the
2204 top basement interface constrains the sediment thickness. Where possible, crosslines are
2205 used to check the interpretation of the top basement reflector. Where young volcanic edifices
2206 within the sediment layer obscure the basement interface, we linearly interpolate between
2207 basement picks.

2208 Onshore, the basement outcrop is constrained using regional geological maps. Between the
2209 onshore basement outcrop and the seismically constrained basement offshore, we linearly
2210 interpolate the basement horizon. This is likely a gross simplification of the true geometry of
2211 the basement interface; however, it avoids the introduction of unjustified complexities in the
2212 gravity modelling. Sensitivity to this simple linear geometry was also tested by modelling
2213 alternative imposed geometries, such as simple basins or rises, within the unconstrained
2214 region.

2215 **3.3.3.1.4. Crustal density and thickness in the ocean and continent**

2216 In order to investigate the nature of the transition from continent to ocean, densities and
2217 thicknesses of the continental and oceanic crust on either side of the transition must first be
2218 constrained.

2219 Offshore, (Coffin et al., 1986) used sonobuoy experiments to determine the thickness and
2220 velocity structure of oceanic crust in the WSB. They showed that the crust has an average
2221 thickness of 5.22 km, which we use to constrain the depth of the Moho below top basement
2222 at the seaward edge of the coincident seismic data. The crust has an average layer 2
2223 thickness of 2.73 km with a velocity of 5.83 +/- 0.27 km/s, and a thin layer 3 averaging just
2224 2.62 km thick with a velocity of 7.03 +/- 0.25 km/s. Using the Nafe-Drake relationship, we
2225 convert these seismic velocities to densities for the upper and lower bounds of the velocity
2226 estimate. We then average the densities of upper and lower crust weighted by the thickness
2227 of each layer to calculate an average crustal density for the oceanic crust. Due to the dense
2228 layer 3 being thin compared to most estimates from normal oceanic crust, the average
2229 oceanic crustal density is also low at between 2.76 and 2.89 g/cm³.

2230 Onshore, a recent study by Globig et al. (2016) incorporating a comprehensive dataset of
2231 Moho depths showed that the average crustal density of the African continent is 2.79 g/cm³.
2232 The continent-scale study also predicted crustal thicknesses along the Rovuma basin as low

2233 as 30 km. To determine the final crustal thickness to be used, we initially perform modelling
2234 phase 1 using crustal thicknesses between 20 and 35 km, with testing at 1 km intervals for
2235 all profiles between 27 and 31 km, and selected the thickness consistently resulting in the
2236 lowest RMSD for use in the final models. The full results from this testing are presented in
2237 the supplementary material (Figure S3.9).

2238 As the average density of the continental crust falls within the range for the oceanic crust,
2239 we model both using a single density of 2.8 g/cm^3 . This provides several advantages: Firstly,
2240 there is no imposed lateral density contrast between the ocean and continent. This allows us
2241 to avoid any circularity in determining the location of the COB from crustal thickness, which
2242 would be influenced by the chosen location of a lateral density contrast. Secondly, by not
2243 differentiating between upper and lower crusts, we avoid the introduction of an additional
2244 unconstrained interface into the model. A disadvantage of this method is that the basement-
2245 sediment interface may be modelled using a slightly higher density contrast than might be
2246 present at these depths.

2247 **3.3.3.2. Model type 2: Determining the margin trend**

2248 To determine the along-strike trend of the margin, we generate a simplified average margin
2249 geometry and model its best fit location along gravity profiles that cross the continental
2250 margin to the north of the Lurio Belt (Figure 3.3d). We use the Matlab code previously
2251 described in section 3.3.3.1, and the best fit location is again determined by calculating the
2252 RMSD between the modelled gravity anomaly and the three gravity datasets.

2253 The simplified average margin basement geometry is generated from seismic and geological
2254 map constraints of the basement interface along profiles 2 and 3, and is defined by 3
2255 inflection points along the basement interface (Figure 3.3c-d). From onshore seaward the
2256 inflection points are: 1) the onshore basement surface outcrop, where the basement interface
2257 begins to dip gently seaward; 2) the top of the basement slope, at a depth of 2.8 km, after
2258 which the basement interface dips steeply at 21° , until; 3) the bottom of the basement slope,
2259 at a depth of 7.8 km, after which the basement interface returns to horizontal. A ramp-style
2260 Moho geometry, determined from the type 1 modelling, defines the base of the crust and has
2261 a slope of 67° , the top of which is positioned 8 km landward and 5.22 km below the bottom
2262 of the basement slope.

2263 Only profiles 2 and 3 are used for the generation of the average margin geometry for two
2264 main reasons. Firstly, it allows us to use profile 1 to test the search algorithm's ability to
2265 correctly locate the base of the basement slope on a profile with coincident seismic data.
2266 Secondly, profile 1 is located to the south of the Lurio Belt, an ENE-WSW trending

2267 Neoproterozoic suture zone separating the northern and southern basement complexes of
2268 northern Mozambique (Emmel et al., 2011), across which basement structure differs (Franke
2269 et al., 2015). The geometry of profile 1 is therefore less likely to be representative of the
2270 margin to the north, making it a poor contribution to the average geometry of the margin. It
2271 does, however, therefore serve as a demanding test for the search algorithm allowing an
2272 assessment of the techniques robustness. We quantify the accuracy of type 2 modelling by
2273 measuring the offset between its predicted margin location and the Moho and basement
2274 slopes determined from seismic data and type 1 modelling. We also perform further testing
2275 of the search algorithm's sensitivity to the inputted average margin geometry, along with
2276 checks on the geological plausibility of required adjustments to type 2 model output in order
2277 to satisfy gravity data.

2278 **3.3.3.3. Model type 3: Detailed 2D gravity models**

2279 Following systematic investigation of preferred Moho geometries using a simple ramp-style
2280 Moho slope, more complex 2D forward modelling is performed with full freedom of the
2281 Moho interface and, within its unconstrained region, top basement interface. This modelling
2282 is performed using Interpex's IX2d-GM software.

2283 This investigates the detailed crustal structure along the profiles, allowing for the
2284 identification of features characteristic of different margin types. Key features that could be
2285 identified by this modelling include: a) marginal ridges or complex rift structures within the
2286 region of unconstrained basement, characteristic of some transform margins and rifted
2287 margins respectively; b) complex Moho geometries, some of which may influence Moho
2288 slope angles determined across the necking zone from type 1 modelling; c) margin flexure,
2289 found at transform margins with mechanically coupled ocean and continental domains, and
2290 d; hyper-thinned continental crust and exhumed mantle found at magma-poor rifted margins,
2291 or exhumed mantle and thin oceanic crust found at transform margins and ocean fracture
2292 zones.

2293 The same layer densities as for type 1 and 2 modelling are used, although we also test
2294 layered sediment densities and two layer crustal densities. The same crustal thicknesses as
2295 for type 1 and 2 modelling are also imposed at the ends of the gravity profiles as boundary
2296 conditions.

2297 **3.4. Results**

2298 3.4.1. Seismic reflection observations

2299 The location of the four seismic reflection lines from the ION East AfricaSPAN dataset are
2300 shown in Figure 3.3. Three of the lines cross the continental margin perpendicularly. Results
2301 for these lines (from north to south: mz1_8100, mz1_8000, and mz1_7500) are shown in
2302 Figure 3.5. A fourth line, mz1_1030, runs perpendicular to the three previous lines and also
2303 crosses the continental margin at a highly oblique angle, and results for this line are shown
2304 in Figure 3.6.

2305 **3.4.1.1. Mz1_8100**

2306 At the western edge of line mz1_8100, a massive 6 km increase in accommodation space
2307 occurs over an extremely short distance of ~17 km (Figure 3.5a and d). The large increase in
2308 accommodation space indicates that the continental crust has been thinned and that this
2309 structure represents the continental margin. No faults are imaged within the steep 24°
2310 basement slope, which is instead overlapped by steeply dipping parallel sequences of post rift
2311 sediments. Immediately at the base of the margin slope a crossline confirms the top
2312 basement pick, which becomes obscured slightly eastwards due to the St Lazare volcanic
2313 edifice. East of St Lazare and of the DFZ, which is obscured by the above volcanics, the top
2314 basement is again imaged and has a hummocky character commonly associated with oceanic
2315 crust. No continuous reflections define the Moho surface for any region of this line and no
2316 evidence for syn-rift volcanics is present, despite extensive post breakup volcanism.

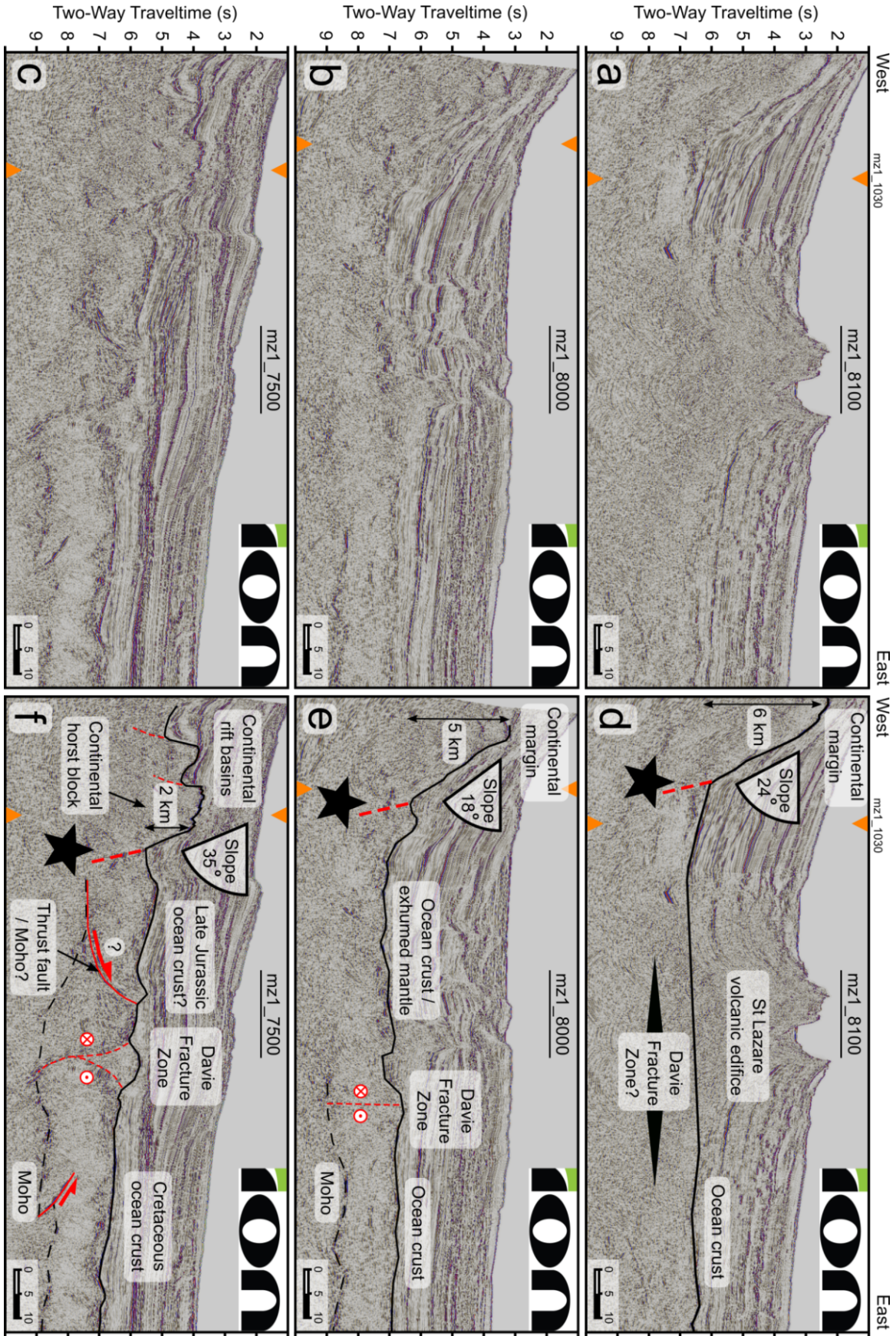
2317 **3.4.1.2. Mz1_8000**

2318 Approximately 35 km to the south a similar setting is observed (Figure 3.5b and e). Again a
2319 steep basement slope, here 18°, defines a large 5 km increase in accommodation space and is
2320 void of any faults. The presence of limited post rift volcanics allows the top basement to be
2321 traced across the entirety of this line. To the west of the DFZ this surface lies at ~7.3 s
2322 TWTT, and shows a rough and hummocky character. No Moho reflections are visible
2323 anywhere to the west of the DFZ, but recent faulting of the overlying sediments may
2324 partially obscure the deep structure of some of this region **due to the disruption of seismic**
2325 **energy by such faults before the basement is imaged and by tectonic overprinting of the**
2326 **original basement structure.** The DFZ itself is defined by a rise in the top basement, and
2327 possible weak Moho reflections define a crustal thickness of ~2.4 s TWTT. To the east of
2328 the DFZ, the top basement is well defined and lies at ~6.8 s TWTT, 0.5 s above that to the
2329 west, and is defined by a hummocky character. In the vicinity of the DFZ, Moho reflections
2330 have a sudden onset and clearly define an average crustal thickness of ~1.8 s TWTT until the
2331 end of the profile.

2332 Aligning the base of the basement slopes (black stars on Figure 3.5) of these two similar
2333 margin profiles (mz1_8100 and mz1_8000) defines a slightly NNW-SSE trend of the
2334 margin, at 172°.

2335 **3.4.1.3. Mz1_7500**

2336 Moving 70 km farther southwards, and crossing the offshore extension of the Lurio Belt, a
2337 change in the margin architecture occurs. On the west, rift grabens filled with divergent
2338 wedges of synrift sediment are bounded by continentward-dipping normal faults, possibly
2339 forming the northern continuation of the Angoche Basin (e.g. Mahanjane, 2014; Figure 3.5c
2340 and f). These half grabens sit at a depth of approximately 4 s TWTT, substantially above the
2341 basement to the east, which lies at between 5 and 7 s TWTT. This is consistent with a
2342 thicker crust beneath this region providing isostatic support, and with a continental origin of
2343 this basement. This faulted crust is bounded seaward by a large horst block, sitting up to 1.5
2344 km above the half grabens. A large (2 km), and extremely steep, basement slope then dips
2345 35° towards the east. This structure lies along the continuation of the 172° trend of the
2346 margin seen on the northern lines, and is steeply overlapped by sediments lacking a divergent
2347 nature. The similar steep slope, sedimentation history, and the along-strike alignment of this
2348 structure with the basement slope seen farther north suggests a genetic relationship between
2349 them. Seaward of this slope, the top basement can be seen to gain a smooth character,
2350 possibly indicating the presence of oceanic crust. This smooth character continues eastwards
2351 of the DFZ. The DFZ at this location is expressed by a positive flower structure, indicating a
2352 compressional component to the strike-slip tectonics along it. Moho reflections beneath the
2353 DFZ, which are stronger on the eastern flank, define a crustal thickness of over 3 s TWTT,
2354 attesting to the transpressional nature of the DFZ in this location. On the western flank of the
2355 DFZ, westward-dipping low angled reflectors can be seen to cut across the crust and are
2356 associated with a slight shallowing of the basement and counter-clockwise rotation of the
2357 upper crust. These structures are associated with crustal thickening around the DFZ and may
2358 represent thrust faults that developed in response to the compression. A similar structure, not
2359 cutting the entire crustal section, also offsets the Moho to the east of the DFZ and is again
2360 associated with a thickening of the crust. In this region, strong Moho reflections define a
2361 crustal thickness of generally between 2.2 and 1.7 s TWTT, and a more seismically
2362 transparent nature of the crust is seen to the east of the DFZ, indicative of oceanic crust.



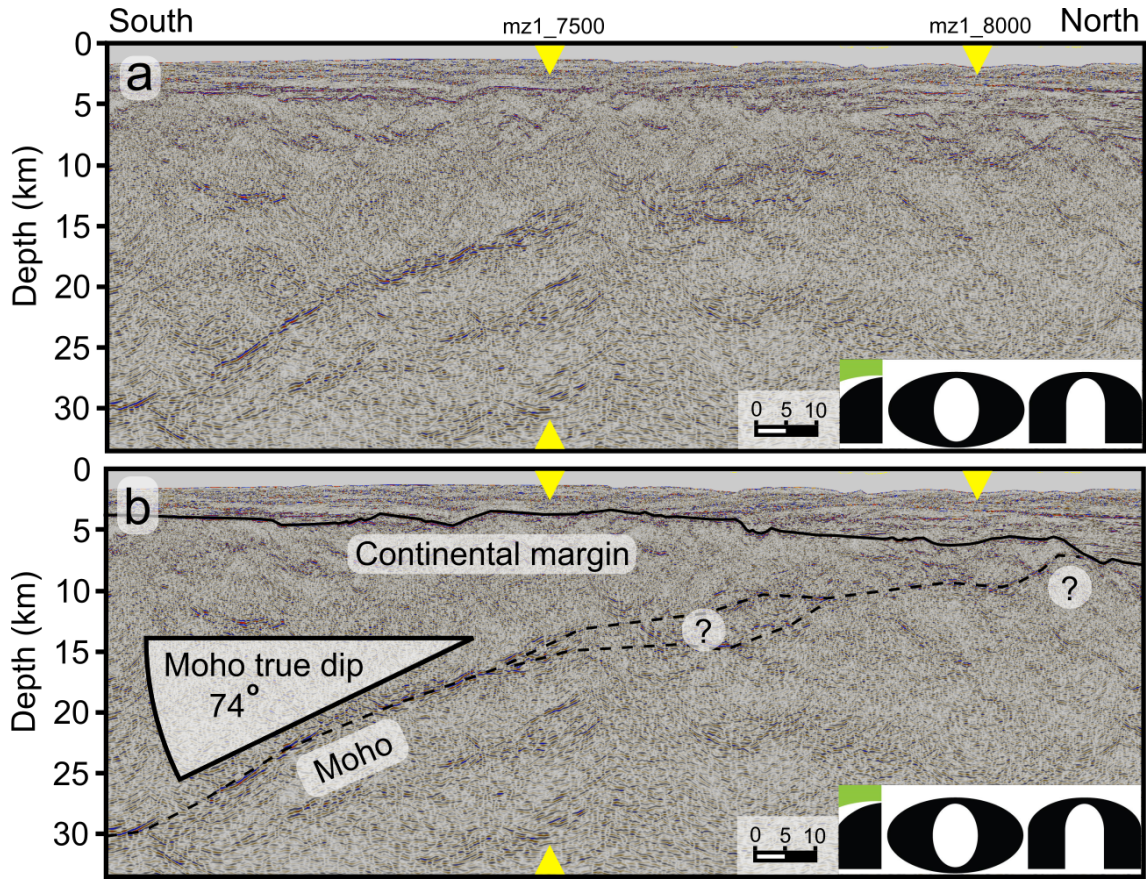
2365 **Figure 3.5.** ION seismic reflection profiles crossing the continental margin are shown
2366 unmarked (a-c) and interpreted (d-f). Line intersections with the perpendicular mz1-1030
2367 profile are marked by orange triangles. For the location of the seismic lines, see Figure 3.3a.
2368 (d-f) The basement interfaces are marked as solid black lines and highlight the steep
2369 continental margin. Basement slopes across the margin are labelled, as is the depth-
2370 converted vertical offset from top to bottom. Possible Moho reflections are indicated by
2371 dashed black lines. Positions of the base of the margin slope as interpreted from seismic are
2372 shown as black stars.

2373 **3.4.1.4. Mz1_1030**

2374 Running perpendicular to the above seismic lines, and at a highly oblique angle to the trend
2375 of the identified basement slope, line mz1_1030 also crosses the continental margin (Figure
2376 3.6.). A deep set of strong reflections, with a southerly apparently dip, lie well below the top
2377 basement and are interpreted as the Moho. At the southern edge of the line these reflections
2378 lie at a depth of ~30 km. Moving northwards, the reflections rise consistently shallower to
2379 where they outcrop at the basement surface just north of line mz1_8000. To the north of this
2380 outcrop, exhumed mantle may therefore form the basement surface.

2381 The rise of the Moho reflections northward indicates that the transition from continent to
2382 ocean occurs in this direction. In map view, the Moho reflections are oriented at 176 (i.e.
2383 almost due N-S, see Figure 3.3a). To transition from continent to ocean in a northerly
2384 direction, the margin must trend more NW-SE than the seismic line (i.e. $<176^\circ$). Onshore,
2385 the basement outcrop along the southern Rovuma Basin has a trend of 172° , the same as the
2386 basement trend of the slope identified from margin-perpendicular seismic lines. Therefore,
2387 assuming a margin trend of 172° , we can correct the apparent dip of the Moho slope from
2388 line mz1_1030 to its true dip. This shows that it dips extremely steeply at $\sim 74^\circ$ towards the
2389 continent.

2390



2391

2392 **Figure 3.6.** Depth-converted ION seismic reflection profile mz1_1030, crossing the margin
2393 at a highly oblique angle. Basement and Moho interfaces are marked as for Figure 3.5 and
2394 intersections with perpendicular seismic lines are marked by yellow triangles. For location,
2395 see Figure 3.3a. The true dip of the Moho, after correction for the obliquity of the profile to
2396 the margin trend, is 74°. The downward dip of the Moho reflections to the south indicates
2397 that the margin must trend in a more NW-SE direction than the seismic profile.

2398 3.4.2. Gravity

2399 **3.4.2.1. Model type 1: Best fit ramp-style Moho geometries across the margin**

2400 Using constraints on the remaining density interfaces, gravity profiles with coincident
2401 seismic data crossing the margin are used to systematically determine best fit Moho
2402 geometries across the margin. An initial set of models is used to test a range of continental
2403 crustal thicknesses and consistently shows minimum RMSD fits to gravity data for 29 km
2404 thick continental crust. Visual best fits of the landward trend of the calculated gravity
2405 anomaly to data also consistently use a crustal thickness of 29 km. This value is in close
2406 agreement with Globig et al., (2016) and all final models therefore use a 29 km thick
2407 continental crust.

2408 Model sensitivity to the geometry of the basement interface within the unconstrained region,
2409 between the basement outcrop and the onset of seismic constraint (e.g. Figure 3.3b), is also
2410 tested by the introduction of basins and ridges. Whilst the inclusion of basins sometimes
2411 results in lower RMSDs, it has little impact on the best fit Moho geometry. The introduction
2412 of complexities in this region is therefore unnecessary to determine best fits for the Moho,
2413 and is thus avoided.

2414 All three profiles (mz1_8100, mz1_8000, and mz1_7500) show a similar pattern of results
2415 with a strong preference for steep Moho slope angles (15-85°) and a relatively narrow band
2416 (~15-30 km) of acceptable slope locations (Figure 3.7). The arcuate pattern of low RMSD
2417 fits reflects the natural trade-off between these two parameters in achieving a good model fit
2418 to the gravity data.

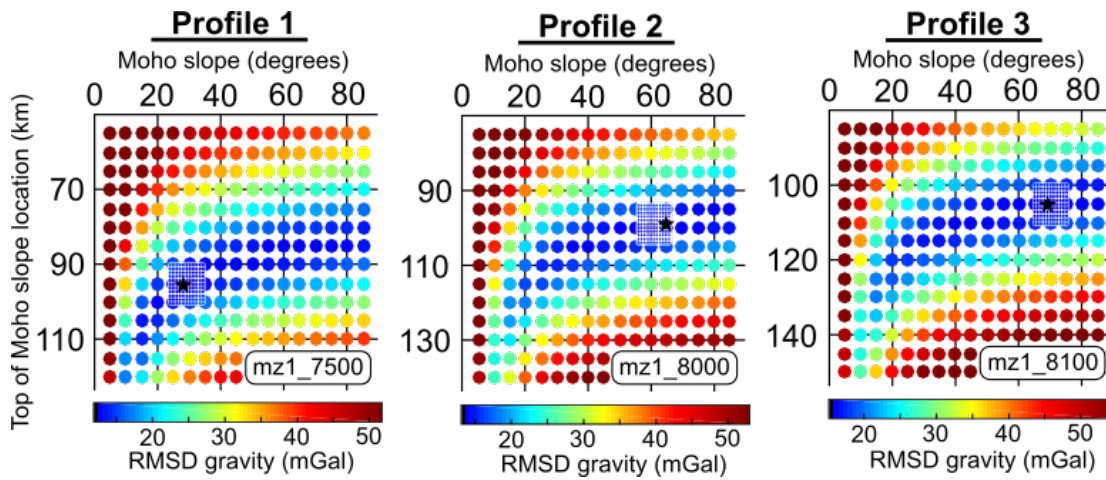
2419 The northernmost profile with coincident seismic data, profile 3 (mz1_8100), is well
2420 constrained by type 1 modelling. Only Moho slopes greater than 25° result in low RMSD
2421 fits and the top of the Moho slope location is also constrained to within a 15 km band,
2422 centred on 107.5 km from the profile's western edge. Minimum RMSD values are achieved
2423 using an extremely steep Moho slope of 69° and a top of Moho slope location 105 km from
2424 the start of the profile. The top of the best-fit Moho slope is located 9.5 km to the west of the
2425 bottom of the basement slope identified in seismic data.

2426 Profile 2 (mz1_8000) shows similarly well constrained Moho interface. Again, only Moho
2427 slopes greater than 25° result in low RMSD fits and the top of the Moho slope location is
2428 also constrained to within 15 km, centred on 102.5 km from the profile's western edge.
2429 Minimum RMSD values are again achieved using an extremely steep Moho slope of 65°,
2430 with a top of Moho slope location 99 km from the start of the profile. This places the top of
2431 the Moho slope 6.5 km to the west of the bottom of the basement slope identified in seismic
2432 data.

2433 Profile 1 (mz1_7500) is the least well constrained of the three profiles by type 1 modelling
2434 and yet low RMSD fits are still only achieved using Moho slopes of 15° or greater. A 30 km
2435 band of low RMSD fits is achieved using Moho slope locations centres around 95 km from
2436 the profile's western edge. Minimum RMSD values are achieved for this profile using steep
2437 Moho slopes of 28°, with the top of the slope positioned at 95 km from the start of the
2438 profile. This places the top of the Moho slope 6 km to the east of the bottom of the basement
2439 slope identified in seismic data.

2440

2441



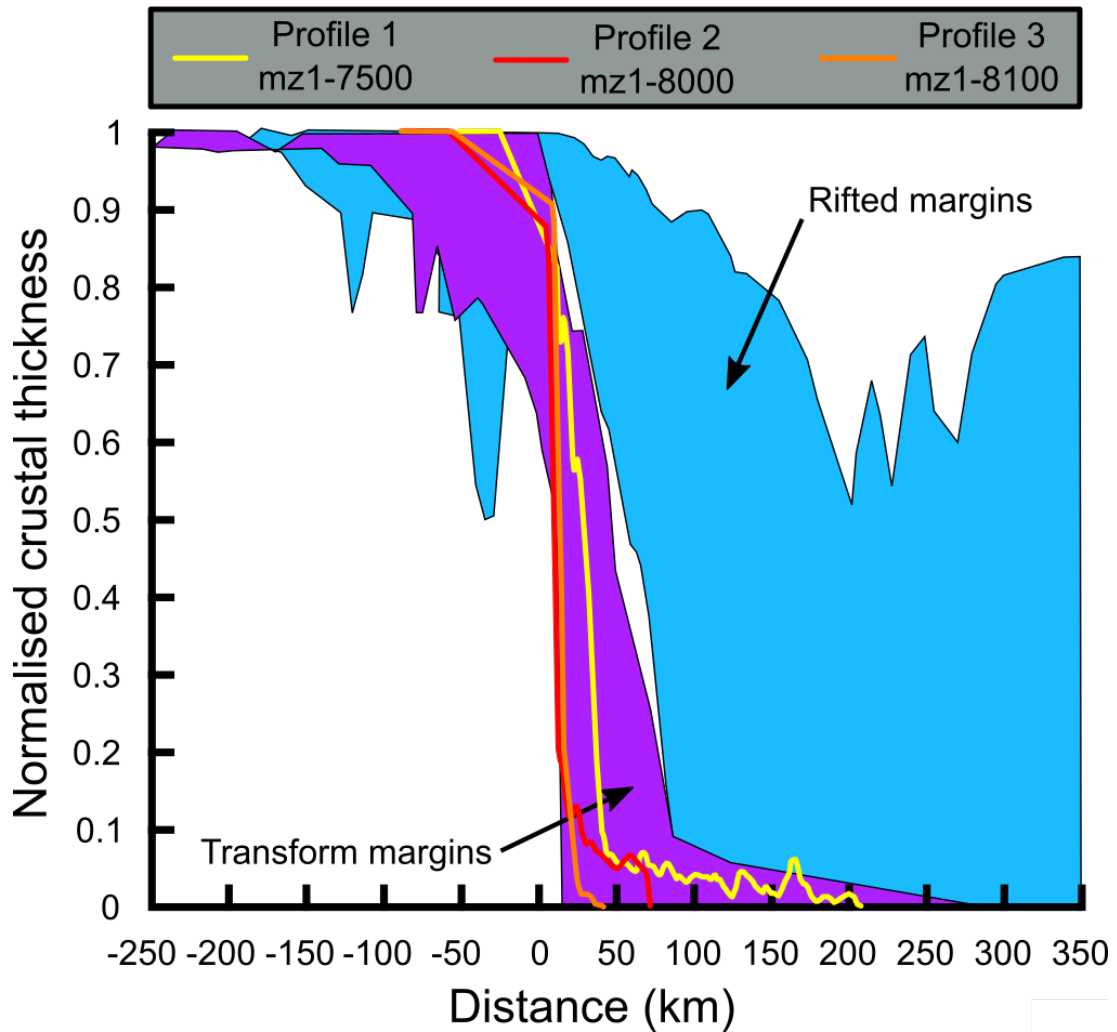
2442

2443

2444 **Figure 3.7.** RMSD fits of Moho location and angle configurations for gravity profiles 1-3 as
2445 determined from type 1 modelling. All profiles show a similar trend, with the majority of the
2446 preferred parameter space covering steeper Moho slopes. Initial models at 5° and 5 km
2447 intervals are followed by models at 1° and 1 km intervals around the best-fitting parameter
2448 space determined during 5° and 5 km modelling. The minimum RMSD combination for
2449 each profile is marked by a black star.

2450 **3.4.2.1.1. Comparison of crustal thickness profiles to a global compilation of**
2451 **margins**

2452 Using the best fit Moho parameters for the three lines we generate crustal thickness profiles
2453 across the margin for comparison to global compilations of margin profiles by Harry et al.,
2454 (2003) and Mercier de Lépinay et al., (2016) (Figure 3.8). All profiles fall firmly within the
2455 transform margin domain, with profiles 2 and 3 lying along its most extreme edge. These
2456 profiles are incompatible with observed profiles from rifted margins, and thus support an
2457 initial interpretation of the Rovuma Margin as a transform margin.



2459

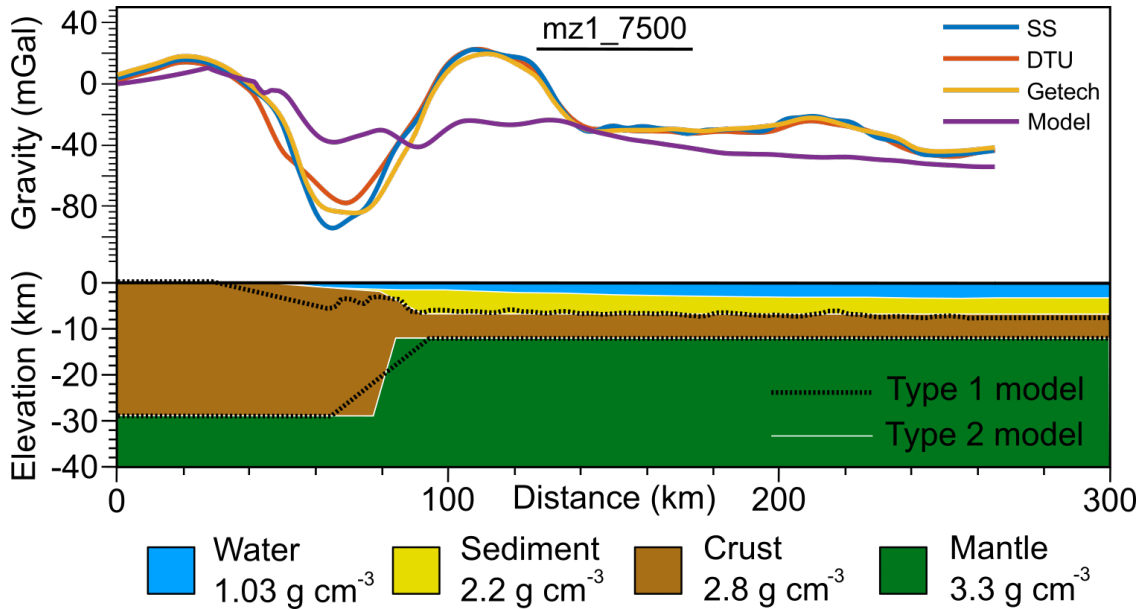
2460 **Figure 3.8.** Normalised crustal thickness profiles across transform (purple) and rifted (blue)
 2461 margins after Harry et al., (2003) and Mercier de Lépinay et al., (2016). Normalised crustal
 2462 thickness profiles derived from type 1 modelling of gravity profiles 1, 2, and 3 are overlain.
 2463 All profiles across the Rovuma margin lie within the transform margin domain.

2464 **3.4.2.2. Model type 2: Best-fit locations for average margin geometries and** 2465 **margin trend**

2466 We first test the search algorithm on profile 1, where it locates the bottom of the basement
 2467 slope just 3.5 km seaward of its location in seismic data, despite the very different
 2468 geometries of profile 1 and the average of profiles 2 and 3. The midpoint of the Moho slope
 2469 is also in good agreement with that derived from type 1 modelling (Figure 3.9), validating
 2470 the search algorithm's effectiveness. The resulting best fit gravity profile, however, differs
 2471 substantially from the gravity data. This is due to complexities in the margin's real geometry
 2472 not present in the tested average geometry. For the effectiveness of the model it is only
 2473 required that the RMSDs of all tested locations are similarly affected by such complexities.
 2474 Due to the simplicity of the input geometry this is to be expected and the only way to further

2475 remove the misfit between modelled and observed gravity profiles is to change the
 2476 geometries in the gravity model (which will be the focus of modelling type 3).

2477



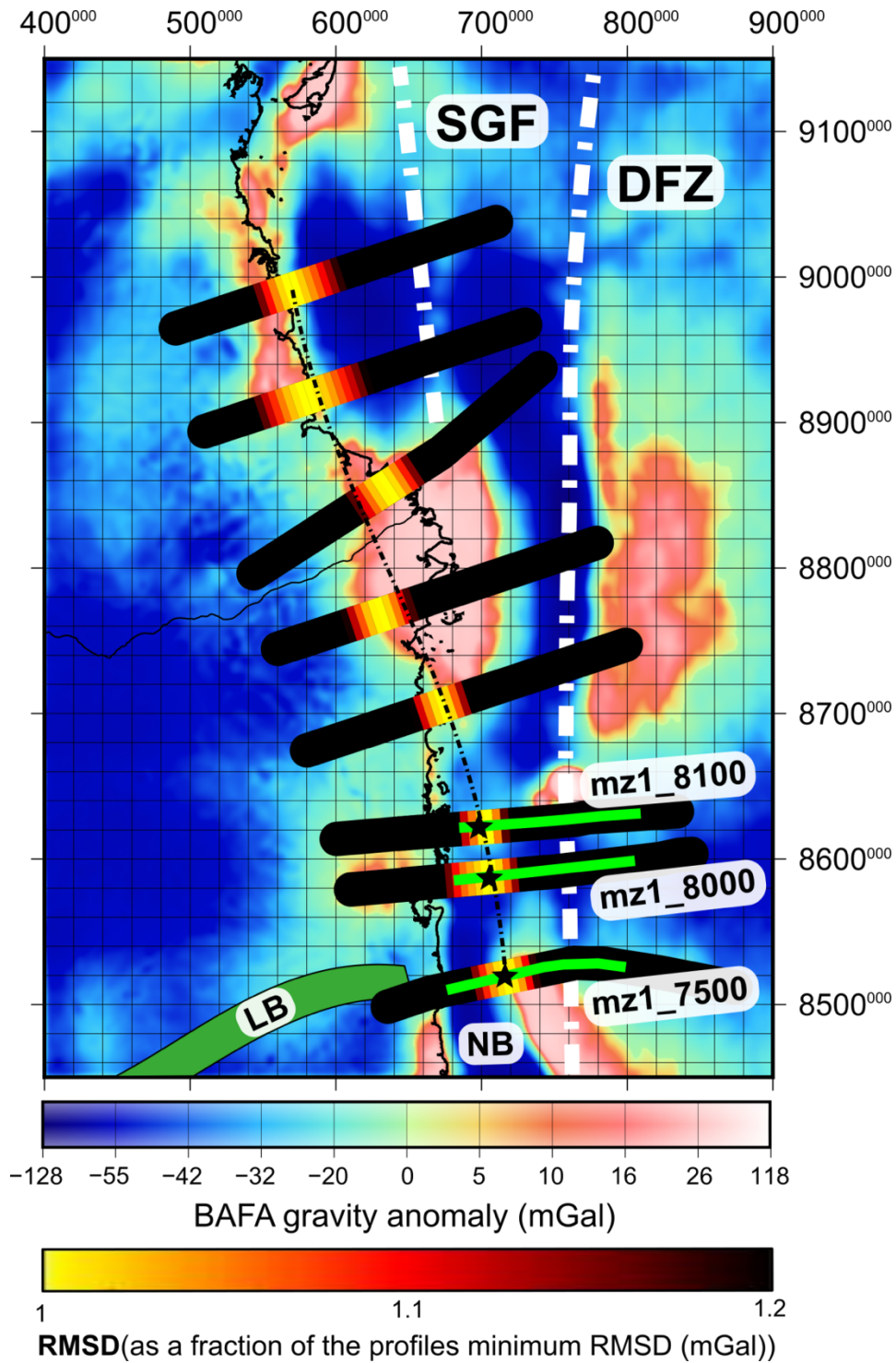
2478

2479 **Figure 3.9.** Calculated gravity profile (purple line) for the best fit location of the average
 2480 margin geometry along profile 1 as determined from type 2 modelling. Despite the
 2481 significant differences between the modelled average geometry and that determined from
 2482 seismic data and type 1 modelling, there is a good agreement of the resulting margin
 2483 locations. Misfits between the modelled gravity anomaly and data that result from
 2484 simplifications in the modelled average geometry derived from the type-1 modelling,
 2485 therefore, have not affected the model's ability to accurately locate the margin.

2486 Application of the methodology on all profiles consistently results in a margin location with
 2487 a sharp, single RMSD minimum (Figure 3.10), and defines a NNW-SSE trend of the margin.
 2488 There is no indication that the continental margin follows the DFZ, and north of profile 3 the
 2489 margin trends slightly more NW (at $\sim 160^\circ$) than farther south (172°). The margin generally
 2490 follows the trend of the basement outcrop on the western edge of the Rovuma Basin along
 2491 its length. Small deviations in best fit locations of the margin from the average trend, of up
 2492 to 25 km, may reflect complications in the margin structure and resulting shifts in the
 2493 location predicted by the model. They may also be due to real variations in the margin's
 2494 trend, and we note that the most significant deviation, across the border of Mozambique and
 2495 Tanzania, is in alignment with the major Sea Gap Fault, which runs \sim NNE-SSW through the
 2496 TCB and may be related. Nonetheless, reasonable RMSD fits of the margin (RMSD \leq
 2497 120% minimum RMSD) can be linked with a smooth curve through the margin, representing
 2498 the margin's general trend.

2499 Additional testing of the search algorithm's sensitivity to the input geometry is performed on
2500 all eight profiles. Steeper and shallower Moho slopes, of 87° and 47° , shift the predicted
2501 margin's location on average by 7.5 km landward and 8.5 km seaward, respectively.
2502 Seaward and landward shifts of the Moho slope location by 8 km relative to the basement
2503 slope shift the predicted margin's location by 16 km and 19 km, respectively. Whilst these
2504 variations are not insignificant, they are small compared to the length scale of the margin
2505 and do not affect the general interpretation of the margin's trend.

2506



2508

2509 **Figure 3.10.** Sandwell and Smith free-air gravity anomaly map overlain with RMSD fits of
 2510 the average margin geometry across the margin for profiles 1-8, as determined from type 2
 2511 modelling. RMSDs show a sharp convergence along each profile and define a NNW trend of
 2512 the margin, marked by the dashed black line. The best fit locations are in close agreement
 2513 with those determined from seismic data (black stars). The margin is significantly offset
 2514 from the DFZ, which runs N-S farther to the east. Coincident seismic lines are shown in
 2515 green. SGF; Sea Gap Fault.

2516 **3.4.2.3. Model type 3: Detailed 2D gravity modelling**

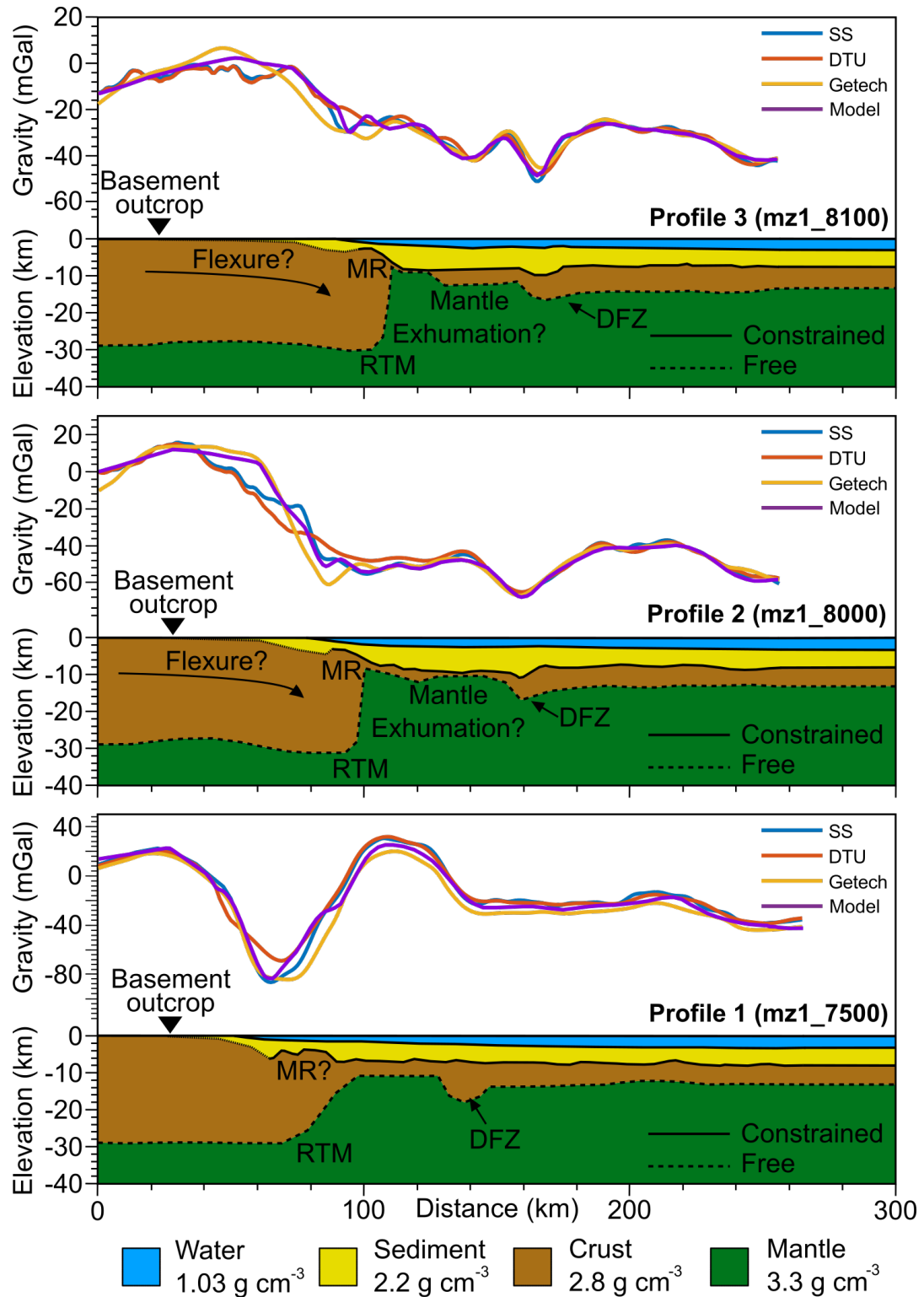
2517 We perform detailed 2D gravity modelling of profiles 1, 2, and 3, which have coincident
2518 seismic data to assist in constraining the seabed and top basement interfaces, using the
2519 software IX2D-GM (Figure 3.11). Using a layered sedimentary package and/or a density
2520 contrast between the upper and lower crusts has little impact on the final result, so we avoid
2521 unnecessary complication and use constant densities for the sediments and crust in our final
2522 models.

2523 The resulting density models from all three profiles are in good agreement with the
2524 preliminary results of type 1 modelling and, in addition, reveal many more aspects of the
2525 margin structure that help to determine the margin type. Moho slope angles and locations
2526 follow the same pattern as seen from type 1 modelling, with extremely steep slopes of up to
2527 82° and 83° for profiles 2 and 3 (mz1_8000 and mz1_8100), respectively, and a shallower
2528 Moho slope of up to 45° for the southernmost profile 1 (mz1_7500). The top of Moho slope
2529 locations can also be seen to lie slightly to the west of the bottom of the basement slope for
2530 profiles 2 and 3, and to the east for profile 1, similar to the type 1 models.

2531 Profiles 2 and 3 again show a great similarity in their detailed structure. Both profiles require
2532 a deepening of the basement interface within the unconstrained region to the west of the
2533 basement slope, defining a marginal ridge structure. These profiles also show a downward
2534 flexure of the margin which increases seawards. This flexure is not only defined by the
2535 Moho architecture, but also by the down-flexed top basement interface. This basement is
2536 covered by an extensive (up to 50 km wide) thin sedimentary layer directly adjacent to the
2537 basement outcrop, which has been deposited within accommodation space generated by the
2538 flexure. On both of these profiles the basement slope is immediately bounded seaward by
2539 extremely thin crust, just 0-3 km thick, or exhumed mantle. This thin crustal layer extends
2540 seawards until the DFZ, although on profile 3 a slight thickening of the crustal layer to a
2541 consistent 4 km also occurs before the DFZ. This interpreted crustal thickening to 4 km is,
2542 however, beneath the St Lazare volcanic edifice, and may therefore be influenced by
2543 intruded dense volcanic rocks above, which would require a low density crustal root to
2544 compensate them. Seaward of the DFZ, these two profiles show fairly consistent crustal
2545 thicknesses of ~6 km, likely representing oceanic crust of the WSB.

2546 Profile 1 does not exhibit the same margin flexure as seen to the north. However, the fault-
2547 bounded blocks of continental crust landward of the basement slope do define a basement
2548 high that could be related to the marginal ridge seen on profiles 1 and 2. Seaward of the
2549 basement slope, the crust is ~4 km thick, thicker than the 0-3 km of profiles 2 and 3, but still
2550 slightly thinner than the 5.2 km typical of the WSB (Coffin et al., 1986). On this

2551 southernmost profile, significant crustal thickening to ~11 km, with a width of ~ 20 km,
2552 defines the DFZ. A slightly thicker than normal oceanic crust also extends ~ 50 km seawards
2553 of the DFZ on this profile, before normal crustal thickness values for the WSB return.



2556 **Figure 3.11.** Detailed crustal structure as determined from type 3 modelling along profiles
 2557 1-3 with coincident seismic data. All profiles show possible marginal ridges adjacent to the
 2558 margin. Profile 1 displays a large thickening of the crust around the DFZ. Profiles 2 and 3
 2559 indicate possible exhumation of the mantle immediately adjacent to the steep basement slope
 2560 of the continental margin, which may have undergone downward flexure.

2561 **3.5. Discussion**

2562 3.5.1 The continental margin of northern Mozambique and southern Tanzania

2563 Following type 1 gravity modelling, we generated crustal thickness profiles across the
2564 continental margin for comparison with the global compilation of Mercier de Lépinay et al.,
2565 (2016; Harry et al., 2003). All three profiles fall well within the transform regime, and
2566 provide a robust and unbiased preliminary interpretation of the margin as a transform
2567 margin. Following this preliminary interpretation, we use additional observations from
2568 seismic reflection data and gravity modelling as an independent check.

2569 Moho slopes across the necking zone identified in profiles 2 and 3 lie between 65-82°, with
2570 the more detailed type 3 modelling preferring the upper end of this estimate. These slope
2571 angles are steeper than any recorded from rifted margins across the globe, and comparably
2572 steep Moho slopes have, to date, only been inferred across the Côte d'Ivoire-Ghana
2573 transform margin, where they are thought to be sub-vertical (Sage et al., 2000). Along
2574 profile 1, type 1 modelling predicts Moho slope angles of an ambiguous 28°, which may be
2575 found across necking zones at both magma-poor divergent margins and transform margins.
2576 This simple ramp-style Moho geometry is, however, a simplification of true necking zone
2577 geometries. More detailed type 3 modelling of this profile reveals Moho slope angles
2578 possibly reaching up to 43°, with an average Moho slope of 32° across the necking zone.
2579 Such Moho slope angles are near to the upper limit of those found at divergent margins
2580 (Figure 3.2) yet lie well within those observed at transform margins worldwide. This
2581 supports the interpretation of this section of the margin as having strong transform affinities.
2582 However, the large reduction in Moho slope angles along profile 1, compared to profiles 2
2583 and 3, may indicate a transition from transform to rifted margin at this location.

2584 Steep basement slopes accommodating a large step in basement depth, without evidence for
2585 normal faulting, are common features of transform margins (e.g. Lorenzo and Wessel, 1997;
2586 Sage et al., 2000). These are identified in all three margin-perpendicular seismic lines and
2587 dip seaward at between 18° and 35°, similar to the equivalent slopes of the Northern and
2588 Newfoundland transform margins, respectively (Greenroyd et al., 2008; Keen et al., 1990).

2589 Landward of the basement slopes identified in seismic data, marginal ridges, common
2590 features of transform margins (e.g. Bird, 2001), have also been identified. Along profile 1,
2591 this feature is represented by a continental horst block, as identified in seismic data (Figure
2592 3.5f), rising ~1.5 km above continentward-dipping half grabens, which bound it to the west.
2593 Along profiles 2 and 3, the tectonic structure of the marginal ridge is unknown as
2594 identification is only possible through gravity modelling. It can, however, be seen to rise a

2595 similar 1-2 km above the basement to the west of the ridge. Seaward flexure of the margin,
2596 seen along profiles 2 and 3, is also indicative of transform margins. It probably developed as
2597 the result of mechanical coupling across the transform margin and thermal subsidence of the
2598 oceanic domain following the cessation of transform tectonics (Mercier de Lépinay et al.,
2599 2016).

2600 Seaward of the marginal ridge and basement slope, thin crust and exhumed mantle is
2601 predicted by detailed 2D gravity modelling (type 3 models) and is supported by observations
2602 from seismic data. Line mz1_1030 shows the Moho outcropping at the surface in the vicinity
2603 of the base of the basement slope between profiles 2 and 3, and exhumed mantle is also
2604 consistent with the lack of Moho reflections adjacent to the basement slope along both of
2605 these profiles. Whilst exhumed mantle may be present at both magma-poor rifted margins
2606 and oceanic fracture zones (e.g. Doré and Lundin, 2015; Tucholke et al., 1998), the
2607 extremely narrow margin width of <50 km, predominantly lacking in rift structures, is
2608 incompatible with other observations of magma-poor rifted margins worldwide, supporting
2609 continent-ocean transform tectonics.

2610 These observations overwhelmingly support the interpretation of the continental margin of
2611 Northern Mozambique and Southern Tanzania as a transform margin. Type 2 modelling and
2612 observations from seismic data constrain the trend of this margin as $\sim 172^\circ$ to the south of
2613 profile 3 and $\sim 160^\circ$ to the north. The margin follows the onshore trend of the Rovuma
2614 Basin's basement outcrop, and the northern section of the transform margin runs onshore,
2615 where it is enveloped beneath the Rovuma Delta which has prograded into the oceanic
2616 domain, similarly to the Niger Delta (e.g. Dickson et al., 2016).

2617 In light of the margin's trend, and its newly recognised status, we term this margin the
2618 Rovuma Transform Margin (RTM) so that it may be distinguished from the DFZ. The DFZ
2619 is an ocean-ocean fracture zone that lies to the east of the RTM and is often coincident with
2620 the Davie Ridge. In the past, the DFZ and Davie Ridge have together been inferred to form
2621 the continental margin of the WSB (e.g. Coffin and Rabinowitz, 1987; Gaina et al., 2013).

2622 3.5.2 Changes in margin style across the Lurio Belt

2623 The RTM can be split into northern and southern sections, roughly bisected by the Lurio
2624 Belt, across which a change in margin geometry, trend, and adjacent ocean domain may
2625 occur. In the southern section, the Moho slope angle is much shallower, dipping at $\sim 30^\circ$
2626 compared to $\sim 70^\circ$ farther north. The vertical offset across the margin's basement slope is
2627 also reduced, here only ~ 2 km compared with ~ 5 km farther north. Furthermore,
2628 continentward-dipping normal faults, forming syn-rift half grabens, also appear to the south

2629 of the Lurio Belt, and may form part of the Angoche Basin. The northward extent of this
2630 basin, however, is not delineated by seismic reflection data.

2631 These observations suggest an increased extensional component may have been present
2632 during continental breakup south of the Lurio Belt, faulting and thinning this lithosphere
2633 prior to plate separation. This is consistent with the change in margin trend that occurs just
2634 to the north of the Lurio belt, in the vicinity of profiles 2 and 3. In this northern section of
2635 the margin, which trends at $\sim 160^\circ$, the occurrence of dextral strike-slip tectonics would lead
2636 to highly oblique plate separation along the margin to the south of the Lurio Belt, which
2637 trends at 172° .

2638 Therefore, during plate separation, strike-slip dominated transtensional rifting may have
2639 occurred along the Angoche Basin to the south of the Lurio Belt. This highly oblique
2640 southern section of the margin was likely linked to the RTM through horsetail splay faults,
2641 requiring normal faults along the edge of West Gondwana to dip towards East Gondwana.
2642 Subsequent isolation of these faults from West Gondwana during the onset of seafloor
2643 spreading and mid-ocean ridge propagation (e.g. Basile, 2015) in the Mozambique Basin
2644 may provide an explanation for the presence of continentward-dipping normal faults inboard
2645 of the margin slope in seismic line mz1_7500. In this case, this region of rifted continent
2646 between the transform margin and unrifted continental crust may represent a marginal
2647 plateau (e.g. Mercier de Lépinay et al., 2016). It should not be ruled out, however, that the
2648 continentward-dipping normal faults may have developed in response to volcanic rifted
2649 margin formation (e.g. Geoffroy, 2005) to the south within the Mozambique Basin (e.g.
2650 Mueller and Jokat, 2017).

2651 Differences between the northern RTM (profiles 2 and 3) and the Angoche Basin (southern
2652 RTM; profile 1) also occur within the oceanic domain. The northern section of the RTM is
2653 immediately abutted by exhumed mantle or extremely thin crust, whereas to the south
2654 adjacent to the Angoche Basin, gravity modelling predicts crust ~ 4 km thick. The northern
2655 region also shows less crustal thickening in the vicinity of the DFZ, around ~ 0.5 s TWTT
2656 thickening, compared to seaward of the Angoche Basin where a larger crustal thickening of
2657 ~ 1 s TWTT around the DFZ is accompanied by compressional thrusting of the crust on
2658 either side. It should be noted, however, that observations of compressional tectonic
2659 structures are less likely in the north due to the obscuring of basement structures by post
2660 breakup volcanics and recent faulting.

2661 Three scenarios may have led to exhumed mantle along the northern margin, yet 4 km thick
2662 crust adjacent to the continental margin along line 7500. Firstly, mantle exhumation may be
2663 local to profiles 2 and 3. This may be the case if oceanic core complexes have formed along

2664 the transform margin, as is common along ocean-ocean fracture zones. The scale of the
2665 exhumed mantle zone, ~50 km wide, is similar to core complexes found along fracture zones
2666 today.

2667 Secondly, mantle exhumation may be widespread along the northern portions of the
2668 transform margin. In this case, the onset of oceanic crustal production along the COTM may
2669 be directly linked with the change in margin trend around the Lurio Belt and corresponding
2670 thinning of the continental lithosphere which occurred during rifting to the south of this
2671 feature. In this case, the lithospheric thinning may have increased heatflow from the mantle
2672 along the Angoche Basin, reducing the amount of heat lost from the MOR as it passed along
2673 the COTM, thereby allowing greater mantle melting and production of a thin oceanic crust.

2674 Finally, it should be considered that the more intense manifestation of compressional
2675 tectonics to the south of the Lurio Belt may have acted to thicken any crust present. It may
2676 also have allowed the introduction of water into the mantle along thrust faults, resulting in
2677 its serpentinisation. The resulting reduction in mantle density at this location would thus
2678 result in the interpretation of a thicker crustal layer when using gravity methods. The top
2679 basement is, however, quite smooth and is not typical of exhumed mantle. Furthermore, the
2680 presence of a possible Moho reflection, although potentially also the manifestation of thrust
2681 faulting, also makes this final scenario is less likely.

2682 3.5.3 Possible plate tectonic models

2683 North of the Lurio Belt, the RTM appears to be void of extensional normal faults and forms
2684 a >400 km transform margin separating the highly oblique Angoche Basin from the TCB.
2685 This large offset between the TCB and Angoche Basin suggests that these rift segments did
2686 not overlap at their ends, and instead a transform fault would have been necessary to link the
2687 two from the onset of rifting (e.g. Basile, 2015). We therefore assume that the strike of this
2688 transform fault formed parallel to the initial extension direction between East and West
2689 Gondwana, supporting the initial SSE spreading direction proposed in Chapter 2, and, to a
2690 lesser extent, the NW-SE spreading directions of Klimke et al., (2017) and Reeves et al.,
2691 (2016). This continental transform fault would go on to form the Rovuma Transform Margin
2692 following the passing of the southern Morondava Basin (Madagascar) along it to the SSE.

2693 This initial phase of SSE drift, followed by a switch to a more southerly drift of East
2694 Gondwana, is also reflected in the outcrop pattern of the volcanic margin of Southern
2695 Mozambique. Here, the Lebombo Monocline shows a similar change in trend, which may in
2696 part have developed in response to the change in spreading direction at ~150 Ma.
2697 Furthermore, offshore of the Mozambique volcanic margin, a possible small microcontinent,

2698 the Biera High, has been identified (e.g. Mueller and Jokat, 2017). Several instances of
2699 microcontinent release have been documented during changes in plate motion, resulting
2700 from the build-up of transpressional stress along long-offset fracture zones (e.g. Schiffer et
2701 al., In Press; Whittaker et al., 2016). It is therefore possible that the cleaving of the Biera
2702 High microcontinent resulted from compressional stress build-up across left-stepping
2703 fracture zones during this clockwise plate rotation near the end of the Jurassic. Recent
2704 evidence for continental crust beneath the Comoros islands, through identification of Pan
2705 African age zircons (533 Ma) within xenoliths of the Grande Comore (e.g. Roach et al.,
2706 2017), points to the occurrence of a similar microcontinent-cleaving event in the WSB,
2707 possibly driven by the same plate rotation.

2708 The DFZ, which sits to the east of the Rovuma Transform Margin, also developed as the
2709 result of this plate rotation (e.g. Reeves et al., 2016; Chapter 2), and forms a major large-
2710 offset ocean-ocean fracture zone. The eastward offset of this structure from the RTM, and
2711 the presence of oceanic crust landward of this fracture zone within the TCB (e.g. Chapter 2;
2712 Sauter et al., 2016), preclude it from forming the COTM of the WSB. Loose-fit plate
2713 tectonic reconstructions, utilising the DFZ without an initial phase of SSE spreading, are
2714 therefore unable to predict the observations of this study.

2715 3.5.4 Transform margin development and impacts

2716 The RTM also crosscuts the pre-existing tectonic fabric of Gondwana (e.g. Reeves and de
2717 Wit, 2000; Windley et al., 1994) and whilst some Karoo-aged sedimentary deposits have
2718 been postulated to be present below parts of the Rovuma Basin (e.g. Salman and Abdula,
2719 1995), these are not exposed at the surface as they are along the Kenya, Tanzania, and
2720 Madagascar margins. Late Triassic to Early Jurassic sediments, drilled within the Mandawa
2721 Basin (northernmost Rovuma Basin; Hudson and Nicholas, 2014), are thought to have been
2722 deposited in response to the Jurassic breakup of East and West Gondwana, and the oldest
2723 succession within isolated early rift grabens along the Rovuma Basin were found to be
2724 Jurassic in age (Smelror et al., 2008). This suggests that, whilst isolated Karoo basins may
2725 have been present beforehand, the development of the RTM was largely not controlled by
2726 pre-existing structures and instead formed as a new tectonic feature in direct response to the
2727 Jurassic breakup of Gondwana.

2728 This new transform fault offset the volcanic Mozambique Basin (e.g. Leinweber et al., 2013)
2729 from the magma-poor Tanzania Coastal Basin (e.g. Chapter 2). Similar variations in
2730 magmatism between rift segments have been observed at other locations including: the Gulf
2731 of California (e.g. Lizarralde et al., 2007), the South Atlantic (e.g. Franke et al., 2007), and
2732 Central Afar (e.g. Stab et al., 2016). It is possible that a causal link between magmatism and

2733 margin segmentation exists. In the case of the Jurassic East Africa breakup, it may be
2734 postulated that the lack of lithospheric thinning along the RTM may have acted as a barrier
2735 to the lateral flow of anomalously hot mantle (postulated beneath the Mozambique basin due
2736 to the upwelling of the Bouvet mantle plume; e.g. Reeves, 2014) into the TCB, resulting in a
2737 lack of magmatism during the breakup of this basin.

2738 Following breakup and an initial phase of SSE spreading, the change in plate motion near
2739 the end of the Jurassic would have resulted in transpression along the RTM. It is possible
2740 that these transpressional tectonics resulted in the development of the marginal ridge along
2741 the RTM inferred from gravity modelling. Such transpressional uplift has been found to
2742 control the development of marginal ridges elsewhere, such as at the Ivory Coast-Ghana
2743 transform margin (Huguen et al., 2001). Recent studies have also shown that a previously
2744 unexpected amount of along-strike variation in transform margin geometry may be common
2745 (Mercier de Lépinay et al., 2016). The basement slope angles and vertical offset across the
2746 margin seen on profiles 2 and 3, change from 18° and 5 km to 24° and 6 km, respectively,
2747 over a distance of ~50 km. Misfits between modelled gravity profiles and gravity data during
2748 type 2 modelling, which uses an average margin geometry, also suggest that variations in the
2749 margin geometry continue along strike, supporting the observations of Mercier de Lépinay et
2750 al., (2016). Such variations likely arise from small deviations in the margin trend along
2751 strike, leading to increased transpression and transtension, or from inherited features from
2752 the continental crust (e.g. Mercier de Lépinay et al., 2016). The seaward flexure of the
2753 margin supports suggestions that mechanical coupling between the continental and oceanic
2754 domains occurred post-transform motions. At this point, thermal subsidence of the oceanic
2755 domain would have induced the observed downward flexure of the continent adjacent to the
2756 margin, as seen along other COTMs (e.g. Lorenzo and Wessel, 1997).

2757 **3.6. Conclusions**

2758 Seismic reflection data reveal a newly identified COTM in the southern Rovuma Basin. The
2759 margin lies landward of the DFZ, which has previously been interpreted as the COTM of the
2760 WSB. We term this newly identified COTM the ‘Rovuma Transform Margin’ (RTM), to
2761 distinguish it from the DFZ.

2762 The presence of a marginal ridge: steep (18° to 35°) basement slopes with large vertical
2763 offsets of up to 6 km, lacking evidence for internal rift structures; rapid crustal thinning from
2764 ~28 km to 2 km over a distances of less than 20 km; seaward flexure of the margin;
2765 extremely steep Moho slopes across the necking zone of up to 83°; and presence of exhumed
2766 mantle and thin oceanic crust adjacent to the margin support its interpretation as a transform

2767 margin. Furthermore, comparison of crustal thickness profiles across the margin to the
2768 global margin compilations of Mercier de Lépinay et al., (2016) confirms the transform
2769 nature of this continental margin.

2770 Inverse gravity modelling shows that the RTM runs NNW-SSE along the Rovuma Basin,
2771 supporting an origin for Madagascar within the Tanzania Coastal Basin and tight-fit
2772 reconstructions of Gondwana fragments.

2773 A slight change in the trend of the margin from 160° in the north to 172° in the south occurs
2774 approximately at the Lurio Belt. The slight bend in the margin controlled a change from pure
2775 transform tectonics to the north of the Lurio belt, to the highly oblique opening of the
2776 Angoche Basin to the south. The oblique nature of the margin is reflected by shallower
2777 Moho slopes across the necking zone and the appearance of half grabens in continental crust.

2778 3.7. References

- 2779 Barton, P.J., Owen, T.R.E., White, R.S., 1990. The deep structure of the east Oman continental
2780 margin: preliminary results and interpretation. *Tectonophysics* 173, 319–331. doi:10.1016/0040-
2781 1951(90)90227-Y
- 2782 Basile, C., 2015. Transform continental margins - part 1: Concepts and models. *Tectonophysics* 661,
2783 1–10. doi:10.1016/j.tecto.2015.08.034
- 2784 Basile, C., Braun, J., 2016. The initiation of pull-apart basins and transform continental margins:
2785 Results from numerical experiments of kinematic partitioning in divergent settings. *Terra Nov.* 28,
2786 120–127. doi:10.1111/ter.12198
- 2787 Bird, D., 2001. Shear margins: Continent-ocean transform and fracture zone boundaries. *Lead. Edge*
2788 20, 150. doi:10.1190/1.1438894
- 2789 Coffin, M.F., Rabinowitz, P.D., 1987. Reconstruction of Madagascar and Africa: Evidence From the
2790 Davie Fracture Zone and Western Somali Basin 92, 9385–9406.
- 2791 Coffin, M.F., Rabinowitz, P.D., Houtz, R.E., 1986. Crustal structure in the Western Somali Basin.
2792 *Geophys. J. R. Astron. Soc.* 331–369.
- 2793 Dickson, W., Schiefelbein, C.F., Odegard, M.E., Zumberge, J.E., 2016. Petroleum systems
2794 asymmetry across the South Atlantic Equatorial Margins. *Geol. Soc. London, Spec. Publ.* 431,
2795 219–233. doi:10.1144/SP431.13
- 2796 Doré, T., Lundin, E., 2015. Hyperextended continental margins — Knowns and unknowns. *Geol.* 43,
2797 95–96. doi:10.1016/0040
- 2798 Ebinger, C., 2005. Continental break-up: the East African perspective. *Astron. Geophys.* 46, 2.16-
2799 2.21. doi:10.1111/j.1468-4004.2005.46216.x
- 2800 Edwards, R.A., Whitmarsh, R.B., Scrutton, R.A., 1997. The crustal structure across the transform
2801 continental margin off Ghana, eastern equatorial Atlantic. *J. Geophys. Res.* 102, 747–772.
2802 doi:10.1029/96JB02098
- 2803 Emmel, B., Kumar, R., Ueda, K., Jacobs, J., Daszinnies, M.C., Thomas, R.J., Matola, R., 2011.
2804 Thermochronological history of an orogen-passive margin system: An example from northern
2805 Mozambique. *Tectonics* 30. doi:10.1029/2010TC002714
- 2806 Fairhead, J.D., Williams, S.E., Fletcher, K.M.U., Green, C.M., Vincent, K., 2009. Trident - A New
2807 Satellite Gravity Model for the Oceans. 71st EAGE Conf. Exhib. Amsterdam 1–5.
- 2808 Franke, D., Jokat, W., Ladage, S., Stollhofen, H., Klimke, J., Lutz, R., Mahanjane, E.S., Ehrhardt, A.,
2809 Schreckenberger, B., 2015. The offshore East African Rift System: Structural framework at the
2810 toe of a juvenile rift. *Tectonics* 34, 2086–2104. doi:10.1002/2015TC003922
- 2811 Franke, D., Neben, S., Ladage, S., Schreckenberger, B., Hinz, K., 2007. Margin segmentation and
2812 volcano-tectonic architecture along the volcanic margin off Argentina/Uruguay, South Atlantic.
2813 *Mar. Geol.* 244, 46–67. doi:10.1016/j.margeo.2007.06.009

2814 Gaina, C., Torsvik, T.H., van Hinsbergen, D.J.J., Medvedev, S., Werner, S.C., Labails, C., 2013. The
2815 African plate: A history of oceanic crust accretion and subduction since the Jurassic.
2816 *Tectonophysics* 604, 4–25. doi:10.1016/j.tecto.2013.05.037
2817 Geiger, M., Clark, D.N., Mette, W., 2004. Reappraisal of the timing of the breakup of Gondwana
2818 based on sedimentological and seismic evidence from the Morondava Basin, Madagascar. *J.*
2819 *African Earth Sci.* 38, 363–381. doi:10.1016/j.jafrearsci.2004.02.003
2820 Geoffroy, L., 2005. Volcanic passive margins. *Comptes Rendus - Geosci.* 337, 1395–1408.
2821 doi:10.1016/j.crte.2005.10.006
2822 Globig, J., Fernández, M., Torne, M., Vergés, J., Robert, A., Faccenna, C., 2016. New insights into
2823 the crust and lithospheric mantle structure of Africa from elevation, geoid, and thermal analysis. *J.*
2824 *Geophys. Res. Solid Earth* 121, 5389–5424. doi:10.1002/2016JB012972
2825 Greenroyd, C.J., Peirce, C., Rodger, M., Watts, A.B., Hobbs, R.W., 2008. Demerara Plateau - The
2826 structure and evolution of a transform passive margin. *Geophys. J. Int.* 172, 549–564.
2827 doi:10.1111/j.1365-246X.2007.03662.x
2828 Harry, D.L., Londono, J., Huerta, A., 2003. Early Paleozoic transform-margin structure beneath the
2829 Mississippi coastal plain, southeast United States. *Geology* 31, 969–972. doi:10.1130/G19787.1
2830 Hudson, W.E., Nicholas, C.J., 2014. The Pindirolu Group (Triassic to Early Jurassic Mandawa Basin,
2831 southern coastal Tanzania): Definition, palaeoenvironment, and stratigraphy. *J. African Earth Sci.*
2832 92, 55–67. doi:10.1016/j.jafrearsci.2014.01.005
2833 Huguen, C., Guiraud, M., Benkhelil, J., Mascle, J., 2001. Synlithification deformation processes of
2834 the cretaceous sediments of the ivory coast-ghana transform margin: A way to detail the margin
2835 history. *Tectonics* 20, 959–975. doi:10.1029/2001TC900015
2836 Keen, C.E., Kay, W.A., Roest, W.R., 1990. Crustal anatomy of a transform continental margin.
2837 *Tectonophysics* 173. doi:10.1016/0040-1951(90)90244-3
2838 Klimke, J., Franke, D., Mahanjane, E.S., Leitchenkov, G., 2017. Tie-points for Gondwana
2839 reconstructions from a structural interpretation of the Mozambique Basin, East Africa, and the
2840 Riiser-Larsen Sea, Antarctica. *Solid Earth Discuss.* 1–28.
2841 Leinweber, V.T., Klingelhoefer, F., Neben, S., Reichert, C., Aslanian, D., Matias, L., Heyde, I.,
2842 Schreckenberger, B., Jokat, W., 2013. The crustal structure of the Central Mozambique
2843 continental margin - Wide-angle seismic, gravity and magnetic study in the Mozambique Channel,
2844 Eastern Africa. *Tectonophysics* 599, 170–196. doi:10.1016/j.tecto.2013.04.015
2845 Lizarralde, D., Axen, G.J., Brown, H.E., Fletcher, J.M., González-Fernández, A., Harding, A.J.,
2846 Holbrook, W.S., Kent, G.M., Paramo, P., Sutherland, F., Umhoefer, P.J., 2007. Variation in styles
2847 of rifting in the Gulf of California. *Nature* 448, 466–469. doi:10.1038/nature06035
2848 Lorenzo, J.M., Wessel, P., 1997. Flexure across a continent-ocean fracture zone: the northern
2849 Falkland/Malvinas Plateau, South Atlantic. *Geo-Marine Lett.* 17, 110–118.
2850 doi:10.1007/s003670050015
2851 Mahanjane, E.S., 2014. The Davie Fracture Zone and adjacent basins in the offshore Mozambique
2852 Margin - A new insights for the hydrocarbon potential. *Mar. Pet. Geol.* 57, 561–571.
2853 doi:10.1016/j.marpetgeo.2014.06.015
2854 Mercier de Lépinay, M., Loncke, L., Basile, C., Roest, W.R., Patriat, M., Maillard, A., De Clarens, P.,
2855 2016. Transform continental margins – Part 2: A worldwide review. *Tectonophysics* 693, 96–115.
2856 doi:10.1016/j.tecto.2016.05.038
2857 Mueller, C.O., Jokat, W., 2017. Geophysical evidence for the crustal variation and distribution of
2858 magmatism along the central coast of Mozambique. *Tectonophysics* 712–713, 684–703.
2859 doi:10.1016/j.tecto.2017.06.007
2860 Parsiegl, N., Stankiewicz, J., Gohl, K., Ryberg, T., Uenzelmann-Neben, G., 2009. Southern African
2861 continental margin: Dynamic processes of a transform margin. *Geochemistry, Geophys.*
2862 *Geosystems* 10. doi:10.1029/2008GC002196
2863 Pavlis, N.K., Holmes, S.A., Kenyon, S.C., Factor, J.K., 2012. The development and evaluation of the
2864 earth gravitational model 2008 (EGM2008). *J. Geophys. Res. Solid Earth* 117, 1–38.
2865 doi:10.1002/jgrb.50167,2013
2866 Phethean, J.J.J., Kalnins, L.M., van Hunen, J., Biffi, P.G., Davies, R.J., McCaffrey, K.J.W., 2016.
2867 Madagascar's escape from Africa: A high-resolution plate reconstruction for the Western Somali
2868 Basin and implications for supercontinent dispersal. *Geochemistry, Geophys. Geosystems* 17,
2869 5036–5055. doi:10.1002/2016GC006624
2870 Rabinowitz, P.D., Coffin, M.F., Falvey, D., 1983. The separation of Madagascar and Africa. *Science*
2871 (80-). 220, 67–69. doi:10.1126/science.220.4592.67
2872 Reeves, C., 2014. The position of Madagascar within Gondwana and its movements during
2873 Gondwana dispersal. *J. African Earth Sci.* 94, 45–57. doi:10.1016/j.jafrearsci.2013.07.011

2874 Reeves, C., de Wit, M.J., 2000. Making ends meet-retracing the transformations of the Indian Ocean
2875 and reconnecting continental shear zones. *Terra* 12, 272–280.

2876 Reeves, C. V, Teasdale, J.P., Mahanjane, E.S., 2016. Insight into the Eastern Margin of Africa from a
2877 new tectonic model of the Indian Ocean. *Geol. Soc. London, Spec. Publ.* 431, 1–24.
2878 doi:10.1144/SP431.12

2879 Reston, T.J., 2009. The structure, evolution and symmetry of the magma-poor rifted margins of the
2880 North and Central Atlantic: A synthesis. *Tectonophysics* 468, 6–27.
2881 doi:10.1016/j.tecto.2008.09.002

2882 Roach, P., Milsom, J., Toland, C., Matchette-Downes, C., Budden, C., Riaroh, D., Houmadi, N.,
2883 2017. New Evidence Supports Presence of Continental Crust beneath the Comoros. PESGB, 16th
2884 African E&P Conf. London.

2885 Sage, F., Basile, C., Mascle, J., Pontoise, B., Whitmarsh, R.B., 2000. Crustal structure of the
2886 continent-ocean transition off the Cote d'Ivoire-Ghana transform margin: Implications for thermal
2887 exchanges across the palaeotransform boundary. *Geophys. J. Int.* 143, 662–678.
2888 doi:10.1046/j.1365-246X.2000.00276.x

2889 Salman, G., Abdula, I., 1995. Development of the Mozambique and Ruvuma sedimentary basins,
2890 offshore Mozambique. *Sediment. Geol.* 96, 7–41. doi:10.1016/0037-0738(95)00125-R

2891 Sandwell, D.T., Muller, R.D., Smith, W.H.F., Garcia, E., Francis, R., 2014. New global marine
2892 gravity model from CryoSat-2 and Jason-1 reveals buried tectonic structure. *Science* (80-). 346,
2893 65–67. doi:10.1126/science.1258213

2894 Sauter, D., Unternehr, P., Manatschal, G., Tugend, J., Cannat, M., Le Quellec, P., Kuszniir, N.,
2895 Munsch, M., Leroy, S., de Lepinay, J.M., Granath, J.W., Horn, B.W., 2016. Evidence for magma
2896 entrapment below oceanic crust from deep seismic reflections in the Western Somali Basin.
2897 *Geology* 44, 407–410. doi:10.1130/G37747.1

2898 Schiffer, C., Peace, A., Phethean, J., Gernigon, L., McCaffrey, K.J.W., Petersen, Kenni, D., Foulger,
2899 G., n.d. The Jan Mayen Microplate Complex and the Wilson Cycle. *Geol. Soc. London, Spec.*
2900 *Publ.*

2901 Smelror, M., Key, R.M., Smith, R. a, Njange, F., 2008. Late Jurassic And Cretaceous
2902 Palynostratigraphy Of The Onshore Rovuma Basin, Northern Mozambique. *Palynology* 32, 63–
2903 76. doi:10.2113/gspalynol.32.1.63

2904 Stab, M., Bellahsen, N., Pik, R., Quidelleur, X., Ayalew, D., Leroy, S., 2016. Modes of rifting in
2905 magma-rich settings: Tectono-magmatic evolution of Central Afar. *Tectonics* 35, 2–38.
2906 doi:10.1002/2015TC003893

2907 Stenseng, L., Piccioni, G., Anderson, O.B., Knudsen, P., 2015. Sea surface retracking and
2908 classification of CryoSat-2 altimetry observations in the Arctic Ocean. *Am. Geophys. Union, Fall*
2909 *Meet.*

2910 Todd, B.J., Reid, I., 1989. The continent - ocean boundary south of Flemish Cap: constraints from
2911 seismic refraction and gravity. *Can. J. Earth Sci.* 26, 1392–1407.

2912 Todd, B.J., Reid, I., Keen, C.E., 1988. Crustal structure across the Southwest Newfoundland
2913 Transform Margin. *Can. J. Earth Sci.* 25, 744–759. doi:10.1139/e88-070

2914 Tucholke, B.E., Lin, J., Kleinrock, M.C., 1998. Megamullions and mullion structure defining oceanic
2915 metamorphic core complexes on the Mid-Atlantic Ridge. *J. Geophys. Res. Solid Earth* 103, 9857–
2916 9866. doi:10.1029/98JB00167

2917 Tugend, J., Manatschal, G., Kuszniir, N.J., Masini, E., 2015. Characterizing and identifying structural
2918 domains at rifted continental margins: application to the Bay of Biscay margins and its Western
2919 Pyrenean fossil remnants. *Geol. Soc. London, Spec. Publ.* 413, 171–203. doi:10.1144/SP413.3

2920 Van Avendonk, H.J.A., Lavier, L.L., Shillington, D.J., Manatschal, G., 2009. Extension of continental
2921 crust at the margin of the eastern Grand Banks, Newfoundland. *Tectonophysics* 468, 131–148.
2922 doi:10.1016/j.tecto.2008.05.030

2923 Wessel, P., Smith, W.H.F., Scharroo, R., Luis, J., Wobbe, F., 2013. Generic Mapping Tools:
2924 Improved Version Released. *Eos, Trans. Am. Geophys. Union* 94, 409–410.
2925 doi:10.1002/2013EO450001

2926 Whittaker, J.M., Williams, S.E., Halpin, J.A., Wild, T.J., Stilwell, J.D., Jourdan, F., Daczko, N.R.,
2927 2016. Eastern Indian Ocean microcontinent formation driven by plate motion changes. *Earth*
2928 *Planet. Sci. Lett.* 454, 203–212. doi:10.1016/j.epsl.2016.09.019

2929 Windley, B.F., Razafiniparany, A., Razakamanana, T., Ackermant, D., 1994. Tectonic framework of
2930 the Precambrian of Madagascar and its Gondwana connections: a review and reappraisal. *Geol.*
2931 *Rundschau* 83, 642–659. doi:10.1007/BF00194168

2932

2933 **3.8. Supplementary material**

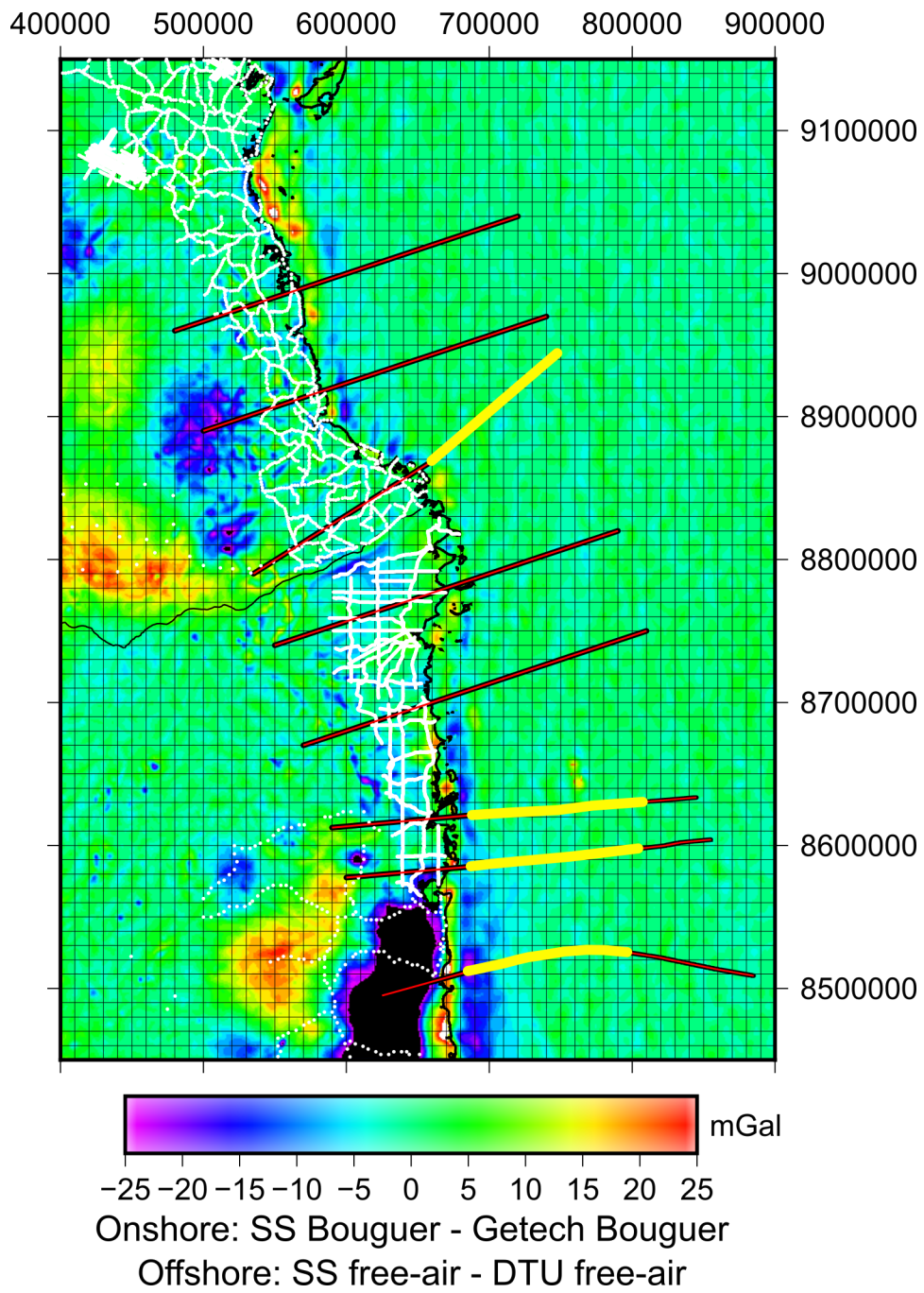
2934 3.8.1. Misfit between gravity datasets

2935 Onshore, the difference between the bouguer anomaly generated from the World Gravity
2936 Map (WGM; used for the onshore SS and DTU anomalies) and Getech's Trident bouguer
2937 anomaly allows for an assessment of the data uncertainty (Figure S3.1). Gravity
2938 measurements included within the Getech Trident dataset are shown as white dots. Gravity
2939 profiles for 2D modelling are located to avoid areas of significant misfit between the
2940 datasets where possible. The largest disparity between the anomalies occurs onshore of the
2941 southern Rovuma Basin (500000-660000, 8450000-8620000). Here, the misfit exceeds 25
2942 mGal over a distance of +100 km. The extent of this misfit coincides with a proprietary
2943 gravity survey included only within the Trident dataset and is therefore likely caused by this
2944 additional data. Therefore, where profile 1 cannot avoid the region of large disagreement
2945 between datasets, Getech data is used to replace data from the SS and DTU bouguer
2946 anomalies.

2947 Offshore, comparison of the SS and DTU free-air anomalies is shown. Generally, misfits are
2948 concentrated in regions of shallow water along the coastline and are smaller than in the
2949 onshore regions. Nonetheless, where possible, profiles are located to avoid regions of larger
2950 disagreement.

2951

2952

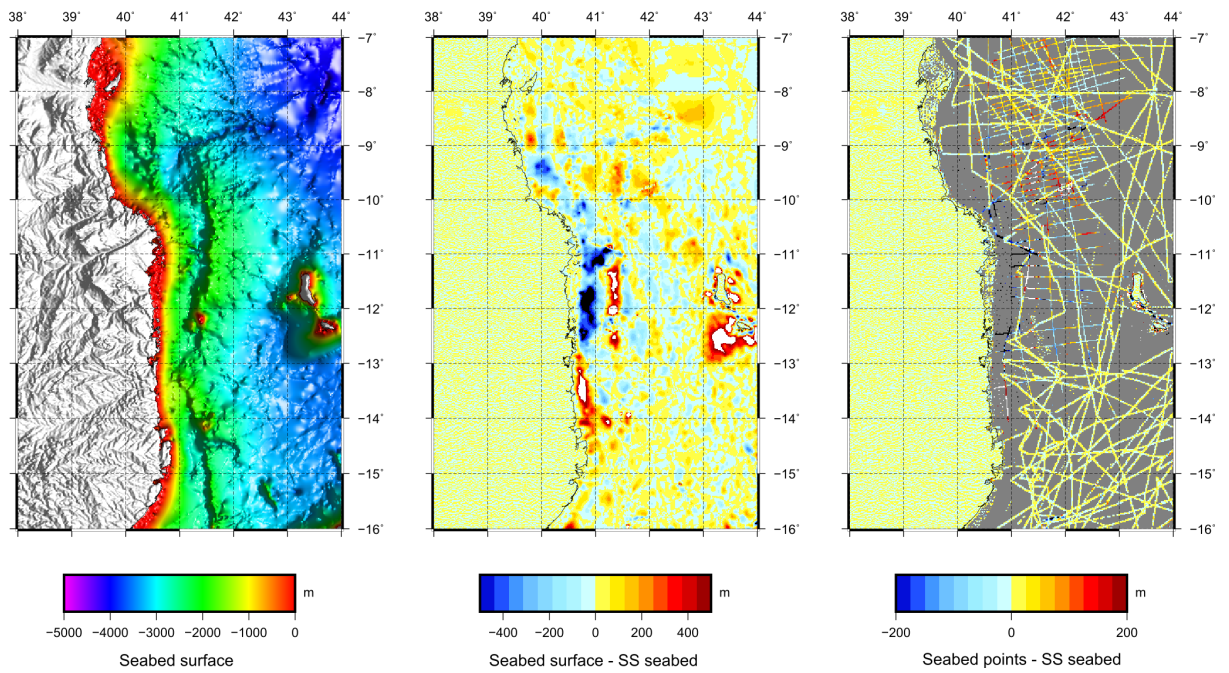


2953

2954 **Figure S3.1.** Comparison of different gravity datasets

2955 3.8.2. Examples of seabed surfaces generated using alternative filter cut-off
 2956 wavelengths
 2957

No wavelength replacement

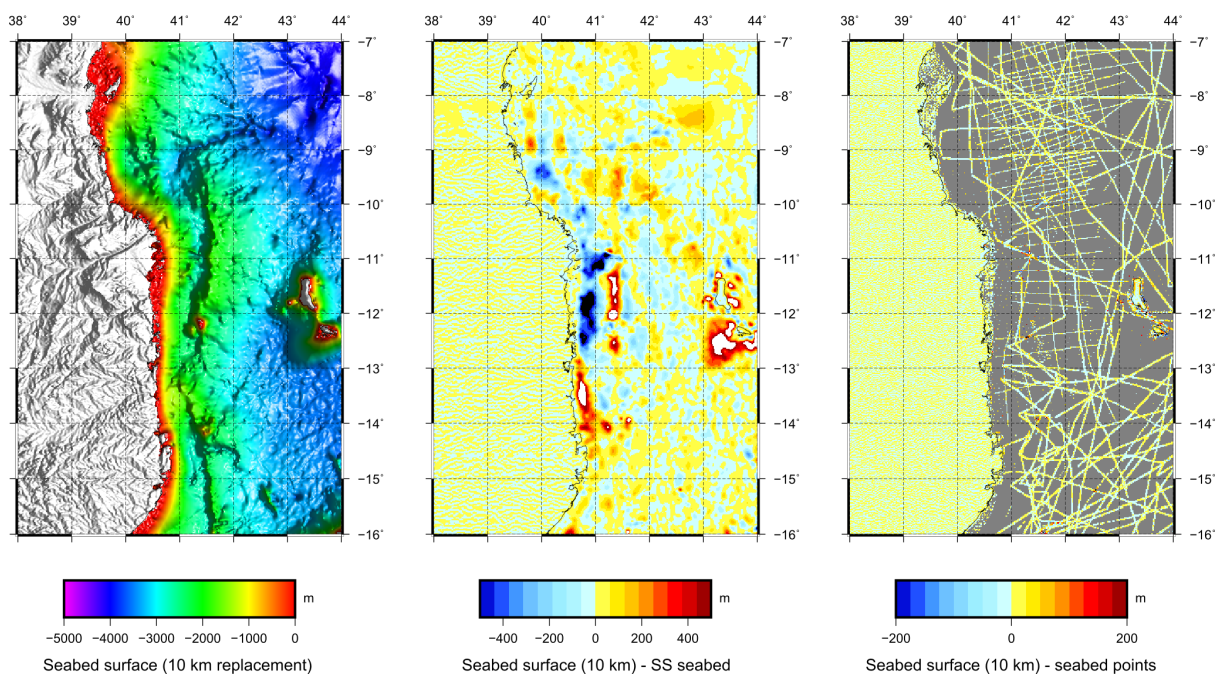


2958

2959 **Figure S3.2.** Seabed surface without short wavelength replacement. N.B. The panel on the
 2960 right of this figure is not comparable with those in Figures S3.3-5.

2961

Replace < 10 km wavelengths

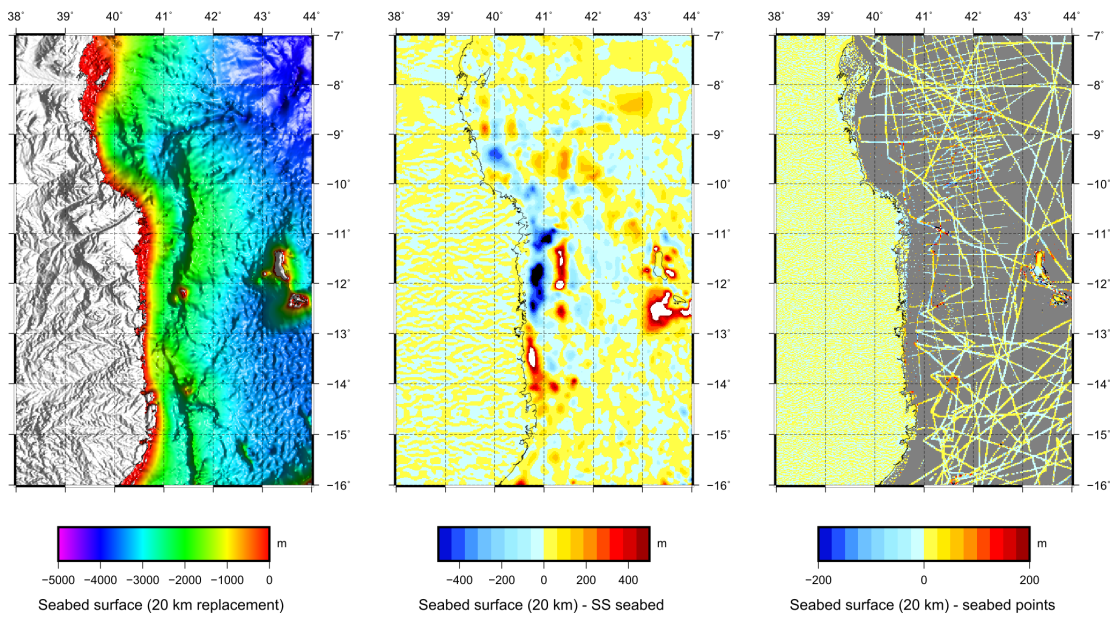


2962

2963 **Figure S3.3.** Seabed surface with replacement of wavelengths <10 km.

2964

Replace < 20 km wavelengths



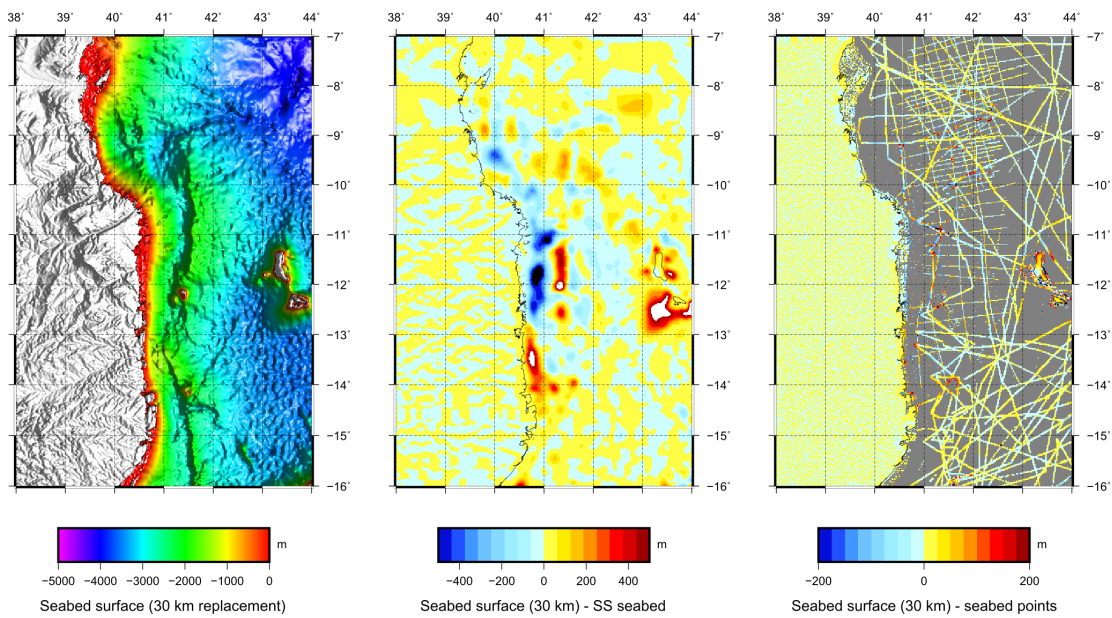
2965

2966 **Figure S3.4.** Seabed surface with replacement of wavelengths <20 km.

2967

2968

Replace < 30 km wavelengths



2969

2970 **Figure S3.5.** Seabed surface with replacement of wavelengths <30 km.

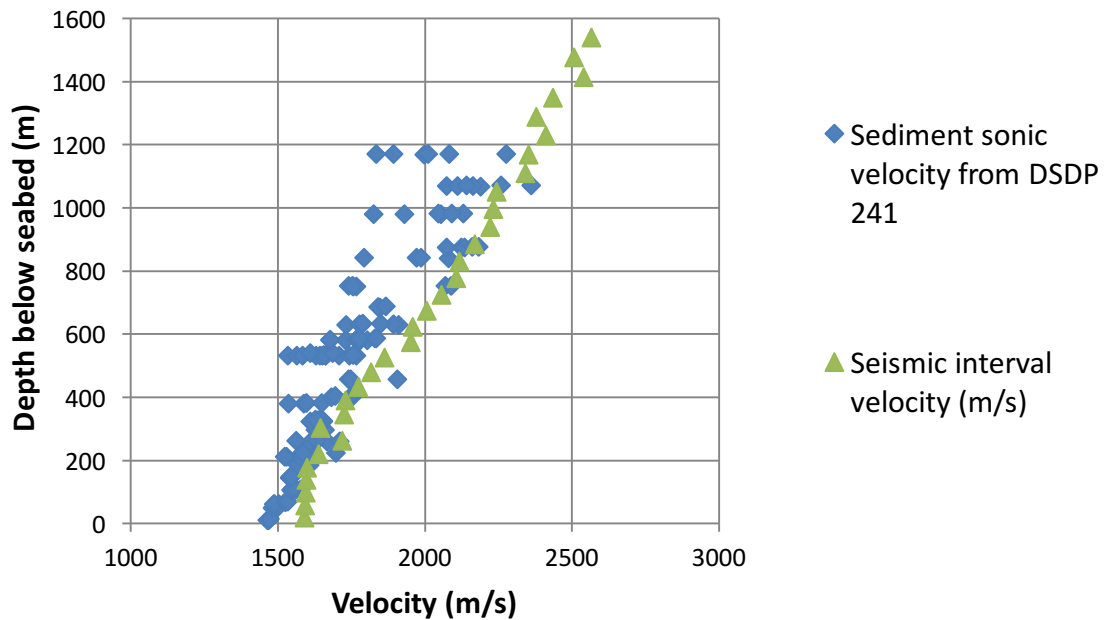
2971

2972 3.8.3. Deriving an average sediment density for the WSB for use in 2D gravity
2973 models

2974 To constrain the density of the sediment layer we use coincident data from the DSDP 241
2975 borehole and the 84v multichannel seismic reflection line shot during the R/V Vema leg
2976 3618, providing a chance to quality-check derived seismic velocities and densities. Seismic
2977 velocities derived during post stack migration processing of line 84v envelope the velocities
2978 measured at DSDP 241 (Figure S3.6).

2979

VEMA 3618 and DSDP 241 velocities



2980

2981 **Figure S3.6.** Measured and seismic-derived sediment velocities from DSDP 241.

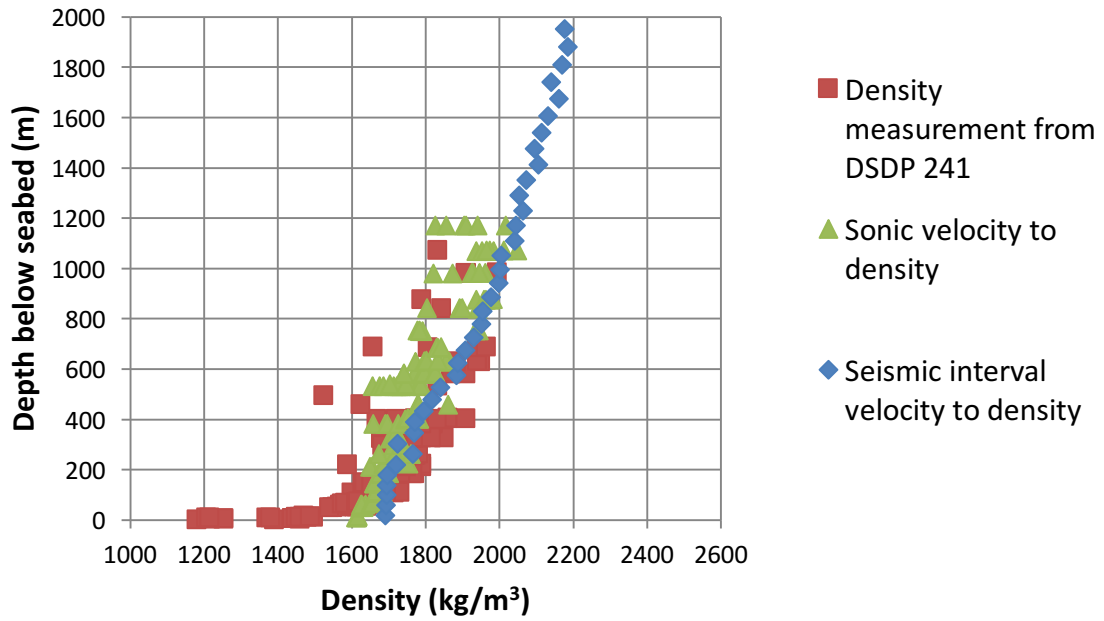
2982

2983 We use the Nafe-Drake relationship between velocity and density to convert the seismic
2984 velocities (Figure S3.7) as it provides a superior fit to density data derived at DSDP 241 than
2985 Gardner's relationship.

2986

2987

VEMA 3618 and DSDP 241 densities



2988

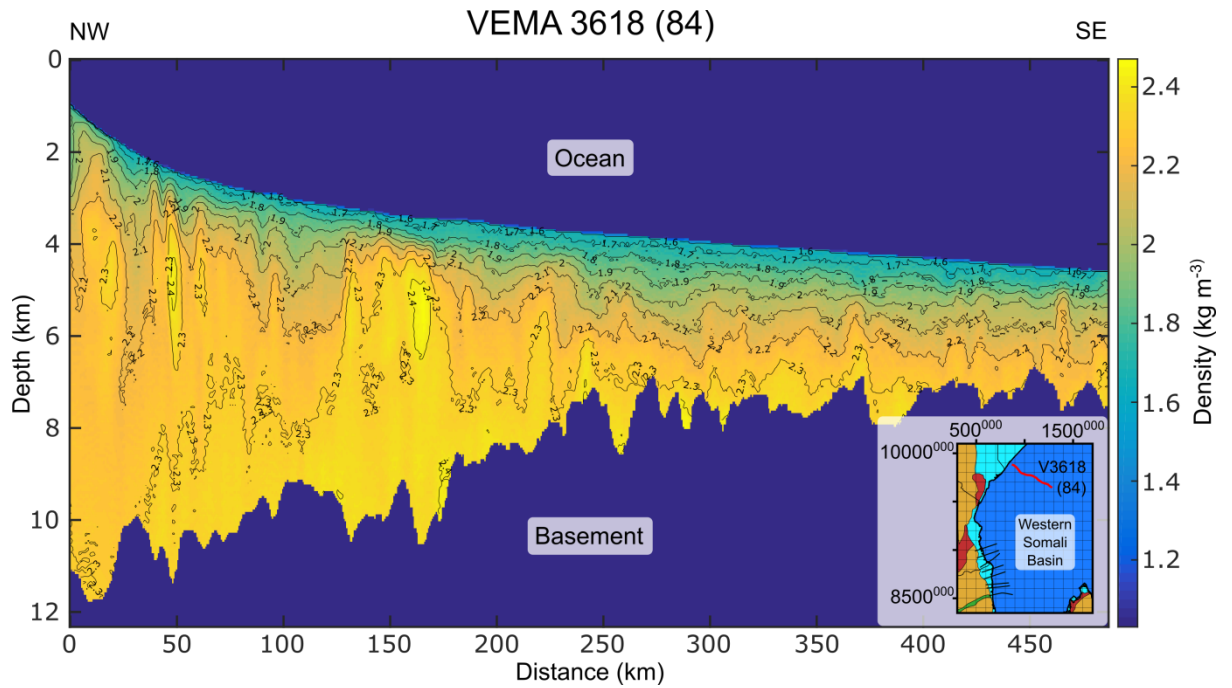
2989 **Figure S3.7.** Measured and seismic-derived sediment densities at DSDP 241.

2990

2991 As the VEMA 3618 (84) line has similar sediment thicknesses to the ION PSDM lines used
2992 for gravity modelling, average sediment densities are calculated between the seabed and top
2993 basement using the entirety of the line (Figure S3.8). Densities range between 1.62 and 2.38
2994 g cm^{-3} , with a mean value of $\sim 2.2 \text{ g cm}^{-3}$.

2995

2996



2997

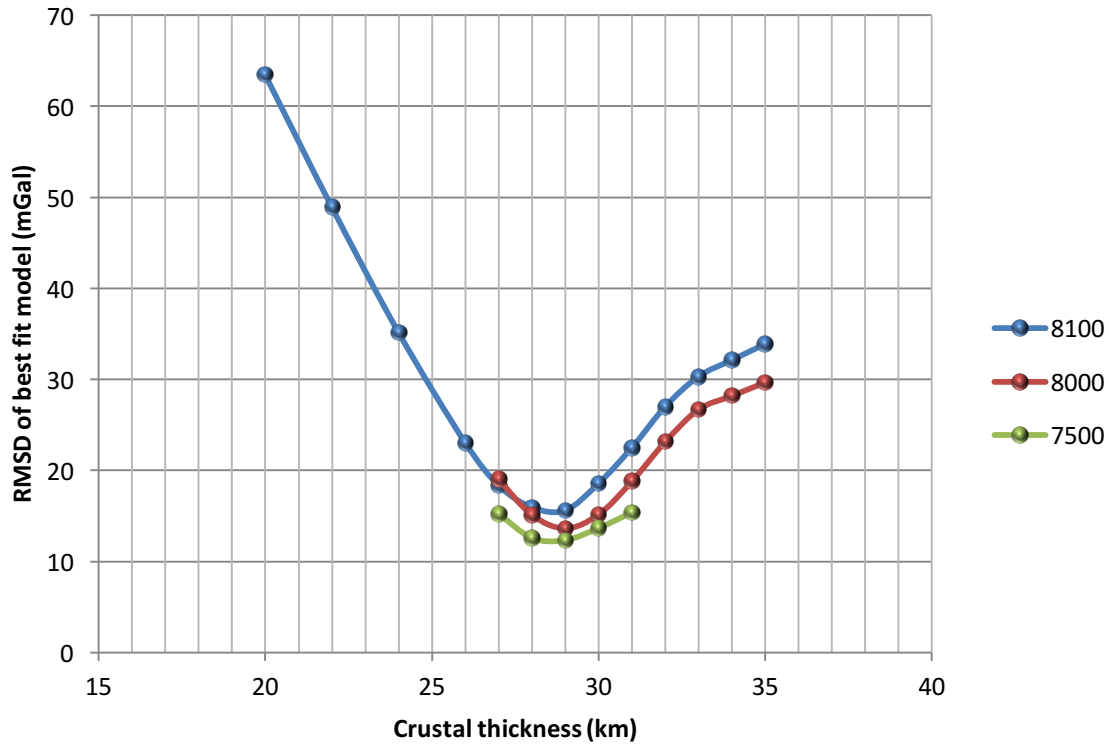
2998 **Figure S3.8.** Seismic-derived sediment densities along seismic line V3618.

2999

3000 3.8.4. Determination of the thickness of continental crust

3001 To determine the crustal thickness for use in all final models, phase 1 modelling was initially
3002 performed using crustal thicknesses between 20 and 35 km. A thickness of 29 km
3003 consistently resulted in the lowest RMSD was used in all final models (Figure S3.9).
3004

Determining the best fit crustal thickness



3005

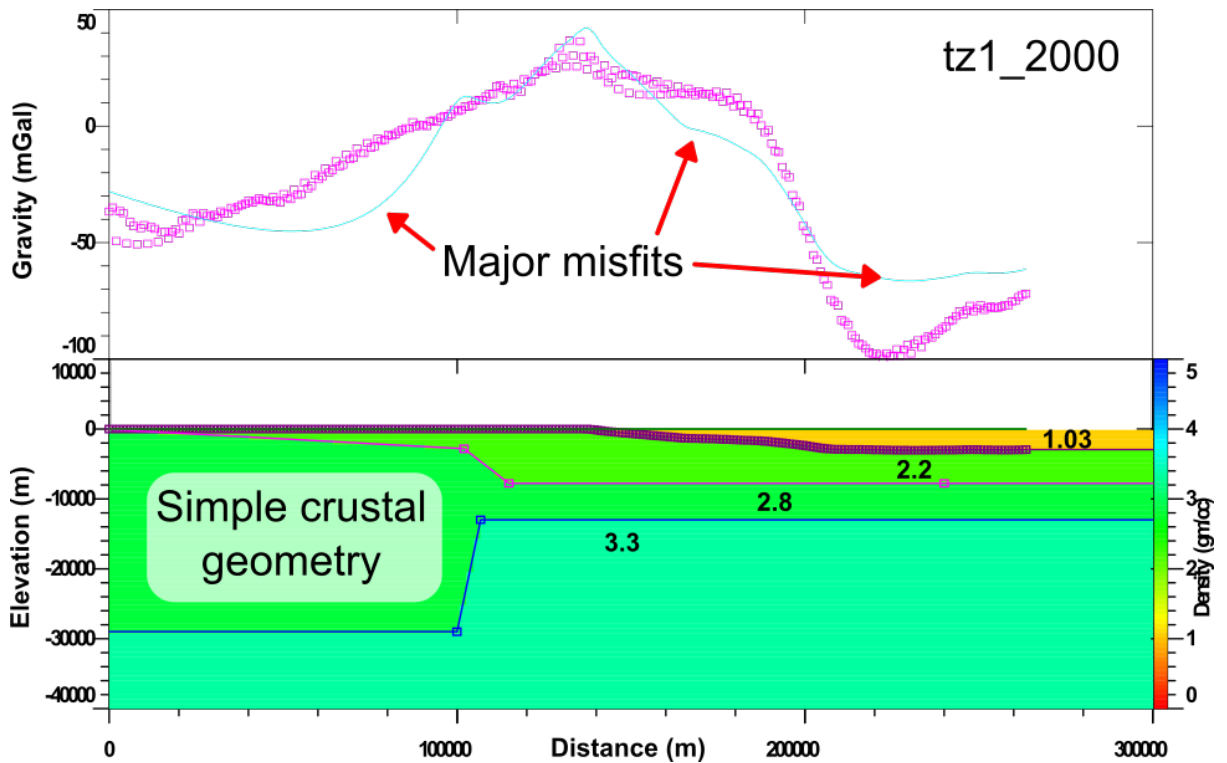
3006 **Figure S3.9.** Type 1 modelling results using different thicknesses for the continental crust.

3007 3.8.5. Resolving gravity misfits of type 2 models

3008 IX2D-GM software was used to model misfits along profile 6 (in addition to profiles 1, 2,
3009 and 3) as it also had coincident seismic constraint on the top basement interface along a
3010 portion of its length (tz1_2000). Unfortunately, as the seismic line does not cross the
3011 continental margin, it was not suitable for type 1 or type 3 modelling.

3012 In order to resolve the misfit inherent to models using the simple margin geometry, profiles
3013 1, 2, and 3 commonly required modifications of the flat basement surface, introduction of a
3014 region of thin crust adjacent to the margin, and/or small adjustments to the slope angle of the
3015 Moho. No adjustment to the margin location as determined from type 2 modelling was
3016 necessary for any profile. Profile 6 (Figure S3.10) was no exception and only required
3017 simple adjustments of the basement interface to resolve the majority of misfit and

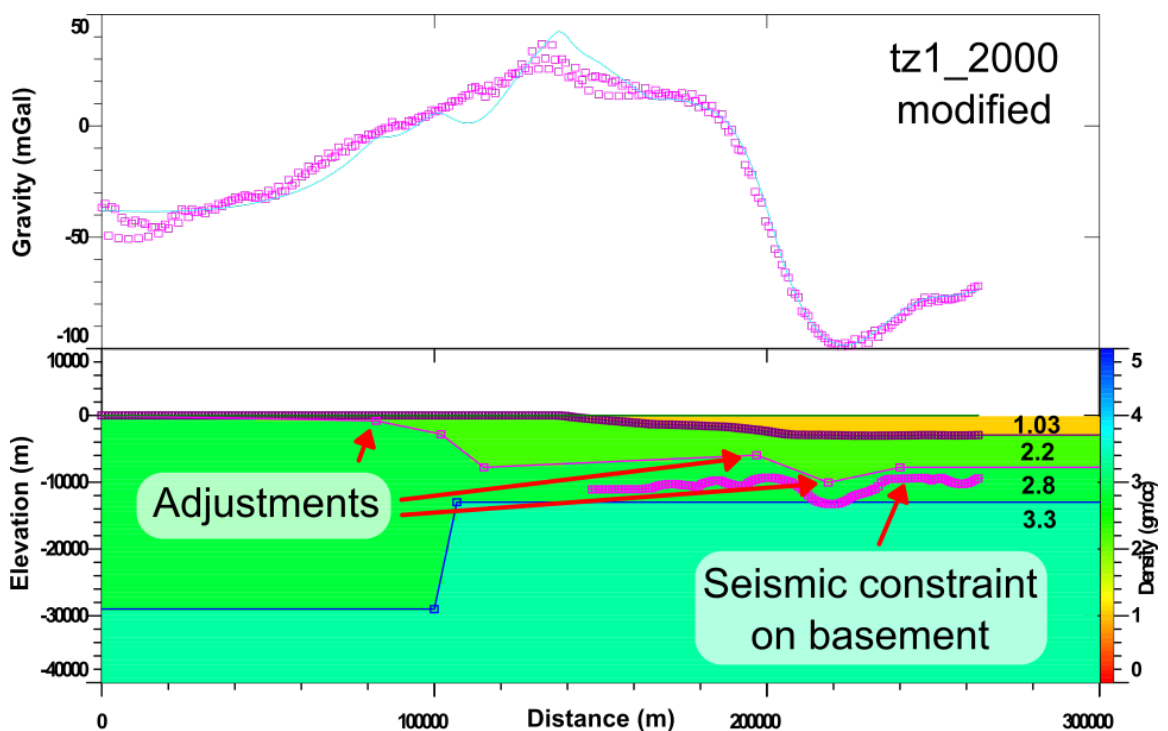
3018 modifications follow the basement interface where constrained by seismic data (Figure
 3019 S3.11).
 3020



3021

3022 **Figure S3.10.** Best-fit result for profile 6 following Type 2 modelling.

3023



3024

3025 **Figure S3.11.** Small geologically plausible alterations are able to remove the majority of
 3026 misfits and follow the trend of seismic constraints.

3027 **4. Compressional consequences of**
3028 **complex spreading: Formation of**
3029 **the Tanzania Coastal Basin and**
3030 **Davie Fracture Zone during the**
3031 **Mesozoic East Africa breakup**

3032 **Abstract**

3033 Changes in plate motion often lead to transpressional deformation along oceanic fracture
3034 zones, due to their incompatibility with the new spreading direction. Here, we present
3035 evidence for compression, which localised along the trend of fracture zones, within the
3036 Tanzania Coastal Basin (TCB) that was coincident with a change in spreading direction near
3037 the end of the Jurassic. This compression of the TCB probably led to the extinction of mid-
3038 ocean ridge segments, development of the 250 km long Tanzania Coastal Basin thrust belt
3039 (TCBtb), and short wavelength (50 km) buckle folding within young (<3 Ma) oceanic crust.

3040 We argue that this change in plate motion was triggered by a coincident alignment of weak
3041 lithosphere, in the form of rifted margins and mid-ocean ridge segments, along the future
3042 trend of the Davie Fracture Zone (DFZ), and was thus not driven by changes in plate driving
3043 forces, but by a reduction in resisting forces along the strong Rovuma Transform Margin.
3044 The cessation of compression within the TCB, possibly related to the development of the
3045 DFZ, migrated from south to north, suggesting a similar northward propagation of the 2000
3046 km DFZ to join the spreading ridges of the Mozambique and Western Somali Basins. Since
3047 its formation, the DFZ was dominated by transpressional deformation, suggesting that the
3048 new plate motions were not fully aligned with plate driving forces. This supports the top-
3049 down concept that the DFZ formed where and when plate configurations ‘allowed’ it, as
3050 opposed to where and when plate driving forces ‘preferred’ it, indicating a first order control
3051 of lithospheric strength on plate motions.

3052 The subsequent drift of East Gondwana along this 2000 km fracture zone led to the collision
3053 of southern Madagascar with the oblique rifted margin of northeast Mozambique, forming

3054 the ‘Davie Compression’ and the ‘Davie ridge’. The Davie Ridge has a similar geometry to
3055 the TCBtb and may also represent a rotated oceanic thrust.

3056 **4.1. Introduction**

3057 Changes in spreading direction have been attributed to both top-down (plate-derived; e.g.
3058 Anderson, 2001) and bottom-up (mantle flow-derived; e.g. King et al., 2002) driving
3059 mechanisms, and can result in transpression or transtension along existing fracture zones due
3060 to their incompatibility with the new spreading direction (Whittaker et al., 2016). Where
3061 strong, long offset transform boundaries exist between plates, plate motion may be restricted
3062 orthogonally to the transform due to the large force required to deform this lithosphere, and
3063 can lead to anisotropic coupling of the plates (Silver et al., 1998).

3064 Where transpressional forces along fracture zones exceed the lithospheric strength,
3065 compressional forces may fold (e.g. McAdoo and Sandwell, 1985; Müller and Smith, 1993),
3066 and thrust (e.g Briggs et al., 2009a; Jiménez-Munt et al., 2010; Massell et al., 2000), oceanic
3067 crust, generally along pre-existing fracture zones (e.g. Briggs et al., 2009b). The strength of
3068 oceanic lithosphere is strongly age dependent, increasing approximately linearly with age
3069 (Mammerickx and Sandwell, 1986), due to cooling and accretion of thicker mantle
3070 lithosphere with time. After 20 Myr, it may be equal in strength to normal continental
3071 lithosphere; however, before this time it may also be preferentially susceptible to
3072 deformation (Vauchez et al., 1998). McAdoo and Sandwell (1985) demonstrated a strong
3073 rheological control on folding of the oceanic lithosphere, with the shortest wavelength folds
3074 occurring in the youngest oceanic lithosphere. Where thrusting occurs, it may be thin or
3075 thick-skinned, with detachment occurring at the Moho or deep in the mantle, respectively.
3076 Generally, the direction of overthrusting has been observed to be age-dependent, where
3077 thrusting exploits pre-existing fracture zones with an age offset across them, with the
3078 younger plate overriding the older (e.g. Gorringer Ridge; Owen Ridge).

3079 If the new plate motion cannot be accommodated gradually by ocean spreading and the
3080 formation of progressively curved fracture zones, plate shearing may be favourable, and can
3081 lead to the calving of microplates and the formation of new spreading axes (e.g. Nunns,
3082 1983; Schiffer et al., In Press; Whittaker et al., 2016). Due to thinning of the crust,
3083 associated development of structural weaknesses and fluid permeation, mechanical and
3084 thermal thinning of the lithospheric mantle, increases in the geotherm, and thermal
3085 blanketing by post-rift sedimentary sequences (Cloetingh et al., 2008), young (<25 Ma)
3086 rifted margins are also inherently weak, and may preferentially succumb to deformation.

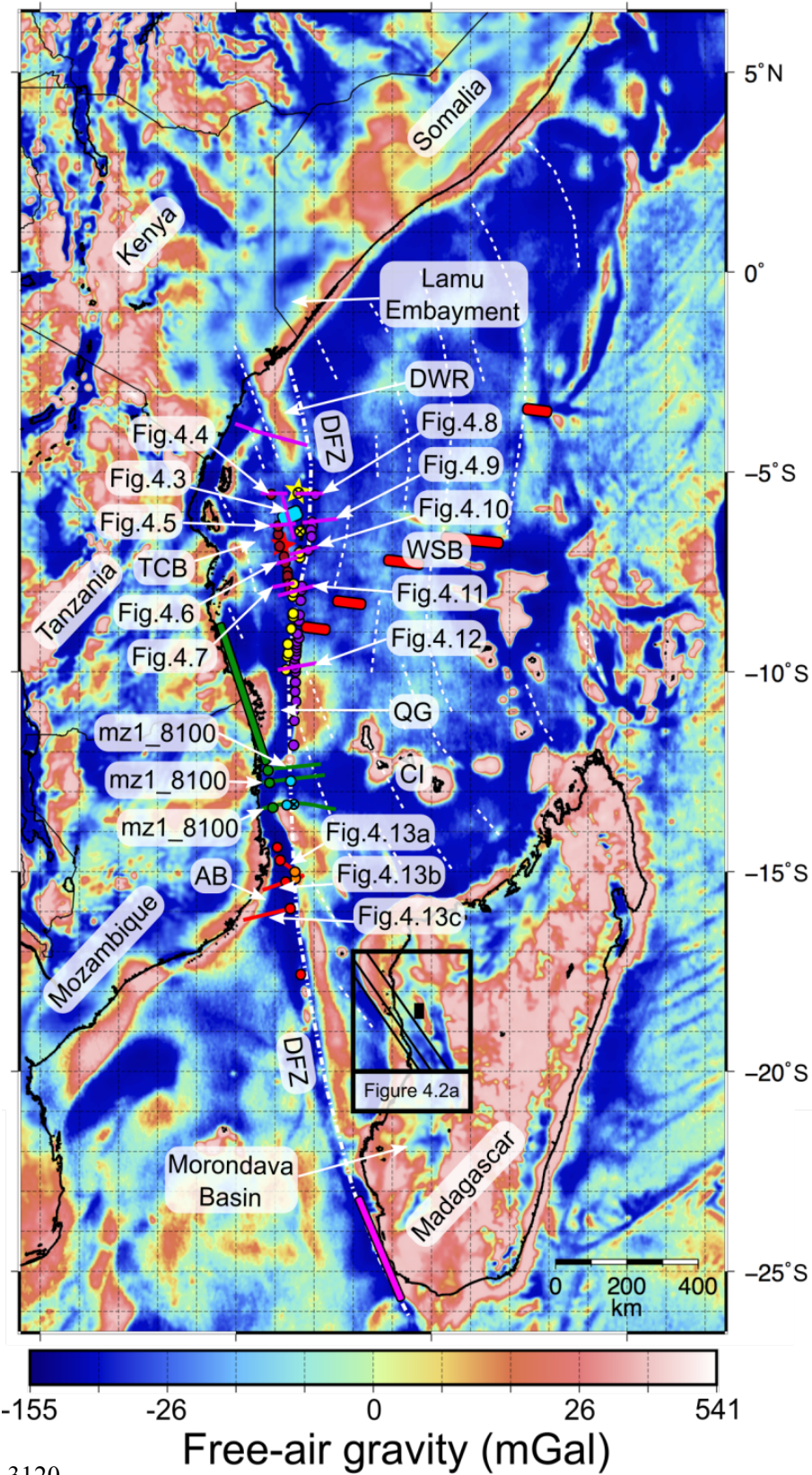
3087 The Early to Middle-Jurassic breakup of East and West Gondwana was coincident with the
3088 impact of the Bouvet plume and eruption of the Karoo Large Igneous Province in SE Africa.
3089 Following breakup, oceanic spreading resulted in the drift of Madagascar to the SSE and the
3090 formation of the TCB (Tanzania Coastal Basin; Figure 4.1) (e.g. Phethean et al., Section 2),
3091 before a switch to N-S spreading around the end of the Jurassic resulted in the southward
3092 drift of East Gondwana, carrying Madagascar to its present day position (Reeves et al.,
3093 2016).

3094 Here, we present evidence for an episode of NE-SW compressional deformation within the
3095 Tanzania Coastal Basin (TCB), which we interpret as the result of plate motion changes near
3096 the end of the Jurassic. Our findings present a rare glimpse into thrust tectonics within
3097 oceanic crust and provide an opportunity to further study controls on plate motion changes.
3098 They also have large consequences for our understanding of the tectono-thermal history of
3099 the TCB and adjacent basins, with widespread implications for paleo-heatflow and trap
3100 development within the associated petroleum province.

3101 **4.2. Database**

3102 The principal data used in this study consist of a subset of the ION East AfricaSPAN deep
3103 imaging seismic reflection dataset, including data from the ke1, tz1, tz3, tz4, and mz1
3104 surveys. The data cover an area of $\sim 450,000 \text{ km}^2$ from offshore Kenya to offshore north-east
3105 Mozambique, including much of the TCB and DFZ. In light of our findings, we also
3106 reinterpret seismic reflection data along the DFZ, immediately to the south of the East
3107 AfricaSPAN, which were presented in Mahanjane (2014). We also supplement our dataset
3108 with reprocessed seismic reflection data from the VEMA 3618 cruise, and two crustal
3109 thickness measurements from the TCB derived from sounobuoy data collected during this
3110 cruise. The locations of seismic sections and crustal thickness measurements, together with
3111 structural picks made from these data, are shown in Figure 4.1. Free-air gravity data, also
3112 shown in Figure 4.1 (SS24; Sandwell et al., 2014), are used for the identification of
3113 structural elements within the basin, and to assist in the determination of their strike and
3114 continuity where seismic data alone are insufficient.

3115 Satellite imagery from the northern Morondava Basin, Madagascar, was used for the
3116 mapping, and determination of the origin of, structural lineaments within this basin. The
3117 geological maps of Besairie (1964) are used to determine the ages of these structures.



Free-air gravity (mGal)

- ▬ Abandoned MOR (Phethean et al., Section 2)
- ▬ Abandoned MOR (This study)
- ▬ Rovuma Transform Margin (Gravity; Phethean et al., Section 3)
- ▬ Inferred location of the South Madagascar Transform Margin
- ★ 6.5 km crustal thickness (Coffin and Rabinowitz, 1986)
- ★ 11.7 km crustal thickness (Coffin and Rabinowitz, 1986)
- Rovuma Transform Margin (Seismic; Phethean et al., Section 3)
- Davie Compression (Mahanjane, 2014)
- Tanzania Coastal Basin Compression (TCBC)
- DFZ (west)
- DFZ (east)
- Davie Fracture Zone (Seismic; Phethean et al., Sec
- Davie Ridge (Mahanjane, 2014)
- ⊗ Fold and/or thrust possibly related to the DFZ
- ▬ Seismic section (this study)
- ▬ Seismic section (Phethean et al., Section 3)
- ▬ Seismic section (Mahanjane, 2

3121 **Figure 4.1.** Free-air gravity anomaly map of East Africa highlighting locations of figures
3122 and seismic lines used in this study. AB, Angoche Basin; DFZ, Davie Fracture Zone ;
3123 DWR, Davie-Walu Ridge ; QG, Quirimbas Graben; CI, Comoros Islands; TCB, Tanzania
3124 Coastal Basin; WSB, Western Somali Basin. Inset shows the location of Figure 4.2a, and
3125 within this, the internal solid black box shows the location of Figures 4.2b and c. Figure
3126 numbers to seismic references: 4.3, tz3_1300; 4.4, tz1_4000 (west); 4.5, tz3_3600 (west);
3127 4.6, tz4_3300; 4.7, tz4_2950; 4.8, tz1_4000 (east); 4.9, tz3_3600 (east); 4.10, tz4_3350;
3128 4.11, tz4_2850; 4.12, tz3_2101; 4.13a, Mahanjane_3a; 4.13b, Mahanjane_2c; 4.13c,
3129 Mahanjane_2b.

3130 **4.3. Pre-breakup position of Madagascar**

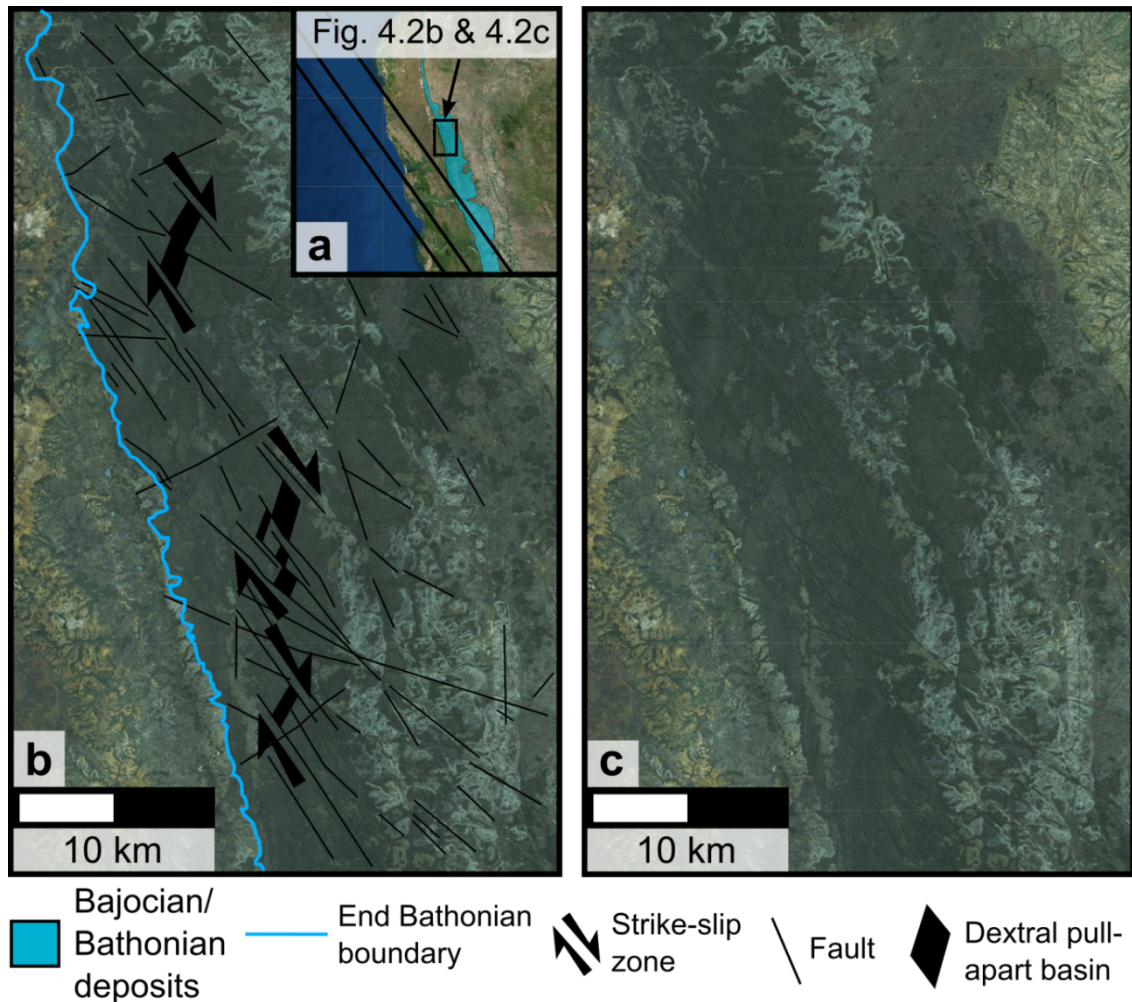
3131 The initial configuration of Gondwana fragments prior to supercontinent disassembly has
3132 been the source of much debate for over 30 years, and Madagascar forms a key piece in this
3133 puzzle. An accurate determination of the origin of this continental fragment has large
3134 repercussions for the fit of the surrounding continents due to its central position and the
3135 presence of several major intercontinental shear zones commonly used to align conjugate
3136 margins. Suggestions for the origin of Madagascar generally fall into one of two groups, and
3137 may be described as ‘tight-fit’ or ‘loose-fit’ reconstructions. Loose fit reconstructions
3138 assume that the N-S trending DFZ represents the continent-ocean transform margin, where
3139 to the west of this feature no oceanic spreading has occurred. These models use the DFZ to
3140 guide Madagascar back to a northern position seaward of the TCB. Tight-fit reconstructions,
3141 on the other hand, allow for an initial NNW-SSE phase of spreading before the formation of
3142 the DFZ and subsequent N-S drift. This results in an initial position of Madagascar within
3143 the TCB (Reeves et al., 2004). This latter model has recently been supported by the
3144 discovery of a transform margin along the Rovuma Basin and oceanic crust within the TCB,
3145 both inboard of the DFZ (Sauter et al., 2016; Chapter 2), which necessitates an initial phase
3146 of oceanic spreading to the west of the DFZ, and thus an origin for Madagascar within the
3147 TCB.

3148 This initial phase of oceanic spreading within the TCB sent Madagascar in a SSE direction,
3149 constrained by the analysis of gravity lineaments related to spreading features (Phethean et
3150 al., 2016), and resulted in strike-slip tectonics between Southern Madagascar and Southern
3151 Tanzania/Northern Mozambique. This strike-slip motion led to the development of the
3152 Rovuma Transform Margin, the location of which has recently been accurately constrained
3153 through combined seismic reflection and gravity modelling studies (Chapter 3). This
3154 transform margin generally follows the trend of the onshore basement outcrop along the

3155 coastlines of the Southern TCB and the Rovuma Basin, and is located ~80 km seaward of
3156 the basement outcrop along its length.

3157 The location and trend of this transform margin further constrains the initial motion of
3158 Madagascar relative to Africa, as the conjugate transform margin in southern Madagascar
3159 must have been in continuous contact along it during the active transform phase.
3160 Ascertaining the location and trend of the transform margin along southern Madagascar is,
3161 however, difficult due to tectonic overprinting and disruption of this margin during the
3162 formation of the DFZ at ~150 Ma (Reeves et al., 2016; Chapter 2). The present day location
3163 of the basement outcrop along southern Madagascar, however, is unlikely to have been
3164 affected by this tectonic overprinting. Therefore, we assume the transform margin of
3165 southern Madagascar also runs parallel to, and ~80 km seaward of, the basement outcrop as
3166 for the conjugate transform margin. This allows for an accurate reconstruction of
3167 Madagascar and Africa by aligning the two transform margins, which not only constrains the
3168 orientation of Madagascar relative to Africa, but also its south-westerly position. The north-
3169 westerly position may then be derived by aligning the eastern edges of the once-adjointing
3170 Selous and Morondava basins to give the absolute location of Madagascar relative to Africa
3171 prior to breakup. Imposing these simple constraints on the position and orientation of
3172 southern Madagascar results in a good alignment of structural features in northern
3173 Madagascar with those of the conjugate East African margin.

3174 Newly recognised strike-slip faults are preserved in the syn-breakup Bajocian-Bathonian
3175 limestones of the northern Morondava Basin (the Karoo-recent aged basin spanning the
3176 entire west coast of Madagascar) and are highly oblique to the trend of this basin (Figure
3177 4.2). The strike-slip nature of these faults is indicated by their highly linear nature and
3178 interlinking pull apart basins, which are similar to others found within Karoo aged deposits
3179 of the Morondava Basin (Schandelmeier, 2004) and indicate a dextral sense of motion across
3180 the faults. These faults closely follow the trend of NNW-SSE coastline segments (Figure
3181 4.2a), and terminate at the End Bathonian boundary (blue line; Figure 4.2b), possibly
3182 indicating the localisation of strike-slip deformation onto oceanic transform faults at this
3183 time. Following the reconstruction of the southern Madagascar and Rovuma Transform
3184 Margins, these strike-slip faults are closely aligned with the SSE trend of the Davie-Walu
3185 ridge (DWR), a prominent gravity high just offshore the conjugate Lamu Embayment
3186 (Figure 4.1). They define the same SSE initial plate motion constrained by the Rovuma
3187 Transform Margin, and together, these features provide an additional robust constraint on
3188 the Mid- to Late-Jurassic relative plate motions of East and West Gondwana.



3190

3191 **Figure 4.2.** (a) Location of Figures 4.2b and c within the Morondava Basin. Black lines
 3192 show the extrapolated trend of structures identified in Figures 4.2b and c. The extent of
 3193 Bajocian/Bathonian deposits is taken from the geological maps of Besairie (1970). The
 3194 location of Figure 4.2a is shown in Figure 4.1. (b) Landsat Satellite imagery of Bajocian-
 3195 Bathonian syn-breakup deposits from the northern Morondava Basin, with fault lineament
 3196 interpretation as black lines. (c) Figure 4.2b without fault interpretation. The location of the
 3197 Morondava Basin is shown in Figures 4.1 and 2.1.

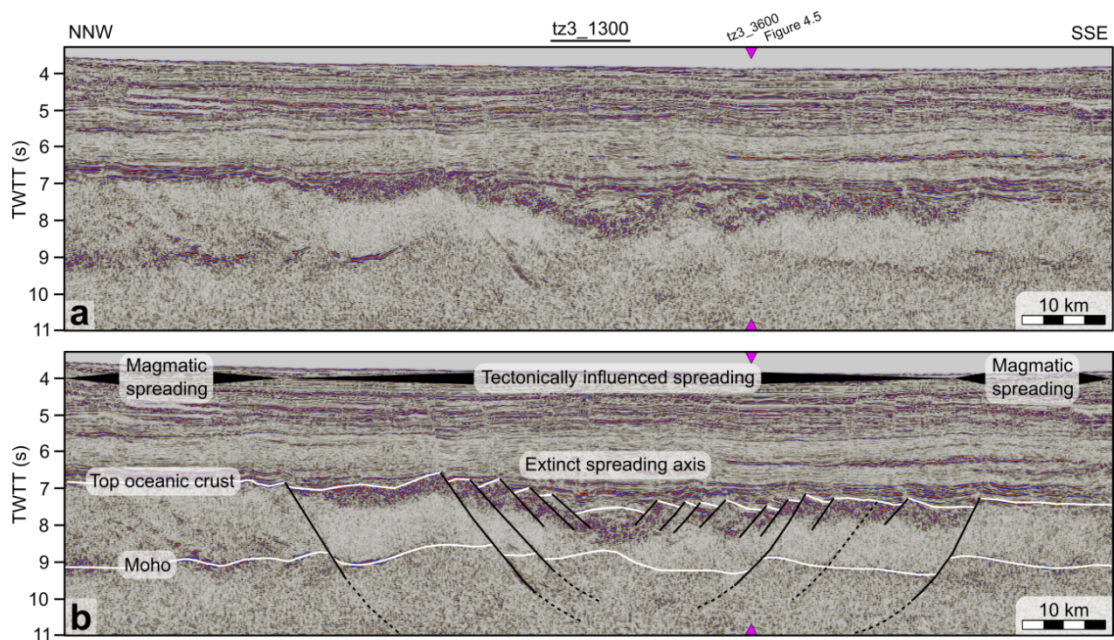
3198 **4.4. Major tectonic signatures of the TCB, DFZ, and Western** 3199 **Somali Basin**

3200 The interpretation of seismic reflection data from the Western Somali Basin (WSB) and
 3201 surrounding coastal basins of East Africa reveals evidence for several major tectonic events.
 3202 Here, we assess the nature of these events and constrain them in relation to the plate tectonic
 3203 framework of (Chapter 2).

3204 4.4.1. Cessation of spreading in the TCB

3205 Within the TCB, at 6.2°S 41.4°E, the SSE trending tz3_1300 line displays a change in
3206 character of the oceanic crust (Figure 4.3; location shown in Figure 4.1). The northernmost
3207 section of the line displays a smooth and continuous top basement reflector, which changes
3208 southwards to a rough and internally reflective layer. Coincident with this change, the mid-
3209 lower crustal layers become more seismically transparent, and the onset of extensional
3210 faulting of the basement, which generates tilted half grabens that dip symmetrically about a
3211 central graben, also occurs. Some of these normal faults offset the Moho by up to 0.5 s
3212 TWTT. In the northern and southern regions of Figure 4.3, Moho reflections define a crustal
3213 thickness of ~2.1 s TWTT, and in places bound the base of the seismically transparent crust.
3214 Where Moho reflections are faint or not present, the base of the seismically transparent body
3215 is, therefore, taken as an indication of the Moho level. This and the high amplitude
3216 reflections of the top basement allow the definition of a roughly symmetrical thinning of the
3217 crust from ~2.1 s at the edges of the central graben to ~ 1 s TWTT at the graben's centre
3218 over a distance of ~ 40 km.

3219



3220

3221 **Figure 4.3.** Extinct ocean spreading segment identified within the TCB. (a) Uninterpreted
3222 section. (b) Interpreted section. Extensional faults (black lines) sometimes offset the Moho
3223 and become increasingly dominant approaching the spreading centre. The crustal thickness
3224 decreases from ~2.1 s TWTT outside of the axial rift, to ~1 s TWTT at the rift centre. An
3225 associated change in the character of the top basement (top white line) occurs alongside
3226 crustal thinning. Moho reflections and the basal termination of the seismically transparent
3227 crust define the base of the oceanic crust (bottom white line). Location shown in Figure 4.1.

3228 Smooth oceanic crust is generated by magmatically dominated spreading, whereas rough
3229 oceanic crust results from an insufficient supply of melt to the spreading axis and the onset
3230 of tectonically accommodated plate separation (Louden et al., 1996; Smith, 2013). As
3231 melting at mid-ocean ridge (MOR) systems is primarily controlled by spreading rate, where
3232 slower spreading results in greater conductive cooling of the upwelling mantle and therefore
3233 less melt production, lower melt supplies generally reflect lower spreading rates (White et
3234 al., 1992). Mid to lower oceanic crust may display a transparent character in seismic
3235 reflection data (e.g. Bécel et al., 2015; Morris et al., 1993), and half grabens within oceanic
3236 crust have been shown to generally dip towards the spreading centre about which they form
3237 (Behn and Ito, 2008). The axial valleys at such spreading centres generally range in width
3238 from 16-62 km, averaging at 35 km (Malinverno, 1990), as measured along the Mid-Atlantic
3239 Ridge.

3240 On line tz3_1300, the reduction in crustal thickness from ~2.1 s to ~ 1 s TWTT over similar
3241 distances to the width of axial spreading valleys and the symmetrical dip of half grabens
3242 about this thinning suggest that this structure represents an abandoned spreading centre
3243 within the TCB. Similar observations of crustal thinning and an associated broad zone of
3244 rotated fault blocks have been observed at the extinct Labrador spreading centre (Louden et
3245 al., 1996). Therefore, a reduction in spreading rate probably occurred in the lead up to the
3246 extinction of the spreading centre, resulting in greater cooling of the upwelling
3247 asthenosphere and less melt production (e.g. Niu and Hékinian, 1997). The resulting
3248 deepening of the brittle-ductile transition may also have allowed normal faults to extend into
3249 the upper mantle (e.g. Harper, 1985), offsetting the Moho.

3250 The abandoned spreading centre is situated ~ 210 km away from the coastline in the paleo
3251 spreading direction; according to the plate tectonic model of (Chapter 2), this places the age
3252 of abandonment at ~150 Ma, close to the end of the Jurassic. At roughly the same time, a
3253 major clockwise rotation of East Gondwana relative to West Gondwana, and the subsequent
3254 formation of the DFZ, occurred (Reeves et al., 2016). Subsequent oceanic spreading
3255 between 150 and 125 Ma, forming the Western Somali Basin, transposed the remaining
3256 MOR segments farther south offsetting the abandoned ridges of the Tanzania Coastal Basin
3257 and younger Western Somali Basin.

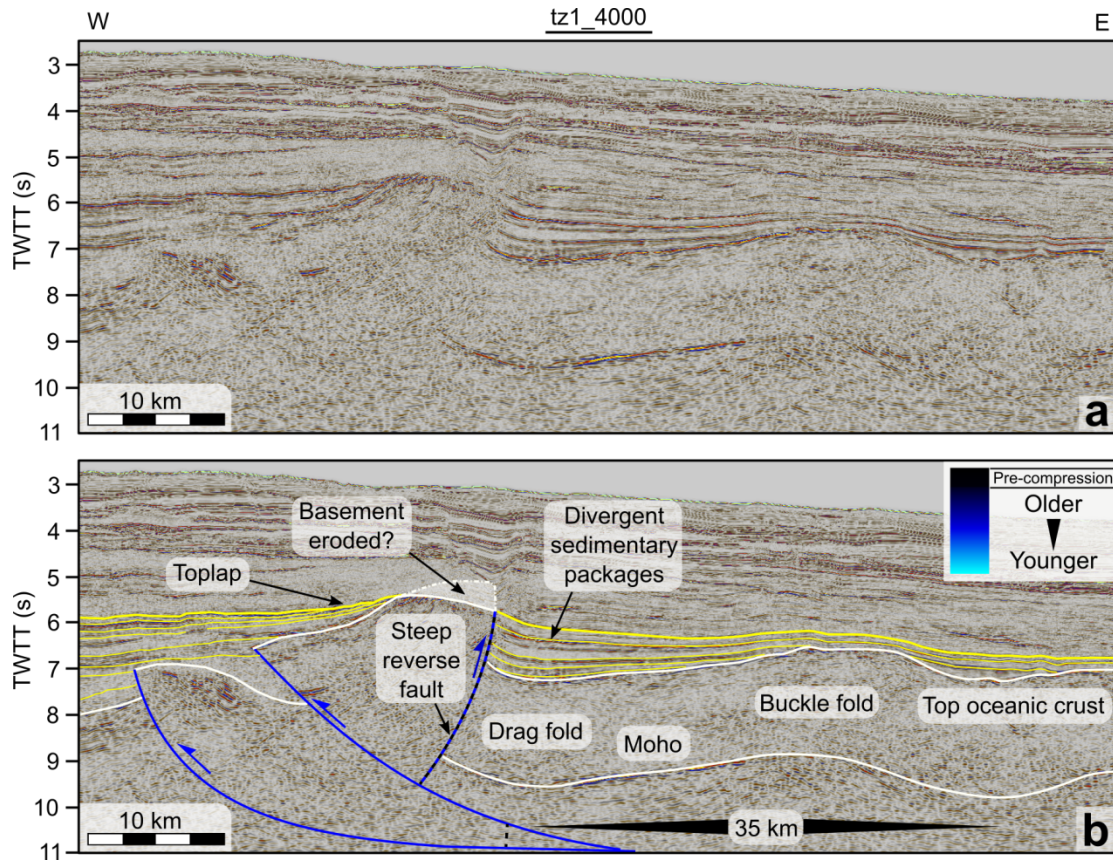
3258 4.4.2. Compression post SSE spreading

3259 Several E-W trending seismic lines within the TCB show evidence for crustal thickening and
3260 compression of the basement, and are described from north to south below.

3261 **4.4.2.1. Line tz1_4000 (west)**

3262 The central and eastern portions of Figure 4.4 display a smooth top basement and clear
3263 Moho reflection, defining oceanic crust with a uniform thickness of ~ 2.2 s TWTT. This
3264 crust forms an open buckle fold, which has a trough to trough wavelength of ~ 35 km. The
3265 crest of the buckle fold sits at a depth of 6.6 s TWTT, and the troughs at 7.3 s TWTT.
3266 Overlying the buckle fold, sedimentary packages onlap, and then overlap, the folded crust,
3267 and diverge towards the troughs of the fold.

3268 At the western edge of the buckle fold, reflections from the sediments, top basement, and
3269 Moho, are bent sharply upwards before terminating abruptly in a steep west dipping line,
3270 perpendicular to the folded crust. To the west, an adjacent basement block with sporadic
3271 internal westward dipping reflections sits at a depth of 5.4 s TWTT. This block has been
3272 uplifted by at least 1.2 s TWTT relative to the surrounding crust, and the rotated internal
3273 reflections are truncated by an erosion surface along the top of the eastern flank that
3274 continues to form top of the divergent sedimentary fill to the east. Above the western side of
3275 this block, toplap of sedimentary packages against the same erosion surface also occurs, but
3276 diminishes westward (Figure 4.4). Between the west-dipping uplifted block, and west-
3277 dipping upper crustal reflectivity at the far west of the line, an ~ 10 km wide block of east-
3278 dipping upper crustal reflectivity is present, and is delineated by offsets in the higher
3279 amplitude top basement reflections.



3281

3282 **Figure 4.4.** Thrusting and folding of the basement along seismic line tz1_4000 (west in
 3283 response to compression. (a) Uninterpreted section. (b) Interpreted section. Yellow lines
 3284 show the top (thick lines) and internal structure (thin lines) of syn-compressional sediments.
 3285 Upper white lines indicate the top basement, where dashes indicate eroded sections, and the
 3286 lower white line indicates the Moho. The interpreted relative ages of faults in this section are
 3287 shown in the key. Location shown in Figure 4.1.

3288 The buckle fold in the eastern half of Figure 4.4b likely developed in response to
 3289 compression, and the divergence of overlying sedimentary packages towards the troughs of
 3290 the buckle suggests that they were deposited syn-compression. The onlap of sediments
 3291 against the crest of the buckle suggests either 1) the presence of an original basement high,
 3292 or 2) the onset of deposition after the onset of compression (e.g. Burbank and Vergés, 1994).
 3293 Assuming a predominantly terrestrial sedimentary source, this onlap and the subsequent
 3294 sedimentary overlap of the fold suggest that uplift rates of the fold crest were less than the
 3295 rate of sedimentary deposition.

3296 To the west of the buckle fold, the uplift and rotation of the basement block has resulted in
 3297 crustal thickening from 2.2 s up to 3.5 s TWTT where it overlies the edge of the buckle fold.
 3298 This crustal thickening also strongly supports compressional tectonics. The abrupt
 3299 termination of sedimentary, top basement, and Moho reflections against the western end of

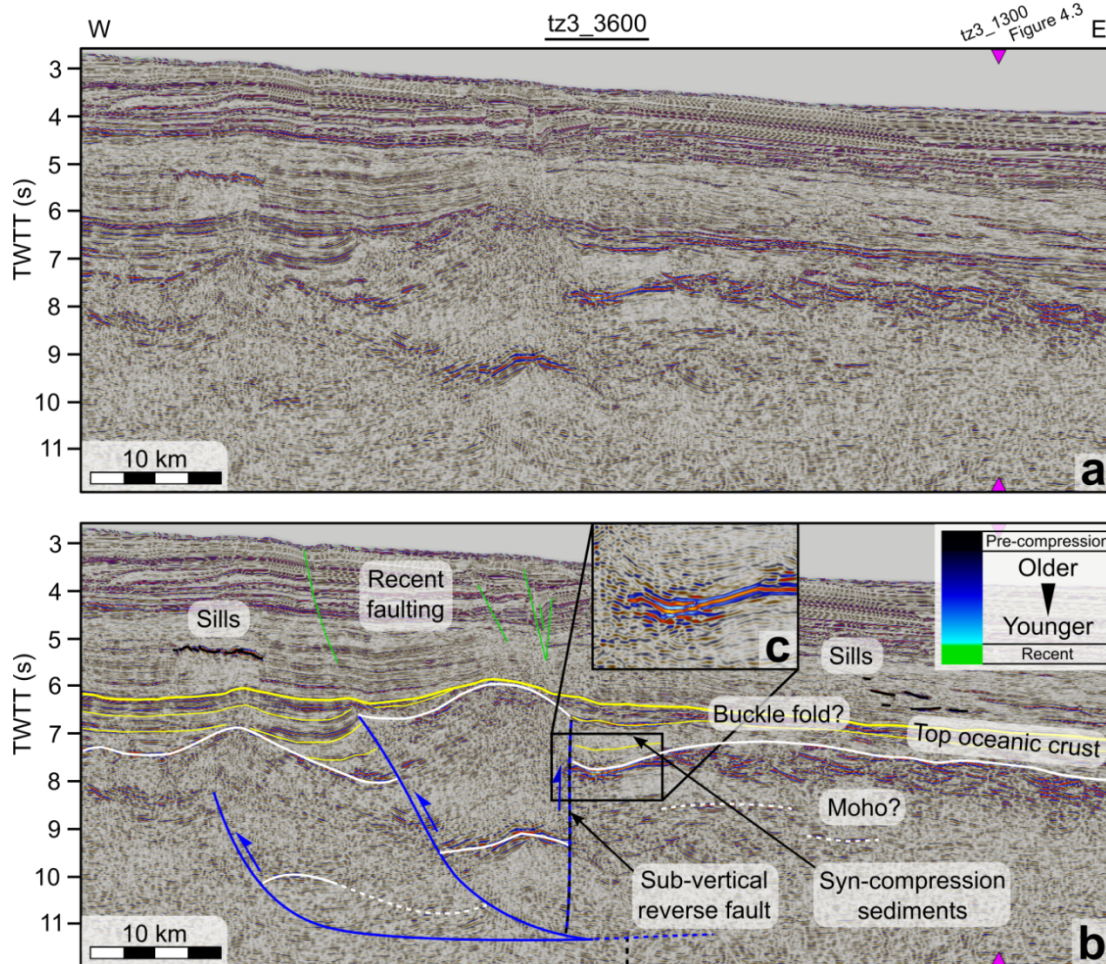
3300 the buckle fold, and the upward bending of reflections immediately before their termination,
3301 suggest reverse faulting in this location (Figure 4.4b). The orthogonality of the reverse fault
3302 to the restored basement section indicates the reactivation of a sub-vertical structure during
3303 compression, and the folding associated with this faulting is therefore interpreted as drag
3304 folding as opposed to fault propagation folding associated with thrust fault initiation.
3305 Erosion of the tip of the uplifted block and toplap of sedimentary packages against this
3306 erosion surface (which may represent a depositional surface farther to the west) suggest that
3307 uplift of this block was faster than the rate of sedimentary deposition (Burbank and Vergés,
3308 1994; Hardy and Ford, 1997). Near the western edge of Figure 4.4, the rotation and offset of
3309 basement reflections may be the result of low angle thrust faulting during the compression,
3310 which allows for the uplift of the basement block along the steep reverse fault.

3311 **4.4.2.2. Line tz3_3600 (west)**

3312 Similar crustal geometries to those along tz1-4000 (west) are seen 90 km to the SSE in Line
3313 tz3_3600 (west), and are shown in Figure 4.5. The eastern half of this figure crosses the
3314 heavily faulted extinct spreading centre of the TCB (i.e. Figure 4.3) at a highly oblique angle
3315 (see Figure 1 for line locations), possibly resulting in the sporadic reflective character of the
3316 top basement and lack of clear Moho reflections in this region. Identification of the
3317 geometry of the top basement, by enveloping top of basement reflections, reveals a possible
3318 folding of the crust, the top of which sits at a depth of 7.2 s TWTT. Above the western flank
3319 of the fold, the sedimentary sequence can be seen to thicken into the trough, although the
3320 internal structure of these sediments is poorly defined and does not allow for an analysis of
3321 their possibly divergent nature.

3322 Before the top basement reflections terminate abruptly to the west, they bend back upwards.
3323 Immediately west of this, a rotated and uplifted basement block sits at a depth of 6 s TWTT,
3324 and west-dipping top basement and upper crustal reflections define its western limb. Strong
3325 Moho reflections, which have been similarly tilted, define the base of the crust, and bend
3326 sharply downwards before their abrupt termination at the eastern edge of the block. Farther
3327 west, east-dipping top basement and upper crustal reflections define a second crustal block,
3328 along the eastern flank of which reflections bend back upwards, as can be seen particularly
3329 clearly in the overlying sedimentary packages (Figure 4.5). West of this block, close to the
3330 western edge of the figure, reflections from the upper crust and top basement are sub-
3331 horizontal.

3332



3333

3334 **Figure 4.5.** Thrusting and folding of the basement along seismic line tz3_3600 (west) in
 3335 response to compression. (a) Uninterpreted section. (b) Interpreted section. (c) Close up of
 3336 the inset region without interpretation showing the curved top basement reflections. Line
 3337 descriptions are as for Figure 4.4. The interpreted relative ages of faults in this section are
 3338 shown in the key and continuation of the structures at depth is speculative. Location shown
 3339 in Figure 4.1.

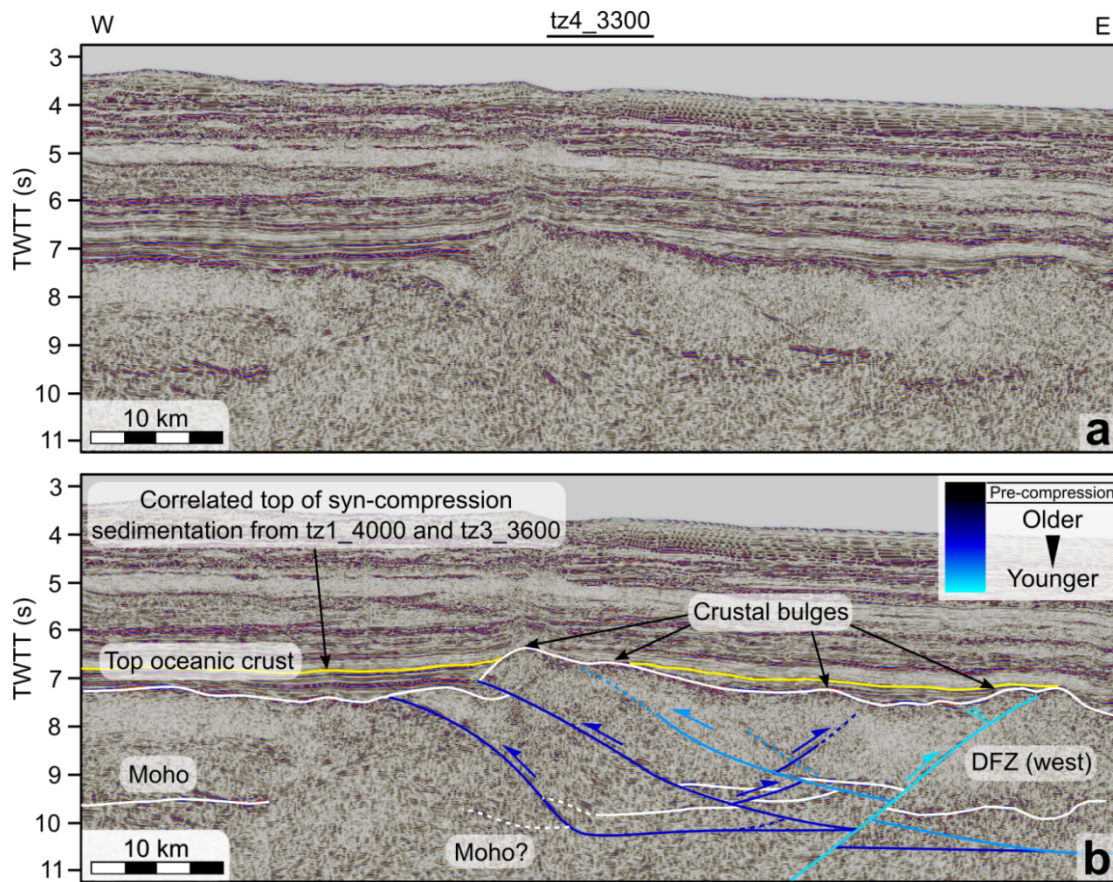
3340 The overall geometry of line tz3_3600 (west) is similar to that seen along line tz1_4000
 3341 (west), despite the 90 km offset between the two lines, and may be interpreted in a similar
 3342 way. Again, buckling and thrusting of the crust have occurred in response to compression,
 3343 and in places the resulting crustal thickness may reach 4 s TWTT. In tz3_3600, the sudden
 3344 termination of reflections against the eastern edge of the uplifted basement block defines
 3345 another sub-vertical reverse fault, similar to the one seen in tz1_4000, again possibly
 3346 reactivating a pre-existing structure. Drag folds have developed along this reverse fault and
 3347 are defined by the top basement reflections to the east, and Moho reflections to the west.
 3348 Similarly to line tz1_4000 (west), uplift along this reverse fault was probably facilitated by

3349 the development of thrusts to the west, which have also rotated and uplifted the crust in this
3350 location.

3351 **4.4.2.3. Line tz4_3300**

3352 Another basement high is imaged within the TCB another 100 km farther to the SSE. Here,
3353 smooth top basement reflections, underlain by a more transparent mid-crust and strong
3354 Moho reflections, are prevalent over the west and east portions of the section (Figure 4.6).
3355 They define a crustal thickness of between 1.7 s and 2.3 s TWTT within undeformed
3356 regions, generally sitting at a depth of around 7.3 s TWTT. The smooth top basement of the
3357 eastern portion of Figure 4.6 shows slight bulges on an approximately 10 km length scale,
3358 and the tips of bulges are commonly aligned with dipping reflections within the crust, and
3359 sometimes also offsets in the Moho. In this eastern portion of the line, a pair of reflective
3360 bands is sometimes present instead of a single band of Moho reflections. Both bands are
3361 offset in several locations, show a similar seismic waveform and amplitude, and do not
3362 always have a consistent vertical separation from one another.

3363 In the central region of the line, the top of the basement has been uplifted to a depth of ~ 6.4
3364 s TWTT, and in places the crust possibly thickens to 3.7 s TWTT. Below and to the east of
3365 the crest of this basement uplift, reflections within the crust dip gently eastwards, whereas
3366 below and to the west of the basement's crest, an ~ 5 km wide block of seismically
3367 transparent crust sits directly above a band of east-dipping high amplitude reflections. Strong
3368 Moho reflections are sparse in the central region, but a short high amplitude reflector dips
3369 eastward ~3.5 s below the crest of the thickened crust. Above the basement, the deep
3370 sedimentary section, correlating to the folded and divergent packages of the syn-
3371 compressional sediments along lines tz1_4000 (west) and tz3_3600 (west), shows little sign
3372 of deformation, and follows the regional sedimentary tilt of the basin. On this line, unlike
3373 along lines tz1_4000 (west) and tz3_3600 (west), no buckle folding has occurred adjacent to
3374 the crustal thickening.



3376

3377 **Figure 4.6.** Thrusting of the basement along seismic line tz4_3300 in response to
 3378 compression. (a) Uninterpreted section. (b) Interpreted section. Dual reflector bands
 3379 around the depth of the Moho result from Moho stacking in response to thrusting and backthrusting.
 3380 Line descriptions are as for Figure 4.4, where the top of the syn-compressional sediments is
 3381 now interpreted to correlate with the top of deformed sediments on lines tz1_4000 (west)
 3382 and tz3_3600 (west). The interpreted relative ages of faults in this section are shown in the
 3383 key and continuation of the structures at depth is speculative. Location shown in Figure 4.1.

3384 Along line tz4_3300, the clear Moho reflections on either side of the crustal thickening, the
 3385 smooth character of the top basement, the undeformed crustal thickness of ~ 2 s TWTT, and
 3386 the seismically more transparent mid-crust indicate oceanic crust. As this oceanic crust
 3387 surrounds, and therefore likely also comprises, the region of uplifted basement, tectonic
 3388 thickening of the crust is likely the cause of the basement uplift. Beneath this, the eastward-
 3389 dipping reflections within the crust and the juxtaposition of crustal blocks, which sometimes
 3390 have seismically transparent internal characteristics, suggest repeated stacking of the crust
 3391 along eastward-dipping thrust faults (Figure 4.6b). The short, high amplitude reflector, seen
 3392 below the crest of the crustal thickening, may therefore form a faulted contact between crust
 3393 and mantle rocks, where shearing of this boundary may have increased its reflectivity.

3394 To the east, bulges in the top basement, as well as east- and west-dipping reflections within
3395 the crust and offsets in the Moho (where offsets occur with the top to both the east and
3396 west), suggest further thrust and back-thrust development in this region. The complex
3397 geometry of the pair of Moho reflection bands in the east may therefore be the result of
3398 Moho stacking along such thrusts (Figure 4.6b). It should be considered, however, that the
3399 lower band of reflections may also have developed in response to early thrusting at this
3400 level, which was subsequently offset by later thrusts. This interpretation is presented in the
3401 supplementary material, but, without sufficient justification for the abandonment of an early
3402 detachment fault in favour of developing a new deeper one, this scenario is less attractive.

3403 Above the thrust stack, sediments correlating to the syn-compressional sedimentary
3404 packages seen farther north along lines tz1_4000 (west; Figure 4.4) and tz3_3600 (west;
3405 Figure 4.5) have been identified (yellow line, Figure 4.6b). These sediments onlap both the
3406 basement thrust stack and the DFZ (west), and show little sign of deformation beyond the
3407 regional background, following the same tilt as the overlying strata. This suggests that
3408 either, 1) the stratigraphic correlation of the sediments does not correspond to a temporal
3409 correlation, or 2) the sediments were deposited following thrusting and development of the
3410 DFZ, in which case the cessation of thrusting and formation of the DFZ must have occurred
3411 earlier farther south.

3412 At the eastern edge of the line, a west-dipping thrust (cyan colour on Figure 4.6b) offsets the
3413 Moho by +0.5 s TWTT, and the lack of counter-clockwise rotation of Moho reflections
3414 within the hanging wall suggests that the thrust does not curve and sole out in the immediate
3415 vicinity. This fault may therefore cut the older west verging thrusts, in which case it would
3416 be younger. This fault tips out in the DFZ (west), where it contributes to crustal thickening.

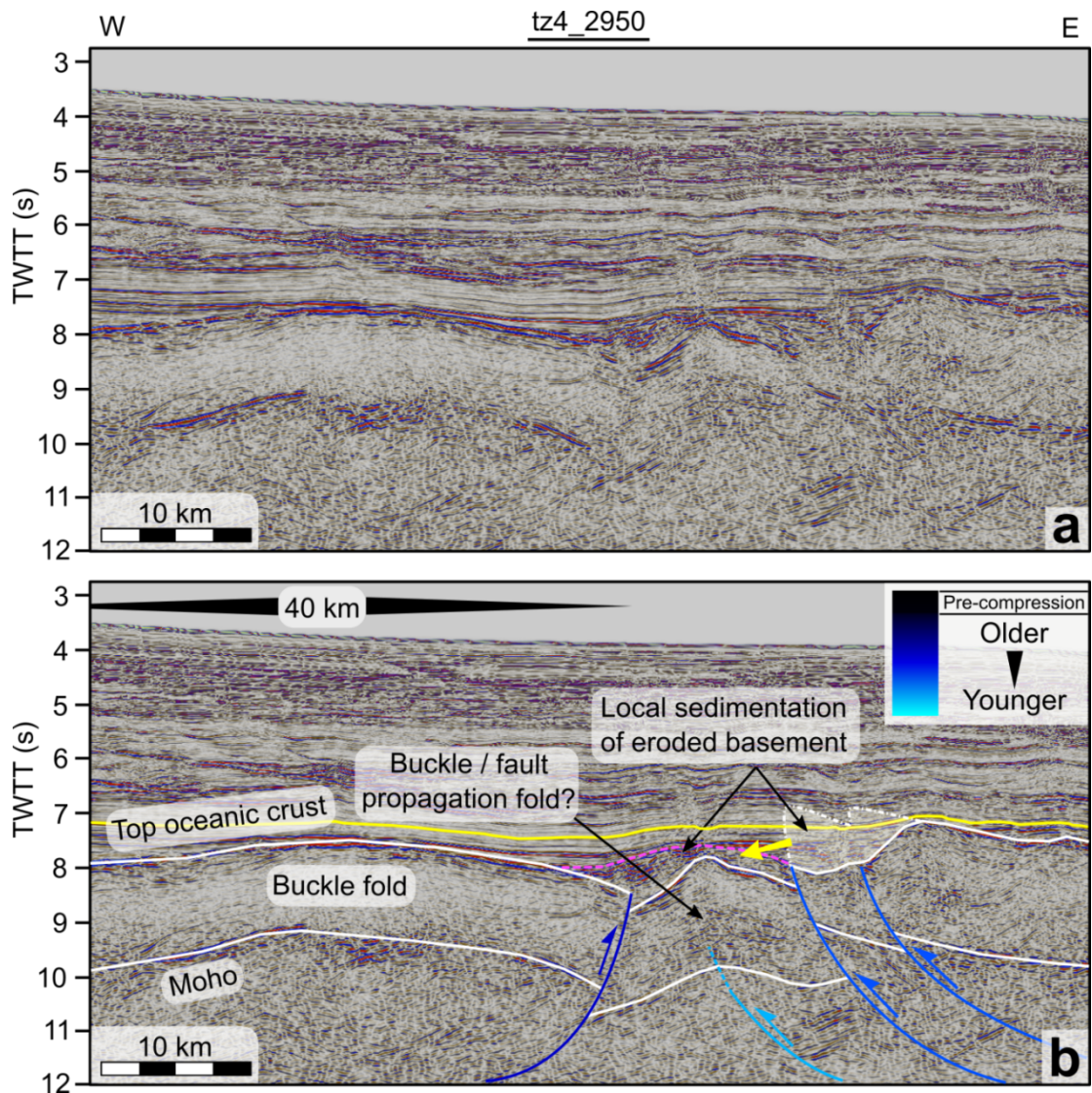
3417 **4.4.2.4. Line tz4_2950**

3418 Approximately 65 km farther to the SSE, just before intersecting the main trace of the DFZ,
3419 basement uplift and folding of the crust has again occurred, and is shown in Figure 4.7.
3420 Here, as to the north, smooth and high amplitude reflections define the top and bottom of
3421 oceanic crust, which also commonly displays a seismically transparent mid-crust. In the
3422 western part of the section, the crust forms an open buckle fold, with a trough to trough
3423 wavelength of ~40 km. The crest of the buckle fold sits at a depth of 7.6 s TWTT, and the
3424 troughs at ~8 s TWTT. At the eastern edge of the buckle fold, the east-dipping smooth top
3425 basement reflections, low reflectivity mid-crust, and Moho reflections step down, and a
3426 sharp change to a westward dip of these reflections occurs. It should be noted, however, that
3427 below 10 s TWTT, patches of west-dipping reflections occur sporadically in several places
3428 on this line, and may interfere with the Moho interpretation. Less than 10 km to the east, the

3429 west-dipping top basement reflections are tightly folded to dip back eastwards, before
3430 terminating abruptly ~6 km on. The basement topography immediately above the tight fold
3431 has been partially filled by a layer of discontinuous, moderate to high amplitude reflections,
3432 which roughly follow the dip of the top basement.

3433 Along the eastern edge of the line, a block of uplifted basement sits at 7.2 s TWTT, and clear
3434 top basement and Moho reflections dip eastwards. Between this uplifted block, and the
3435 tightly folded crust to the west, additional east-dipping reflections are slightly offset below
3436 the trend of Moho reflections beneath the uplifted block. These reflections are bounded
3437 above by a region of reduced reflectivity, and below by chaotic reflections.

3438 Similarly to line tz4_3300, sediments that correlate with deformed or divergent sedimentary
3439 packages farther north (along lines tz1_4000 (west) and tz3_3600 (west)), onlap the
3440 basement and do not form large divergent growth wedges as seen farther north. They have
3441 also not been subject to deformation beyond the regional background, and follow the same
3442 trend as the overlying strata.



3444

3445 **Figure 4.7.** Folding and thrusting of the basement along seismic line tz4_2950 in response
 3446 to compression. (a) Uninterpreted section. (b) Interpreted section. Line descriptions are as
 3447 for Figure 4.4, where the top of the syn-compressional sediments is now interpreted to
 3448 correlate with the top of deformed sediments on lines tz1_4000 (west) and tz3_3600 (west),
 3449 and the dashed pink line shows the top of locally sourced sediments deposited during
 3450 compression. The interpreted relative ages of faults in this section are shown in the key.
 3451 Location shown in Figure 4.1.

3452 The termination and step down of top basement and Moho reflections at the eastern end of
 3453 the buckle fold imply a faulted contact between the buckle fold and the tight fold to the east.
 3454 The eastward step from the Moho terminations to the top basement terminations suggests
 3455 this fault is west-dipping and, therefore, a reverse fault, consistent with other observations of
 3456 basement compression. The sharp folding of oceanic crust immediately to the west is

3457 uncharacteristic of the buckle folding elsewhere, and may have required the influence of a
3458 propagating fault to localise the deformation.

3459 Immediately east of the fault-propagation fold, the presence of a lower reflectivity area
3460 above the east-dipping reflections is compatible with the interpretation of these reflections as
3461 the Moho, with overlying seismically transparent oceanic crust. The relative uplift of this
3462 basement during compression, with top to the east offset, implies the presence of east-
3463 dipping thrusts, as interpreted elsewhere along the compressional structures of the TCB. To
3464 the east, Moho reflections of the uplifted block are offset slightly upwards. A second thrust
3465 fault, offsetting the Moho and further uplifting the eastern block, is therefore likely. Between
3466 the uplifted block and the fault-propagation fold, the shallow level of the Moho and
3467 relatively low top basement, therefore, imply a large amount of erosion of this crust during,
3468 and following, its uplift. It is possible that local deposition of the derived sediment occurred
3469 above the developing limbs of the fault-propagation fold, where continuous steepening of
3470 the fold limbs resulted in deformation and re-deposition of these sediments, resulting in their
3471 chaotic nature. The later deposition of onlapping and undeformed sediments, which correlate
3472 to syn-compressional sediments in the north of the basin, may again support the earlier
3473 cessation of compression in this more southern location, as compared to the north of the
3474 TCB.

3475 **4.4.2.5. Summary of compressional deformation within the TCB**

3476 Regions of highly tilted and uplifted basement associated with 1) coincident offsets in the
3477 Moho, 2) thickening of oceanic crust, and 3) in some cases, large adjacent drag folds provide
3478 strong evidence of thrust tectonics within the TCB. Furthermore, the development of buckle
3479 folds is compatible with these observations of compressional tectonics.

3480 Observations of crustal thickening from Figures 4.4 - 4.7 suggest that the crust has been
3481 locally thickened from approximately 2 s TWTT to, from north to south, 3.5 s, 4.0 s, 3.7 s,
3482 and, before significant erosion, 3.3 s TWTT. This thickening is very similar to a crustal
3483 thickness measurement of 3.6 s TWTT (converted here to TWTT assuming a crustal velocity
3484 of 6.5 km/s) performed by Coffin et al., (1986), which sits between the observed thrusts on
3485 seismic lines tz3_3600 (west) and tz4_3300, and independently confirms the observations
3486 from seismic reflection data.

3487 This similar level of crustal thickening across each of the thrust structures, with an apparent
3488 continuity between seismic observations; consistent west vergence of thrust structures; and
3489 alignment of all thrust structures along a SSE trending gravity anomaly that also follows
3490 other gravity lineaments within the TCB (Figure 4.1) suggest that the observed thrusting

3491 within the TCB may all form part of a single structure. This structure, which we term the
3492 Tanzania Coastal Basin thrust belt (TCBtb), runs from at least 5.5°S to 7.8°S along a SSE
3493 trend, spanning over 250 km. This makes the TCBtb, to the best of our knowledge, the
3494 longest intraplate oceanic thrust complex known on the globe. Its SSE trend, similar to the
3495 Rovuma Transform Margin, spreading lineaments of the TCB, and strike-slip faults related
3496 to initial plate separation in Madagascar, in conjunction with evidence for the reactivation of
3497 sub-vertical faults during thrusting and termination of an extinct MOR segment against this
3498 structure suggests that the TCBtb developed along a pre-existing fracture zone in the oceanic
3499 lithosphere of the TCB.

3500 Buckle folds that have developed alongside the TCBtb have short wavelengths, between 35
3501 and 40 km. As the wavelength of buckle folds in oceanic lithosphere is strongly dependent
3502 on the age of the lithosphere, where younger lithosphere results in shorter fold wavelengths,
3503 the compression of the TCBtb must have occurred < 3 Myr after of the formation of the
3504 buckled crust (McAdoo and Sandwell, 1985). This may account for the cessation of buckle
3505 folding on the east of the TCBtb with increasing lithospheric age to the south of the extinct
3506 MOR. The appearance of buckle folds to the west of the TCBtb yet farther south may
3507 therefore indicate an approach towards an offset MOR segment, which lay in the vicinity of
3508 the present day DFZ.

3509 The distance between the abandoned MOR of the northern TCB (Figure 4.3), and the
3510 northernmost observed buckle folding along line tz1_4000 (west; Figure 4.4), is ~80 km.
3511 Assuming a palaeospreading rate of ~ 20 mm/y (half rate; Phethean et al., Section 2), a
3512 rough relative age of this crust may be calculated, which is ~ 4 Myr older than the extinct
3513 MOR. This suggests that the compression of this basin predated and overlapped the
3514 abandonment of spreading. Due to several assumptions made during this calculation (i.e.
3515 wavelength of folding not affected by decoupling along thrusts, constant spreading rate
3516 before extinction, etc.), however, we prefer to simplify this finding to say that the
3517 compressional event and extinction of the MOR occurred at roughly the same time.

3518 As changes in plate motion can lead to the build-up of transpressional stress along fracture
3519 zones (Section 4.1), which is seen in the TCB, we propose that the plate motion change near
3520 the end of the Jurassic (e.g. Chapter 2; Reeves et al., 2016) may have been the ultimate cause
3521 of compression along the TCBC. This change may have also resulted in the extinction of
3522 MOR segments incompatible with the new spreading direction, accounting for the
3523 contemporaneity of compression and MOR extinction. The absence of a sedimentary record
3524 of the compressional event along the southern TCBtb, despite the presence of sediments

3525 equivalent to those that record such a compression farther north along this structure,
3526 suggests diachronous cessation of compression from south to north.

3527 4.4.3. The DFZ

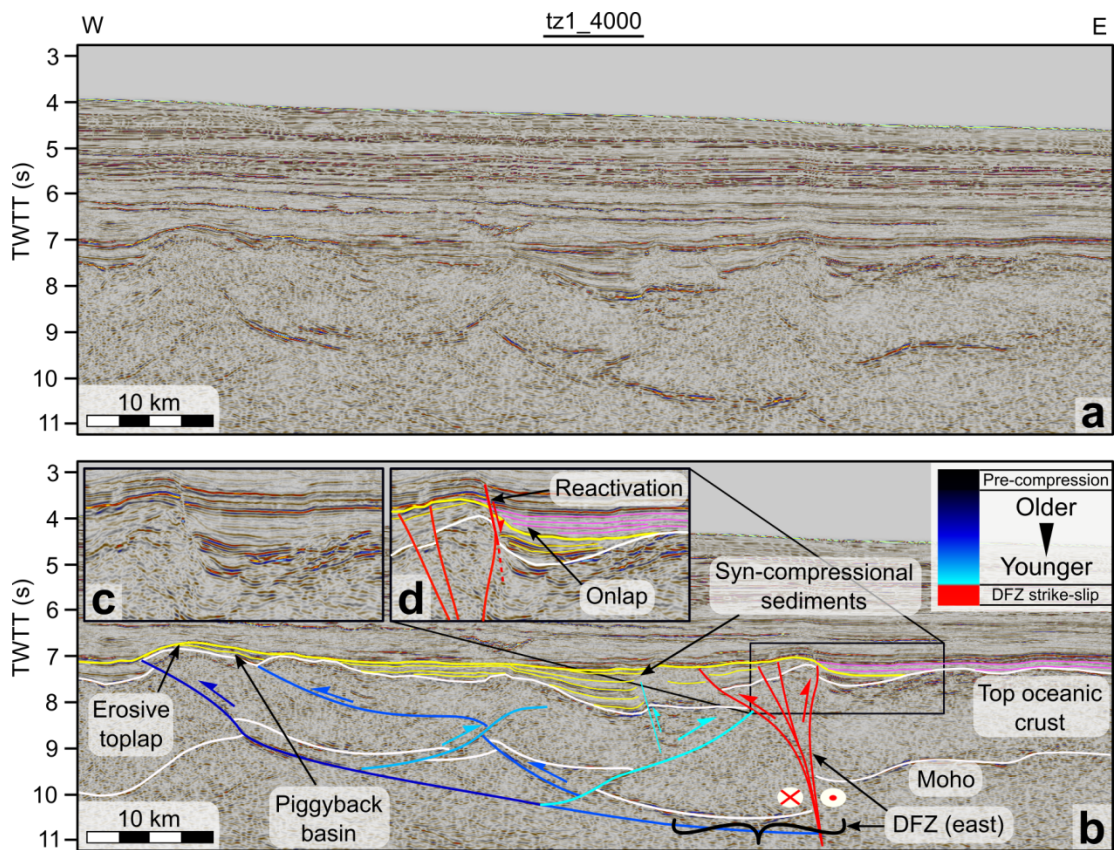
3528 The DFZ forms the eastern boundary of the TCB, and is readily recognisable in free-air
3529 gravity data as an arcuate low gravity anomaly, which spans from just offshore Kenya at
3530 $\sim 5^{\circ}\text{S}$, to the southwestern tip of Madagascar at -25°S (Figure 4.1). This large-offset fracture
3531 zone separates the Jurassic oceanic crust of the TCB from the younger crust of the central
3532 WSB. The DFZ developed in response to a change in plate motion from NNW-SSE
3533 spreading to $\sim\text{N-S}$ spreading near the end of the Jurassic, after which East Gondwana was
3534 translated southwards along this major transform fault (e.g. Chapter 2; Reeves et al., 2016).
3535 To the north of the WSB's spreading centre, which was abandoned when Madagascar
3536 reached its present day latitude at ~ 125 Ma, the DFZ experienced a variable cumulative
3537 offset along its length. This is due to the cessation of transform motions following the
3538 southward passage of the MOR, which means that the cumulative dextral offset along the
3539 DFZ to the north of the extinct spreading centre increases from north to south.

3540 **4.4.3.1. Line tz1_4000 (east)**

3541 Near the northern limit of the TCB, just to the south of the Davie-Walu Ridge, line tz1_4000
3542 (east) crosses the DFZ (Figure 4.8). Smooth or hummocky top basement reflections and high
3543 amplitude Moho reflections define crustal thicknesses of between 1.5 s and 2.4 s TWTT in
3544 regions of undeformed crust. To the west of the DFZ, within the TCB, the crust has been
3545 folded and buckled, sometimes in association with offsets in the top of the basement and
3546 Moho. High amplitude convex downward reflections, which are also present beneath the
3547 level of Moho reflections, are aligned with basement offsets and the steepening of crustal
3548 folds. Above the basement, sedimentary deposits that correlate with syn-deformational
3549 sediments elsewhere along line tz1_4000 (west; i.e. Figure 4.4), show both onlap and toplap
3550 relationships, and diverge into the trough of the central fold. In the centre of this trough, a
3551 small step up in the basement occurs moving east and above this the layered reflections of
3552 the sedimentary package has been disrupted. Both of the edges of the disrupted region dip to
3553 the east, but the eastern edge propagates farther through the stratigraphy than the western,
3554 which is onlapped by later deposits. East of this, a block of uplifted crust in the shape of an
3555 inverted triangle sits adjacent to a small basin on the east, and is shown in detail in Figures
3556 4.8c and d. The western edge of this crustal block is defined by reflections in the mid crust
3557 which become more steeply dipping downwards, and may align with the offset in the top of
3558 the basement along the eastern edge of the disrupted sediments. The eastern edge of the
3559 block is defined by the termination of top basement and mid-crustal reflections from the

3560 east, and may also steepen downwards to align with an offset of Moho reflections. An
 3561 erosion surface, truncating the sedimentary packages that overlie the uplifted block, bounds
 3562 local deposits to the east of the block, which have a high amplitude reflectivity (Figure 4.8c
 3563 and d). Above this erosion surface, sedimentary deposits onlap the palaeobathymetric high,
 3564 and a small normal fault has developed along the edge of the uplifted block. East of the
 3565 uplifted block, the Moho locally deepens before flattening to the east, and the top basement
 3566 surface does the same. This crust, to the east of the DFZ, shows a slightly more seismically
 3567 transparent nature than crust to the west, and, away from the DFZ, remains at a relatively
 3568 consistent depth.

3569



3570

3571 **Figure 4.8.** Folding, thrusting, and strike slip deformation along seismic line tz1_4000 (east)
 3572 in response to compression and development of the DFZ. (a) Uninterpreted section. (b)
 3573 Interpreted section. (c) Close up of the inset region without interpretation. (d) Close up of
 3574 the inset region with interpretation. Line descriptions are as for Figure 4.4, and pink lines
 3575 depict the structure of the post-deformation sequences. The relative ages of the faulting are
 3576 shown in the key and continuation of the structures at depth is speculative. Location shown
 3577 in Figure 4.1.

3578 The thickness of the crust, and smooth high amplitude top basement reflections, indicate an
 3579 oceanic nature of the basement in this region. To the west of the DFZ, within the TCB, the

3580 folding of crust and offsets in the top basement and Moho reflections are similar to
3581 observations along the TCBtb. In Figure 4.8, as along the TCBtb, buckle folding and
3582 thrusting have accommodated compressional deformation, resulting in some crustal
3583 thickening, particularly around the DFZ. The tightening of the folding to the west of the
3584 DFZ, resulting in the deepening of the central syn-deformation basin, is coincident with a
3585 convex downward reflector in the mid crust, and is likely influenced by a propagating thrust.
3586 The western edge of the band of disrupted stratigraphy in the middle of this basin is
3587 coincident with an offset in the top of the basement, and likely results from back thrusting
3588 along a large Moho-offsetting thrust. The matching tops of divergent sedimentary packages
3589 here, and syn-compressional stratigraphies elsewhere in the north of the TCB, suggests that
3590 compression occurred at the same time here as farther west around the northern TCBtb.

3591 The western fault boundary of the uplifted triangular block crosscuts the entire overlying
3592 syn-compressional sedimentary sequence, and is therefore one of the latest structures to form
3593 in this region. The downward steepening of these reverse faults is characteristic of positive
3594 flower structure geometries that develop during transpression, suggesting strike-slip
3595 deformation across this structure. These observations are consistent with satellite gravity
3596 data that suggest that the DFZ passes through this region, and the change in the character of
3597 the oceanic crust across the strike-slip zone further supports the presence of a major crustal
3598 discontinuity. Crust to the east of the DFZ has, therefore, only been accreted adjacent to the
3599 DFZ following the passing of the MOR and cessation of strike-slip deformation. The very
3600 limited and localised deposition of sediments below the erosional surface bounding the syn-
3601 deformation sedimentary packages on the east of the DFZ (Figure 4.8c and d) suggests that
3602 this crust formed after, or at a similar time to, the cessation of compressional deformation. It
3603 is likely that these localised deposits were sourced from the eroding DFZ flower structure,
3604 and rapidly deposited in new accommodation space being generated at the passing spreading
3605 centre. In this case, the intercalation of these sediments with volcanic deposits at the MOR
3606 may have resulted in their high amplitude nature, and the loading of this zero-age crust may
3607 have contributed to the local subsidence and depression of the Moho. Following this, further
3608 loading of this crust by post-compressional sediments, which onlap the unconformity
3609 bounding the syn-deformation sediments, and thermal subsidence may have resulted in the
3610 partial reactivation of the DFZ as a normal fault (Figure 4.8d).

3611 **4.4.3.2. Line tz3_3600 (east)**

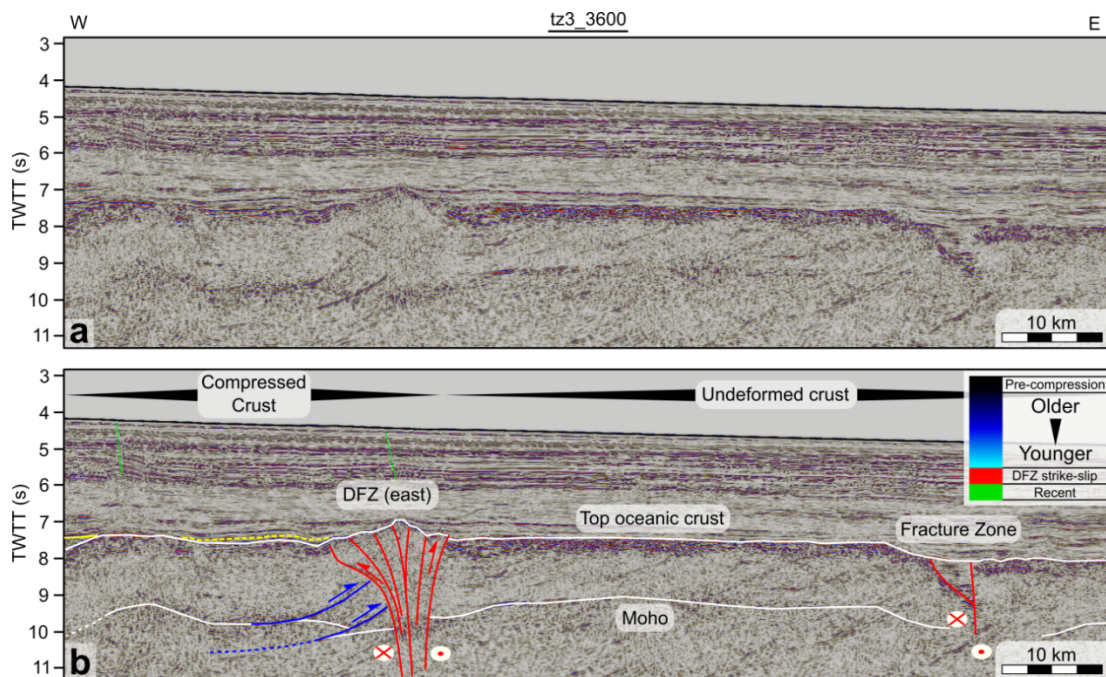
3612 75 km to the south, line tz3_3600 (east) crosses the DFZ and two other deviations of the top
3613 basement interface (Figure 4.9). At the western end of the section, the top basement, upper
3614 crustal reflections, and a band of less reflective mid-lower crust dip to the west, defining a
3615 small (~15 km) fold, which uplifts the top basement at its crest by 0.2 s TWTT. The top of

3616 this fold is overlapped by the syn-compressional sediments identified to the west (i.e. Figure
 3617 4.5). The available data do not constrain the continuation of this package to the east;
 3618 however, there is little evidence that it continues to the east of the DFZ, with the possible
 3619 exception of local deposits as seen in Figure 4.8. Just east of the fold, the crust, which has a
 3620 thickness of approximately 2.3 s TWTT, has flat top basement and Moho reflections until
 3621 near the DFZ. At this point, a thickening of the crust to 3.2 s TWTT occurs as the top
 3622 basement becomes tilted to the west and the Moho dips to the east, and the reflective nature
 3623 of the upper crust becomes subdued. On the other side of the DFZ, the opposite occurs,
 3624 returning the crust to a normal thickness.

3625 Beneath, and to the east, of the DFZ, straight low-angle reflections of low-mid amplitude are
 3626 common in the crust and mantle. Within the crustal thickening of the DFZ, however, a high
 3627 amplitude convex downward reflector dips to the west, and may coincide with an offset in
 3628 the Moho. The upper termination of this reflector coincides with the downward continuation
 3629 of an east dipping reflector that steepens downwards.

3630 Crust to the east of the DFZ shows a generally consistent thickness, with flat Moho and top
 3631 basement interfaces spanning ~50 km. The eastern limit of this flat crust is defined by an
 3632 offset in the top of the basement down to the east and an ~3 km wide inverted triangular
 3633 trough, containing flat-lying reflective material, which separates it from more flat-lying
 3634 oceanic crust to the east.

3635



3636

3637 **Figure 4.9.** Folding, thrusting, and strike slip deformation along seismic line tz3_3600 in
 3638 response to compression and development of the DFZ. (a) Uninterpreted section. (b)

3639 Interpreted section. Line descriptions are as for Figure 4.4, where the dashed yellow line is
3640 the inferred top of syn-compressional sediments. The relative ages of the faulting are shown
3641 in the key. Location shown in Figure 4.1.

3642 The small fold at the western end of the profile, with a slightly uplifted crest, is to the west
3643 of the DFZ, and therefore within the TCB. The same compressional event that resulted in the
3644 thrusting and folding of the basement elsewhere within the TCB may, therefore, have also
3645 generated this fold structure. The wavelength of the fold is shorter than other buckle folds
3646 seen within the TCB, and may have been influenced by a propagating thrust fault, as thought
3647 to result in tighter folds elsewhere within the TCB. The lack of clear Moho reflections,
3648 however, precludes the determination of any Moho offsets that would confirm this
3649 interpretation. The oceanic crust adjacent to this fold has a thickness typical of that
3650 elsewhere in the TCB, at ~ 2.3 s TWTT, and does not appear to have been thickened.
3651 Approaching the DFZ, however, the tilting of the crust and the presence of high amplitude
3652 convex downward reflections, which may correspond to sheared crust and the sheared crust-
3653 mantle boundary, suggest that east verging thrusts have developed in this location and
3654 contribute to the crustal thickening of the DFZ. The truncation of these thrusts by later faults
3655 that steepen downwards and have contributed to the uplift of the top basement interface
3656 suggests that a positive flower structure developed at a later stage in response to an
3657 increasing strike-slip component of deformation here. These steeply dipping strike-slip faults
3658 may have destroyed the initially reflective structure of the upper oceanic crust within the
3659 DFZ.

3660 To the east of the DFZ, the flat oceanic crust has a thickness of ~ 1.8 s TWTT, typical for the
3661 oceanic crust of the WSB (Coffin et al., 1986). This crust shows no sign of compressional
3662 deformation, despite the transpression experienced locally along the DFZ here, and farther
3663 north along line tz1_4000 (east). This suggests that this crust formed later than both the
3664 compressional episode that affected the TCB and the transpression along the DFZ, and is
3665 consistent with its accretion on the north of the MOR in the WSB.

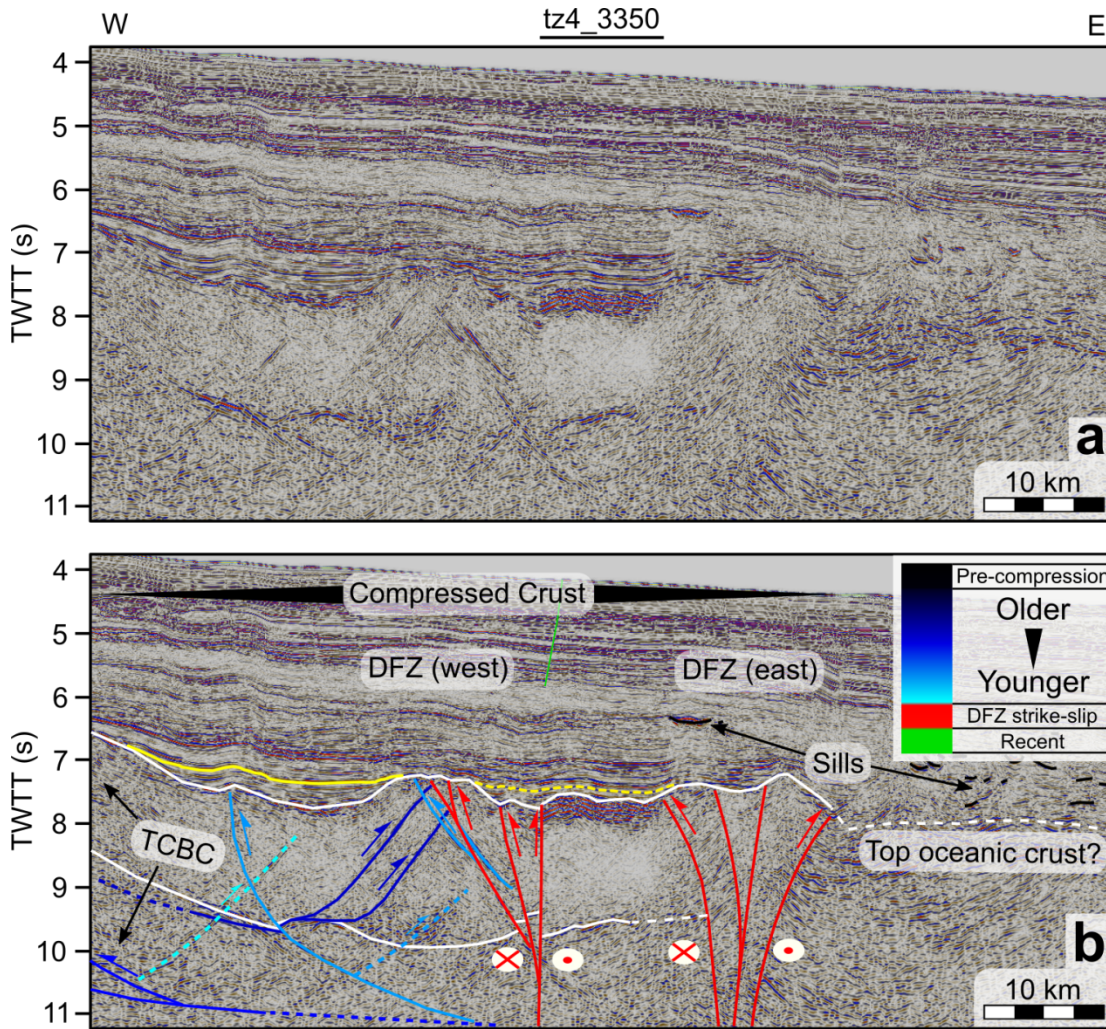
3666 As line tz3_3600 (east) is oriented perpendicular to the palaeo-spreading direction of the
3667 WSB, and would therefore be expected to crosscut fracture zones related to oceanic
3668 spreading, the step down in the top of the oceanic crust farther east and accompanying basin
3669 likely represent a locally transtensional fracture zone that developed between spreading
3670 segments of the WSB.

3671 **4.4.3.3. Line tz4_3350**

3672 Approximately 80 km farther south, seismic line tz4_3350 images both the DFZ and the SSE
3673 trending TCBtb as they come into proximity (Figure 4.10). At the western edge of the
3674 section, the basement has been uplifted to ~6.5 s TWTT, above the adjacent crust at 7.7 s
3675 TWTT, and forms part of the TCBtb. On the eastern flank of the TCBtb, an ~0.2 s TWTT
3676 offset in the top basement uplifts crust to its east. This offset may align with east dipping
3677 reflections in the mantle via a disrupted zone of Moho reflectivity, across which the Moho is
3678 possibly offset, and weak east dipping reflections within the crust. In the same location, mid
3679 and low amplitude reflections in the crust and mantle, respectively, may be aligned and dip
3680 to the west, but are not associated with any resolvable offset. In this western region of Figure
3681 4.10, clear top basement and Moho reflections and a seismically transparent mid crust define
3682 an oceanic crustal thickness of ~1.7 s TWTT. Moving eastwards, the crust thickens to 2.7 s
3683 TWTT and mid-crustal reflectivity increases. The top basement and Moho reflections form a
3684 bulbous shape, similar to that which forms the DFZ (east) farther north. This thickened crust
3685 contains several prominent crosscutting reflections, dipping to both the east and west, which
3686 may align with hummocks in the top of the basement. This crustal thickening is offset to the
3687 west of the trend of the DFZ (east) by ~20 km.

3688 East of the thickened crust, a sharp onset of chaotic and high amplitude reflections in the top
3689 of the crust and seismic transparency in the mid-lower crust occurs across a sub-vertical
3690 boundary, which possibly also connects offsets in the top basement and Moho. East of this
3691 boundary, a clear Moho reflection defines the base of flat lying oceanic crust. The top of this
3692 crust lies at a depth of 7.7 s TWTT and has a thickness of 1.8 s TWTT. This crustal strip,
3693 with a width of approximately 10 km, loses its character to the east beneath an intruded sill,
3694 which disrupts imaging of the basement structures. A rise in the top basement to 7.5 s
3695 TWTT, however, is imaged just to the east of the sill. This basement uplift has a width of
3696 between 10 and 15 km, similar to the bulbous crustal thickening to the west and the DFZ
3697 (east) to the north (i.e. Figure 4.9). It is also aligned with the trend of the DFZ (east) as
3698 derived from lines tz1_4000 and tz3_3600. Beneath, and on either side of, the uplifted top
3699 basement interface, mid-crustal reflections bend upwards before terminating against
3700 boundaries that possibly steepen downwards. To the east of this uplifted basement, an
3701 intruded sill complex obscures detailed investigation of the basement structures.

3702



3703

3704 **Figure 4.10.** Folding, thrusting, and strike slip deformation along seismic line tz4_3350 in
 3705 response to compression and development of the DFZ. (a) Uninterpreted section. (b)
 3706 Interpreted section. Line descriptions are as for Figure 4.4, where the top of the syn-
 3707 compressional sediments is now interpreted to correlate with the top of deformed sediments
 3708 on lines tz1_4000 (west) and tz3_3600 (west) and the dashed yellow line is inferred. The
 3709 relative ages of the faulting are shown in the key. Location shown in Figure 4.1.

3710 The TCBtb, at the western edge of Figure 4.10, has a similar geometry to the TCBtb in
 3711 Figure 4.6, located 10 km to the south, and likely formed in a very similar way. The top
 3712 basement offset in its flank, coincident with dipping reflections in the crust and mantle and a
 3713 possible offset in the Moho, likely developed in response to a west verging thrust. As this
 3714 structure does not offset crosscutting, east verging reflections, it likely developed at an
 3715 earlier stage. The bulbous crustal thickening in the western half of Figure 4.10 contains
 3716 dipping reflections that may be coincident with hummocks in the top of the basement, and
 3717 likely results from thrusting of the crust, similar to that seen along line tz3_3600 (east).
 3718 Possible offsets of the dipping reflections may indicate a time progression of thrusting. Sub-

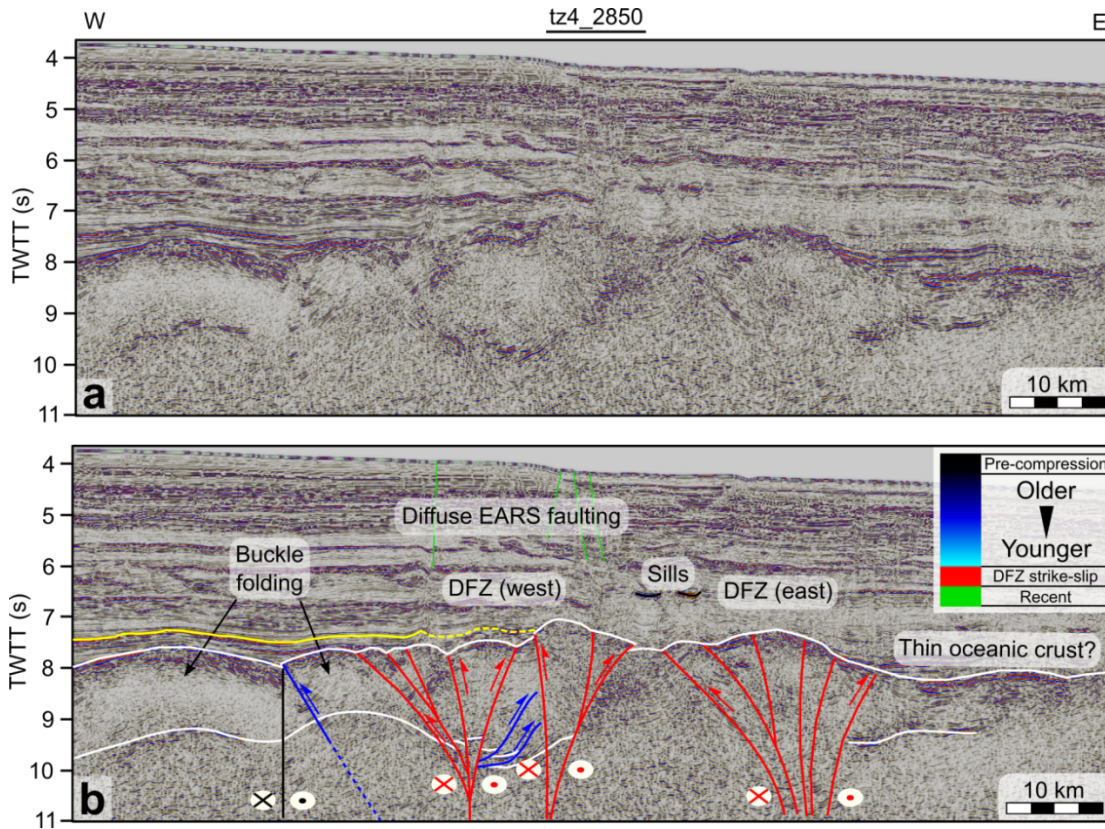
3719 vertical faults, offsetting the basement and bounding areas of different crustal characteristics,
3720 likely separate the crustal thickening from undeformed crust to the east and offset earlier
3721 thrusts. The steepness of these faults and inconsistent offsets of Moho and top basement
3722 interfaces along them indicate a strike-slip nature. These faults may therefore form part of a
3723 transform system related to, but offset from, the DFZ (east), which we therefore term the
3724 DFZ (west). 20 km to the east, the second crustal thickening, with reflections possibly
3725 dragged upwards into it along downward steepening faults, likely forms part of the DFZ
3726 (east). This is supported by its similar positive flower geometry and alignment with the trend
3727 of this structure. The two branches of the DFZ are separated by a thin 10 km strip of
3728 undeformed oceanic crust.

3729 **4.4.3.4. Line tz4_2850**

3730 Another 110 km to the south, the DFZ nearly intersects the TCBtb (Figure 4.11). In the west,
3731 folded top basement and Moho interfaces are separated by a seismically transparent mid
3732 crust. This oceanic crust has a thickness of 1.8 s TWTT. The eastern termination of the fold
3733 is marked by the termination of upper crustal reflectivity and mid crustal seismic
3734 transparency along a sub-vertical boundary. A sudden flip in the dip angle of the top
3735 basement, which is also possibly upthrown on the east, occurs just above this and lies along
3736 the trend of the TCBtb. In this location, beneath the west dipping top basement, short,
3737 segmented mid-crustal reflections also dip to the west.

3738 To the east by ~10 km, the top basement interface and internal reflections of the crust are
3739 segmented and folded on a short (~1-3 km) length scale. Beneath this and to the east,
3740 segmented and offset Moho reflections, which dip to the east before reversing to dip to the
3741 west, define the base of a bulbous or lens-shaped thickening of the crust. Several offsets and
3742 hummocks in the top of the basement also define this crustal thickening, which in places
3743 reaches a thickness of ~2.4 s TWTT. This structure lies ~20 km to the west of the trend of
3744 the DFZ (east), and, as seen farther north, therefore likely represents the DFZ (west). Along
3745 the trend of the DFZ (east), a second lens-shaped segment of thickened crust is present,
3746 likely representing this fracture zone. Along the top basement interface of the DFZ (east),
3747 variations in reflector amplitude, dip, and continuity, occur. Below this, reflections which
3748 dip into the central region of the DFZ (east) may align with some of these variations in the
3749 top of the basement. Between the two regions of thickened crust, the structure of the
3750 basement is obscured by sills intruded into the overlying sediments, which precludes a
3751 determination of the crustal thickness in this region. East of the DFZ (east), within the WSB,
3752 strong top basement reflections are underlain by a reflective crustal layer, below which a
3753 high amplitude reflector, possibly the Moho, defines a thin (~1.1 s TWTT) oceanic crust.

3754



3755

3756 **Figure 4.11.** Folding, thrusting, and strike slip deformation along seismic line tz4_2850 in
 3757 response to compression and development of the DFZ. (a) Uninterpreted section. (b)
 3758 Interpreted section. Line descriptions are as for Figure 4.4. The relative ages of the faulting
 3759 are shown in the key. Location shown in Figure 4.1.

3760 In the western part of Figure 4.11, the sudden change in the dip of the top basement at the
 3761 eastern end of the fold suggests a decoupling of the fold from crust to the east. This may
 3762 have occurred along the sub vertical boundary between zones of different crustal reflectivity,
 3763 and/or east dipping thrust faults, which may have also offset and folded the top basement
 3764 interface and mid crustal reflections. These thrust faults lie along the trend of the TCBtb and
 3765 likely form part of this structure. Here, however, at this southern limit of the TCBtb, very
 3766 little crustal thickening has occurred. This is consistent with an earlier cessation of
 3767 compression in the south, as inferred from the deformation of sedimentary packages
 3768 overlying the TCBtb (i.e. Section 4.4.2.5), which would result in less crustal thickening in
 3769 this southern location. The presence of a buckle fold to the west of the TCBtb, is consistent
 3770 with earlier observations of a swap from the development of buckles on the east of the
 3771 TCBtb in the north to on the west in the south, likely related to the age of the crust before
 3772 deformation.

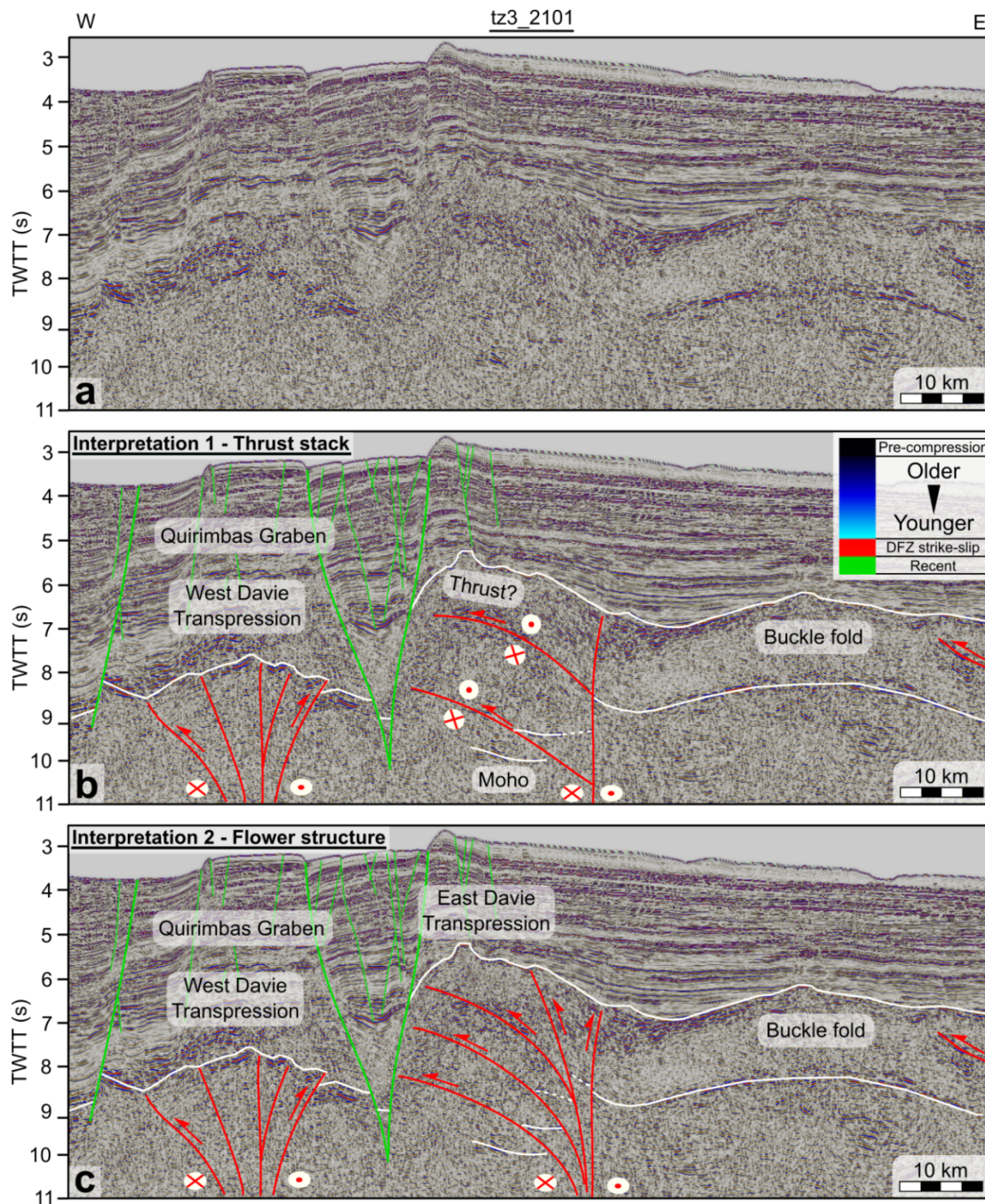
3773 Slightly to the east, the folded and offset segments of crust that form part of the DFZ (west)
3774 may be bounded by discontinuities that dip towards the centre of the lens-shaped area of
3775 thickened crust, defining a positive flower structure. In the central region of the DFZ (west),
3776 thrust faults, which stack and thicken the crust, may also present. In this interpretation, these
3777 gently dipping faults have been cut by later, steeper, strike-slip faults, consistent with the
3778 onset of strike-slip deformation after thrusting, as inferred elsewhere along the DFZ (e.g.
3779 tz3_3600 (east)). The DFZ (east), which likely also forms a positive flower structure, is
3780 again offset from the DFZ (west) by ~20 km, suggesting that these features run parallel to
3781 each other. This is confirmed by observations made at several other locations as summarised
3782 in Figure 4.1.

3783 **4.4.3.5. Line tz3_2101**

3784 Line tz3_2101 intersects the DFZ some 215 km to the south of the previous line. It is located
3785 to the south of the extinct spreading centre of the WSB (Chapter 2), and shows elements of
3786 the Quirimbas Graben (Franke et al., 2015). This recent extension is related to the East
3787 African Rift System and overprints deformation associated with the DFZ (Figure 4.12).
3788 Nonetheless, at the western edge of the section beneath the Quirimabas Graben, top
3789 basement reflections are identifiable and step down to the west across normal faults.
3790 Approximately 20 km from the western edge of Figure 4.12, normal faulting becomes
3791 reduced and a horst structure forms a relatively uplifted area of seafloor. Beneath the horst,
3792 segmented, but high amplitude, basement reflections define a generally domed shape of the
3793 top basement, which sits nearly along the trend of the DFZ (west). To the east, a subsidiary
3794 basin separates this basement dome from a second region of uplifted basement, which sits at
3795 depths as shallow as 5.3 s TWTT, as much as 1.7 s TWTT above the surrounding basement.
3796 Beneath this basement uplift, which sits nearly along the trend of the DFZ (east), a diffuse
3797 band of east dipping, mid-high amplitude, reflections sits at a depth of ~6.9 s. Below this, at
3798 depths of 9.3 s and 9.8 s TWTT, other reflections also dip gently to the east or lie sub-
3799 horizontal. These may define an offset in the Moho, which has been upthrown on the east.
3800 Inspection of crosslines to tz3_2101 along the western edge of this uplifted crust reveals that
3801 the faults, with a generally E-W strike, bend northwards as they approach the western edge
3802 of the uplift.

3803 To the east of this belt of crustal thickening, top basement and Moho reflections have been
3804 folded, and define a buckle fold with a wavelength of ~50 km that has developed in the
3805 oceanic crust. Near the eastern edge of Figure 4.12, a step up in the top of the basement is
3806 aligned with a high amplitude east dipping reflector in the mid crust.

3807



3809

3810 **Figure 4.12.** Folding, thrusting, and strike-slip deformation along seismic line tz3_2101 in
 3811 response to compression and development of the DFZ, and graben formation in response to
 3812 extension across the Quirimbas Graben. (a) Uninterpreted section. (b) Interpreted section
 3813 based on the transportation of thrust sheets along the strike of the DFZ (east). (c) Interpreted
 3814 section based on flower structure development along the DFZ (east). Line descriptions are as
 3815 for Figure 4.4. The relative ages of the faulting are shown in the key. Location shown in
 3816 Figure 4.1.

3817 The uplift of the top basement beneath the horst block within the Quirimbas graben is not
 3818 wholly accounted for by the reduced extension across this structure, and may therefore

3819 indicate a relative thickening of the crust in this region. To the east, top basement and Moho
3820 reflections record a crustal thickening to 4.7 s TWTT, more than twice the original crustal
3821 thickness. Allowing for 5 – 12 km of recent extension across the DFZ (Franke et al., 2015),
3822 the two regions of thickened crust in Figure 4.12 are closely aligned with the trends of the
3823 large offset DFZ (east) and DFZ (west), suggesting that they are the southern continuations
3824 of these structures.

3825 The geometry of the top of the basement around the DFZ (west) is consistent with a
3826 compressional flower structure, as seen elsewhere along this fracture zone. The amount of
3827 crustal thickening recorded at the DFZ (east), however, is greater than anywhere else along
3828 this structure. Eastward dipping reflections within the crust and an offset in the Moho imply
3829 a general tilting of the crust to the east due to east dipping compressional faults. The detailed
3830 nature of the crustal structure is, however, not well constrained by the data, and in Figure
3831 4.12 b and c, we therefore present two scenarios that are consistent with the main
3832 observations. Interpretation 1 (Figure 4.12b) employs a sequence of stacked thrusts sliding
3833 along each other, into the plane of Figure 4.12, to achieve greater than twice the original
3834 crustal thickness in this location. Interpretation 2 (Figure 4.12c) employs steeper faults,
3835 within a large flower structure, to achieve a similar effect.

3836 The cause of this possible change in style and amount of crustal thickening in this location
3837 may be revealed by the presence of E-W trending faults that bend northwards as they
3838 approach the western boundary of the DFZ (east). Ordinarily, normal faults generated at an
3839 oceanic spreading centre near to a MOR transform offset bend in the direction of the
3840 adjacent spreading centre (Davies et al., 2005). This is caused by a rotation of σ_1 on
3841 approach to the transform fault due to the local influence of opposing plate motions across
3842 the fault. Within the WSB, MOR segments have a left lateral offset (e.g. Cochran, 1988;
3843 Chapter 2), and the adjacent MOR segment across the DFZ lies in the Mozambique basin.
3844 Ordinarily, therefore, faults within the WSB adjacent to the DFZ should bend to the south,
3845 opposite to the observed trend. Faults that develop along the borders of transpressional
3846 stepover basins, however, can show the opposite trend (e.g. (McClay and Bonora, 2001)). A
3847 step to the east, when moving south along the DFZ (east), would result in such a
3848 transpressional push-up structure, with faults within the WSB bending to the north adjacent
3849 to the DFZ (east). The large offset across the DFZ would likely supply a large amount of
3850 crust into this transpressional zone, allowing a large amount of observed crustal thickening.
3851 Both low-angled thrusts and steep faulted flower structures have been shown to develop
3852 under such transpressional conditions from analogue modelling (e.g. McClay and Bonora,

3853 2001), and it is likely that a combination of these structures, from both Figure 4.12b and c,
3854 contributed to the crustal thickening of the DFZ (east).

3855 Recent extension across the Quirimbas Graben is localised along the flanks of the DFZ (east
3856 and west), and likely reactivates these structures, resulting in the development of a horst
3857 above the DFZ (west). The northward termination of extension associated with the
3858 Quirimbas Graben coincides with the extinct MOR system of the WSB. It is possible,
3859 therefore, that coupling across the DFZ to the north of the Quirimbas Graben due to the
3860 passing of a spreading centre and associated magmatism stopped the extensional reactivation
3861 of the DFZ farther north.

3862 East of the DFZ, a buckle fold and thrust fault, which results in a step in the top of the
3863 basement on the east flank of the fold, have developed. These observations oppose those
3864 from farther north along the DFZ, where to the east of the DFZ (east), the oceanic crust
3865 shows little sign of compressional deformation. Figure 4.12, however, is located to the south
3866 of the MOR system of the WSB, which may provide an explanation for the observed
3867 compressional deformation in this location. To the north of the MOR, no relative motion
3868 occurs across the DFZ subsequent to the formation of adjacent oceanic crust. To the south
3869 of the MOR, however, this is no longer true. Oceanic crust accreted to the south of the
3870 MOR, and adjacent to the DFZ, formed part of the East Gondwana plate. This crust will
3871 have, therefore, subsequently undergone a protracted history of transportation along the
3872 transpressional DFZ, until the final cessation of spreading in the WSB at ~125 Ma. This
3873 transpression may have resulted in the observed buckle folding and compressional
3874 deformation of Figure 4.12. Transpression of this crust would have begun immediately after
3875 its formation at the MOR, and is consistent with the short 50 km wavelength of the buckle
3876 fold, which must have formed in extremely young oceanic lithosphere.

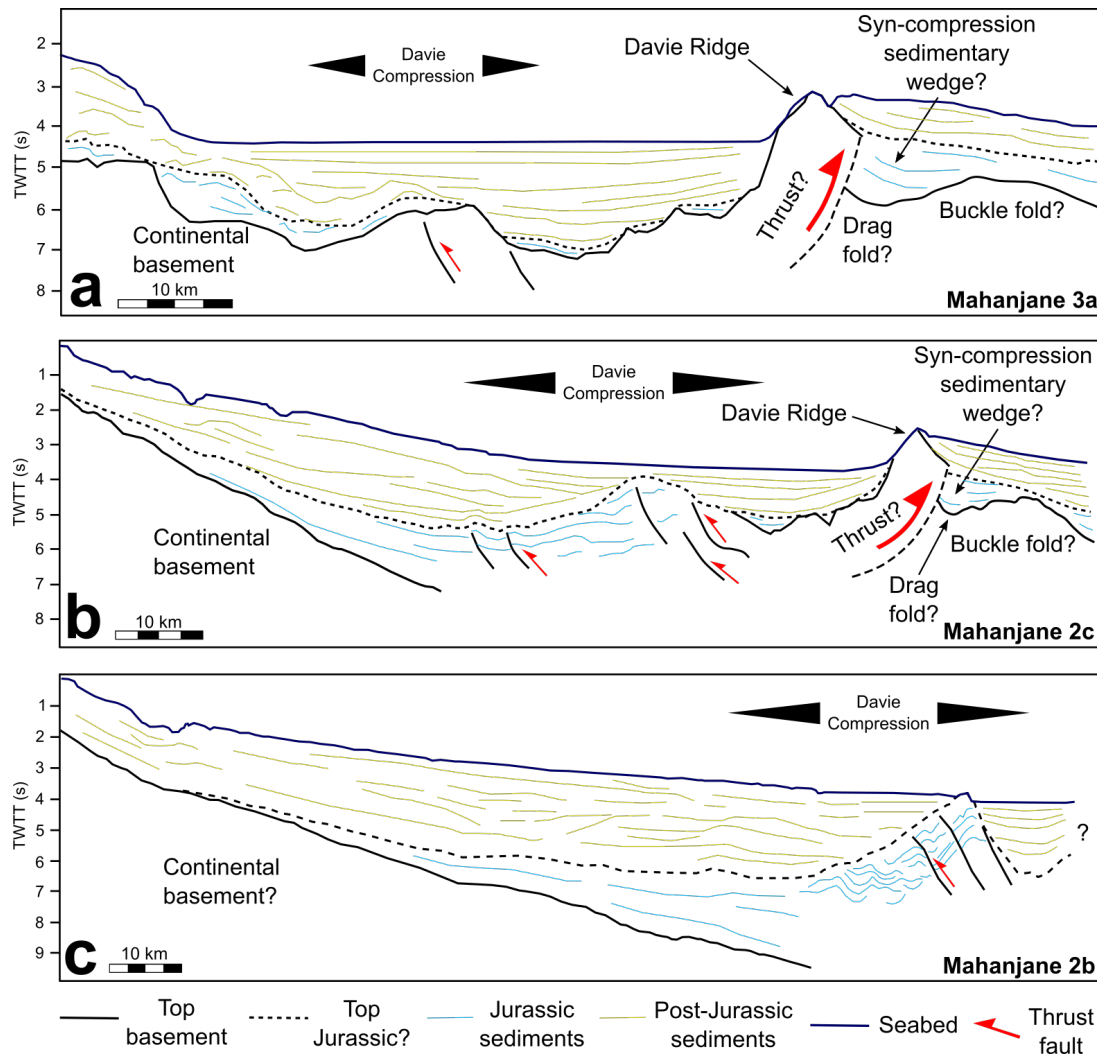
3877 **4.4.3.6. South of the Quirimbas Graben**

3878 To the south of the Quirimbas Graben, gravity modelling and investigation of seismic
3879 reflection lines mz1_8100, mz1_8000, and mz1_7500, has been performed in Chapter 3
3880 (Figures 3.5 and 3.11). Along line mz1_8100, The DFZ is obscured by the St Lazare
3881 volcanic edifice, but lines mz1_8000 and mz1_7500 are clear of volcanics, and allow for an
3882 investigation of basement structures associated with the DFZ. Along the trend of the DFZ
3883 (east), line mz1_8000 displays a thickening of the crust from 2 s TWTT to 2.5 s TWTT. To
3884 the west of the DFZ (east), a zone of possible exhumed mantle exists, which may result in
3885 the lack of observed crustal thickening along the trend of the DFZ (west). The amount of
3886 crustal thickening along the DFZ (east) is similar to observations along the northern DFZ,
3887 and the large amount of crustal thickening observed along line tz3_2101, possibly associated

3888 with a transpressional stepover basin along the DFZ (east), does not continue to this point.
3889 380 km to the south of this, line mz1_7500 displays a well-developed positive flower
3890 structure along the approximate trend of the DFZ (west), and a 20 km wide zone of 3.3 s
3891 TWTT thick crust has developed. However, 20 km to the east no evidence for strike-slip
3892 tectonics along the trend of the DFZ (east) is present and instead a thrust fault, which offsets
3893 the Moho, thickens the crust in this location.

3894 The Rovuma Transform Margin (Figure 4.1, dark green symbols) has also been identified
3895 along these three seismic and gravity profiles (Chapter 3), and runs in a SSE direction. It is
3896 aligned with the Davie Compression (Figure 4.1, red circles), a SSE trending fold and thrust
3897 belt composed predominantly of Jurassic and basement rocks (Mahanjane, 2014; Figures
3898 4.13a, b, and c). The natural prolongation of the large offset Rovuma Transform Margin into
3899 the trend of the Davie Compression (Figure 4.1), suggests a genetic relationship between
3900 these two features, and we propose that the Davie Compression forms the transform
3901 continent-ocean boundary along the eastern edge of the Angoche basin.

3902 To the east of the SSE trending Davie Compression, the Davie Ridge, an ~N-S trending
3903 prominent basement high which generally protrudes 2-3 s TWTT above the surrounding
3904 basement (Figure 4.13a and b), forms the natural extension of the DFZ farther north (Figure
3905 4.1). This uplifted basement structure has previously been interpreted as a rift shoulder uplift
3906 (e.g. Mahanjane, 2014), similar to the uplifted flanks of the Quirimbas Graben farther north.
3907 However, dredge samples recovered from the DFZ show a metamorphic P-T path associated
3908 with compressional tectonics, (Bassias, 1992). The geometry of the Davie Ridge, visible in
3909 published seismic sections (e.g. Mahanjane, 2014), shares characteristics with thrusts
3910 observed along the TCBtb. To the east of the Davie Ridge, flexure of the basement has led to
3911 the development of a sedimentary basin and, approaching the ridge, the top basement is bent
3912 upwards towards the uplifted basement. An erosion surface has developed along the top of
3913 the highly rotated basement of the Davie Ridge, and possibly bounds syn-compressional
3914 sediments deposited in the adjacent basin (Figure 4.13.a and b). This is similar to the
3915 geometries that developed along the TCBtb in response to compressional flexure, thrust
3916 faulting, and associated fault drag folding. We therefore tentatively suggest that the Davie
3917 Ridge may, in fact, be composed of oceanic crust and meta-sediments, compressed and
3918 uplifted by thrusting. If the Davie Ridge is such a thrust structure, it likely developed in
3919 response to the compressional stresses that led to the development of the Davie
3920 Compression, or during the compression near the end of the Jurassic, when this crust may
3921 have been attached to East Gondwana, conjugate to the compressed crust within the TCB.



3923

3924 **Figure 4.13.** Line drawings of seismic reflection data from Mahanjane (2014), which have
 3925 been re-interpreted in this study. (a) Figure 3a of Mahanjane (2014). (b) Figure 2c of
 3926 Mahanjane (2014). (c) Figure 2b of Mahanjane (2014). Location shown in Figure 4.1.

3927 4.4.3.7. Summary of the DFZ formation

3928 Bounding the eastern edge of the TCB and the Mozambique Basin, the DFZ appears as a
 3929 2000 km arcuate free-air gravity low between -5°S and -25°S (Figure 4.1), following a
 3930 single small circle with the pole of rotation at $10.15\text{ S}, 74.30\text{ E}$. Our interpretation of seismic
 3931 reflection data supports the presence of steep strike-slip faults and transpressional flower
 3932 structures along the DFZ, and different tectonic crustal histories on either side of the DFZ.
 3933 This combined evidence supports the interpretation of this structure as a large-offset fracture
 3934 zone along which East Gondwana was transported southwards. Along the majority of the
 3935 DFZ, crustal thickening, generally to $\sim 2.8\text{ s TWTT}$, but possibly of up to 4.7 s TWTT ,
 3936 results from thrusting and the development of transpressional flower structures. Faults
 3937 associated with strike-slip motion and flower development generally cut older thrust faults,

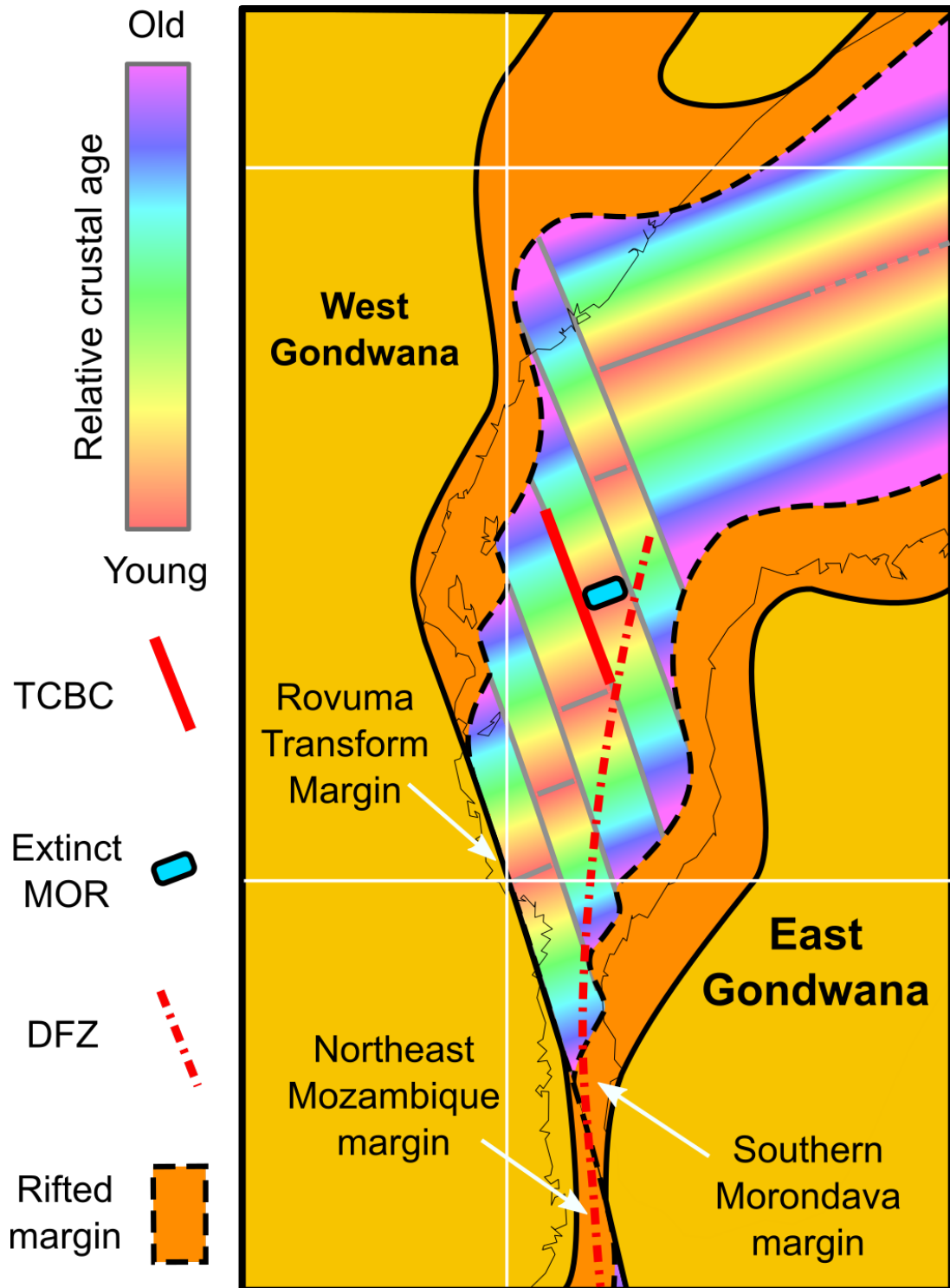
3938 possibly reflecting a shift from compression to transpression over time. In general,
3939 deformation along the DFZ has been dominated by transpression throughout its history, and
3940 little evidence for transtension is present.

3941 Along most of the length of the WSB, the DFZ is comprised of a pair of transpressional
3942 fracture zones, which run parallel to each other from 7°S to just below the Comoros Islands
3943 c. 13°S. North and south of these latitudes, evidence for strike-slip motion only exists along
3944 the trends of the DFZ (east) and DFZ (west), respectively, with a termination of strike-slip
3945 deformation along the trend of the other DFZ branch. The northern termination of the DFZ
3946 (west), however, lies at the intersection of a SSE trending fold and thrust belt within the
3947 TCB (Figure 4.1). Given that SSE trending thrust belts within the TCB seem to have
3948 developed along pre-existing fracture zones, the initiation of the DFZ (west) at an
3949 intersection with such a thrust belt may indicate a genetic link between these two structures.
3950 In the south, along the trend of the DFZ (east) on line mz1_7500, the presence of a thrust,
3951 but no indication of strike-slip motion, may suggest a similar termination of the DFZ (east)
3952 into a pre-existing SSE trending FZ. Whether such a join between the DFZ and SSE trending
3953 fracture zones occurred gradually, through the formation of arcuate fracture zones, or
3954 suddenly, through the development of crosscutting faults, is not constrained by the available
3955 data. However, the lack of bending of the southern TCBtb into the DFZ suggests that any
3956 previous fracture zone in this location was cut by the DFZ, rather than merging with this
3957 structure. This is supported by the extinction of the MOR to the NE of the TCBtb (Figure
3958 4.3), suggesting a sudden abandonment of the spreading configuration, as opposed to a
3959 gradual change in spreading directions, which might have allowed this spreading centre to
3960 remain active.

3961 Formation of the DFZ, whether gradual or sudden, resulted from a change in plate motion
3962 near the end of the Jurassic (e.g. Reeves et al., 2016; Chapter 3), when an alignment between
3963 the obliquely rifted northeast Mozambique margin and southern Morondava margin
3964 occurred (Figure 4.14). To the north of these juxtaposed margins, plate tectonic modelling
3965 (e.g. Phethean et al., 2016) predicts a series of left-stepping spreading centres running north-
3966 south, close to the eastern edge of the present day TCB. The presence of an extinct MOR
3967 segment near to the DFZ in the north of the TCB, and the occurrence of short wavelength
3968 buckle folds, which are associated with young (< 3 Myrs) oceanic crust, close to the DFZ on
3969 the SW side of the TCBtb, is consistent with this prediction. This alignment of weak rifted
3970 margins and young oceanic lithosphere (Figure 4.14) may have influenced the timing of the
3971 plate rotation, and the location of the DFZ development. The plate rotation, near the end of
3972 the Jurassic, likely resulted in transpression along incompatible fracture zones in the TCB,

3973 and presents a possible driving mechanism for the compression seen there. Development of
3974 the DFZ, which was compatible with the new plate motion, however, would remove this
3975 driving mechanism of compression within the TCB. As the sedimentary record along the
3976 TCBtb suggests an earlier cessation of compression along the south of this structure,
3977 compared to north, it may also be the case that the DFZ developed from the south,
3978 propagating northwards to form the edge of the TCB.

3979



3981

3982 **Figure 4.14.** Plate configuration around the end of the Jurassic. Transformation of East
 3983 Gondwana along the Rovuma Transform Margin has led to the alignment of the southern
 3984 Morondava and north-east Mozambique oblique rifted margins, and release of East
 3985 Gondwana from the constraints of strong lithosphere along this transform boundary. A
 3986 contemporaneous alignment of young oceanic crust to the north may have influenced the
 3987 location at which the DFZ developed.

3988 **4.5. Regional tectonic interpretation**

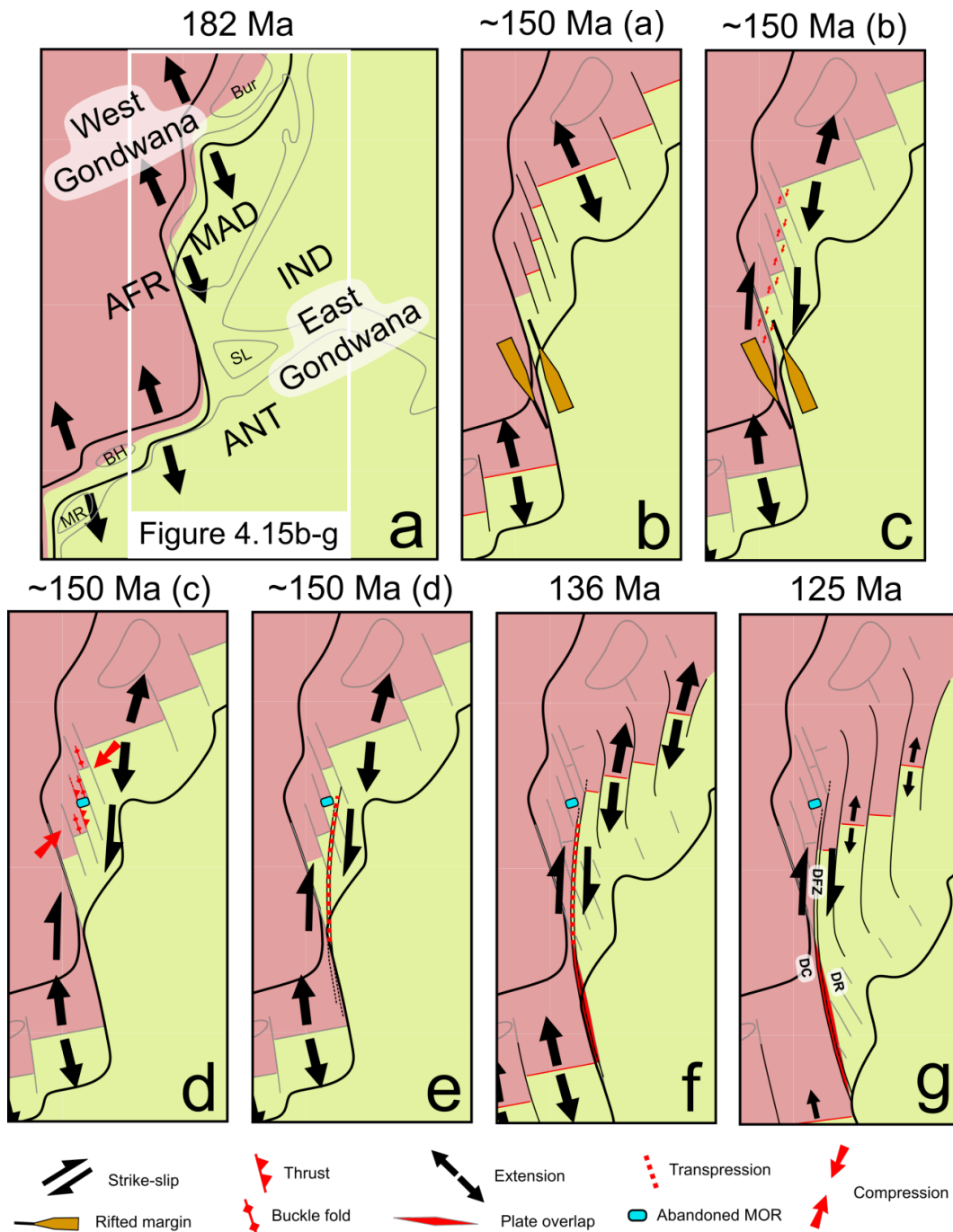
3989 Observations of compression within the TCB, followed by strike-slip and transpression
3990 along the DFZ, likely result from the change in plate motions of East Gondwana relative to
3991 West Gondwana during plate separation. These observations are, therefore, tied to this
3992 broader regional tectonic context below:

- 3993 • Following a tight initial fit of Madagascar within Africa (Section 4.3), rifting
3994 between East and West Gondwana began at ~182 Ma (Figure 4.15a; Geiger et al.,
3995 2004), coincident with the eruption of the Karoo large igneous province in
3996 Mozambique (e.g. Riley and Knight, 2001). This resulted in oblique margin
3997 formation along northeastern Mozambique and the Southern Morondava Basin in
3998 Madagascar (Chapter 3).
- 3999 • Following continental breakup at ~170 Ma (e.g. Chapter 2), an initial phase of SSE
4000 plate separation translated Southern Madagascar (attached to East Gondwana) along
4001 the Rovuma Transform Margin of Northern Mozambique (Figure 4.15a-b; Chapter
4002 3). Due to the large offset of the Angoche Basin and Tanzania Coastal Basin across
4003 the Rovuma Transform Margin (Chapter 3), these basins are unlikely to have
4004 overlapped and were, therefore, likely connected by transform faults at the onset of
4005 rifting (Section 1.2.2.1). This means no rifting of the lithosphere along the Rovuma
4006 Transform Margin would have occurred prior to strike-slip motions, maintaining the
4007 thickness and strength of this lithosphere.
- 4008 • At ~150 Ma, an alignment of the obliquely rifted margins of northeastern
4009 Mozambique and the Southern Morondava Basin occurred across the Rovuma
4010 Transform Margin (Figure 4.15b). Around this time, MOR segments to the north
4011 within the TCB were also aligned with these opposed rifted margins (Figure 4.14).
4012 The timing of this alignment, near the end of the Jurassic, was coincident with a
4013 change in plate motion from SSE to N-S, (Figure 4.15b-c) and it is possible that the
4014 alignment of weaker lithosphere, along the rifted margins and MOR segments,
4015 influenced this change.
- 4016 • This new southerly plate motion was incompatible with SSE trending fracture zones
4017 within the TCB, and resulted in the build-up of transpressional deformation along
4018 these structures (Figure 4.15c), leading to thrusting of oceanic crust along pre-
4019 existing fracture zones and short wavelength buckle folding of young (<3 Ma)
4020 oceanic crust (Figure 4.15d). The extinction of spreading centres within the TCB at
4021 the same time as the onset of compression was probably ultimately caused by this
4022 change in spreading direction. A prediction of this model, which may be tested in

4023 future as more widespread data becomes available, is that this compressional event
4024 will have also affected the Jurassic oceanic crust to the west and northwest of
4025 Madagascar, which at the time was attached to East Gondwana.

- 4026 • This compression, which continued for longer in the north of the basin, was most
4027 likely ended by the development of the DFZ, which propagated northwards and
4028 accommodated the new plate motion (Figure 4.15e). This fracture zone was,
4029 nonetheless, dominated by transpression throughout its history.
- 4030 • Subsequent to the formation of the DFZ at ~ 150 Ma, the southward drift of East
4031 Gondwana led to the overlap of the East and West Gondwana plates across the
4032 southern Rovuma Transform Margin (Figure 4.15f), and thus the collision of south
4033 Madagascar with the obliquely rifted margin of northeast Mozambique (red area,
4034 Figure 4.15f). The Davie Compression, a thrust and inverted sequence of Jurassic
4035 and basement rocks along the eastern edge of the Angoche Basin (Mahanjane,
4036 2014), likely resulted from this plate collision (Figure 4.15g), and may therefore
4037 represent the continent-ocean boundary in this region. The Davie Ridge, which may
4038 be a highly rotated oceanic thrust, may have also developed during this collision.
4039 This is supported by the metamorphic P-T paths from along this structure, which
4040 show a pattern generally associated with collisional settings (Bassias, 1992).

4041



4043

4044 **Figure 4.15.** Plate tectonic model showing the change in plate motion between West
 4045 Gondwana (pink) and East Gondwana (green) at ~ 150 Ma, possibly influenced by the
 4046 alignment of rifted margins offshore Mozambique and Madagascar, and of MOR segments
 4047 in the north. This plate motion change may have resulted in compression within the TCB,
 4048 extinction of MOR segments within the TCB, and development of the DFZ. Subsequently,
 4049 the collision of southern Madagascar with the oblique rifted margin of northeast
 4050 Mozambique during the southward drift of East Gondwana may have led to the development
 4051 of the Davie Compression and Davie Ridge. AFR, Africa; ANT, Antarctica; BH, Biera

4052 High; Bur, Bur High; DC, Davie Compression; DR, Davie Ridge; IND, India; MAD,
4053 Madagascar; MR, Mozambique Rise; SL, Sri Lanka.

4054 **4.6. Implications for plate motion controls**

4055 Plate motions are classically inferred to be controlled by a number of driving forces
4056 originating from the lithosphere and mantle, including: mantle convection (e.g. Ziegler,
4057 1993); slab-pull (Lithgow-Bertelloni, 2014); ridge-push (e.g. Mahatsente and Coblentz,
4058 2015); orogenic collapse (e.g. Rey et al., 2001); and mantle plumes (e.g. Larson, 1991). The
4059 largest change in plate driving forces within the basins surrounding Gondwana was the onset
4060 of subduction along the NeoTethys. However, this was before the Late Jurassic change in
4061 plate motions (Stampfli, 2000). The diachronous subduction of the NeoTethys spreading
4062 ridge, however, may have still been occurring at the time of plate motion changes (e.g.
4063 Stampfli and Borel, 2002). However, the sharp change in spreading direction, indicated by
4064 the cutting of the TCBtb by the DFZ, would be unlikely to have been generated by this
4065 gradual subduction process. In contrast, the alignment of the obliquely rifted northeast
4066 Mozambique margin and Southern Morondava margin with young oceanic spreading centres
4067 farther north occurred relatively rapidly, and at the moment of plate motion change.
4068 Furthermore, following plate rotation and the formation of the DFZ, this large-offset fracture
4069 zone was dominated by transpression throughout its history, suggesting it did not form in
4070 perfect alignment with plate driving forces.

4071 We therefore argue that this change in plate motion was not ‘driven’ by alterations to plate
4072 driving forces, but was partly the consequence of a reduction in resisting forces along the
4073 Rovuma Transform Margin. This reduction was caused by the alignment of weak, rifted
4074 and/or young, lithosphere along the N-S trend of the future DFZ, which provided a new
4075 alternate pathway for East Gondwana that was more, but not perfectly, compatible with plate
4076 driving forces. In this case, prior to the end of the Jurassic, the driving forces required for a
4077 more southerly drift of East Gondwana would have already been active, but were resisted by
4078 plate boundary forces along the strong Rovuma Transform Margin, resulting instead in the
4079 slip of East Gondwana along the trend of this margin. This would have led to transpression
4080 along the Rovuma Transform Margin, and so structural investigations along this margin
4081 could be used to test this model.

4082 **4.7. Conclusions**

4083 A change in the plate motion of East Gondwana near the end of the Jurassic from SSE to
4084 southwards drift led to build-up of transpressional forces along SSE trending fracture zones
4085 within the TCB. This resulted in the onset of compressional tectonics within this basin,
4086 including the development of the SSE trending TCBtb, possibly along a pre-existing fracture
4087 zone, and short wavelength buckle folds, possibly associated with young oceanic crust in
4088 proximity to MOR segments. At the same time, the extinction of spreading centres within
4089 the TCB likely also resulted from the change in spreading direction. This model for the onset
4090 of compression within the TCB predicts that crust that lay conjugate to the TCB, now
4091 situated offshore northern and western Madagascar, would also have been affected by
4092 compression, allowing it to be tested when data becomes available in these regions.

4093 The onset of this plate motion change was coincident with the passing of southern
4094 Madagascar beyond the strong lithosphere of the Rovuma Transform Margin and the
4095 alignment of weak and/or young lithosphere, associated with rifted margins and oceanic
4096 spreading centres, along the future trend of the DFZ. This reduction in lithospheric strength
4097 may have triggered the change in plate motion and would imply first-order control of
4098 resisting forces along transform plate boundaries on the motions of plates during the
4099 dispersal of Gondwana. In this case, prior to the change in plate motions, the Rovuma
4100 Transform Margin may have been under transpression; therefore, structural analyses of this
4101 margin could test this hypothesis.

4102 The development of the DFZ likely ended compression within the TCB, and the earlier
4103 cessation of compression in the south of the basin, as compared to the north, may represent a
4104 south to north propagation of the DFZ along what was to become the eastern boundary of
4105 the TCB. The subsequent drift of East Gondwana along this 2000 km fracture zone was
4106 dominated by transpression, and led to the collision of southern Madagascar with the oblique
4107 rifted margin of northeast Mozambique, forming the Davie Compression, which may
4108 represent the continent-ocean boundary in this region. The Davie Ridge, which may be a
4109 rotated oceanic thrust, may have also developed during this collision.

4110 **4.8. References**

- 4111 Anderson, D.L., 2001. Plate Tectonics as a Far- From- Equilibrium Self-Organized System. *Plate*
4112 *Bound. Zo.* doi:10.1029/GD030p0411
4113 Bassias, Y., 1992. Petrological and geochemical investigation of rocks from the Davie fracture zone
4114 (Mozambique Channel) and some tectonic implications. *J. African Earth Sci.* 15, 321–339.
4115 doi:10.1016/0899-5362(92)90018-8

- 4116 Bécél, A., Shillington, D.J., Nedimović, M.R., Webb, S.C., Kuehn, H., 2015. Origin of dipping
4117 structures in fast-spreading oceanic lower crust offshore Alaska imaged by multichannel seismic
4118 data. *Earth Planet. Sci. Lett.* 424, 26–37. doi:10.1016/j.epsl.2015.05.016
- 4119 Behn, M.D., Ito, G., 2008. Magmatic and tectonic extension at mid-ocean ridges: 1. Controls on fault
4120 characteristics. *Geochemistry, Geophys. Geosystems* 9. doi:10.1029/2008GC001965
- 4121 Besairie, H., 1964. Carte Géologique de Madagascar, Service Géologique de Madagascar, scale
4122 1:1000000.
- 4123 Briggs, S.E., Cartwright, J., Davies, R.J., 2009a. Crustal structure of the deepwater west Niger Delta
4124 passive margin from the interpretation of seismic reflection data. *Mar. Pet. Geol.* 26, 936–950.
4125 doi:10.1016/j.marpetgeo.2008.07.003
- 4126 Briggs, S.E., Davies, R.J., Cartwright, J., Morgan, R., 2009b. Thrusting in oceanic crust during
4127 continental drift offshore Niger Delta, equatorial Africa. *Tectonics* 28, 1–16.
4128 doi:10.1029/2008TC002266
- 4129 Burbank, D.W., Vergés, J., 1994. During Active Thrusting. *J. Geophys. Res.* 99, 20281–20297.
- 4130 Cloetingh, S., Beekman, F., Ziegler, P.A., van Wees, J.-D., Sokoutis, D., 2008. Post-rift
4131 compressional reactivation potential of passive margins and extensional basins. *Geol. Soc.*
4132 *London, Spec. Publ.* 306, 27–70. doi:10.1144/SP306.2
- 4133 Cochran, J.R., 1988. Somali Basin, Chain Ridge, And Origin Of The Northern Somali Basin Gravity
4134 And Geoid Low. *J. Geophys. Res.* 93, 11985–12008. doi:10.1029/JB093iB10p11985
- 4135 Coffin, M.F., Rabinowitz, P.D., Houtz, R.E., 1986. Crustal structure in the Western Somali Basin.
4136 *Geophys. J. R. Astron. Soc.* 331–369.
- 4137 Davies, R.J., MacLeod, C.J., Morgan, R., Briggs, S.E., 2005. Termination of a fossil continent-ocean
4138 fracture zone imaged with three-dimensional seismic data: The Chain Fracture Zone, eastern
4139 equatorial Atlantic. *Geology* 33, 641–644. doi:10.1130/G21530.1
- 4140 Franke, D., Jokat, W., Ladage, S., Stollhofen, H., Klimke, J., Lutz, R., Mahanjane, E.S., Ehrhardt, A.,
4141 Schreckenberger, B., 2015. The offshore East African Rift System: Structural framework at the
4142 toe of a juvenile rift. *Tectonics* 34, 2086–2104. doi:10.1002/2015TC003922
- 4143 Geiger, M., Clark, D.N., Mette, W., 2004. Reappraisal of the timing of the breakup of Gondwana
4144 based on sedimentological and seismic evidence from the Morondava Basin, Madagascar. *J.*
4145 *African Earth Sci.* 38, 363–381. doi:10.1016/j.jafrearsci.2004.02.003
- 4146 Hardy, S., Ford, M., 1997. Numerical modeling of trishear fault propagation folding. *Tectonics* 16,
4147 841–854. doi:10.1029/97TC01171
- 4148 Harper, G.D., 1985. Tectonics of slow spreading mid-ocean ridges and consequences of a variable
4149 depth to the brittle/ductile transition. *Tectonics* 4, 395–409. doi:10.1029/TC004i004p00395
- 4150 Jiménez-Munt, I., Fernández, M., Vergés, J., Afonso, J.C., Garcia-Castellanos, D., Fullea, J., 2010.
4151 Lithospheric structure of the Gorringe Bank: Insights into its origin and tectonic evolution.
4152 *Tectonics* 29, 1–16. doi:10.1029/2009TC002458
- 4153 King, S.D., Lowman, J.P., Gable, C.W., 2002. Episodic tectonic plate reorganizations driven by
4154 mantle convection. *Earth Planet. Sci. Lett.* 203, 83–91. doi:10.1016/S0012-821X(02)00852-X
- 4155 Larson, R.L., 1991. Geological consequences of superplumes. *Geology* 19, 963–966.
4156 doi:10.1130/0091-7613(1991)019<0963:GCOS>2.3.CO
- 4157 Lithgow-Bertelloni, C., 2014. Driving Forces: Slab Pull, Ridge Push BT - Encyclopedia of Marine
4158 Geosciences, in: Harff, J., Meschede, M., Petersen, S., Thiede, J. (Eds.), . Springer Netherlands,
4159 Dordrecht, pp. 1–6. doi:10.1007/978-94-007-6644-0_105-1
- 4160 Loudon, K.E., Osler, J.C., Srivastava, S.P., Keen, C., 1996. Formation of oceanic crust at slow-
4161 spreading rates: New constraints from an extinct spreading center in the Labrador Sea. *Geology* 24,
4162 771–774.
- 4163 Mahanjane, E.S., 2014. The Davie Fracture Zone and adjacent basins in the offshore Mozambique
4164 Margin - A new insights for the hydrocarbon potential. *Mar. Pet. Geol.* 57, 561–571.
4165 doi:10.1016/j.marpetgeo.2014.06.015
- 4166 Mahatsente, R., Coblentz, D., 2015. Ridge-push force and the state of stress in the Nubia-Somalia
4167 plate system. *Lithosphere* 7, 503–510. doi:10.1130/L441.1
- 4168 Malinverno, A., 1990. A Quantitative Study of the Axial Topography of the Mid-Atlantic Ridge. *J.*
4169 *Geophys. Res.* 95, 2645–2660.
- 4170 Mammerickx, J., Sandwell, D., 1986. Rifting of old oceanic lithosphere. *J. Geophys. Res.* 91, 1975.
4171 doi:10.1029/JB091iB02p01975
- 4172 Massell, C.G., Coffin, M.F., Mann, P., Mosher, S., Frohlich, C., Schuur, C.L., Karner, G., Ramsay,
4173 D., Lebrun, J.-F., 2000. Neotectonics of the Macquarie Ridge Complex, Australia-Pacific plate
4174 boundary. *J. Geophys. Res.* 105, 13,457–13,480. doi:10.1029/1999JB900408

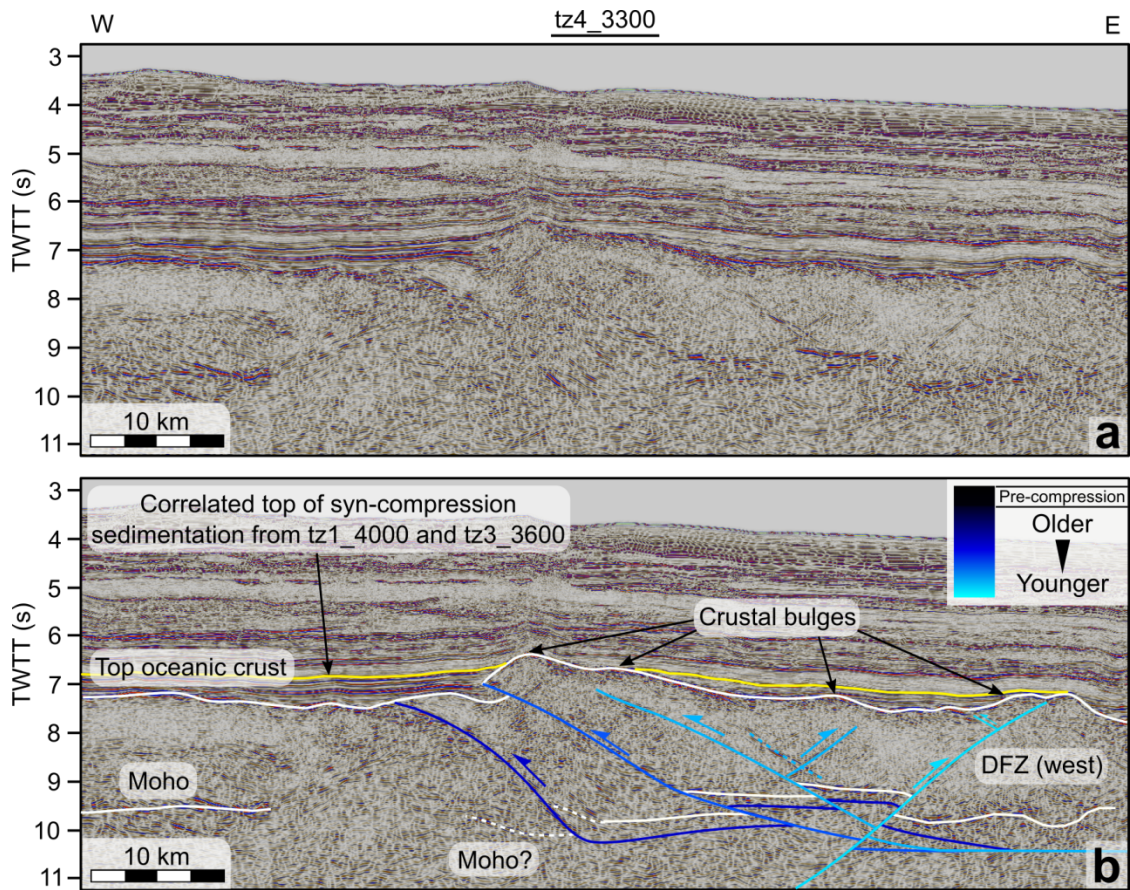
- 4175 McAdoo, D.C., Sandwell, D.T., 1985. Folding of Oceanic Lithosphere. *J. Geophys. Res.* 90, 8563–
4176 8569.
- 4177 McClay, K., Bonora, M., 2001. Analog models of restraining stepovers in strike-slip fault systems.
4178 *Am. Assoc. Pet. Geol. Bull.* 85, 233–260. doi:10.1306/8626C7AD-173B-11D7-
4179 8645000102C1865D
- 4180 Morris, E., Detrick, R.S., Minshull, T.A., Mutter, J.C., White, R.S., Su, W., Buhl, P., 1993. Seismic
4181 Structure of Oceanic Crust in the Western North Atlantic. *J. Geophys. Res.* 98, 13879–13903.
4182 doi:10.1029/93JB00557
- 4183 Müller, R.D., Smith, W.H.F., 1993. Deformation of the oceanic crust between the North American
4184 and South American Plates. *J. Geophys. Res. Solid Earth* 98, 8275–8291. doi:10.1029/92JB02863
- 4185 Niu, Y., Hékinian, R., 1997. Spreading-rate dependence of the extent of mantle melting beneath ocean
4186 ridges. *Nature*. doi:10.1038/385326a0
- 4187 Nunns, A.G., 1983. Plate Tectonic Evolution of the Greenland-Scotland Ridge and Surrounding
4188 Regions BT - Structure and Development of the Greenland-Scotland Ridge: New Methods and
4189 Concepts, in: Bott, M.H.P., Saxov, S., Talwani, M., Thiede, J. (Eds.), . Springer US, Boston, MA,
4190 pp. 11–30. doi:10.1007/978-1-4613-3485-9_2
- 4191 Reeves, C.V., de Wit, M.J., Sahu, B.K., 2004. Tight Reassembly of Gondwana Exposes Phanerozoic
4192 Shears in Africa as Global Tectonic Players. *Gondwana Res.* 7, 7–19. doi:10.1016/S1342-
4193 937X(05)70302-6
- 4194 Reeves, C. V, Teasdale, J.P., Mahanjane, E.S., 2016. Insight into the Eastern Margin of Africa from a
4195 new tectonic model of the Indian Ocean. *Geol. Soc. London, Spec. Publ.* 431, 1–24.
4196 doi:10.1144/SP431.12
- 4197 Rey, P., Vanderhaeghe, O., Teyssier, C., 2001. Gravitational collapse of continental crust: definitions,
4198 regimes, mechanisms and modes. *Tectonophysics* 342, 435–449.
- 4199 Riley, T.R., Knight, K.B., 2001. Age of pre-break-up Gondwana magmatism. *Antarct. Sci.* 13, 99–
4200 110. doi:10.1017/S0954102001000177
- 4201 Sandwell, D.T., Muller, R.D., Smith, W.H.F., Garcia, E., Francis, R., 2014. New global marine
4202 gravity model from CryoSat-2 and Jason-1 reveals buried tectonic structure. *Science* (80-.). 346,
4203 65–67. doi:10.1126/science.1258213
- 4204 Sauter, D., Unternehr, P., Manatschal, G., Tugend, J., Cannat, M., Le Quellec, P., Kuszniir, N.,
4205 Munsch, M., Leroy, S., de Lepinay, J.M., Granath, J.W., Horn, B.W., 2016. Evidence for magma
4206 entrapment below oceanic crust from deep seismic reflections in the Western Somali Basin.
4207 *Geology* 44, 407–410. doi:10.1130/G37747.1
- 4208 Schandelmeier, H., Bremer, F., Holl, H.G., 2004. Kinematic evolution of the Morondava rift basin of
4209 SW Madagascar - From wrench tectonics to normal extension. *J. African Earth Sci.* 38, 321–330.
4210 doi:10.1016/j.jafrearsci.2003.11.002
- 4211 Schiffer, C., Peace, A., Phethean, J., Gernigon, L., McCaffrey, K.J.W., Petersen, Kenni, D., Foulger,
4212 G., In Press. The Jan Mayen Microplate Complex and the Wilson Cycle. *Geol. Soc. London, Spec.*
4213 *Publ.*
- 4214 Silver, P.G., Russo, R.M., Lithgow-Bertelloni, C., 1998. Coupling of South American and African
4215 Plate Motion and Plate Deformation. *Science* (80-.). 279, 60–63.
4216 doi:10.1126/science.279.5347.60
- 4217 Smith, D., 2013. Tectonics: Mantle spread across the sea floor. *Nat. Geosci.* 6, 247–248.
4218 doi:10.1038/ngeo1786
- 4219 Stampfli, G.M., 2000. Tethyan oceans. *Geol. Soc. London, Spec. Publ.* 173, 1–23.
4220 doi:10.1144/GSL.SP.2000.173.01.01
- 4221 Stampfli, G.M., Borel, G.D., 2002. A plate tectonic model for the Paleozoic and Mesozoic
4222 constrained by dynamic plate boundaries and restored synthetic oceanic isochrons. *Earth Planet.*
4223 *Sci. Lett.* 196, 17–33. doi:10.1016/S0012-821X(01)00588-X
- 4224 Vauchez, A., Tommasi, A., Barruol, G., 1998. Rheological heterogeneity, mechanical anisotropy and
4225 deformation of the continental lithosphere. *Tectonophysics* 296, 61–86. doi:10.1016/S0040-
4226 1951(98)00137-1
- 4227 White, R.S., McKenzie, D., O’Nions, R.K., 1992. Oceanic crustal thickness from seismic
4228 measurements and rare earth element inversions. *J. Geophys. Res.* 97, 19683–19715.
4229 doi:10.1029/92JB01749
- 4230 Whittaker, J.M., Williams, S.E., Halpin, J.A., Wild, T.J., Stilwell, J.D., Jourdan, F., Daczko, N.R.,
4231 2016. Eastern Indian Ocean microcontinent formation driven by plate motion changes. *Earth*
4232 *Planet. Sci. Lett.* 454, 203–212. doi:10.1016/j.epsl.2016.09.019
- 4233 Ziegler, P.A., 1993. Plate-moving mechanisms: their relative importance. *J. Geol. Soc. London.* 150,
4234 927–940. doi:10.1144/gsjgs.150.5.0927

4235 **4.9. Supplementary material**

4236 4.9.1. Alternative interpretation of seismic line tz4_3300

4237

4238



4239

4240 **Figure S4.1.** The lower of the dual bands of reflections around the level of the Moho may
4241 alternatively represent a shear boundary, which has been subsequently offset. The
4242 continuation of the structures at depth is speculative.

4243 **5. Discussion, conclusions, and** 4244 **future work**

4245 Plate tectonic modelling of the WSB, based on the analysis of gravity lineaments related to
4246 ocean spreading features, shows that two phases of spreading led to the development of this
4247 basin. The more recent phase, between the Late Jurassic (~150 Ma) and Aptian (~125 Ma),
4248 involved a simple north-south translation of East Gondwana along the DFZ, and has been
4249 recognised previously (e.g. Coffin and Rabinowitz, 1987; Gaina et al., 2013). The Earlier
4250 phase between Middle Jurassic (~170Ma) and Late Jurassic, however, deviates from the
4251 previous academic consensus for the region and involves a NNW-SSE motion of East
4252 Gondwana. This motion places the origin of Madagascar within the TCB, inboard of the
4253 DFZ, which is supported by the identification of oceanic crust inboard of the DFZ. The
4254 initial SSE motion also predicts the existence of a SSE trending transform margin along the
4255 Rovuma Basin (Chapter 2). Subsequent identification of the Rovuma Transform Margin
4256 using seismic and gravity methods (Chapter 3), confirms this controversial phase of NNW-
4257 SSE spreading during the Jurassic. This changes the interpretation of the DFZ, previously
4258 thought to be a continent-ocean fracture zone, to an ocean-ocean fracture zone and
4259 consequently shifts the location of the continent-ocean transition landward within the TCB.
4260 This changes our understanding of the crustal affinity within the TCB, and the hydrocarbon
4261 industry should now consider that significant portions of the TCB may be oceanic in nature.
4262 This may affect the likelihood of source rock presence in these regions and should also be
4263 taken into account during paleoheatflow modelling.

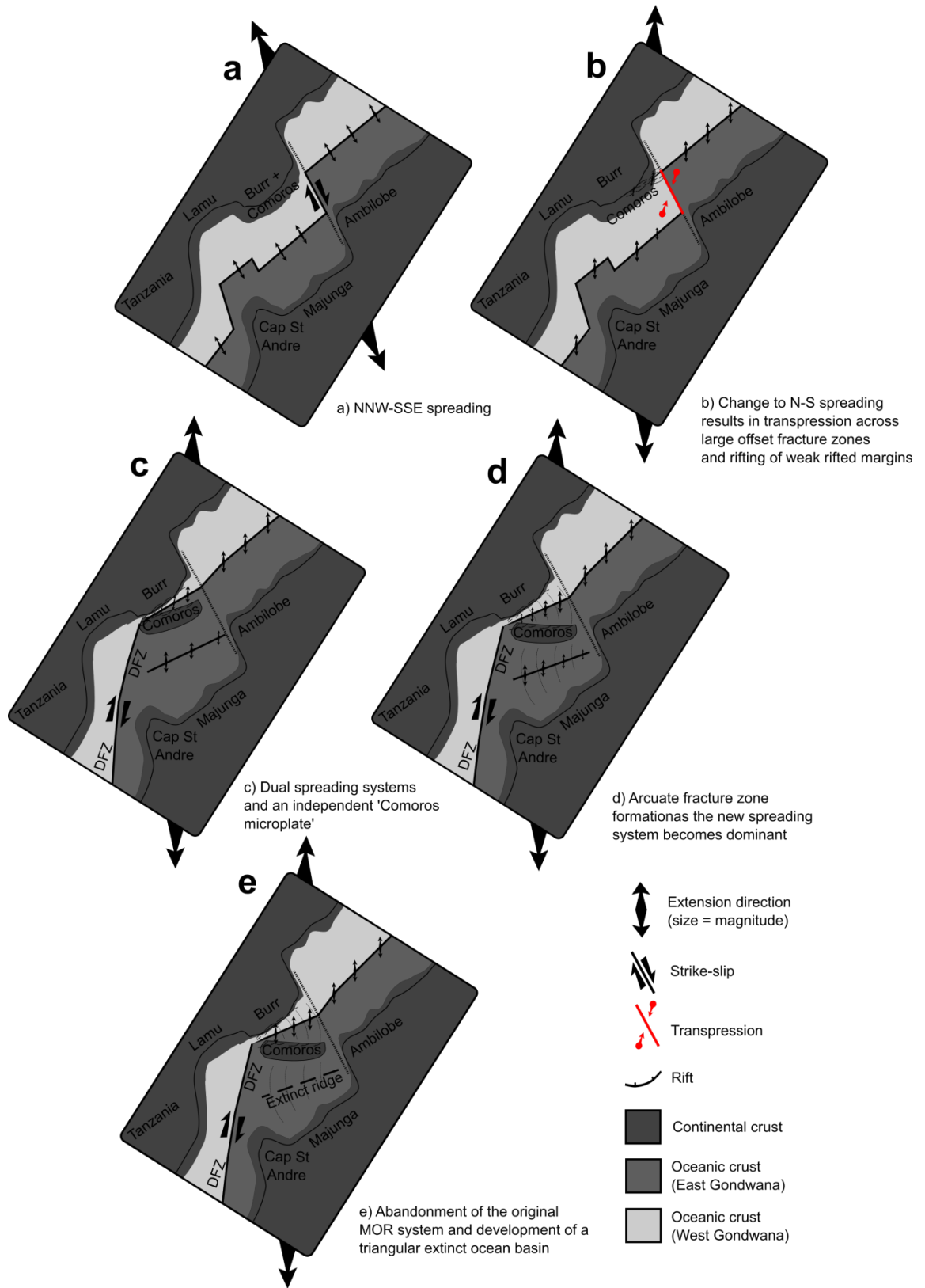
4264 The origin of Madagascar within the TCB also supports a tight initial fit of Gondwana
4265 fragments (Chapter 2), which, combined with the newly determined initial SSE drift of East
4266 Gondwana, has large implications for the types of margins that surround the WSB. The
4267 northern margins of the WSB likely developed roughly orthogonal to the extension direction
4268 and may therefore be interpreted as rifted margins. The western margins, however,
4269 developed at an oblique angle to the extension direction and are therefore likely highly
4270 segmented and/or obliquely rifted margins (Chapter 2). Between these two margins an offset
4271 is required along the western border of the Lamu Embayment to satisfy the fit of
4272 Madagascar within this basin. The offset has a similar trend to the Rovuma Transform
4273 Margin and suggests the presence of another transform margin in this region. This is
4274 supported by the observation of strike-slip faults within the conjugate Bajocian deposits of
4275 Madagascar (Chapter 4). The formation of these different types of margin surrounding the

4276 WSB may have been facilitated by several mechanisms suggested to assist continental
4277 rupture. The northern margins follow branches of the Karoo rift system and pre-existing
4278 lithospheric weaknesses may therefore have influenced continental breakup (e.g. Audet and
4279 Bürgmann, 2011). The western margins of the WSB and TCB also follow the pre-existing
4280 Karoo rift system, and additionally have undergone oblique rifting, both of which may have
4281 facilitated breakup (e.g. Brune et al., 2012). The Rovuma Transform Margin, however, did
4282 not follow any apparent pre-existing rift system, but was highly oblique (Chapter 3). Rifting
4283 in the Mozambique basin to the south was contemporaneous with large amounts of
4284 volcanism and, therefore, thermal weakening due to magmatism may have played an
4285 important role in facilitating continental breakup in this basin (e.g. Buck, 2007). This
4286 suggests that a collaboration of different rifting facilitators led to the breakup of Gondwana.
4287 The prolonged and episodic phase of Karoo rifting prior to volcanism in Mozambique and
4288 subsequent Gondwana dispersal may reflect this necessity for interplay of mechanisms to
4289 achieve successful supercontinent breakup (Chapter 2). Chapter 4 shows that the change in
4290 spreading direction during the Late Jurassic may have been triggered by the alignment of
4291 lithospheric weaknesses along the future trend of the DFZ. This suggests that plate motion
4292 changes are not necessarily driven by changes in bottom-up driving forces, and,
4293 consequently, that plate motions may not purely reflect such driving forces but are also
4294 subject to top-down controls on plate motion of a first-order significance (e.g. Brune et al.,
4295 2016). This questions whether observations of plate motions may be used to make inferences
4296 about dynamic processes in the mantle which are thought to drive plate tectonics, and
4297 therefore has large consequences for future academic studies in this field (e.g. Becker and
4298 Faccenna, 2011).

4299 The change in plate motions during the Late Jurassic (Chapters 2 and 4) led to the formation
4300 of the DFZ, yet contradictory evidence exists as to whether this occurred sharply by the
4301 cutting of new faults, or gradually by the formation of curved fracture zones. Chapter 2
4302 shows that curved gravity lineaments from the northern and southern regions of the WSB are
4303 best accounted for by a gradual plate rotation. Chapter 4, however, presents evidence for the
4304 crosscutting of a SSE trending fracture zone (the TCBtb) by the DFZ suggesting a sharp
4305 plate motion change in this region. Two important factors allow for these observations to be
4306 reconciled. Firstly, in Chapter 4, a significant amount of internal plate deformation within
4307 the TCB is also observed, which, despite local manifestation as sharp crosscutting indicators
4308 of plate motion, could allow for gradual plate motion changes away from this deformation.
4309 This emphasises the importance of introducing such internal plate deformation (e.g. Eakin et
4310 al., 2015) into future generations of plate tectonic models. Secondly, Chapter 3 contains
4311 suggestions that the recent discovery of Pan African age (533 Ma) zircons within the

4312 xenoliths of Grande Comore may indicate a microcontinent cleaving event during the Late
4313 Jurassic change in plate motions (Roach et al., 2017). Such a cleaving event would allow for
4314 a period of simultaneous ocean spreading along two overlapping MOR systems within the
4315 WSB. Whilst the same total amount of extension in the WSB would result as predicted in
4316 Chapter 2, the gradual reduction in spreading and eventual extinction of the original MOR
4317 system at the expense of increased spreading along the propagating (cleaving) MOR system
4318 would lead to the development of arcuate fracture zones and the abandonment of a triangular
4319 ocean basin (Figure 5.1; e.g. Nunns, 1983). The Comoros Basin, between the Comoros
4320 island chain and the northern margin of Madagascar, has such a triangular geometry (e.g.
4321 Figure 2.4) and this scenario is thus worthy of further investigation. Microcontinent release
4322 during such plate motion changes possibly offers a new mechanism to explain the large
4323 numbers of enigmatic microcontinents being discovered within oceanic domains (e.g.
4324 Whittaker et al., 2016). These continental fragments, e.g. the recently interpreted Biera High
4325 microcontinent offshore Mozambique (e.g. Mueller et al., 2016), may offer new prospective
4326 zones for hydrocarbon exploration, and understanding their development is crucial for
4327 locating potential future resource exploration opportunities.

4328



4330

4331 **Figure 5.1.** Schematic of the proposed 'Comoros Microcontinent' cleaving during the Late
 4332 Jurassic change in plate motions. The sudden change in plate motion may form arcuate
 4333 fracture zones due to the development of a second spreading axis which gradually takes over
 4334 from the first.

4335 **5.1. References**

- 4336 Audet, P., Bürgmann, R., 2011. Dominant role of tectonic inheritance in supercontinent cycles. *Nat.*
4337 *Geosci.* 4, 184–187. doi:10.1038/ngeo1080
- 4338 Becker, T.W., Faccenna, C., 2011. Mantle conveyor beneath the Tethyan collisional belt. *Earth*
4339 *Planet. Sci. Lett.* 310, 453–461. doi:10.1016/j.epsl.2011.08.021
- 4340 Brune, S., Popov, A.A., Sobolev, S. V., 2012. Modeling suggests that oblique extension facilitates
4341 rifting and continental break-up. *J. Geophys. Res. Solid Earth* 117, 1–16.
4342 doi:10.1029/2011JB008860
- 4343 Brune, S., Williams, S.E., Butterworth, N.P., Müller, R.D., 2016. Abrupt plate accelerations shape
4344 rifted continental margins. *Nature* 536, 201–204. doi:10.1038/nature18319
- 4345 Buck, W.R., 2007. Dynamic Processes in Extensional and Compressional Settings: The Dynamics of
4346 Continental Breakup and Extension. *Treatise Geophys.* 335–376.
- 4347 Coffin, M.F., Rabinowitz, P.D., 1987. Reconstruction of Madagascar and Africa: Evidence From the
4348 Davie Fracture Zone and Western Somali Basin 92, 9385–9406.
- 4349 Eakin, C.M., Long, M.D., Scire, A., Beck, S.L., Wagner, L.S., Zandt, G., Tavera, H., 2015. Internal
4350 deformation of the subducted Nazca slab inferred from seismic anisotropy. *Nat. Geosci.* 9, 56–59.
4351 doi:10.1038/ngeo2592
- 4352 Gaina, C., Torsvik, T.H., van Hinsbergen, D.J.J., Medvedev, S., Werner, S.C., Labails, C., 2013. The
4353 African plate: A history of oceanic crust accretion and subduction since the Jurassic.
4354 *Tectonophysics* 604, 4–25. doi:10.1016/j.tecto.2013.05.037
- 4355 Mueller, C., Jokat, W., Schreckenberger, B., 2016. The crustal structure of Beira High, central
4356 Mozambique—Combined investigation of wide-angle seismic and potential field data.
4357 *Tectonophysics* 683, 233-254.
- 4358 Nunns, A.G., 1983. Plate Tectonic Evolution of the Greenland-Scotland Ridge and Surrounding
4359 Regions BT - Structure and Development of the Greenland-Scotland Ridge: New Methods and
4360 Concepts, in: Bott, M.H.P., Saxov, S., Talwani, M., Thiede, J. (Eds.), . Springer US, Boston, MA,
4361 pp. 11–30. doi:10.1007/978-1-4613-3485-9_2
- 4362 Roach, P., Milsom, J., Toland, C., Matchette-Downes, C., Budden, C., Riaroh, D., Houmadi, N.,
4363 2017. New Evidence Supports Presence of Continental Crust beneath the Comoros. PESGB, 16th
4364 African E&P Conf. London.
- 4365 Whittaker, J.M., Williams, S.E., Halpin, J.A., Wild, T.J., Stilwell, J.D., Jourdan, F., Daczko, N.R.,
4366 2016. Eastern Indian Ocean microcontinent formation driven by plate motion changes. *Earth*
4367 *Planet. Sci. Lett.* 454, 203–212. doi:10.1016/j.epsl.2016.09.019
- 4368